Molecular dynamics studies of peptide-membrane interactions: Insights from coarse-grained models

Paraskevi Gkeka

A thesis submitted for the degree of Doctor of Philosophy
The University of Edinburgh
April 16, 2010

Abstract

Peptide-membrane interactions play an important role in a number of biological processes, such as antimicrobial defence mechanisms, viral translocation, membrane fusion and functions of membrane proteins. In particular, amphipathic α-helical peptides comprise a large family of membrane-active peptides that could exhibit a broad range of biological activities. A membrane, interacting with an amphipathic α-helical peptide, may experience a number of possible structural transitions, including stretching, reorganization of lipid molecules, formation of defects, transient and stable pores, formation of vesicles, endo- and pinocytosis and other phenomena. Naturally, theoretical and experimental studies of these interactions have been an intense on-going area of research. However, complete understanding of the relationship between the structure of the peptide and the mechanism of interaction it induces, as well as molecular details of this process, still remain elusive. Lack of this knowledge is a key challenge in our efforts to elucidate some of the biological functions of membrane active peptides or to design peptides with tailored functionalities that can be exploited in drug delivery or antimicrobial strategies.

In principle, molecular dynamics is a powerful research tool to study peptide-membrane interactions, which can provide a detailed description of these processes on molecular level. However, a model operating on the appropriate time and length scale is imperative in this description. In this study, we adopt a coarse-grained approach where the accessible simulation time and length scales reach microseconds and tens of nanometers, respectively. Thus, the two key objectives of this study are to validate the applicability of the adopted coarse-grained approach to the study of peptide-membrane interactions and to provide a systematic description of these interactions as a function of peptide structure and surface chemistry.

We applied the adopted strategy to a range of peptide systems, whose behaviour has been well established in either experiments or detailed atomistic simulations and outlined the scope and applicability of the coarse-grained model. We generated some useful insights on the relationship between the structure of the peptides and the mechanism of peptide-membrane interactions. Particularly interesting results have been obtained for LS3, a membrane spanning peptide, with a propensity to self-assembly into ion-conducting channels. Firstly, we captured, for the first time, the complete process of self-assembly of LS3 into a hexameric ion-conducting channel and explored its properties. The channel has structure of a barrel-stave pore with peptides aligned along the lipid tails. However, we discovered that a shorter version of the peptide leads to a more disordered, less stable structure often classified as a toroidal pore. This link between two types of pores has been established for the first time and opens interesting opportunities in tuning peptide structures for a particular pore-inducing mechanism. We also established that different classes of peptides can be uniquely characterized by the distinct energy profile as they cross the membrane. Finally, we extended this investigation to the internalization mechanisms of more complex entities such as peptide complexes and nanoparticles. Coarse-grained steered molecular dynamics simulations of these model systems are performed and some preliminary results are presented in this thesis.

To summarize, in this thesis, we demonstrate that coarse-grained models can be successfully used to underpin peptide interaction and self-assembly processes in the presence of membranes in their full complexity. We believe that these simulations can be used to guide the design of peptides with tailored functionalities for applications such as drug delivery vectors and antimicrobial systems. This study also suggests that coarse-grained simulations can be used as an efficient way to generate initial configurations for more detailed atomistic simulations. These multiscale simulation ideas will be a natural future extension of this work.

Declaration of originality

I hereby declare that the research recorded in this thesis and the thesis itself was composed and originated entirely by myself in the School of Engineering, The University of Edinburgh.

Paraskevi Gkeka

"By chance, like people say, I suddenly found a strange refuge. However, this kind of luck does not exist. When someone needs something and tries to have it, it is not the luck that gives it to him, but his own will and effort that makes him look for it."
Herman Hesse (Demian)

Dedication

Στην οικογὲνειὰ μου.
Σας ευχαριστὼ για ὸλα.

To my teachers.
Through simple luck, divine intervention or both, I have been fortunate to have had exceptional teachers during my educational years.

Acknowledgements

I would like to take this opportunity to acknowledge those who have helped me complete this thesis. First and foremost, I would like to express my gratitude to my supervisor, Dr. Lev Sarkisov - his encouragement, support, and thoughtful advice have been immensely valuable for me. I am particularly grateful to him for his elegant and interesting research ideas, which were the best motivations for me to work. Lev, I truly enjoyed working with you.

I would like to thank my second supervisor, Dr. Tina Düren, for her helpful advice during these years of my PhD. I also wish to thank my examiners Prof. Mark Sansom and Dr. Perdita Barran for their comments on my thesis and the interesting discussion during my viva.

Finally, I would like to thank the Institute of Materials and Sciences of the University of Edinburgh for the financial support.

Contents

List of figures

List of tables

CHAPTER 1

Introduction

In this thesis, I apply coarse-grained molecular models to elucidate mechanisms of peptide-membrane interactions. The objective of this chapter is to introduce the components of the system (peptides, lipid membranes and bilayers), and their key characteristics. I will elaborate on why it is important to study and understand peptide-membrane interactions, how computer simulations and molecular modelling can be instrumental in gaining this knowledge and review the state of the art in this field. Finally, I will formulate the scope and objectives of this thesis and provide an outline of its structure.

1.1 Biological background

1.1.1 The biological membranes and lipid bilayers

The cell membrane is the basic structural part of the cell that encapsulates its contents and defines the intra- and extra- cellular space. It provides the integrity of the cell structure, preventing contents of the cell from leaking out, it regulates the transport of molecules across the cell (ions, nutrients etc.) and maintains the cell potential. Furthermore, the cell membrane serves as a protective barrier, which prevents transport of undesired molecules and pathogens into the cell. Molecular recognition mechanisms at the membrane surface, which allow the cell to detect a pathogen, also play an important role in cell signalling, and other forms of cell-cell interactions.

The most accepted representation of biological membranes, which was introduced by Singer and Nicolson in 1972, is the fluid mosaic model (Figure 1.1) [1]. In this description, a membrane is composed mainly of lipids and proteins that form a thin (from 6 nm to 10 nm width) bilayer film with membrane proteins either embedded in this structure or located at the surface of the membrane. Cell membranes consisting of several layers of this type are also possible. Other components of the cell membrane may include cholesterol, sugars and other organic species. The membrane structure is highly flexible and allows the lateral diffusion of both proteins and lipids.

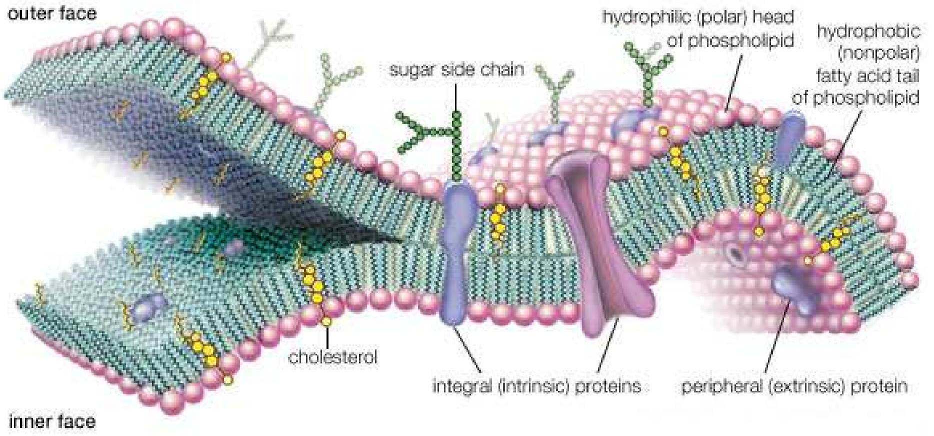

Figure 1.1: **The fluid mosaic model**. The membrane is composed of a bilayer structure, integral and peripheral proteins and several other organic molecules. The membrane proteins and the lipids are free to diffuse laterally in the bilayer. The figure was adapted from Encyclopedia Britannica web page [2].

Although most of the specific membrane functions (such as regulated ion conduction, molecular recognition, signalling etc.) are performed by membrane proteins, a number of membrane properties (such as mechanical elasticity, defects formation, phase behaviour and passive transport) are defined by the lipid bilayer. As a cell membrane is difficult to obtain in its full complexity in vitro, a lipid bilayer often serves as a model cell membrane in the studies of various membrane properties and functions.

Let us review the key characteristics of lipid bilayers, which one can view as cell membranes, with membrane proteins and other biomolecules that are usually incorporated in them removed. Even in this reduced form the lipid bilayer is a complex structure. Membrane lipids are small amphipathic molecules, made of two major components: fatty acids and a phosphate group. The fatty acids are the hydrophobic tails and the phosphates are the polar head-groups of the lipids. There are several different types of lipids including phosphatidyleserine (PS), phosphatidylglycerol (PG), phosphatidylcholine (PC) and phosphatidylethanolamine (PE). In the case of PS and PG lipids the head-group is negatively charged.

Due to this amphipathic nature, lipids are able to spontaneously form lamellar structures, such as lipid bilayers, at specific environmental conditions and lipid-water compositions. Other than lipid bilayers, lipids can form micelles or vesicles. In Figure 1.2, I present a phase diagram of the lipid phase transitions. In this study we are interested in lipid bilayers.

The lipid tails of the lipid bilayer are normally highly fluid. In the liquid crystal state, the lipid tails are disordered and in constant motion. At lower temperature, the lipid bilayer undergoes transition to a crystalline state in which fatty acid tails are fully extended, packing is highly ordered, and the van der Waals interactions between adjacent chains are maximal. Different types of lipid bilayers have different transition temperatures. For example, a DPPC lipid bilayer has a transition temperature of 325 K whereas DOPC has a transition temperature of 300 K.

In the fluid state, the hydrophobic core of the lipid bilayer is about 3-4 nm thick, depending on the type of lipids it has. Other key characteristics of a lipid bilayer include the area per lipid and the order parameters of the lipid configuration. These two characteristics are often used to compare simulation results with experiments. For exam-

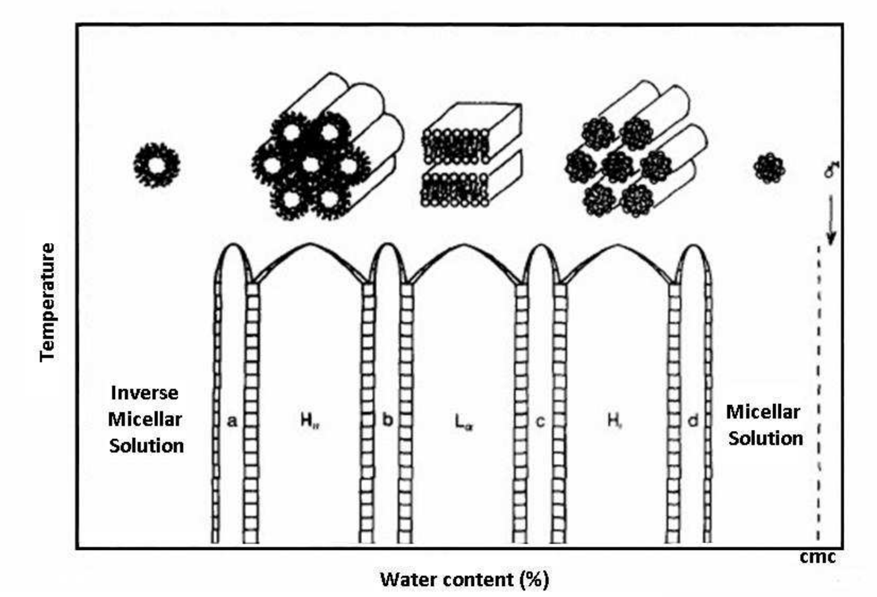

Figure 1.2: **Lipid phase diagram**. The figure was adapted from [3].

ple, a DOPC lipid bilayer has an area per lipid of 72.2 $Å^2$ [4] and this value can be used to validate a force field or as a point of reference for a simulation result. The order parameter is a measure of ordering of the lipids. It can indicate possible structural deformations of a lipid bilayer and thus it constitutes an important characteristic.

The composition of real cell membranes is complex, but quite often, at least as a starting point, in membrane studies and membrane-protein studies, a model system of a bilayer consisting of one specific lipid (usually DOPC and DPPC) is employed. A similar approach will be adopted here.

1.1.2 Peptides

A peptide is composed of amino acids. In general, there are 20 different amino acids commonly found in peptides and proteins. Each of them is formed by an amino group, a carboxyl group, a central CH group (the carbon of this central CH group is usually called α-carbon or C_α) and a specific side chain (Figure A.1, Appendix A). The sequence of C_α atoms connected through covalent peptide bonds, including the N-terminus (free NH2 initial group) and C-terminus (free COOH final group) is called the peptide backbone. It is the main structural part of the peptide that determines its overall geometric properties. The side-chains of a peptide define its physical and chemical properties.

The structure of a peptide or a protein can be described at different levels (Figure A.2, Appendix A). The *primary structure* of the peptide describes the actual sequence of amino acids, or residues, within the peptide. The term *secondary structure* refers to the geometry or conformational behaviour of this primary sequence. A disordered peptide chain is often called a random coil. However, many peptides have well-defined three-dimensional secondary structure. Three of the most frequently occurring structures are the *α-helix*, the *β-sheet* and *β-turns*. In a larger protein, the three dimensional arrangement, or packing of secondary units, is characterized by the *tertiary structure*, whereas assemblies of several proteins are classified as *quaternary structures*.

A common secondary structural motif in biologically active peptides is the amphipathic α-helix. An α-helix is formed when a chain of amino acids twists around itself in a well-ordered way (Figure 1.3(a)). This helical structure is stabilized by a network of backbone hydrogen bonds between the backbone carbonyl oxygen of residue i and the amide proton of residue i+4, with the side groups of the amino acid residues protruding outward from the helical backbone. The rise along the helical axis for every two successive α-carbons is 1.5 Å and the respective rotation is about 100 degrees. Moreover, each helical turn extends for about 5.4 Å along the long axis of the helix, resulting in 3.6 residues per turn (Figure 1.3(a)). Another important feature of an α-helical peptide is the inherent net dipole that exists along its axis due to the synergy of each of the small dipoles that exist in each peptide bond (Figure 1.3(b)). The helical dipole plays an important role in pore formation and stabilization and ion transport across membranes.

An α-helix is called amphipathic when it has both hydrophobic and hydrophilic residues positioned along its axis. This distribution of hydrophobicity has been shown to play an important role in the way with which the amphipathic α-helical peptides interact with the biological membranes [6]. Amphipathic α-helices are the peptides of interest in this study and more details about their function will be given in the next chapters.

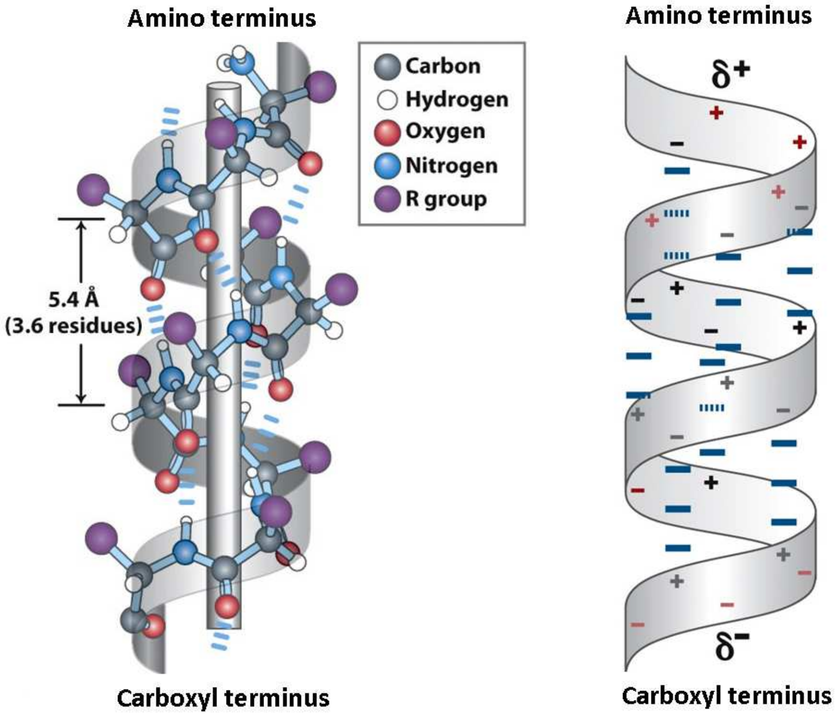

(a) **Ball-and-stick representation of an α-helix.** (b) **Helix dipole.**

Figure 1.3: **The α-helix**. (a) Ball-and-stick representation of an α-helix, showing the hydrogen bonds between the i^{th} and $i^{th} + 4$ residues. (b) A helical dipole is created by the transmission of the electric dipole of the peptide bonds along the helical axis. The figure has been adapted from [5].

1.2 Peptide-membrane interactions

Peptide-membrane interactions are at the heart of a number of important biological processes. For example, antimicrobial peptides are a family of peptides with a particular propensity to recognize and disintegrate bacterial pathogens. A number of these peptides have been identified as key components of the natural immune defence system [7]. A related family of peptides is the so-called cell-penetrating peptides (CPPs) capable of efficient translocation through the cell membrane, either by themselves or together with a molecular cargo [8]. These peptides are being explored as potential programmable drug delivery vectors. As a part of larger proteins, ion-conducting channel peptides form well-organized transmembrane bundles capable of selective transport of ions. Other peptides are believed to play a key role in mediation of various complex cellular processes, such as membrane fusion. It is clear that a better understanding of peptide-membrane interactions on molecular level not only is important in the elucidation of various biological processes, but also could be instrumental in designing peptides with tailored functionalities, for example, for antibiotic and drug delivery applications.

Peptide-membrane interactions are complex and beautifully diverse phenomena. Depending on their composition, charge, and structure different peptides evoke different interaction mechanisms with the membrane. Here, I present some of the most commonly seen scenarios in the studies of peptide-membrane interactions. In this analysis, I exclusively focus on α-helical peptides. There are two reasons for this. First, α-helical secondary structure is abundant among membrane active peptides. Second, development of a fully comprehensive description of peptide-membrane interactions is a challenging task. Having the peptide in a well-defined structure eliminates at least one additional degree of complexity associated with the conformational behaviour of the peptide itself. Thus, α-helical peptides are a natural starting point in the construction of this description.

Let us first consider different peptide internalization mechanisms. These mechanisms can be categorized into endocytosis mediated entry and direct penetration in the membrane. *Endocytosis* is an important biological process, used by the cell for transport of various molecular species across the cell membrane. In the case of peptide transport, its mechanism can be described as follows; first, several peptides form an aggregate in the aqueous phase, then the cell absorbs the aggregate from the outside environment by engulfing it with its cell membrane and finally, a vesicle (endosome) is formed and released on the inner side of the membrane (Figure 1.4(a)). In principle, spontaneous formation of an endosome is possible as a result of membrane fluctuation and budding. However, more commonly, endocytosis is a receptor mediated and energy dependent process. Several classes of cell-penetrating peptides are believed to induce this mechanism.

Direct penetration mechanisms, on the other hand, are receptor and energy independent, and may also be classified in several distinct scenarios. One of these mechanisms is the *sinking raft model*. In this model, the peptides form aggregates of limited size and associate with one of the faces of the membrane. The mass imbalance of the lipid bilayer due to this association induces curvature that provides the driving force for the translocation of peptides across the bilayer [14] (Figure 1.4(b)). This mechanism has been proposed for several antimicrobial peptides, for example delta-Lysin [10] . Another scenario of direct penetration is the *formation of an inverted micelle*. In this case, a peptide interacts with the negatively charged phospholipids, inducing the formation of an inverted micelle inside the lipid bilayer (Figure 1.4(c)). Then, either the peptide is entrapped within the micelle and then released into the cell, or the formation of the micelle perturbs locally the membrane and induces a new peptide insertion event.

The formation of transmembrane pores is another way of interaction between α-helical peptides and membranes. Three different pore structures, the barrel-stave, the carpet and the toroidal pore model, have been proposed and investigated. The main differences between these models lie in the lipid structure around the pores and the pore stability. In the barrel-stave model, the lipids are parallel to each other and the peptides form a well-defined, very stable bundle, which, if it is of a sufficient diameter, can serve as a pore. This is believed to be the structure of the peptides in ion-conducting channels, either as a part of a larger protein, or formed through a self-assembly process. In the case of the toroidal model, the lipids create a toroidal-shaped (or donut-shaped) opening covered with the peptides in different orientations. Toroidal pores are generally less stable (i.e. they are transient) than the barrel-stave pores. Some studies suggest that this mechanism is involved in membrane disruption action of some antimicrobial peptides, leading to cell leaking out its contents [15].

In the carpet model, peptides accumulate on the membrane until its integrity is breached and transient holes are formed. These holes, when the peptides are in high concentrations, may result into the complete collapse of the membrane. Again, this mechanism has been proposed, among others, as permeabilization mechanism of α-helical *antimicrobial peptides* (AMPs) (Figure 1.4(d)).

Several peptide-membrane interaction mechanisms involve a peptide inserted in the membrane. In membrane fusion, the fusion peptides, short hydrophobic parts of fusion proteins, destabilize the lipid bilayer structure by adopting an oblique orientation within the membrane [6]. This orientation has been linked to the gradient of hydrophobicity along the helical axis of the peptides. In Figure 1.4(e), I show one of the proposed scenarios, as presented in [12]. Other peptides, with different distribution of hydrophobicity, adopt interfacial or transmembrane orientations relative to the membrane.

Many mechanisms include several stages of interaction between peptides and membrane or between different peptides. For example, in the case of Pep-1, a cell-penetrating peptide with high efficiency as drug-delivery vector, one of the proposed internalization mechanisms consists of four steps: a number of Pep-1 helices form a complex with the cargo, other helices form a pore, the cargo-peptide complex passes through the pore and finally it is released into the cytoplasmic side [13] (Figure 1.4(f)).

The mechanisms mentioned above have been validated for some specific peptides. For example, the formation of pores can be confirmed from the observation of leaking cell contents (marked with fluorescent agents). The role of endocytosis can be probed by blocking specific receptors responsible for some of the stages of the process. Properties of ion-conducting bundles (such as for example, their inner diameter) have been investigated through ion-conduction experiments [16–20]. Formation of a complex of several peptides with a cargo, as a requirement for a successful membrane translocation has also been confirmed, in the studies where translocation efficiency was measured as a function of peptide concentration [13].

However, the exact manner in which the peptides interact with membranes and molecular details of this process are still an area of active research and a matter of extensive debate and controversy. Different peptides utilize different interaction mechanisms or combinations of mechanisms that are not limited in one class of peptides or the other. Furthermore, the mechanisms of interaction can change depending on the conditions of the system, such as pH, temperature and concentration of peptide. The principal challenge remains as follows: in order to understand the biological processes, based on peptide-membrane interactions, or to design peptides with tailored functionalities for specific applications, we need to establish, with molecular resolution, the link between the structure and physical characteristics (for example hydrophobicity distribution or charge) of the peptide and the particular interaction mechanism it induces.

In the next section, I will briefly review some of the experimental techniques that can be used to acquire this knowledge.

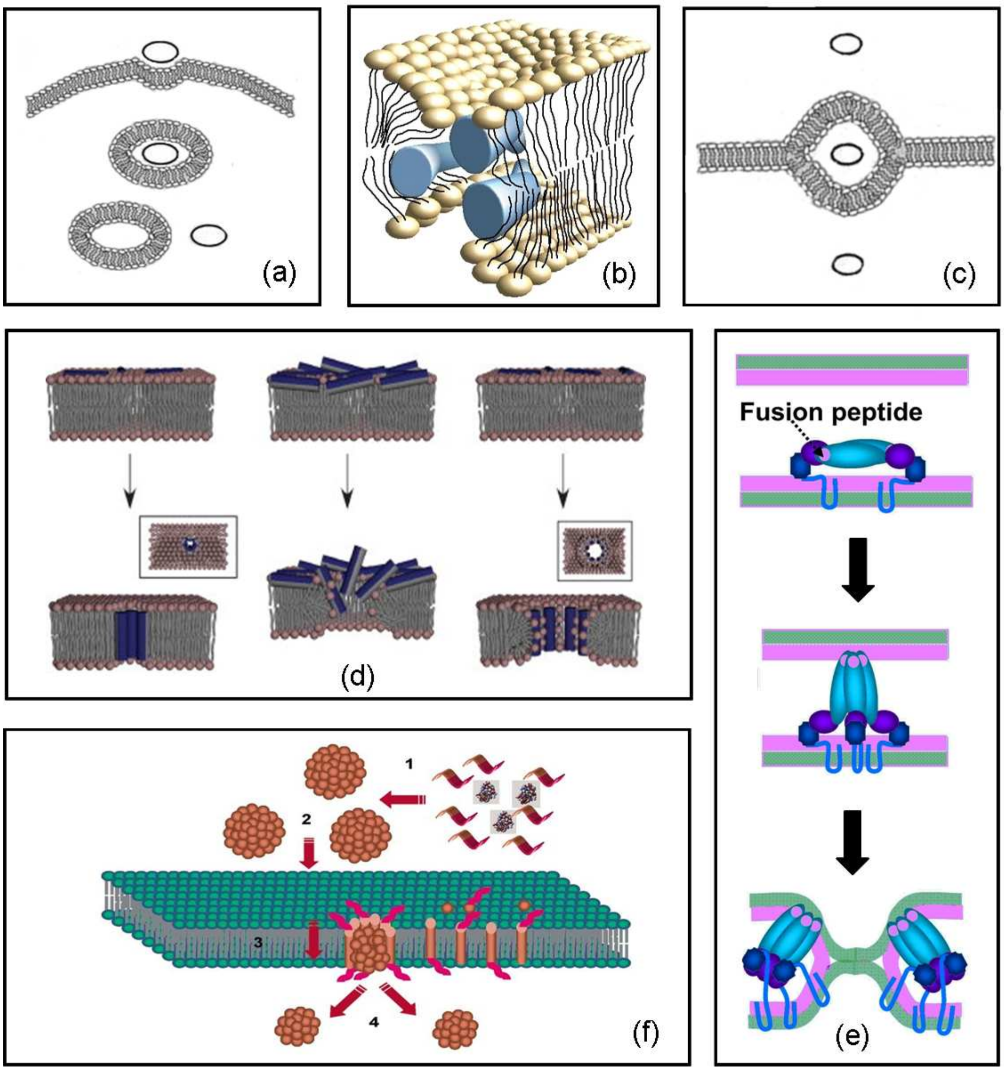

Figure 1.4: **Schematic of possible peptide-membrane interactions**. (a) Endocytosis. Figure adapted from [9] (b) The sinking-raft model, adapted from [10]. (c)The inverted micelle model. Figure adapted from [9]. (d) Different pore formations proposed for α-helical antimicrobial peptides, adapted from [11]. (e) One of the proposed mechanisms for fusion, adapted from [12]. (f) Proposed schematic model for the internalization of the Pep-1/cargo complex through the membrane, adapted from [13].

1.3 Experimental techniques and limitations

During the last decades, several experimental techniques have been developed and applied to biological systems. These techniques differ in the nature (alive, preserved or sectioned) and the size of the sample they can be used for, their sensitivity and the type and resolution of information they can provide. In this section, I will present some of the most recent and the most significant methods and studies and I will discuss their limitations.

The location and orientation of a peptide relative to a lipid bilayer as well as lipids rearrangement in the presence of a peptide are two important structural characteristics of peptide-membrane interactions. Experimental techniques that have been used to get structural information include *Fourier Transform Infrared Spectroscopy* (FTIR) [21–27], *X-ray* and *Neutron Diffraction* methods [28, 29] as well as *Nuclear Magnetic Resonance* (NMR) [30–38]. However, the possibilities of using for example X-ray or neutron diffraction to gain detailed insights into peptide-membrane systems are limited, since these systems lack long-range crystalline order. NMR and specifically solid-state NMR has numerous applications in peptide systems over the last years [33–39]. A series of NMR studies by Opella and co-workers has provided important insights in peptide orientation [40–42]. *Atomic Force Microscopy* (AFM) has also been used for the structural characterization of peptide-membrane systems. Ripple phases in lipid bilayers induced by lipopeptides, destabilization of a bilayer due to fusion peptides, and restructuring of the membrane in the presence of specific peptides are some of the examples where AFM has been used to get information about peptide-membrane interactions [43–45]. On the other hand, however detailed are the structural characteristics captured by AFM, the method generally does not provide any chemical information of the system under study. A recent improvement in this area is the use of functionalized AFM tip [46].

There are also experimental techniques that can be used in order to map the position of different molecules in a peptide-lipid bilayer system. *Imaging Mass Spectrometry* (IMS), like MALDI[1] imaging and secondary ion mass spectrometry (SIMS), is one of the latest techniques to be developed and among the most powerful ones [47–49]. An-

---

[1] MALDI: matrix-assisted laser desorption ionization

other promising imaging technique is *Surface Plasma Resonance* (SPR) spectroscopy, that allows for the real-time observation of peptide binding to phospholipid bilayers [50, 51] and membrane-mediated cell signalling [52]. Other imaging techniques used in peptide-lipid studies are *Light Scattering Spectroscopy* (SLS (static) or DLS (dynamic)) [53], *Fluorescence Spectroscopy* [54].

Even with this broad arsenal of experimental techniques it is still difficult to obtain complete and detailed information about the modes of peptide-membrane interactions. Let us illustrate the challenges in some of the experimental techniques using an example of a direct relevance to the current study. Bradshaw and co-workers have performed a series of important experimental studies on the SIV fusion peptide [29, 55, 56]. In one of them, the authors carried out neutron diffraction measurements from stacked multilayers of DOPC and determined the location and orientation of specifically deuterated SIV fusion peptides within the bilayer. The results from this study showed that there are two different populations of peptides. One major population close to the bilayer surface, and a smaller population hidden in the hydrophobic core. Two equally plausible orientations at 55^o and 78^o with respect to the bilayer normal, were found consistent with the experimental observations. However, based on the additional FTIR data from previous studies, the oblique orientation at 55^o was accepted as the most probable one.

This illustration also highlights several issues, characteristic for most of the experimental techniques. First and foremost, the obtained data corresponds to an equilibrium average over multiple peptide-membrane configurations (in this specific case, average over various angle and location distributions). Thus, detailed information about a particular configuration of interest or the detailed information about dynamics of peptide-membrane assembly is beyond the scope of this approach. Furthermore, to interpret the obtained data, a model is required, construction or contemplation of which may be a challenge in itself. Unambiguous behaviour, quite often, can be derived only using several complementary experimental techniques (in this case, additional data from FTIR were required). Finally, although as I have already mentioned, some of the experimental methods are now able to provide a more detailed and dynamic information, it is also important to remember that in general experimental studies are expensive and time consuming.

Thus, we still need a description of peptide-membrane interactions which would consider behaviour of an individual or several peptide molecules, elucidate the dynamics of the peptide-membrane assembly process, provide a link between the observed behaviour and the data measured in experiments and be sufficiently modest in the resources required to systematically explore a large number of systems. I believe these issues can be addressed within computer simulations, and specifically molecular dynamics. I will review recent progress in the area with a focus on peptide-membrane interactions in the next section.

1.4 Molecular modelling and computer simulations of peptide-membrane interactions

Over the years, a number of theoretical and computer simulation approaches have been developed to describe membrane behaviour and peptide-membrane interactions. These approaches vary in the way the peptide-membrane system is modelled and what type of information can be obtained from this model. For example, a lipid bilayer can be modelled as essentially an infinite hydrophobic slab (with varying degree of complexity) through some effective field function. This approach is usually adopted in various mean-field models developed over the years. Quite often, to reduce the computational load, solvent is not included in the model explicitly, and its presence is accounted for through some effective interactions between the remaining components.

In its general form, a mean-field method indicates that the lipid bilayer and the surrounding water are described by an empirical energy function. In Figure 1.5 there is a schematic of the lipid bilayer and the water phase and one of the possible energy functions $f(z)$ used in the mean-field methods to define the different levels of hydrophobicity in the system. When a peptide or protein is considered (represented by a cylinder in the schematic), a hydrophobic term is included in the potential energy function. This term shows the contribution of each residue of the peptide in the peptide-membrane interactions.

An approach based on the mean-field theory is the *self-consistent field* (SCF) theory. In SCF theory the van der Waals-type interactions are used for the different types of

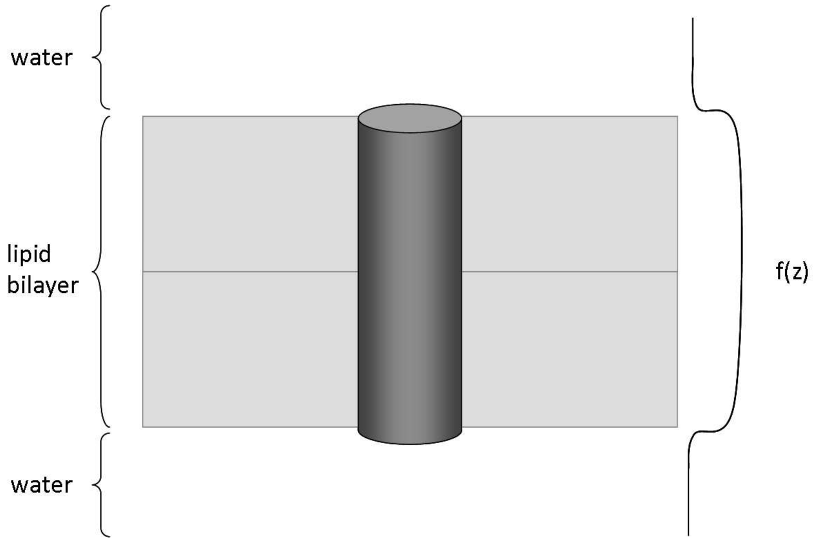

Figure 1.5: **Mean-field model for the treatment of peptide-membrane interactions**. The lipid bilayer is represented by a hydrophobic slab.

particles as well as the configurational entropy of the lipid tails. Leermakers and co-workers have applied SCF theory in a series of membrane and membrane-peptide studies [57–59]. In a recent study, SCF theory was also used by Liang and Ma to study the effects of inclusions in supported mixed lipid bilayers [60]. In [61] and [62], the same authors combined SCF theory and density functional theory to investigate the structural organization of membrane proteins in lipid bilayers as well as the effect of nanosized hydrophobic inclusions in lipid bilayers. Mean-field theory was also used by Lague and co-workers [63–65]. The authors employed a mean-field approach based on results from fully detailed atomistic simulations, to develop a theory for defining the structure of the lipid chains around a model membrane protein and to study the lipid-mediated protein-protein interactions. Also, La Rocca et al. used mean-field theory to determine the optimal orientation of a helical peptide in a lipid bilayer [66, 67].

Another implicit-solvent approach is the generalized Born/surface area (GB/SA) models [68]. Im *et al.* in a series of studies have used the GB/SA approach to study membrane peptides [69, 70]. Also, Ulmschneider and co-workers developed an implicit-membrane representation and applied it in influenza M2 peptide and glycophorin A dimer [71, 72].

One of the most important limitations of mean-field based approaches are the simplifications that need to be made in order to develop feasible analytical theories. The description of the lipid bilayer by a free energy functional cannot capture the complexity that lies at the molecular level of the membrane. Moreover, the difficulty in linking the parameters used in these models with physical properties constitutes an important disadvantage.

In order to select an appropriate approach from a huge number of models and methods developed over the last 40-50 years, it is important to formulate the long term goals of this study. I would like to develop a capability to describe peptide-membrane interaction processes in their entire complexity, from the dynamics of the self-assembly processes to equilibrium properties of peptide-membrane systems. This objective imposes several key restrictions on our choice of methods. It is evident, that peptide-membrane self-assembly processes, such as formation of trans-membrane pores, requires significant structural rearrangement of both peptides and the membrane. This process also seems to be mediated (at least to some extent) by the solvent. Thus, our description must be based on a reasonably detailed model of all the components of the system, i.e. solvent, peptides, lipid bilayer. This restriction excludes the models based on membrane as an effective hydrophobic medium and implicit solvent models. Next, I am interested not only in the final equilibrium properties of the system, but in the actual process of self-assembly. Therefore, it seems that most of the conventional Monte Carlo approaches would not be appropriate here. On the other hand, Molecular Dynamics seems to satisfy all the required conditions and, therefore, in the review of the recent studies of peptide-membrane interactions I will mostly focus on this approach, with occasional diversion into other methods.

There has been significant progress in the field of molecular dynamics simulations of biomolecular systems since the first simulation of a protein in vacuum, reported 33 years ago [73] (see Table A, Appendix A). Some of the first studies of membrane-peptide interactions employing molecular dynamics simulations on a sub-nanosecond timescale include the study of a model peptide designed to anchor to bilayer surfaces [74], amphipathic α-helices [75] and the bee venom peptide melittin [76].

Recently, several atomistic molecular simulation studies attempted to address long-scale peptide-membrane phenomena in their full complexity. In one of these studies, Leontiadou and co-workers captured toroidal pore formation in simulations of antimicrobial peptide magainin-H2 and a model phospholipid membrane [77]. Studies of toroidal pore formation and its structural characteristics have been further extended by Sengupta and co-workers [78]. In another example, Herce and Garcia applied fully atomistic simulations to propose a complex multistage mechanism of HIV-1 TAT peptide translocation across the membrane [79]. Formation of a transient pore was observed, with the peptides diffusing on the surface of the pore to cross the membrane. An alternative mechanism, based on micropinocytosis, has been suggested for TAT translocation in fully atomistic studies by Yesylevskyy and co-workers. In micropinocytosis a cluster of peptides wraps the membrane around itself to form a small vesicle [80]. A similar mechanism of translocation was reported by the same group for another cell-penetrating peptide, Penetratin. None of these simulations however spanned timescale beyond several hundred of nanoseconds, and in many cases the simulations were limited to tens of nanoseconds. Routine operation on longer time scale still remains prohibitively expensive in atomistic simulations. This limitation imposed by atomistic simulations led to the development of coarse-grained approaches to study complex biomolecular phenomena.

Coarse-grained approaches are based on the idea of systematically reducing the level of detail in the way the system is represented, and thus increasing the time/length scale of the simulation. One way of doing this is by modelling the system as a group of effective particles ('beads'). Each of these beads represents an ensemble of atoms whose atomistic degrees of freedom do not play an important role in the process under consideration and are integrated out. This leads to several implications. First of all, it results in the expected improvement in computational efficiency of the model due to the reduced number of degrees of freedom (depending on the level of coarse-graining). Furthermore, as has been noted in a number of studies, smoothing out of fine-grained degrees of freedom in CG models reduces the effective friction between the molecules. As a result, many complex processes such as biomolecular self-assembly occur on a shorter effective time scale.

Several strategies to construct CG models have been offered over the years. For example, the interactions between coarse-grained beads can be calibrated to reproduce the forces between the corresponding groups of atoms in atomistic simulations [81]. Alternatively, the coarse-grained model can be calibrated to reproduce certain physical characteristics of the system of interest, such as density, phase transitions and structure [82]. In Figure 1.6, some representative coarse-grained models for lipids are shown. he article by Venturoli and co-workers is an excellent review of the current developments and achievements in this field [83]. State-of-the-art in atomistic and CG simulation studies of lipid membranes, including peptide-membrane interactions, has also been recently reviewed by [84]. Another recent review on the advances in the area of multi-scale modelling is the one by Murtola *et al.* [85].

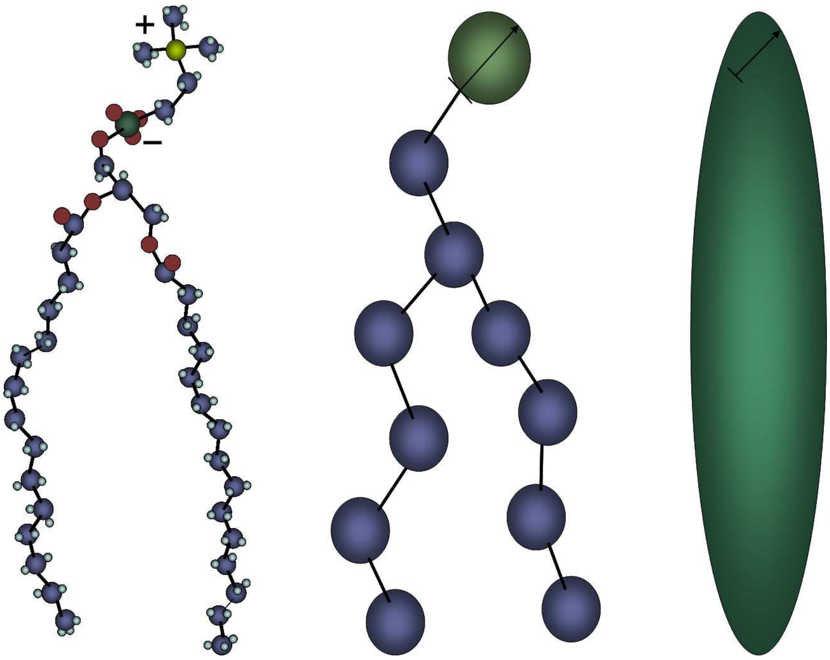

Figure 1.6: **Coarse-grained models for lipids**. (a) Atomistic representation. (b) Group of ∼4-5 atoms is represented as a 'bead' [82]. (c) Every lipid is represented as a Gay-Berne particle [86].

Using coarse-grained models, it has been possible to investigate a number of processes related to biomembrane physics, which have been difficult to study by MD simulation methods on all-atom models. In the early 90's, Smit and co-workers developed a CG model of oil/water/surfactant system. Two types of particles are defined, labeled with the letters *o* and *w*. In this model, oil molecules are represented by a single *o* particle, water molecules by a single *w* particle and surfactant molecules are represented by a chain of two *w* particles followed by five *o* particles, each bound to its neighbour by a strong harmonic force. Simulations showed for the first time the spontaneous formation of micelles [87, 88].

Some years later, Groot and Warren introduced the Dissipative Particle Dynamics (DPD) technique into the field of biological systems [89]. In this technique, the forces are grouped together to yield an effective friction and a fluctuating force between the interacting sites. Kranenburg *et al.* employed DPD combined with a Monte Carlo scheme to achieve the natural state of a tensionless bilayer and managed to describe the phase behaviour of phospholipid bilayers [90]. Smit model has also been extended to study the structural changes resulting from the inclusion of a rod-like objects serving as an idealized protein [91]. Recently, this approach was used to systematically compute the potential of mean force (PMF) between two proteins as a function of the hydrophobic mismatch of the proteins [92, 93].

In the late 90's, a different kind of coarse-grained model was proposed. Goetz and Lipowsky, introduced an even simpler, idealised CG bilayer model, capable of qualitatively describing some fundamental membrane characteristics [94]. In this model, only two types of Lennard-Jones sites are included: hydrophilic sites, used to describe both solvent and lipid-head particles, and hydrophobic sites to model lipid-tail segments. Some of the phenomena captured by this model were bilayer self-aggregation, diffusion, and area compressibility.

Klein and co-workers developed a different coarse-grained model for simulating hydrated DMPC lipid bilayers which was one of the first attempts to include an explicit, but simplified, treatment of electrostatic interactions in a CG model. In this model, 118 atoms of a DMPC lipid are represented by a 13 CG sites. The two choline and phosphate head-groups were assigned +e and -e charges, respectively, and the potentials were parameterised in order to mimic structural properties obtained from atomistic simulations and experimental data. Water was modelled as spherically symmetric sites each representing a group of three water molecules. In 2001, Shelley et. al, using this model, studied the self-assembly of phospholipids into various phases, both in the absence and in the presence of biomolecules such as anaesthetics and alkanes [95, 96].

In 2004, Marrink *et al.* introduced a very simple, flexible and efficient CG model for lipid simulations [82], to describe properties of lipid-water systems. In their model, every four heavy atoms (i.e. not hydrogens) are represented by one effective bead. Four major types of beads and several variants were introduced to describe different levels of polarity and charge. The parameters used in this model were optimized using a trial and error procedure, in order to satisfactorily reproduce the experimental densities of pure water and alkane at room temperature and other experimentally obtained physical parameters. The model has been validated against several processes, such as lipid phase transitions, micellar and vesicle behaviour as well as lipid bilayer formation, clearly demonstrating that such complex processes are within its scope [97–99].

In the following years several attempts have been made to extend the original model of Marrink and co-workers to proteins, peptides and other biological entities. One of these extended models was recently proposed by Bond and Sansom [100, 101]. They introduced a model of proteins, where a representation for each amino acid was based on its properties (tendency to form hydrogen bonds, hydrophobicity/hydrophilicity and charge). The same idea of a four-to-one mapping was followed, with the amino acids modelled by one, two or three beads, one representing the backbone of the amino acid and the others the side chain. More information about the model can be found in the original publication [100]. With this protocol, the authors investigated different peptides in membranes, capturing, among other effects, the insertion and dimerization of Glycophorin A (GpA) [100], the insertion of OmpA protein and WALPs into a lipid bilayer [100] and the interfacial orientation of LS3 peptide in monomeric form [101]. The model has also been used for the prediction of several processes such as the insertion of DNA in a lipid bilayer [102], the interaction of membrane enzymes with lipid bilayers [103] and the dependence of peptide-membrane interactions on the initial structure of the peptide in different lipid environments [104].

Recently, a new version of the force field proposed by Marrink and co-workers has been developed, with an extension to proteins [105, 106]. The proposed model, MARTINI, features a larger number of bead types and interactions, and has been optimized to reproduce some key properties of amino acids, such as oil/water partition coefficients and association constants between different amino acids. Moreover, the model has been shown to accurately capture peptide-membrane interactions for several helical peptides [105], and to correctly reproduce the formation of a toroidal pore by magainin-H2, confirming earlier atomistic simulations [77]. Other applications of the MARTINI include the effect of temperature and membrane composition on the properties of liposomes in the limit of high curvature [107], the self assembly of cyclic peptides near or within membranes [108] and the formation of a barrel-stave pore by LS3 synthetic peptide [109].

Several other studies and approaches should also be mentioned. An innovative multiscale approach was followed by Izvekov and Voth in [110]. The authors developed a CG model for hydrated DMPC bilayers using a multiscale approach in which explicit atomistic forces are propagated in scale to the coarse-grained level. This method is not dependent on the matching of selected thermodynamic data, but it makes use of the calculated atomic forces from an underlying atomic level (AL) model. An improved version of this model was recently introduced and applied to studies of two peptides, Ala-15 and V_5PGV_5, and it exhibited good agreement with the structural properties of the peptides [111].

Another promising approach is the introduction of a new, very simple CG model for lipids proposed by Michel and Cleaver (Figure 1.6(c)). The model is a combination of spherical Lennard-Jones beads (for the choline and phosphate moieties) with Gay-Berne soft uniaxial ellipsoids (for the glycerol and hydrocarbon tails). In [86], the authors examined the ability of the model to exhibit amphiphilicity by studying the behaviour of appropriately tuned Gay-Berne particles immersed in a solvent of Lennard-Jones particles. The model is proved to be suitable for studying the effects of molecular interaction parameters on a range of self-assembly processes. A similar approach has been employed by Essex and co-workers in an effort to include different levels of detail in the system [112–114]. For example, in [114], the authors have studied the permeability of small molecules in atomistic representation across a lipid bilayer represented by Gay-Berne and LJ potentials.

Taken together, the aforementioned simulation studies demonstrate the power of molecular simulations in investigating the membrane-peptide interactions. In particular, molecular dynamics simulations have provided us with important information about the different interaction mechanisms at a molecular level. The overall strategy of this study is based on coarse-grained MD simulations combined, when necessary, with more detailed information taken from atomistic simulations as well as free energy calculations by means of umbrella sampling.

1.5 Nanoparticle membrane interactions

Because of the wide use of nanoparticles in a variety of products, varying from drug and gene delivery materials to consumer products like paints, it is important to understand how these materials interact with cell membranes [115–117]. In particular, the cytoxicity of these materials is one of the parameters that needs to be further studied, as it can either lead to a hazardous event or be used as targeted drug delivery, for example in cancer therapy.

There are numerous studies about the membrane internalization mechanisms and the cytoxicity of different types of nanoparticles [118]. In a recent study, Verma *et al*. used gold nanoparticles, coated with anionic and hydrophobic groups either at random positions or at striations of alternating groups [119]. The radius of the nanoparticles was approximately 6 nm. This study showed that the 'striped' nanoparticles were able to cross the cell membrane without bilayer disruption, whereas the other nanoparticles followed an endocytic pathway and were trapped in endosomes (Figure 1.7).

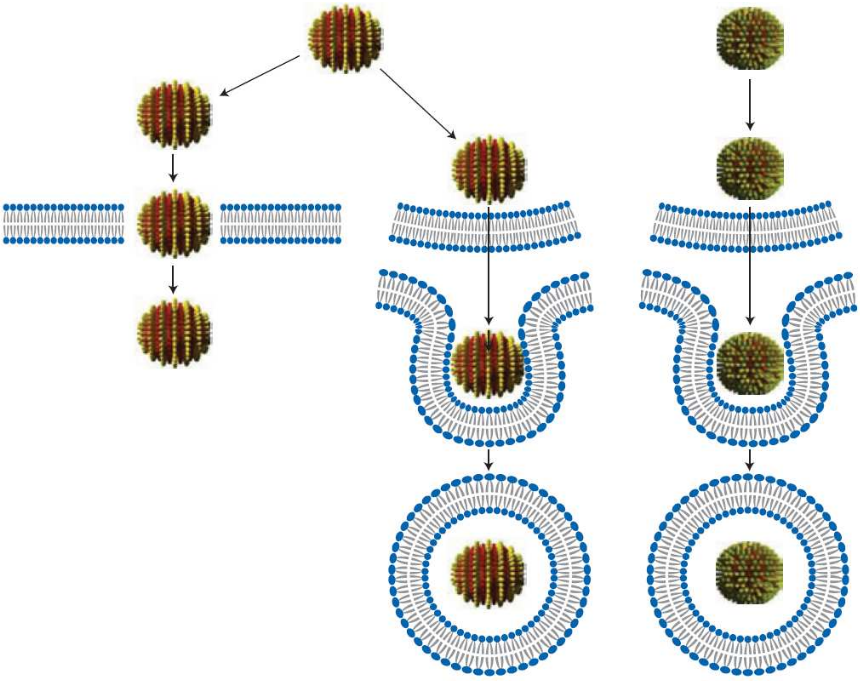

Figure 1.7: **Different uptake mechanisms of nanoparticles with different coatings**. The 'striped' nanoparticles are able to cross the cell membrane either directly without bilayer disruption *(left)* or by endocytosis *(centre)*, whereas the other nanoparticles follow an endocytic pathway and are mostly trapped in endosomes *(right)*. Figure adapted from [120].

In another study, Leroueil *et al*. used nanoparticles of different sizes injected onto supported lipid bilayers [121]. They found that cationic nanoparticles with a diameter of about 5-6 nm induced membrane disruption. Nanoparticles of a 50 nm size led to the formation of holes in the lipid bilayers.

Recently, a study with nanoparticles with sizes ranging from 1 nm to 140 nm was carried out by Roiter and co-workers [122]. In this work, the authors used AFM to capture the structural differences of a lipid bilayer after interacting with silica nanoparticles of different sizes. The results are shown in Figure 1.8. The lipid bilayer forms uniformly in the case of nanoparticles with diameter less than 1.2 nm. For nanoparticles larger than 1.2 nm or smaller than 22 nm thinning of the bilayer and formation of pores are observed. For nanoparticles larger than 22 nm, with and without bumps, coverage or incomplete coverage due to the bumps is observed. A similar study was performed by Ahmed and Wunder [123]. In this work, nanoparticles with a diameter of 5 nm induced the transition of the lipid bilayer from the lamellar to an interdigitated state.

Simulation studies have also been performed in the area of nanoparticle-membrane interactions. In [124], the authors captured the formation of holes in lipid bilayers induced by clusters of dendrimers at their surface. They used coarse-grained MD simulations, and in particular the MARTINI force field. Water and ions could pass through the pores which had diameters of 1-5 nm. In another study, the authors used DPD method in a stretched bilayer and observed the formation of holes under the dendrimer cluster as well as at other points of the bilayer [125]. In the case where a 'not stretched' bilayer was used, the dendrimers seemed to diffuse in the lipid bilayer and the clusters were deformed. Also, D'Rozario *et al*. performed coarse-grained MD simulations with particles of a diameter about 1.1 nm to study the interactions of pristine C_{60} and its derivatives with lipid bilayers [126]. The nanoparticles were represented as spheres with 20 evenly spaced coarse-grained particles of different types on their surfaces. Pristine was represented only by hydrophobic coarse-grained beads. Its derivatives $C_{60}(OH)_N$, with N = 5, 10, 15 or 20, were constructed by replacing N number of hydrophobic beads with polar ones. This replacement was either done at a patch of the nanoparticle, or at random positions. The authors performed MD simulations and they showed that the apolar and amphipathic fullerenes are mainly within the lipid bilayer, with the amphipathic nanoparticles being closer to the lipid

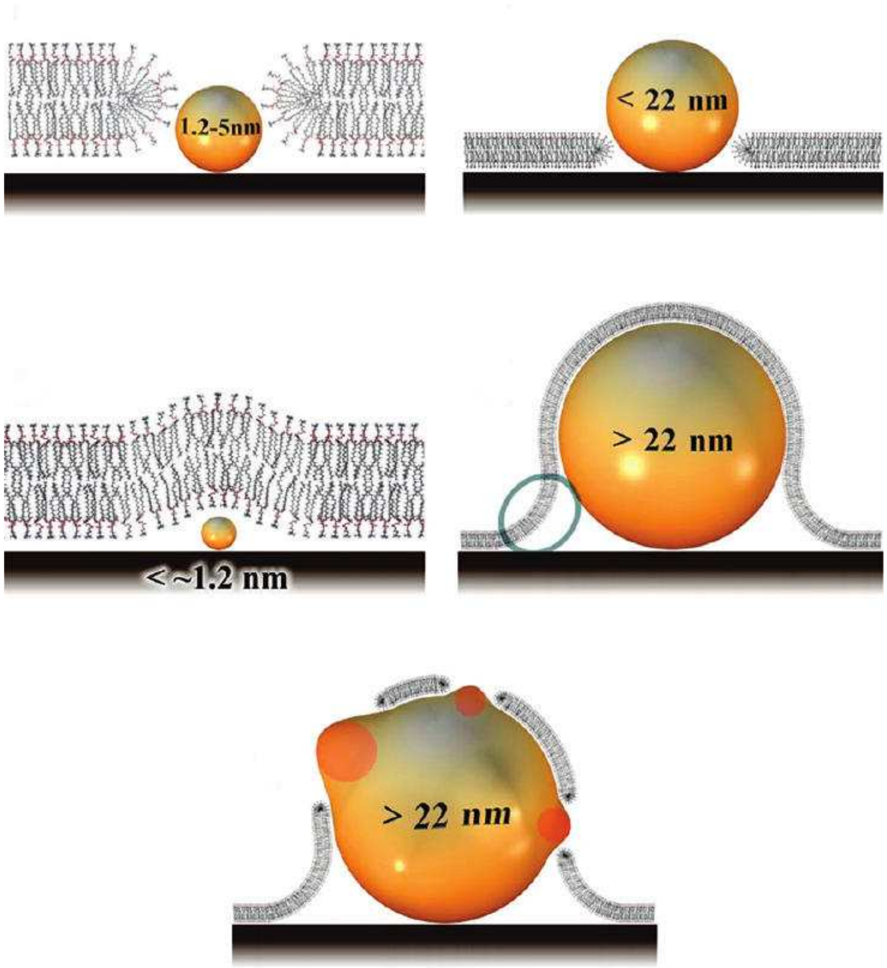

Figure 1.8: **Lipid bilayer fusion on rough surfaces**. For nanoparticles larger than 1.2 nm or smaller than 22 nm the formation of pores is observed *(top)*. The lipid bilayer has the same topography with the nanoparticles with diameter less than 1.2 nm *(centre, left)*. For nanoparticles larger than 22 nm, with and without bumps, coverage *(centre, right)* or incomplete coverage *(bottom)* due to the bumps is observed. Figure adapted from [122].

heads. PMF calculations were also carried out and were in good agreement with the simulation observations. Recently, Li and Gu presented a simulation study of interactions between charged nanoparticles and charge-neutral phospholipid membranes [127]. They employed the MARTINI force field and showed that due to the increase of the electrostatic energy, the charged nanoparticle can be partially wrapped by the membrane.

In this study, an effort to get insights of the interaction of nanoparticles of different sizes and surface chemistry with lipid bilayer has been made.

1.6 Objectives and scope of the thesis

The main objective of this work is to test the scope and applicability of coarse-grained models to capture peptide interaction and self-assembly processes in the presence of membranes as well as to provide a systematic description of these interactions as a function of peptide structure and surface chemistry. The bulk of this thesis is devoted to the interactions of α-helical peptides with lipid bilayers. In the last part of the thesis, I employed CG MD simulations to study the interactions of nanoparticles with membranes. Short chapter summaries are given below.

Chapter 2 / Methodology: Description of the methods used in this work. An introduction to statistical mechanics and the link to molecular dynamics simulations is given. This introduction includes potential of mean force calculations, implementation issues, pressure and temperature control methods and other concepts needed in MD simulations. In the second part of the chapter, a description of the model used is provided. I close the chapter with the simulation parameters used in this work and the analysis tools developed for the analysis of our results.

Chapter 3 / Coarse-grained model validation in application to different classes of amphipatic peptides: MD simulations of different α-helical peptides in a lipid bilayer are performed. The MARTINI CG force field is employed and the results are compared with the available experimental or atomistic simulation data. Potential of mean force calculations are also performed by means of the umbrella sampling method. Different PMF patterns are calculated for the peptides, leading to a possible classification linked to their hydrophobicity.

Chapter 4 / Pore formation by synthetic peptides: MD simulations of LS3 pore forming peptide are carried out. The MARTINI CG force field is employed in extensive MD simulations with different concentrations of peptides in lipid bilayers. Different complexes are observed, including the formation of a hexameric barrel-stave pore. Structural and dynamical details of the pore are calculated. Simulations are also performed for a shorter version of LS3 peptide. This peptide seems to form complexes of different shape, toroidal-like bundles, smaller in size and unstable. A link between the length of the peptides and their ability to induce the formation of different types of pore is established.

Chapter 6 / Cell-penetrating peptides: A study on the interaction of two cell-penetrating peptides with a lipid bilayer. Coarse-grained molecular dynamics simulations are performed. Formation of complexes of different sizes and membrane perturbation are two of the main results in this chapter. Steered MD simulations are also performed in an effort to capture early stages of an endocytic pathway.

Chapter 7 / Interactions between nanoparticles and lipid membranes: MD and Steered MD simulations of nanoparticles of different size and nature in a lipid bilayer system are used to study the effect of nanoparticle size, hydrophobicity and charged is examined. Deformation of the lipid bilayer and interdigitated state have been observed.

Chapter 8: Conclusion and summary.

1.7 Publications and presentations

Publications

- *P. Gkeka and L. Sarkisov*, J. PHYS. CHEM. B., *113 (1), pp. 6-8*.
  Spontaneous formation of a barrel-stave pore in a coarse-grained model of the synthetic LS3 peptide and a DPPC lipid bilayer. (Jan. 2009)
- *P. Gkeka and L. Sarkisov*, J. PHYS. CHEM. B.,*114 (2), pp. 826-839*.
  Interactions of phospholipid bilayers with several classes of amphiphilic α-helical peptides: insights from coarse-grained molecular dynamics simulations. (Jan. 2010)

Presentations

- 2009 AICHE ANNUAL MEETING.
  Linking Atomistic and Mesoscales: Atomistic and Simple Coarse-Grained Models in Application to Biomolecular Problems. (Nov. 2009)
- PSI-K SUMMER SCHOOL ON 'SIMULATION APPROACHES TO PROBLEMS IN MOLECULAR AND CELLULAR BIOLOGY'.
  Coarse-grained simulations and free energy calculations of α-helical peptides. (Sept. 2009)
- FARADAY DISCUSSION 144: MULTISCALE MODELLING OF SOFT MATTER.
  Coarse-grained simulations of α-helical peptides. (July 2009)
- CCP5 ANNUAL MEETING: SURFACES AND INTERFACES.
  Coarse-grained modelling of membrane-peptide interactions. (Sept. 2008)
- CONFERENCE ON MOLECULAR SIMULATIONS IN BIOSYSTEMS AND MATERIAL SCIENCE (SIMBIOMA) .
  Coarse-grained modelling of membrane translocation mechanisms of α-helical cell-penetrating peptides. (April 2008)

CHAPTER 2

Methodology

This chapter is a short description of the methodology used in this work. In this thesis, molecular dynamics (MD) is a primary tool. The roots of MD and other molecular modelling approaches employed in this study lie in statistical mechanics, an area of science, which aims to construct macroscopic properties of a system from basic information about intermolecular interactions. Thus, before I address the specific area of peptide-membrane interactions, I will introduce some basic ideas of statistical mechanics, and building on these ideas, review the principles of molecular dynamics, free energy calculations and other methods employed in this work.

In the second part of this chapter, I will provide a more detailed description of the model used in this study. Specifically, a short description of the MARTINI coarse-grained model, the molecular mapping and in particular the representation of lipids, lipid bilayers and peptides will be presented. Finally, at the end of the chapter, there is a presentation of the tools developed during this work for the calculation of different parameters and the description of the systems under study.

2.1 Fundamentals of molecular dynamics

Molecular dynamics (MD) is a computer simulation technique, where the classical equations of motion of atoms or molecules are used to calculate the time evolution of the system. In the following sections, I will derive the principles of molecular dynamics starting from a fundamental statistical mechanics description of a system with constant number of particles, volume and energy. I will discuss how the properties of the system can be extracted from MD simulations. I will then focus on several key issues associated with the implementation of MD, such as integration algorithms. Finally, I will extend our review to advanced MD in systems with constant temperature and pressure.

2.1.1 Statistical mechanics of the microcanonical ensemble

Let us consider a system of N particles in volume V. If the system is isolated, its energy E is constant. In statistical mechanics this system corresponds to the microcanonical ensemble (NVE). A microcanonical MD trajectory may be seen as an exchange of potential and kinetic energy, with the total energy being conserved.

In the NVE ensemble, the probability density is proportional to the factor

$$\delta(\mathcal{H}(\mathbf{r}^N, \mathbf{p}^N) - E), \tag{2.1}$$

where $\mathcal{H}$ is the Hamiltonian of the system and $\mathbf{r}^N$ and $\mathbf{p}^N$ are the positions and the momenta of the N particles of the system respectively, with

$$\begin{aligned} \mathbf{r}^N &= (\mathbf{r}_1, \mathbf{r}_2, \ldots, \mathbf{r}_N), & (2.2) \\ \mathbf{p}^N &= (\mathbf{p}_1, \mathbf{p}_2, \ldots, \mathbf{p}_N) & (2.3) \end{aligned}$$

and

$$\mathbf{p}_i = m_i \dot{\mathbf{r}}_i. \tag{2.4}$$

The microcanonical partition function can be written as:

$$Q_{NVE} = \frac{1}{\hbar^{3N} N!} \int \int \delta(\mathcal{H}(\mathbf{r}^N, \mathbf{p}^N) - E) d\mathbf{r}^N d\mathbf{p}^N, \tag{2.5}$$

where the factor $\frac{1}{\hbar^{3N} N!}$ is a measure of the volume of the phase space, $\hbar$ is the Planck constant and the indistinguishable nature of the particles is accounted through $N!$.

According to the principles of statistical mechanics, any property $A(\mathbf{r}^N, \mathbf{p}^N)$ of the system can be calculated as an ensemble average

$$\langle A \rangle = \frac{1}{Q_{NVE}} \frac{1}{\hbar^{3N} N!} \int \int A(\mathbf{r}^N, \mathbf{p}^N) \delta(\mathcal{H}(\mathbf{r}^N, \mathbf{p}^N) - E) d\mathbf{r}^N d\mathbf{p}^N. \tag{2.6}$$

Moreover, knowledge of the partition function defines all thermodynamic properties of the system. Specifically, in the microcanonical ensemble, the link between the partition function and the entropy is given by the following formula:

$$S = k_B \ln Q_{NVE}, \tag{2.7}$$

where k_B is the Boltzman constant.

In practice, direct evaluation of the partition function or integrals like the one in Equation (2.6) is possible only for a few special cases. For other cases, we must resort to simulation methods to recover properties of the system in each specific ensemble. The main idea of any simulation method is to generate a series of states of the system with the probability density corresponding to a particular ensemble. In this case, any property of the system will be the average of this property, observed in a series of generated states of the system. In principle, two types of simulation methods exist, based on stochastic approaches (Monte Carlo) and based on deterministic approaches (Molecular Dynamics), with several hybrid variations spanning the range between them.

In this thesis, I am interested in a range of dynamic properties of the systems of interest, such as self-diffusion, and the evolution of the system from non-equilibrium states towards equilibrium. Thus, molecular dynamics is the method of choice throughout this study. Let us outline the principles of this method, by examining how it is applied to the microcanonical ensemble.

2.1.2 Molecular dynamics in the microcanonical ensemble

The basic idea of molecular dynamics is to solve numerically the equations of motion of N interacting atoms or molecules. Thus, the next step in our review of molecular dynamics is to derive these equations.

In the microcanonical ensemble, as the positions $\mathbf{r}^N$ and the momenta $\mathbf{p}^N$ change with time, the system as a whole evolves in the $(\mathbf{r}^N, \mathbf{p}^N)$ phase space along an isoenergetic surface $\mathcal{H}(\mathbf{r}^N, \mathbf{p}^N) = E$, and therefore the Hamiltonian is a conserved property:

$$\frac{d\mathcal{H}(\mathbf{r}^N, \mathbf{p}^N)}{dt} = 0. \tag{2.8}$$

Thus,

$$\frac{d\mathcal{H}(\mathbf{r}^N, \mathbf{p}^N)}{dt} = \sum_{i=1}^{N} \frac{\partial \mathcal{H}(\mathbf{r}^N, \mathbf{p}^N)}{\partial \mathbf{p}_i} \cdot \dot{\mathbf{p}}_i + \sum_{i=1}^{N} \frac{\partial \mathcal{H}(\mathbf{r}^N, \mathbf{p}^N)}{\partial \mathbf{r}_i} \cdot \dot{\mathbf{r}}_i = 0. \tag{2.9}$$

The Hamiltonian $\mathcal{H}$ of the system in the microcanonical ensemble can be written as the sum of kinetic and potential energy functions,

$$\mathcal{H}(\mathbf{r}^N, \mathbf{p}^N) = \mathcal{K}(\mathbf{p}^N) + \mathcal{V}(\mathbf{r}^N) \tag{2.10}$$

where $\mathcal{K}$ and $\mathcal{V}$ are the kinetic and potential energy functions respectively. The kinetic energy $\mathcal{K}$ can be expressed as

$$\mathcal{K}(\mathbf{p}^N) = \sum_{i=1}^{N} \frac{\mathbf{p}_i^2}{2m_i}. \tag{2.11}$$

Then, by replacing Equation (2.11) in Equation (2.10), we obtain

$$\mathcal{H}(\mathbf{r}^N,\mathbf{p}^N)=\sum_{i=1}^{N}\frac{\mathbf{p}_i^2}{2m_i}+\mathcal{V}(\mathbf{r}^N), \tag{2.12}$$

and the time derivative of this Hamiltonian will be

$$\frac{d\mathcal{H}(\mathbf{r}^N,\mathbf{p}^N)}{dt}=\sum_{i=1}^{N}\frac{\mathbf{p}_i}{m_i}\cdot\dot{\mathbf{p}}_i+\sum_{i=1}^{N}\frac{\partial\mathcal{V}(\mathbf{r}^N)}{\partial\mathbf{r}_i}\cdot\dot{\mathbf{r}}_i. \tag{2.13}$$

Again, from Equations (2.8) and (2.13), it holds that

$$\sum_{i=1}^{N}\frac{\mathbf{p}_i}{m_i}\cdot\dot{\mathbf{p}}_i+\sum_{i=1}^{N}\frac{\partial\mathcal{V}(\mathbf{r}^N)}{\partial\mathbf{r}_i}\cdot\dot{\mathbf{r}}_i=0. \tag{2.14}$$

From Equations (2.9) and (2.14), we get

$$\sum_{i=1}^{N}\frac{\partial\mathcal{H}(\mathbf{r}^N,\mathbf{p}^N)}{\partial\mathbf{p}_i}\cdot\dot{\mathbf{p}}_i+\sum_{i=1}^{N}\frac{\partial\mathcal{H}(\mathbf{r}^N,\mathbf{p}^N)}{\partial\mathbf{r}_i}\cdot\dot{\mathbf{r}}_i=\sum_{i=1}^{N}\frac{\mathbf{p}_i}{m_i}\cdot\dot{\mathbf{p}}_i+\sum_{i=1}^{N}\frac{\partial\mathcal{V}(\mathbf{r}^N)}{\partial\mathbf{r}_i}\cdot\dot{\mathbf{r}}_i \tag{2.15}$$

and thus, for every particle i with $i \in \{1,2,\cdots,N\}$, it holds that

$$\frac{\partial\mathcal{H}(\mathbf{r}^N,\mathbf{p}^N)}{\partial\mathbf{p}_i}=\frac{\mathbf{p}_i}{m_i} \tag{2.16}$$

and

$$\frac{\partial\mathcal{H}(\mathbf{r}^N,\mathbf{p}^N)}{\partial\mathbf{r}_i}=\frac{\partial\mathcal{V}(\mathbf{r}^N)}{\partial\mathbf{r}_i}. \tag{2.17}$$

If we substitute Equation (2.4) into Equation (2.16), we get

$$\boxed{\frac{\partial\mathcal{H}(\mathbf{r}^N,\mathbf{p}^N)}{\partial\mathbf{p}_i}=\dot{\mathbf{r}}_i,\ \forall\, i \in \{1,2,\cdots,N\}} \tag{2.18}$$

Equation (2.9), after substituting Equation (2.18), becomes

$$\sum_{i=1}^{N} \dot{\mathbf{r}}_i \cdot \dot{\mathbf{p}}_i + \sum_{i=1}^{N} \frac{\partial \mathcal{H}(\mathbf{r}^N, \mathbf{p}^N)}{\partial \mathbf{r}_i} \cdot \dot{\mathbf{r}}_i = 0 \Longrightarrow \sum_{i=1}^{N} \left(\dot{\mathbf{p}}_i + \frac{\partial \mathcal{H}(\mathbf{r}^N, \mathbf{p}^N)}{\partial \mathbf{r}_i} \right) \cdot \dot{\mathbf{r}}_i = 0 \tag{2.19}$$

As the vectors of velocities $\dot{\mathbf{r}}_i$ are independent, Equation (2.18) holds if and only if

$$\boxed{\frac{\partial \mathcal{H}(\mathbf{r}^N, \mathbf{p}^N)}{\partial \mathbf{r}_i} = -\dot{\mathbf{p}}_i, \ \forall\, i \ \in \ \{1, 2, \cdots, N\}} \tag{2.20}$$

Equations (2.18) and (2.20) are also known as Hamilton equations of motion and are equivalent to Newton's second law,

$$\mathbf{F}_i = m_i \ddot{\mathbf{r}}_i. \tag{2.21}$$

Indeed, from Equation (2.4) we have

$$\dot{\mathbf{p}}_i = m_i \ddot{\mathbf{r}}_i. \tag{2.22}$$

If we now substitute Equation (2.22) into Equation (2.20), we get

$$\frac{\partial \mathcal{H}(\mathbf{r}^N, \mathbf{p}^N)}{\partial \mathbf{r}_i} = -m_i \ddot{\mathbf{r}}_i, \ \forall\, i \ \in \ \{1, 2, \cdots, N\}. \tag{2.23}$$

From Equations (2.17) and (2.23) it follows that

$$\mathbf{F}_i = -\frac{\partial \mathcal{H}(\mathbf{r}^N, \mathbf{p}^N)}{\partial \mathbf{r}_i} = -\frac{\partial \mathcal{V}(\mathbf{r}^N)}{\partial \mathbf{r}_i}, \ \forall\, i \ \in \ \{1, 2, \cdots, N\}. \tag{2.24}$$

which combined with Equation (2.23) yields Newton's second law (Equation (2.21)). Numerical integration of Equations (2.18) and (2.20) in time constitutes the molecular dynamics simulation.

2.1.3 Determination of properties in MD

As mentioned in the previous section, during a molecular dynamics simulation in the NVE ensemble, the system moves in the $(\mathbf{r}^N, \mathbf{p}^N)$ phase space along the larger surface of constant energy E. A generic physical property A of the system that is a function of either positions, momenta or both will also evolve along this trajectory,

$$A(t) = f(\mathbf{r}^N(t), \mathbf{p}^N(t)). \tag{2.25}$$

The central idea of molecular dynamics is that the average of A over time

$$\langle A \rangle = \lim_{t \to \infty} \frac{1}{t} \int_{t_0}^{t_0+t} A(\tau) d\tau \tag{2.26}$$

is equal to the equilibrium ensemble average (Equation (2.6)). In order for this to be true, the system of interest must satisfy several conditions. Omitting detailed discussion, at least in principle, the system should be able to visit all the states of the ensemble during the simulation.

As an MD simulation progresses, the system reaches equilibrium, where various properties (as estimated from time averages) do not change with the time of the simulation. Below, I discuss some of the key properties measured in a molecular dynamics simulation.

Temperature

The temperature of the system is related to its kinetic energy. For a system of N monoatomic molecules this relation is expressed by the *equipartition* function

$$\langle \mathcal{K} \rangle = \lim_{t \to \infty} \frac{1}{t} \int_{t_0}^{t_0+t} \mathcal{K}(\mathbf{p}^N) d\tau = \frac{3}{2} N k_B T, \tag{2.27}$$

where k_B is the Boltzmann constant.

Alternatively, as the simulation progresses, the temperature of the system can be expressed as a function of time (by substituting Equation (2.11) into Equation (2.27))

$$T(t) = \frac{2}{3}\frac{K}{Nk_B} = \frac{1}{3Nk_B}\sum_{i=1}^{N}\frac{\mathbf{p}_i^2}{m_i} = \sum_{i=1}^{N}\frac{m_i\mathbf{v}_i^2(t)}{k_B N}. \tag{2.28}$$

Finally, although it is more convenient to show this in canonical (NVT) ensemble, the distribution of kinetic energies of molecules must follow the Maxwell-Boltzman distribution in the microcanonical ensemble as well.

Pressure

For the calculation of the average pressure the Clausius virial function is usually used

$$W(\mathbf{r}^N) = \sum_{i=1}^{N}\mathbf{r}_i \cdot \mathbf{F}_i^{total}, \tag{2.29}$$

where $\mathbf{F}_i^{total}$ is the total force exerted on atom i. From Equation (2.29) and Newton's second law, the average of W is given by

$$\langle W \rangle = \lim_{t\to\infty}\frac{1}{t}\int_{t_0}^{t_0+t}\sum_{t=1}^{N}\mathbf{r}_i(\tau)\cdot m_i\ddot{\mathbf{r}}_i(\tau)d\tau. \tag{2.30}$$

Integrating by parts, results:

$$\langle W \rangle = -\lim_{t\to\infty}\frac{1}{t}\int_{t_0}^{t_0+t}\sum_{t=1}^{N}m_i\left|\dot{\mathbf{r}}_i(\tau)\right|^2 d\tau. \tag{2.31}$$

From Equations (2.27) and (2.31),

$$\langle W \rangle = -3Nk_BT, \tag{2.32}$$

with N the total number of particles and k_B the Boltzmann constant.

The total force exerted on a particle is composed of the interatomic interactions and the external force from the walls of the system,

$$\mathbf{F}_i^{total} = \mathbf{F}_i^{inter} + \mathbf{F}_i^{ext}, \ \forall \, i \ \in \ \{1, 2, \cdots, N\}. \tag{2.33}$$

Equation (2.29), after substituting Equation (2.33), becomes

$$W(\mathbf{r}^N) = \sum_{i=1}^{N} \mathbf{r}_i \cdot \mathbf{F}_i^{int} + \sum_{i=1}^{N} \mathbf{r}_i \cdot \mathbf{F}_i^{ext}. \tag{2.34}$$

If we now assume that the system is enclosed in a parallelepipedic container with dimensions L_x, L_y and L_z, from Equation (2.29) we get

$$\left\langle W^{ext} \right\rangle = L_x(-PL_yL_z) + L_y(-PL_xL_z) + L_z(-PL_xL_y) = -3PV. \tag{2.35}$$

Then, Equation (2.34) becomes

$$\langle W \rangle = \left\langle \sum_{i=1}^{N} \mathbf{r}_i \cdot \mathbf{F}_i^{int} \right\rangle - 3PV. \tag{2.36}$$

From Equations (2.32) and (2.36), we get

$$\left\langle \sum_{i=1}^{N} \mathbf{r}_i \cdot \mathbf{F}_i^{int} \right\rangle - 3PV = -3Nk_BT, \tag{2.37}$$

or,

$$P = \frac{1}{V} \left[Nk_BT - \frac{1}{3} \left\langle \sum_{i=1}^{N} \mathbf{r}_i \cdot \mathbf{F}_i^{int} \right\rangle \right]. \tag{2.38}$$

Finally, in the case that the interatomic interactions are described by a potential $\mathcal{V}$ we have

$$P = \frac{1}{V} \left[Nk_BT - \frac{1}{3} \left\langle \sum_{i=1}^{N} \sum_{j=i+1} \mathbf{r}_{ij} \cdot \frac{d\mathcal{V}}{dr}|_{r_{ij}} \right\rangle \right], \tag{2.39}$$

where r_{ij} is the distance between particles i and j.

Mean square displacement and self-diffusion coefficient

According to Fick's first law of diffusion, the flux of matter $\mathcal{J}$ is equal to the diffusion coefficient (D) multiplied by the concentration gradient. For one-dimensional diffusion, this is

$$\mathcal{J} = -D\frac{dC}{dx}, \tag{2.40}$$

where C is the concentration. From Equation (2.40) and the mass balance, we get

$$\frac{\partial C}{dt} = -\frac{\partial \mathcal{J}}{\partial x} = \frac{\partial}{\partial x}\left(D\frac{dC}{dx}\right) = D\frac{\partial^2 C}{\partial x^2}, \tag{2.41}$$

which is Fick's second law. The solution of Equation (2.41) with N_0 particles at $t = 0$ having $x = 0$ is given by

$$C = \frac{N_0}{2\sqrt{\pi D t}} \exp\left[-\frac{x^2}{4Dt}\right], \tag{2.42}$$

Equation (2.42) is a Gaussian function with a peak at $x = 0$. In other words, as time evolves, particles diffuse away from the origin. The *mean square displacement* of a group of particles A is defined as

$$msd = \left\langle \|\mathbf{r}_i(t) - \mathbf{r}_i(0)\|^2 \right\rangle, \tag{2.43}$$

which for any time with $t > 0$, will be given by the second moment of the distribution

$$\left\langle \|\mathbf{r}_i(t) - \mathbf{r}_i(0)\|^2 \right\rangle = \frac{1}{N_0}\int x^2 C dx \overset{(2.42)}{=} 2Dt, \tag{2.44}$$

which is valid for t larger than the average time between collisions of atoms. Finally, in three dimensions

$$\lim_{t\to\infty} \left\langle \|\mathbf{r}_i(t) - \mathbf{r}_i(0)\|^2 \right\rangle = 6Dt. \tag{2.45}$$

Equations (2.44) and (2.45) are known as the Einstein relations for the self-diffusion coefficient in one and three dimensions respectively.

Structural parameters of lipid bilayers

Radial distribution function (RDF) is a very useful way to get details about the structure of a system. The radial distribution function, $g(r)$, is the probability of finding a pair of particles at a distance r, relative to what is expected for an ideal gas at the same density (i.e. uniform random distribution),

$$\rho g(r) = \frac{1}{N} \left\langle \sum_{i=1}^{N} \sum_{j \neq i}^{N} \delta(r - r_{ij}) \right\rangle, \tag{2.46}$$

where N is the total number of atoms, $\rho = N/V$ is the number density and r_{ij} is the distance between two particles i and j. The radial distribution function can be used to distinguish between different lipid bilayer phases, as it gives information about its structure and can be directly compared with available experimental data [128].

Another important measure of the structure of a lipid bilayer is their order parameters. The P_2 or second-rank order parameter is given by

$$P_2 = \frac{1}{2} \left(3 \cos^2 \theta - 1 \right) \tag{2.47}$$

and is calculated for consecutive bonds, with θ the angle between the direction of the bond and the bilayer normal. $P_2 = 1$ indicates perfect alignment, $P_2 = -0.5$ perfect antialignment and $P_2 = 0$ a random orientation.

The area per lipid and the volume per lipid molecule are also two characteristics of a lipid bilayer. The area per lipid molecule can be easily calculated by dividing the surface area of the lipid bilayer by the number of lipids that are present in each leaflet. For the volume per lipid the following formula can be used

$$V_L = \frac{A_L L_z}{2} - N_w V_w, \tag{2.48}$$

where A_L is the area per lipid, L_z is the length of the simulation box in the direction of the bilayer normal, N_w is the number of waters per lipid molecule and V_w is the volume per water.

2.1.4 Molecular dynamics in other ensembles

A system simulated in a microcanonical ensemble will evolve towards equilibrium T and P. However, it is difficult to *a priori* estimate what these equilibrium values will be. A more convenient and realistic approach is to study a system with defined temperature, pressure or both. In the next section, I will introduce the statistical mechanics principles of canonical (NVT) and isothermal-isobaric (NPT) ensembles and then review the methods available to control the pressure and the temperature in MD simulations.

The canonical ensemble

In the *canonical* or *NVT ensemble*, the number of particles N, the volume of the system V and the temperature T are kept fixed. In this ensemble the probability density of the system is proportional to

$$\exp\left(-\frac{\mathcal{H}(\mathbf{r}^N,\mathbf{p}^N)}{k_B T}\right), \tag{2.49}$$

and the partition function is given by

$$Q_{NVT} = \frac{1}{\hbar^{3N} N!}\int\int \exp\left(-\frac{\mathcal{H}(\mathbf{r}^N,\mathbf{p}^N)}{k_B T}\right) d\mathbf{r}^N d\mathbf{p}^N. \tag{2.50}$$

The factor $\frac{1}{\hbar^{3N} N!}$ is a measure of the volume of the phase space where $\hbar$ is the Planck constant and $N!$ accounts for the indistinguishable nature of the particles.

The Hamiltonian of the system can be written as the sum of kinetic and potential energy, thus Equation (2.50) gives

$$Q_{NVT} = \frac{1}{\hbar^{3N} N!} \int \exp\left(-\frac{\mathcal{K}(\mathbf{p}^N)}{k_B T}\right) d\mathbf{p}^N \int \exp\left(-\frac{\mathcal{V}(\mathbf{r}^N)}{k_B T}\right) d\mathbf{r}^N = Q^{kin}_{NVT} Q^{pot}_{NVT}. \quad (2.51)$$

For an ideal gas ($\mathcal{V} = 0$)

$$Q^{kin}_{NVT} = \frac{V^N}{N! \Lambda^{3N}}, \quad (2.52)$$

where Λ is the thermal de Broglie wavelength

$$\Lambda = \left(\frac{\hbar^2}{2\pi m_i k_B T}\right)^{1/2}. \quad (2.53)$$

For the contribution of potential energy we have

$$Q^{pot}_{NVT} = \frac{1}{V^N} \int \exp\left(-\frac{\mathcal{V}(\mathbf{r}^N)}{k_B T}\right) d\mathbf{r}^N \quad (2.54)$$

or

$$Z_{NVT} = \int \exp\left(-\frac{\mathcal{V}(\mathbf{r}^N)}{k_B T}\right) d\mathbf{r}^N \quad (2.55)$$

where Z_{NVT} is the *configurational integral*.

Finally, for the canonical ensemble we have

$$Q_{NVT} = \frac{1}{\Lambda^{3N} N!} \int \exp\left(-\frac{\mathcal{V}(\mathbf{r}^N)}{k_B T}\right) d\mathbf{r}^N = \frac{1}{\Lambda^{3N} N!} Z_{NVT}. \quad (2.56)$$

The link between canonical ensemble and macroscopic thermodynamic functions is provided by the following relation

$$A = -k_B T \ln Q_{NVT}, \tag{2.57}$$

where A is the Helmholtz free energy.

The isobaric-isothermal ensemble

In the *isothermal-isobaric ensemble* (NPT), the number of molecules (N), the pressure (P) and the temperature (T) are kept fixed. For this ensemble, the probability density is proportional to

$$\exp\left(-\frac{\mathcal{H}(\mathbf{r}^N, \mathbf{p}^N) + PV}{k_B T}\right). \tag{2.58}$$

In this ensemble the volume plays an important role, as it is the parameter that determines the pressure and must vary in order to keep pressure constant. The partition function in this case is given by

$$\Delta_{NPT} = \frac{1}{N!\hbar^{3N} V_0} \int\int\int \exp\left(-\frac{\mathcal{H}(\mathbf{r}^N, \mathbf{p}^N) + PV}{k_B T}\right) d\mathbf{r}^N d\mathbf{p}^N dV, \tag{2.59}$$

where V_0 is the basic unit of volume.

The configurational integral in the NPT ensemble is

$$Z_{NPT} = \int \exp\left(-\frac{PV}{k_B T}\right) dV \int \exp\left(-\frac{\mathcal{V}(\mathbf{r}^N)}{k_B T}\right) d\mathbf{r}^N. \tag{2.60}$$

Moreover, the Gibbs free energy G can be defined as

$$G = -k_B T \ln \Delta_{NPT}. \tag{2.61}$$

2.2 Pressure and temperature control in MD simulations

Over the years, a number of schemes have been proposed in order to maintain constant temperature and pressure conditions in MD simulations. The most rigorous approaches satisfy two main constraints: the Hamiltonian of the system must be conserved and the distribution must correspond to the appropriate ensemble. These methods have been developed within the extended Hamiltonian framework. Thus, I will first focus on them and then briefly review less rigorous approaches.

2.2.1 Baro- and thermostats using the extended Hamiltonian approach

Barostat control of MD simulation by means of an extended system method was originally proposed by Andersen [129], and then extended and generalized to temperature control by Nosé [130] and Hoover [131, 132]. As it is intuitively easier to understand the principles of the barostat, this will be the starting point of our analysis.

The main idea of this method is that the physical system is extended to a composite system consisting of the system of interest and an external one [130]. In order to control the pressure, the volume of the simulation cell must be free to fluctuate. As proposed by Andersen, the volume should be treated as a dynamic variable just like particle positions and velocities.

Consider a simulation box which is a cube with an edge length L. Two sets of variables are considered: real $\{\mathbf{r}_i, \mathbf{v}_i, \mathbf{p}_i\}$ and virtual $\{\boldsymbol{\rho}_i, \boldsymbol{\nu}_i, \boldsymbol{\pi}_i\}$ ones. The positions, velocities and momenta are scaled by L as

$$\begin{aligned}\mathbf{r}_i &= L\boldsymbol{\rho}_i \\ \mathbf{v}_i &= L\dot{\boldsymbol{\rho}}_i = L\boldsymbol{\nu}_i \\ \mathbf{p}_i &= \boldsymbol{\pi}_i,\end{aligned} \tag{2.62}$$

where $L = V^{1/3}$. Moreover, a piston is imposed on the system in order to control the volume. This piston can be seen as the external system mentioned before that will be used to maintain the pressure constant. The Hamiltonian of the extended system, expressed in terms of virtual variables is given by

$$\mathcal{H}^* = \sum_{i=1}^{N} \frac{V^{-2/3}\boldsymbol{\pi}_i^2}{2m_i} + \mathcal{V}(V^{1/3}\boldsymbol{\rho}_i^N) + \frac{p_\epsilon^2}{2W} + P_{ext}V, \tag{2.63}$$

where $\boldsymbol{\rho}_i$ and $\boldsymbol{\pi}_i$ are the scaled position and momentum of the i^{th} particle, V is the volume of the system, p_ϵ is the barostat momentum (or conjugate momentum of the volume), W is the barostat inertia parameter corresponding to the piston mass and P_{ext} is the external pressure. The term $P_{ext}V$ corresponds to the potential energy associated with the volume change whereas the necessary work is $P_{ext}\Delta V$.

The equation of motion for the volume is

$$\begin{aligned} W\frac{d^2V}{dt^2} &= -\frac{\partial \mathcal{H}^*}{\partial V} = \frac{1}{3V}\left(\sum_{i=1}^{N}\frac{V^{-2/3}\boldsymbol{\pi}_i^2}{m_i} - \sum_{i=1}^{N}\sum_{j=i+1} V^{1/3}\boldsymbol{\rho}_{ij}\cdot\frac{\partial \mathcal{V}}{\partial \mathbf{r}_{ij}}\right) - P_{ext} \\ &= \frac{1}{3V}\left[\sum_{i=1}^{N}\frac{\mathbf{p}_i^2}{m_i} - \sum_{i=1}^{N}\sum_{j=i+1}\mathbf{r}_{ij}\cdot\frac{\partial \mathcal{V}}{\partial \mathbf{r}_{ij}}\right] - P_{ext} = P_{int} - P_{ext}, \end{aligned} \tag{2.64}$$

where we made use of the virial theorem. From Equation (2.64) it follows that the change of the volume is governed by the fluctuations between the internal and external pressure.

A similar idea was followed by Nosé for the formulation of a thermostat based on one extended system [133, 134]. The idea of this method is to capture the effect of one external system, acting as heat reservoir, through an additional degree of freedom s. This heat reservoir controls the temperature of the given system, causing small fluctuations around a set value.

In a similar manner as for the barostat, two sets of variables, real $\{\mathbf{r}_i, \mathbf{p}_i\}$ and virtual $\{\boldsymbol{\rho}_i, \boldsymbol{\pi}_i\}$, are defined. The effect of the heat reservoir to the system is expressed by scaling the velocity by the new variable s, which is also treated as a dynamical variable in the extended system. s is defined as $s = \frac{d\tau}{dt}$ with τ and t being the virtual and real time respectively.

The Hamiltonian of the new extended system, in virtual coordinates, is

$$\mathcal{H}^* = \sum_{i=1}^{N} \frac{\boldsymbol{\pi}_i^2}{2m_i s^2} + \mathcal{V}(\boldsymbol{\rho}^N) + \frac{\pi_s^2}{2Q} + gk_BT\ln(s), \tag{2.65}$$

where $g = 3N + 1$ is the number degrees of freedom of the extended system (N particles + 1 the new degree of freedom) and Q is the effective 'mass' associated with s[1]. p_s is defined as $p_s = Q\dot{s}$. The transformation from the real variables $\{\mathbf{r}_i, \mathbf{p}_i\}$ to the virtual ones $\{\boldsymbol{\rho}_i, \boldsymbol{\pi}_i\}$ is performed according to $\boldsymbol{\rho}_i = \mathbf{r}_i$ and $\boldsymbol{\pi}_i = \mathbf{p}_i/s$.

From Equation (2.65), we get the following equations of motion

$$\begin{aligned}
\dot{\boldsymbol{\rho}}_i &= \frac{\partial\mathcal{H}^*}{\partial\boldsymbol{\pi}_i} = \frac{\boldsymbol{\pi}_i}{m_i s^2} \\
\dot{\boldsymbol{\pi}}_i &= -\frac{\partial\mathcal{H}^*}{\partial\boldsymbol{\rho}_i} = -\frac{\partial\mathcal{V}}{\partial\boldsymbol{\rho}_i} \\
\dot{s} &= \frac{\partial\mathcal{H}^*}{\partial\boldsymbol{\pi}_s} = \frac{\boldsymbol{\pi}_s}{Q} \\
\dot{\pi}_s &= -\frac{\partial\mathcal{H}^*}{\partial s} = \sum_{i=1}^{N} \frac{\boldsymbol{\pi}_i^2}{m_i s^3} - \frac{gk_BT}{s}
\end{aligned} \tag{2.66}$$

Hoover simplified the system (2.66), by introducing a new variable ξ (*friction constant*) [131],

$$\xi = s\frac{ds}{dt} = s\frac{ds}{d\tau}\frac{d\tau}{dt} = s\frac{\partial\mathcal{H}^*}{d\boldsymbol{\pi}_s}\frac{d\tau}{dt} = s^2\frac{\pi_s}{Q}. \tag{2.67}$$

---

[1] The parameter Q is a thermal inertia parameter, which determines the rate of the heat transfer. The value of this parameter must be set carefully, because if it is chosen to be too small the phase space of the system will not be canonical, and if it is chosen to be too large the temperature control will not be efficient.

By transforming the system (2.66) back into the real variables $\{\mathbf{r}_i, \mathbf{p}_i\}$, we get:

$$\begin{aligned}\dot{\mathbf{r}}_i &= \frac{\mathbf{p}_i}{m_i}\\ \dot{\mathbf{p}}_i &= -\frac{\partial \mathcal{V}}{\partial \mathbf{r}_i} - \xi \mathbf{p}_i\\ \frac{d\ln(s)}{dt} &= \xi\\ \dot{\xi} &= \frac{1}{Q}\left(\sum_{i=1}^{N}\frac{\mathbf{p}_i^2}{2m_i} - gk_BT\right)\end{aligned} \tag{2.68}$$

The system (2.68) describes the Nosé-Hoover thermostat.

In Appendix B, Figure B.1, I show the evolution of ξ and $d\xi/dt$ with time. This simulation was performed with our NVT program with a thermal inertia parameter $Q = 10$, 125 particles and the Gear Predictor-Corrector algorithm (for more information about the MD program see Appendix B). From the figure, we can see that the friction coefficient ξ is not constant. It depends on the fluctuations of kinetic energy around the average value $(g/2)k_BT$. For example, when the kinetic energy is larger than the average, $d\xi/dt$ will be positive, followed by an increase in the value of ξ. This is a negative feedback mechanism as the friction coefficient changes opposite to the energy fluctuations.

It can be shown that equations (2.68) sample a canonical ensemble [131] and have the following conserved quantity

$$\mathcal{H}' = \sum_{i=1}^{N}\frac{\mathbf{p}_i^2}{2m_i} + \mathcal{V}(\mathbf{r}^N) + \frac{s^2 p_s^2}{2Q} + gk_BT\ln(s). \tag{2.69}$$

If we now combine the different contributions from the barostat and the thermostat the Hamiltonian of the system will be

$$\mathcal{H}' = \sum_{i=1}^{N}\frac{\mathbf{p}_i^2}{2m_i} + \mathcal{V}(\mathbf{r}^N) + \frac{s^2 p_s^2}{2Q} + gk_BT\ln(s)\frac{p_\epsilon^2}{2W} + P_{ext}V. \tag{2.70}$$

and the corresponding equations of motion are:

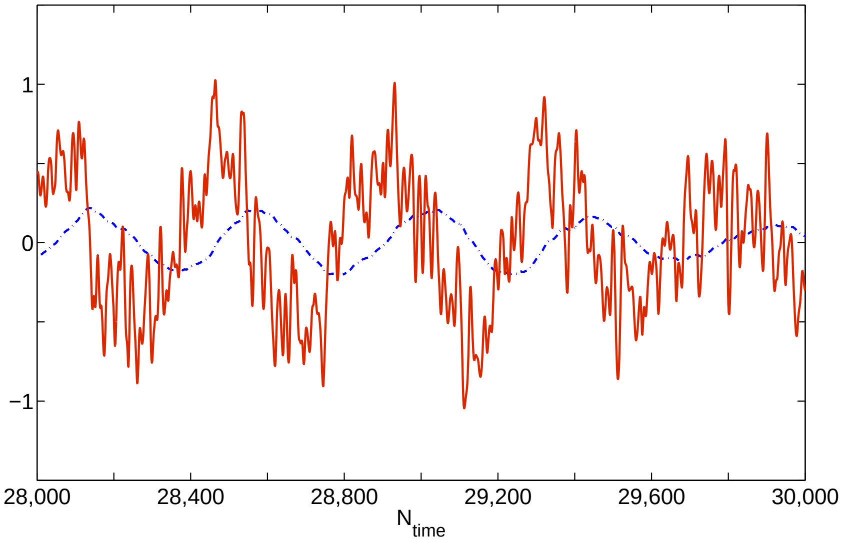

Figure 2.1: **Nosé-Hoover negative feedback mechanism**. Time evolution of the friction coefficient ξ (dashed blue line) and its derivative $\dot{\xi}$ (solid red line). The oscillations around zero and the relative evolution of ξ and $\dot{\xi}$ are two of the main characteristics of the Nosé-Hoover (NH) thermostat. This simulation was performed with our NVT program with the thermal inertia parameter $Q = 10$, 125 particles and the Gear Predictor-Corrector algorithm. More details about the program and the actual simulation can be found in Appendix A. All the values are dimensionless.

$$\begin{aligned}
\dot{\mathbf{r}}_i &= \frac{\mathbf{p}_i}{m_i} + \frac{p_\epsilon}{W}\mathbf{r}_i, \\
\dot{\mathbf{p}}_i &= \mathbf{F}_i - \frac{p_\epsilon}{W}\mathbf{p}_i - \frac{p_\xi}{Q}\mathbf{p}_i, \\
\dot{V} &= \frac{3Vp_\epsilon}{W}, \\
\dot{p}_\epsilon &= 3V(P_{int} - P_{ext}) - \frac{p_\xi p_\epsilon}{Q}, \\
\dot{\xi} &= \frac{p_\xi}{Q}, \\
\dot{p}_\xi &= \sum_{i=1}^{N} \frac{\mathbf{p}_i^2}{m_i} + \frac{p_\epsilon^2}{W} - gkT,
\end{aligned} \tag{2.71}$$

where $\mathbf{F}_i$ is the force, P_{ext} is the applied pressure and P_{int} is the internal pressure defined by the virial theorem.

An MD program has been developed as part of this PhD for an in-depth understanding

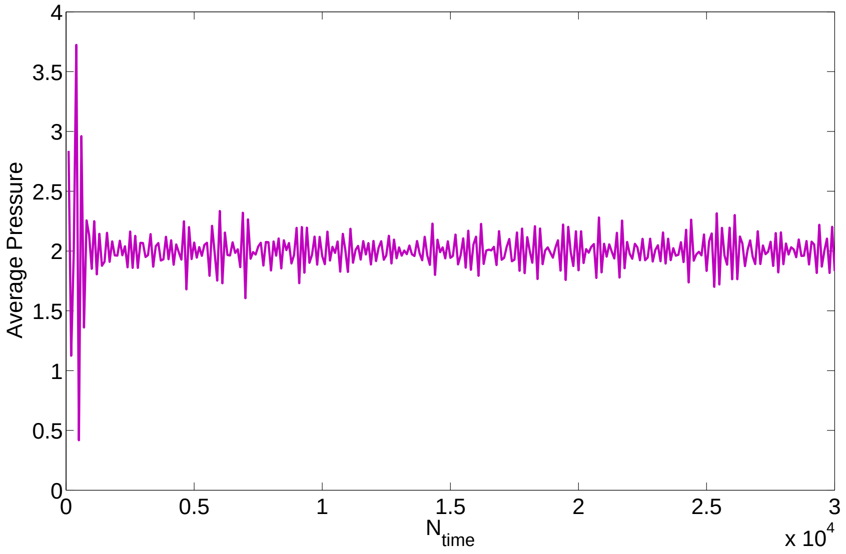

Figure 2.2: **A pressure versus number of time steps for the NPT ensemble, using the Nosé-Hoover baro- thermostat**. The pressure fluctuates around an average value. These fluctuations constitute one of the characteristics of Nosé-Hoover baro- thermostat. The pressure is in dimensionless units.

of the different methods used in a molecular dynamics simulation, the different algorithms, temperature and pressure control approaches and their dependence on several parameters, such as the thermal inertia parameter Q or the barostat inertia parameter W. In this context, the NPT ensemble has been programmed with the Nosé-Hoover baro- and thermostat. In Figure 2.2, I show the time evolution of the average pressure of a system of 1000 Argon atoms, with barostat inertia parameter $W = 150$.

2.2.2 Other methods to control pressure and temperature

The conservation of the temperature and pressure is one of the most computationally demanding calculations in a molecular dynamics simulation. Some times faster and less rigorous thermostats and barostats constitute a more efficient approach. In most of our studies, I employed Berendsen baro- and thermostat and for this reason I will focus on this approach.

Berendsen barostat: In this approach, the volume of the system is scaled by a factor μ^3 at each time step[2]. The parameter μ is given by:

$$\mu = \left[1 - \frac{\Delta t}{\tau_P}\left(P - P_0\right)\right]^{1/3}, \tag{2.72}$$

where P is the instantaneous pressure, P_0 is the desired pressure, Δt is the time step and τ_P is a user defined time constant, with which user can adjust the strength of pressure coupling.

One of the main advantages of Berendsen barostat, apart from its simplicity, is the choice of having either isotropic or anisotropic coupling by just using different scaling factors for every dimension of the system.

Berendsen thermostat: Berendsen thermostat [135] is a proportional type of thermostat, that follows the same general idea; the velocities of all particles are scaled at each step by a factor λ,

$$\lambda = \left[1 + \frac{\Delta t}{\tau_T}\left(\frac{T_0}{T_i} - 1\right)\right]^{1/2}, \tag{2.73}$$

where T_i is the instantaneous temperature, T_0 is the desired temperature, Δt is the time step and τ_T is a user defined time constant. τ_T is a parameter that is used to adjust the strength of the coupling of the system to a hypothetical heat bath.

The equation of motion corresponding to the Berendsen thermostat is:

$$m_i \ddot{\mathbf{r}}_i = \mathbf{F}_i(t) - \frac{1}{2}\tau_T^{-1}\left[\frac{T_0}{T(t)} - 1\right]\dot{\mathbf{r}}_i. \tag{2.74}$$

A system coupled with a heating bath using the Berendsen thermostat does not strictly follow the canonical ensemble [136]. However, in practice, the deviation from canonical is usually small.

To close this section, I need to mention that there are several other approaches for thermostats and barostats. More information can be found in [137–139].

---

[2] In the case of non-cubic systems, each coordinate is scaled by a factor of μ.

2.3 Implementation issues

2.3.1 Time integration algorithm

Now that I have formulated the equations of motion for a system of N particles in various ensembles, I can introduce the main idea behind molecular dynamics. From Equation (2.21), one can calculate the forces on each of the particles of the system at a particular time. Once the forces are computed, Equation (2.21) is integrated numerically in order to produce the new positions and new velocities of each particle of the system. Then, the new coordinates are used to calculate the potential energy again. For this procedure a time integration algorithm is needed.

The time integration algorithms are based on finite difference methods. The idea behind these methods is that the time is broken down into smaller stages, separated by a time step dt, creating a finite grid. At a point of this grid, corresponding to time t, the positions and a number of their derivatives are known (or can be calculated), and are used in order to estimate the same quantities at a time $t + dt$ as Taylor series expansions,

$$\begin{aligned}
\mathbf{r}(t+dt) &= \mathbf{r}(t) + dt\mathbf{v}(t) + \frac{1}{2}dt^2\mathbf{a}(t) + \frac{1}{6}dt^3\mathbf{b}(t) + \frac{1}{24}dt^4\mathbf{c}(t) + \cdots && (2.75)\\
\mathbf{v}(t+dt) &= \mathbf{v}(t) + dt\mathbf{a}(t) + \frac{1}{2}dt^2\mathbf{b}(t) + \frac{1}{6}dt^3\mathbf{c}(t) + \cdots && (2.76)\\
\mathbf{a}(t+dt) &= \mathbf{a}(t) + dt\mathbf{b}(t) + \frac{1}{2}dt^2\mathbf{c}(t) + \cdots && (2.77)\\
\mathbf{b}(t+dt) &= \mathbf{b}(t) + dt\mathbf{c}(t) + \cdots && (2.78)
\end{aligned}$$

where $\mathbf{v}$ is the first derivative of the positions with respect to time (velocity), $\mathbf{a}$ is the second derivative of the positions (acceleration), $\mathbf{b}$ is the third derivative and so on.

There are several different algorithms used in molecular dynamics with the *Verlet algorithm* [140] and its variations being the most widely used. In the majority of our studies, one of these variations, the so-called *leap-frog algorithm* is used for the integration of the equations of motion [141]. The relationships used in leap-frog algorithm are

$$\begin{aligned}\mathbf{r}\left(t+dt\right) &= \mathbf{r}\left(t\right)+dt\mathbf{v}\left(t+\frac{1}{2}dt\right) &(2.79)\\ \mathbf{v}\left(t+\frac{1}{2}dt\right) &= \mathbf{v}\left(t-\frac{1}{2}dt\right)+dt\mathbf{a}\left(t\right) &(2.80)\end{aligned}$$

and it can be easily shown that the velocity is calculated by making use of the half intervals,

$$\mathbf{v}\left(t\right)=\frac{\mathbf{v}\left(t+\frac{1}{2}dt\right)+\mathbf{v}\left(t-\frac{1}{2}dt\right)}{2}. \tag{2.81}$$

Overall, in the leap-frog algorithm, the velocities at $t+\frac{1}{2}dt$ are calculated from the velocities at $t-\frac{1}{2}dt$ and the accelerations at t. From the calculated velocities and the position at time t, the new positions at $t+dt$ are estimated.

2.3.2 Periodic boundary conditions

In the majority of the applications of MD simulations, in order to get a realistic view of a phenomenon, one would like to be able to treat the system in a bulk environment, and not in a simulation cell of limited dimensions. In order to achieve this 'bulk' behaviour of the system, a technique known as *periodic boundary conditions* (PBC) is used. In this technique, the single simulation cell is infinitely replicated in the three Cartesian dimensions[3]. So, if one particle is located at position $\mathbf{r}$, then this particle represents an infinite number of particles at the following positions,

$$\mathbf{r}+k\boldsymbol{\alpha}+l\boldsymbol{\beta}+m\gamma, \qquad k,\ l\ and\ m\in\mathbb{Z} \tag{2.82}$$

where $\boldsymbol{\alpha}$, $\boldsymbol{\beta}$ and γ the three vectors representing the dimensions of the simulation cell.

The most important feature of PBC is that every particle can interact not only with the

---

[3] There are cases where, depending on the system and the phenomenon under study, this replication is done in one or two dimensions.

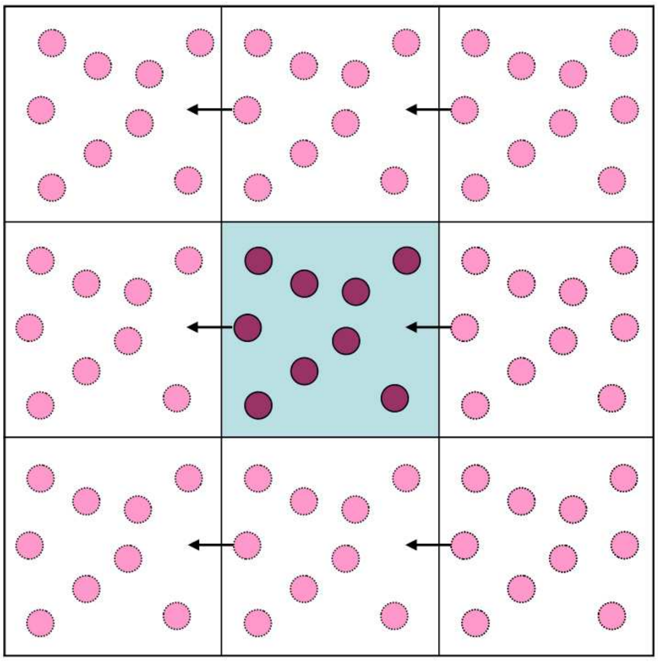

Figure 2.3: **Periodic boundary conditions**. A two dimensional representation of the periodic boundary conditions. The simulation cell, which is coloured grey, is infinitely replicated in three dimensions. Once a particle 'leaves' the simulation cell, it reenters to it from the opposite side and the total number of particles in each cell is constant.

particles that are already in the simulation cell, but also with the ones located in the neighbouring cells. This way, any surface effects due to the finite dimensions of the cell are eliminated. However, with the PBC there could be effects associated with the artificial periodicity of the system. Also, any movement of a particle outside the cell does not affect its interaction with the particles close to it, as the particle 'leaves' the cell and re-enters to it from the opposite side (Figure 2.3).

Another technique used in combination with the PBC is the minimum image convention.

The minimum image convention

In the *minimum image convention*, every particle i interacts only with the closest image of particle j. There are some assumptions to be made so that this condition holds.

As described before, a usual treatment for a potential is to neglect all the interactions after a cut-off distance r_c between two particles. If now we assume that the simulation cell is larger than $2r_c$, it is clear that under these conditions there is at most one pair formed by particle i in the cell and all the images of a particle j.

2.3.3 Neighbour list

Neighbour list is a method used in combination with cut-off for the calculation of interactions between particles. In addition to a cut-off radius r_c, another radius r_n, larger than r_c, is defined. This radius is used in the creation of a 'neighbour list' that includes the atoms that are located at a distance smaller than r_n. In the calculation of short-range interactions, only the particles in each particle's neighbour list are considered. While the simulation proceeds, particles move in or out of the boundaries of r_n. It is thus necessary that the neighbour list is updated regularly throughout the simulation. In order for this to be done periodically and not at each step, r_n should be chosen so that the difference $r_n - r_c$ is large enough.

It is also important to note here, that the neighbour list method leads to a noticeable speedup in the calculation of the forces, as the time to examine all pair separations in a system of N particles is proportional to N^2 and this calculation is avoided between the updates of the list.

2.3.4 Pressure coupling protocols

Apart from the different barostats, there are three different ways to implement pressure coupling, as illustrated in Figure 2.4:

- *isotropic*: in this case all three pressure contributions are coupled, i.e. a change in volume is implemented by changing the length of the box edges by the same increment.
- *semiisotropic*: with this option, only the pressure contributions in x and y directions are coupled.
- *anisotropic*: there is no coupling between any of the pressure contributions.

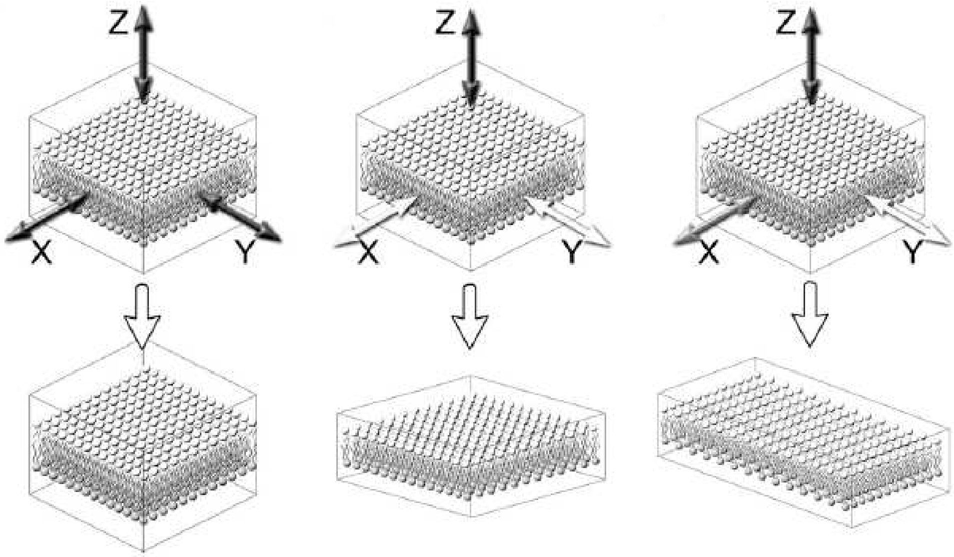

Figure 2.4: **Pressure coupling protocols**: isotropic *(left)*, semi-isotropic *(middle)* and anisotropic *(right)* pressure coupling. The figure has been adapted from [142].

As far as peptide-lipid bilayer simulations are concerned, one must consider that the isotropic pressure coupling does not allow fluctuations in the surface area, which is really important in the study of membranes. On the other hand, although anisotropic pressure coupling enables fluctuations of the surface area, it can also lead to large deformations of the whole system. Consequently, the semiisotropic pressure coupling is the most appropriate in the case of membrane systems.

2.4 Potential of mean force

The *Potential of Mean Force* (PMF) is an estimate of the free energy change along some reaction coordinate and provides the most complete information about the thermodynamics of the system under study.

PMF calculations have been playing an increasingly important role in the characterization of effective biomolecular interactions and processes. In the calculation of the PMF, the system must follow a reaction coordinate, while the other degrees of freedom are integrated out. Supposing that the chosen reaction coordinate is ξ, then

$$A(\xi) = -k_B T \ln \mathcal{P}(\xi), \tag{2.83}$$

where A is the free energy of the system and $\mathcal{P}$ is the probability distribution to find the system at a specific value of the reaction coordinate.

Ideally, one would be able to calculate the free energy difference by counting how often the system samples the different values of the reaction coordinate ξ. However, with simple MD simulations it is not possible to sample two states separated by a high energy barrier, and it is thus an inefficient method for this type of calculations. In these studies, I choose one of the most used and validated methods for the calculation of PMF, the umbrella sampling method [143].

In umbrella sampling, the potential function of the system is modified so that the all the possible states are sampled sufficiently. Considering a reaction coordinate ξ, the modified potential is given by

$$\mathcal{V}'(\xi) = \mathcal{V}(\xi) + \mathcal{W}(\xi), \tag{2.84}$$

where $\mathcal{W}$ is a weighting function, also referred as the *biasing potential*[4]. Usually, the weighting function has the following form

$$\mathcal{W}(\xi) = k(\xi - \xi_0)^2, \tag{2.85}$$

and acts as a spring that encourages barrier crossing. The furthest the system is from the equilibrium state ξ_0, the largest the value of the weighting function, leading to a non-Boltzmann distribution.

A range of values for the reaction coordinate ξ is chosen, (ξ_{min}, ξ_{max}), and is divided into N windows centered around chosen values of ξ_i, with $i = 1, \ldots, N$. In each window, the reference system is under the influence of the weighting function $\mathcal{W}_i$ and the reaction coordinate is sampled. The biased probability function is given by

---

[4] It is important to note that since the potential has changed, the probability function will be determined using this potential.

$$\mathcal{P}_i^{'}(\xi) = \frac{Z_0}{Z_i} \exp^{-\mathcal{W}_i(\xi)} \mathcal{P}_0(\xi), \tag{2.86}$$

where 0 denotes the reference position and i the window.

It can be shown that the unbiased free energy is given by,

$$A(\xi) = -k_B T \ln \mathcal{P}^{'}(\xi) - \mathcal{W}(\xi) + K, \tag{2.87}$$

where K is a free energy constant and depends on $\mathcal{W}(\xi)$. An efficient way of estimating this constant is by using the *weighted histogram analysis method* (WHAM).

Weighted histogram analysis method

The weighted histogram analysis method is an optimization procedure to calculate the constants K^i, so that the estimate for the unbiased distribution function is the weighted sum over the individual unbiased distribution functions of all the N windows used [144]

$$\mathcal{P}_0(\xi) = \frac{\sum_{i=1}^{N} n_i \mathcal{P}_i^{'}(\xi)}{\sum_{i=1}^{N} n_i \exp[-(\mathcal{W}^i(\xi) - K^i)/k_B T]} \tag{2.88}$$

where n_i is the number of observations used to construct the biased distribution function. Also,

$$K^i = -k_B T \ln \sum_{i=1}^{N} \mathcal{P}^{'}(\xi) \exp[-\mathcal{W}^i(\xi)/k_B T]. \tag{2.89}$$

Finally, Equations (2.88) and (2.89) are solved via iterative procedures.

2.5 Molecular force field

Force field is a system of equations that describes the basic physical interactions in a molecular system. It represents the total potential energy of a system of particles and can be described by the sum of intramolecular interactions, pairwise potentials, three-body potentials and so on. The force field is typically divided into bonded and non-bonded categories. Non-bonded interactions include intermolecular van der Waals and Coulombic interactions, and usually in molecular dynamics simulations, for reasons of computational efficiency, only pairwise potentials are considered. Many force fields, like the one employed in this study, have been parametrized in such a way as to include other many body effects, and for this reason sometimes are called *effective pair potentials*. Bonded interactions include intramolecular forces due to bonding, angle bending and torsions (see Figure 2.5). The total energy of a system is given by:

$$\mathcal{V}_{total} = \sum_{pairs} \mathcal{V}_{LJ} + \sum_{pairs} \mathcal{V}_{coul} + \sum_{bonds} \mathcal{V}_{bonds} + \sum_{angles} \mathcal{V}_{angles} + \sum_{dihendral} \mathcal{V}_{dihendral}. \quad (2.90)$$

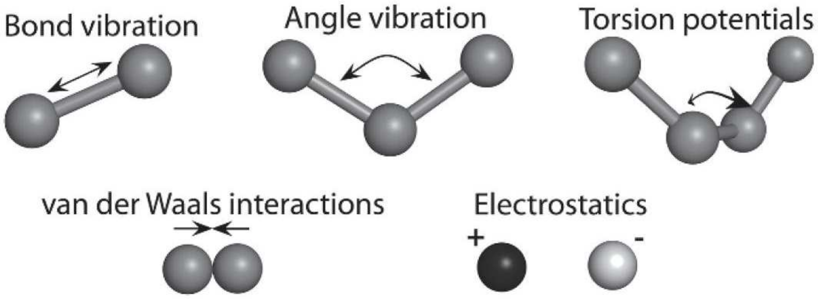

Figure 2.5: **Examples of interactions in a force field**. Basic physical interactions in a molecular system. The interactions are typically divided into bonded and nonbonded categories. Non-bonded interactions include intermolecular van der Waals and Coulombic interactions, whereas bonded interactions include intramolecular forces due to bonding, angle bending and torsions. Figure adapted from [145].

2.5.1 Non-bonded interactions

van der Waals Interactions

In order to calculate the forces on each particle of a system, one needs a description of interparticle interactions, or potentials. One of the simplest and most used potentials to describe the van der Waals interactions is the Lennard-Jones (LJ) 12-6 potential. For a pair of atoms i and j located at $\mathbf{r}_i$ and $\mathbf{r}_j$ the LJ 12-6 potential energy is

$$\mathcal{V}_{LJ}(r_{ij}) = 4\epsilon \left[\left(\frac{\sigma}{r_{ij}} \right)^{12} - \left(\frac{\sigma}{r_{ij}} \right)^{6} \right], \tag{2.91}$$

where $\mathbf{r}_{ij} = \mathbf{r}_i - \mathbf{r}_j$ and $r_{ij} = \|\mathbf{r}_{ij}\|$, ϵ is the depth of the potential and σ is the collision diameter. The potential described by Equation (2.91) includes both a short-range, repulsive component due to electronic clouds overlap, and an attractive component due to dispersion forces.

Since intermolecular forces are necessarily conservative, the force that atom j exerts on atom i is given by

$$\mathbf{F}_{ij} = \left(\frac{48\epsilon}{\sigma^2} \right) \left[\left(\frac{\sigma}{r_{ij}} \right)^{14} - \frac{1}{2} \left(\frac{\sigma}{r_{ij}} \right)^{8} \right] \mathbf{r}_{ij}. \tag{2.92}$$

As depicted in Figure 2.6, the contribution of remote particles to the total LJ-potential can be considered insignificant. We can thus neglect pair interactions beyond some cut off radius r_c in order to save computational time.

A common choice for r_c is 2.5σ as for $r_{ij} = r_c$, $\mathbf{F}_{ij}$ has a comparatively small value.

Usually in practice, in order to avoid large errors and the noise induced by the cut-off effects, the truncated forces are replaced by forces that are continuous with continuous derivatives at the cut-off radius. This method is called shift.

The shifted force $\mathbf{F}^s$ will be given by

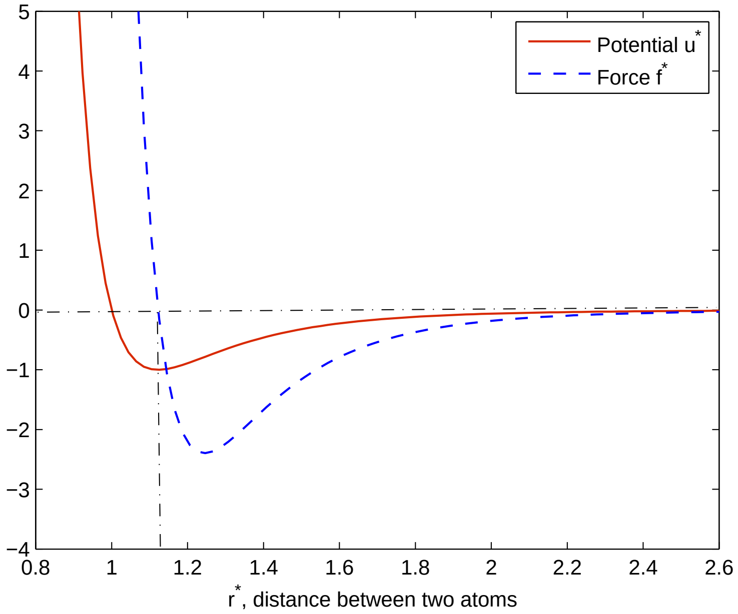

Figure 2.6: **Lennard-Jones (12,6) pair potential and pair force in reduced units.** $(r^* = r/\sigma, u^* = u/\epsilon, f^* = f\sigma/\epsilon)$

$$\mathbf{F}^s(\mathbf{r}_{ij}) = \begin{cases} -\dfrac{d\mathcal{V}_{LJ}}{dr_{ij}} + \Delta F & , r_{ij} < r_c, \\ 0 & , r_{ij} \geq r_c, \end{cases} \tag{2.93}$$

where ΔF is the magnitude of the shift,

$$\Delta F = -F(\mathbf{r_c}) = \left(\frac{d\mathcal{V}_{LJ}}{dr}\right)_{r_c} . \tag{2.94}$$

By integrating Equation (2.93), we obtain

$$\mathcal{V}^s_{LJ}(r_{ij}) = \begin{cases} \mathcal{V}_{LJ}(r_{ij}) - \mathcal{V}_{LJ}(r_c) - (r_{ij} - r_c)\left(\dfrac{d\mathcal{V}_{LJ}}{dr}\right)_{r_c} & , r_{ij} < r_c, \\ 0 & , r_{ij} \geq r_c. \end{cases} \tag{2.95}$$

Coulombic electrostatic potential

The electrostatic interaction between two molecules (or between different parts of the same molecule) is given by Coulomb's law:

$$\mathcal{V}_{coul}(\mathbf{r}_{ij}) = \frac{q_i q_j}{4\pi\epsilon_0 r_{ij}}, \tag{2.96}$$

where ϵ_0 is the permittivity in vacuum, q_i and q_j represent the charges on particles i and j respectively, and $\mathbf{r}_{ij}$ is the distance between particles i and j.

The Coulombic force that atom j exerts on atom i is

$$\mathbf{F}_{ij}^{coul} = \frac{q_i q_j}{4\pi\epsilon_0 \mathbf{r}_{ij}^2}. \tag{2.97}$$

The treatment of electrostatic interactions has become a subject of controversy in the area of molecular dynamics simulations. The use of a cut-off is reasonably efficient for van der Waals interactions with r^{-6} radial dependence, such as the Lennard-Jones potential. However, this treatment may lead to artefacts in the case of electrostatic interactions, since they have considerably longer range (they decay as a function of r^{-1}). A more efficient approach is the Ewald summation technique.

In Ewald summation method, the slowly converging charge distribution is treated as the sum of two reciprocal space distributions, which converges much faster. Supposing that we have a system of N particles, treated with periodic boundary conditions and with a dielectric constant ϵ_0, we have

$$\mathcal{V}_{coul} = \frac{1}{2}\sum_{\mathbf{n}}\sum_{i=1}^{N}\sum_{j=1}^{N}\frac{q_i q_j}{4\pi\epsilon_0|\mathbf{r}_{ij}+\mathbf{n}|}, \tag{2.98}$$

where $\mathbf{n} = (n_x L_x, n_y L_y, n_z L_z)$, with L_x, L_y, L_z the dimensions of the simulation box and n_x, n_y, n_z integer indicating the position at the cubic lattice created from the periodic boundary conditions. In the case that $|n| = 0$, i.e. we are in the central box, the first sum is for all the i and j with $i \neq j$.

Equation (2.98) converges very slowly. The key to this method is that instead of waiting for Equation (2.98) to converge, the summation is broken into two series that converge much faster. Each point charge is surrounded by a Gaussian charge distribution,

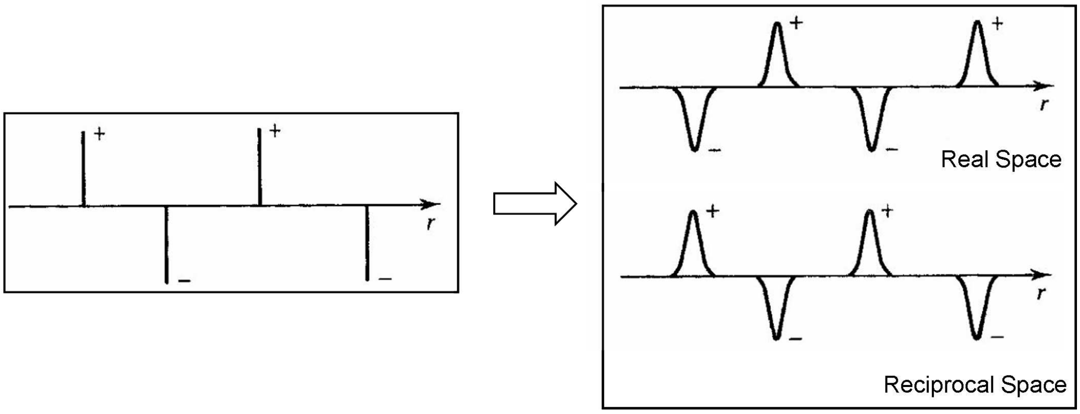

Figure 2.7: **Ewald summation**. The initial set of charges (left) are surrounded by a Gaussian distribution calculated in the real space (top right) and then cancelled by a Gaussian distribution calculated in the reciprocal space (bottom right).

$$\rho_i(\mathbf{r}) = \frac{q_i\alpha^3}{\pi^{3/2}}\exp(-\alpha^2 r^2), \forall\, i \in 1,\ldots,N, \tag{2.99}$$

where α is a positive parameter that determines the width of distribution. These Gaussians are cancelled with the corresponding Gaussians of negative sign in reciprocal space, in order to determine the original coulombic potential (Figure 2.7).

There are several variations of Ewald summation method, with the *particle mesh Ewald* (PME) being one of the most widely used in molecular dynamics simulations. Briefly, in PME, only the 27 nearest points in the three dimensions are used in the calculation of potential. From this 27-point mesh of charge density, through the use of fast Fourier transform, and interpolation, the potential at each of the particles is calculated.

Apart from the cut-off and the lattice-sum techniques, like the PME, there are the reaction field approaches (RF). In these methods, a correction term is added to the cut-off result based on a continuum electrostatics description of the solvent outside the cut-off sphere [142]. This way the effect of long-range electrostatic interactions is also included. However, due the structure of lipid bilayers, this approach is not appropriate for the description of electrostatic interactions for peptide-membrane systems.

More detailed description of the different approaches for the treatement of the electrostatics can be found in Allen and Tildesley [139], Leach [137] and Frenkel and Smit

[138].

2.5.2 Bonded interactions

In order to describe the structure of a molecule, one uses the interatomic distances constrained by chemical bond lengths between two particles, the bond angles between three particles and dihedral angles between three consecutive bond vectors. I will shortly present the most common approaches for the treatment of bonded interactions.

Bond length

The bond length (stretching) between two particles is often modelled using a harmonic spring potential:

$$\mathcal{V}_{bond}(r) = \frac{1}{2}k_b(r - r_b)^2, \tag{2.100}$$

where k_b is the bond force constant representing the stiffness of the bond, r_b is the equilibrium bond length and r is the distance between the two bonded atoms.

Angle bending

Angle bending, like the bond length interaction, can be represented by a harmonic potential as a function of θ, which is the angle formed by three particles:

$$\mathcal{V}_{angle}(\theta) = k_\theta(\theta - \theta_0)^2, \tag{2.101}$$

where k_θ is the angle force constant and θ_0 is the optimal equilibrium angle.

Torsions

The dihedral angle potentials describe the interaction arising from torsional forces between particles and they require the specification of four atomic positions. One of the mainly used expressions for the dihedral angle potential is:

$$\mathcal{V}_{dihendral}(\phi) = k_{\phi}(1 + cos(n\phi - \delta)), \tag{2.102}$$

where ϕ is the dihedral angle, k_{ϕ} is the dihendral force constant, n is the multiplicity, and δ is the phase of the potential.

2.6 The molecular model

2.6.1 Molecular mapping and interaction sites

In the studies presented in this thesis, the species are described using the model of lipids and peptides recently proposed by Marrink and co-workers (MARTINI) [105, 106]. The MARTINI was developed in an effort to expand an already successful coarse-grained protocol for membranes to proteins. In the following sections, I will present a general description of the model and force field parameters, and I will focus on the representations and parameters used for the modelling of membranes and peptides.

In the MARTINI, every four heavy atoms (i.e. not hydrogens) are represented by one effective bead, with an exception made for ring structures. There are four main types of beads representing different levels of interaction: polar (P), apolar (C), nonpolar (N), and charged (Q). Apart from these main types, each bead is assigned a further subtype, in order to describe more accurately the overall chemical nature of the represented group of atoms. In this description, hydrogen-bonding capability (d=donor, a=acceptor, da=both and 0=none) and different levels of polarity (from 1=low polarity, to 5=high polarity) are included. All the beads are assigned a mass of m=72 amu (four water molecules) for reasons of computational efficiency (for the beads that take part in ring structures this value is equal to 45 amu).

2.6.2 The molecular force field

In the MARTINI, the van der Waals interactions are described using a shifted Lennard-Jones 12-6 potential. An effective size of σ=0.47 nm is used (this value is slightly smaller, σ=0.43 nm, for the ringlike structures[5]. Ten different values of the characteristic energy ϵ are available to represent possible interactions among various bead types (these values are scaled to 75% to describe interactions between particles belonging to a ring molecule). In Tables 2.1 and 2.2, I present the different levels of interactions and a bead interaction matrix as presented in the original publication [106]. The charged particles interact through a Coulombic potential energy with a relative dielectric constant $\epsilon_{rel} = 20$.

For both van der Waals and Coulombic interactions a cut-off of 1.2 nm is used. A shift to zero is also used between 0.9 and 1.2 nm in the case of van der Waals interactions and between 0 and 1.2 nm for the electrostatic interactions.

Table 2.1: **Levels of interaction** (same as in [106]).

	Description	ϵ_{ij} (kJ/mol)	σ (nm)
O	supra attractive	5.6	0.47
I	attractive:	5.0	0.47
II	almost attractive	4.5	0.47
III	semi attractive	4.0	0.47
IV	intermediate	3.5	0.47
V	almost intermediate	3.1	0.47
VI	semi repulsive	2.7	0.47
VII	almost repulsive	2.3	0.47
VII	repulsive	2.0	0.47
IX	super repulsive	2.0	0.62

The bonds between the CG sites are described by a harmonic spring potential. For the description of angles a harmonic cosine potential is used. Moreover, in the MARTINI, the secondary structure is held fixed by dihedral angle potentials. The force field has been validated against several key properties of different amino acids, such as oil/water partition coefficients and free energy profiles of amino acid insertion into a model lipid bilayer [105]. More detailed description of the force field parameters can be found in the article by Monticelli *et al.* [105].

---

[5] A prefix *S* will be used from now on to signify beads belonging to the special class of beads that are used in the ringlike structures.

Table 2.2: **Interaction matrix** (same as in [106]).

		Q				P					N				C				
		da	d	a	0	5	4	3	2	1	da	d	a	0	5	4	3	2	1
Q	da	O	O	O	II	O	O	O	I	I	I	I	I	IV	V	VI	VII	IX	IX
	d	O	I	O	II	O	O	O	I	I	I	III	I	IV	V	VI	VII	IX	IX
	a	O	O	I	II	O	O	O	I	I	I	I	III	IV	V	VI	VII	IX	IX
	0	II	II	II	IV	I	O	I	II	III	III	III	III	IV	V	VI	VII	IX	IX
P	5	O	O	O	I	O	O	O	O	O	I	I	I	IV	V	VI	VI	VII	VIII
	4	O	O	O	O	O	I	I	II	II	III	III	III	IV	V	VI	VI	VII	VIII
	3	O	O	O	I	O	I	I	II	II	II	II	II	IV	IV	V	V	VI	VII
	2	I	I	I	II	O	II	II	II	II	II	II	II	III	IV	IV	V	VI	VII
	1	I	I	I	III	O	II	II	II	II	II	II	II	III	IV	IV	IV	V	VI
N	da	I	I	I	III	I	III	II	II	II	II	II	II	IV	IV	V	VI	VI	VI
	d	I	III	I	III	I	III	II	II	II	II	III	II	IV	IV	V	VI	VI	VI
	a	I	I	III	III	I	III	II	II	II	II	II	III	IV	IV	V	VI	VI	VI
	0	IV	IV	IV	IV	IV	IV	IV	III	III	IV	IV	IV	IV	IV	IV	IV	V	VI
C	5	V	V	V	V	V	V	IV	IV	IV	IV	IV	IV	IV	IV	IV	IV	V	V
	4	VI	VI	VI	VI	VI	VI	V	IV	IV	V	V	V	IV	IV	IV	IV	V	V
	3	VII	VII	VII	VII	VI	VI	V	V	IV	VI	VI	VI	IV	IV	IV	IV	IV	IV
	2	IX	IX	IX	IX	VII	VII	VI	VI	V	VI	VI	VI	V	V	V	IV	IV	IV
	1	IX	IX	IX	IX	VIII	VIII	VII	VII	VI	VI	VI	VI	VI	V	V	IV	IV	IV

2.6.3 Coarse-grained description of a peptide-membrane system

The membrane

The membranes used in the coarse-grained simulations of this thesis have been represented with the MARTINI force field. As described in the Introduction, a membrane is composed mainly of lipids and proteins. For reasons of simplicity, I will represent the membrane as a lipid bilayer, without undervaluing the importance of membrane proteins in the overall functionality of a cell membrane.

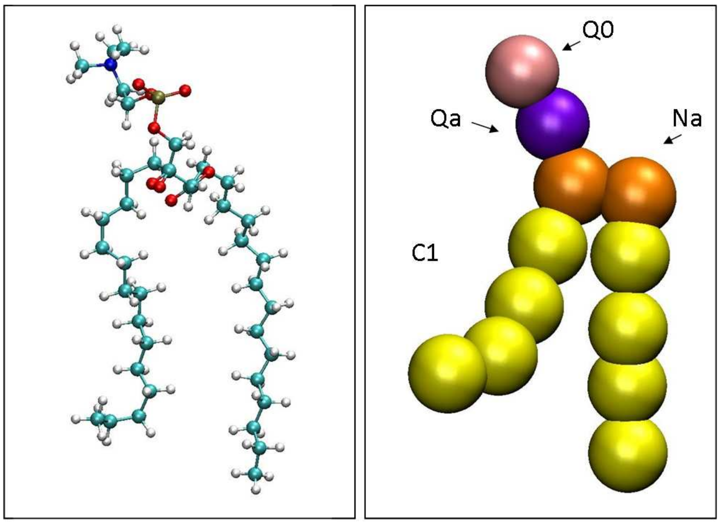

Figure 2.8: **Atomistic and coarse-grained representations for a DPPC lipid.** Atomistic (*left*) and coarse-grained (*right*) representations for a DPPC lipid. We can note the dramatic reduction in system size from the AL to the CG representation. This reduces significantly the time and memory requirements of the simulation. Colours: a) for the atomistic representation: carbon=light blue, oxygen=red, nitrogen=dark blue, hydrogen=white, b) for the coarse-grained representation: lipid tails (C1 type)=yellow, glycerol moiety (Na-type)=orange, phosphate moiety (Qa-type)=purple and choline group (Q0-type)=pink.

In Figure 2.8, there are the atomistic and coarse-grained representations of a DPPC lipid. The lipid tails are represented as C1-type beads, the glycerol moiety as Na-type, the phosphate moiety as Qa-type and the choline group as Q0-type beads. Moreover, in the MARTINI, four water molecules are represented by a P4-type bead. A lipid bilayer described by the MARTINI force field is depicted in Figure 2.9.

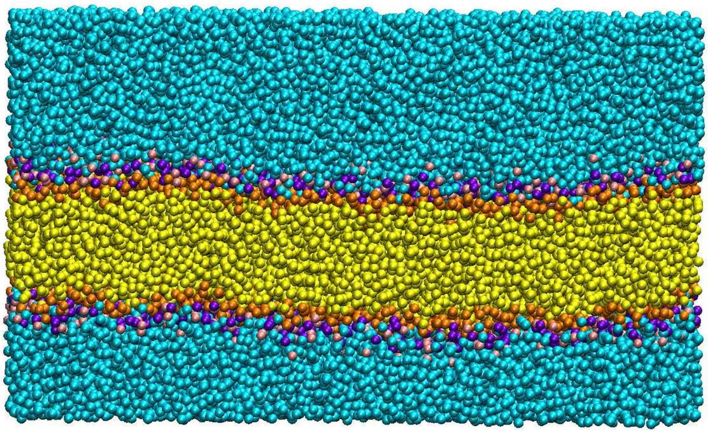

Figure 2.9: **Coarse-grained representation of a lipid bilayer**. Colours: lipid tails (C1 type)=yellow, glycerol moiety (Na-type)=orange, phosphate moiety (Qa-type)=purple, choline group (Q0-type)=pink and water beads (P4-type)=light blue.

The peptides

The coarse-grained representation of the different natural amino acids is done in the same way described above. The side chains of the amino acids are mapped to the coarse-grained beads that describe appropriately their properties. The hydrophobic amino acids are mapped to C-type beads, the hydrophilic to P-type beads and for the representation of the charged amino acids Q-type beads are used. The ring-like side chains of the bulkier amino acids are represented by three or four beads of ring particles [6]. In Table 2.3, I summarize this mapping. The beads that are shown in brackets correspond to the protonated state of the amino acids. Alanine and glysine are represented only by the backbone bead. The backbone bead types depend on the secondary structure of the peptide or protein that they describe. For example, in the case of α-helices the backbone structure is mapped into N0-type beads apart from the termini. For a capped α-helix the termini are represented by Nd-type and Na-type beads for the N-terminus and C-terminus respectively. In the case where an uncapped helix is considered, charged beads (Qd and Qa) are used to represent the termini. Also, the three closest to the termini backbone beads are represented by Nd and Na types for the N- and C-terminus respectively. The overall mapping of the backbone of a capped peptide is shown in Table 2.4. In Figure 2.10, I show the atomistic and coarse-grained representations of LS3 synthetic peptide. From the figure, we can see the dramatic

---

[6] These particles are slightly smaller, σ=0.43 nm, and for their description an S is put before the name of the assigned bead.

reduction of degrees of freedom; 390 atoms in the atomistic model and 42 beads in the coarse-grained model.

Table 2.3: **CG representation of the amino acids** (same as in [105]).

Amino acid	**Coarse-grained representation**
Leu	C1
Ile	C1
Val	C2
Pro	C2
Met	C5
Cys	C5
Ser	P1
Thr	P1
Asn	P5
Gln	P4
Asp	Qa (P3)
Glu	Qa (P1)
Arg	N0-Qd (N0-P4)
Lys	C3-Qd (C3-P1)
His	SC4-SP1-SP1
Phe	SC4-SC4-SC4
Tyr	SC4-SC4-SP1
Trp	SC4-SP1-SC4-SC4

Table 2.4: **CG representation of the backbone structure of a peptide** (same as in [105]).

	coil	helix	helix (N-terminus/C-terminus)	β-strand turn
backbone	P5	N0	Nd/Na	Nda
Gly	P5	N0	Nd/Na	Nda
Ala	P4	C5	N0	N0
Pro	Na	C5	N0/Na	N0

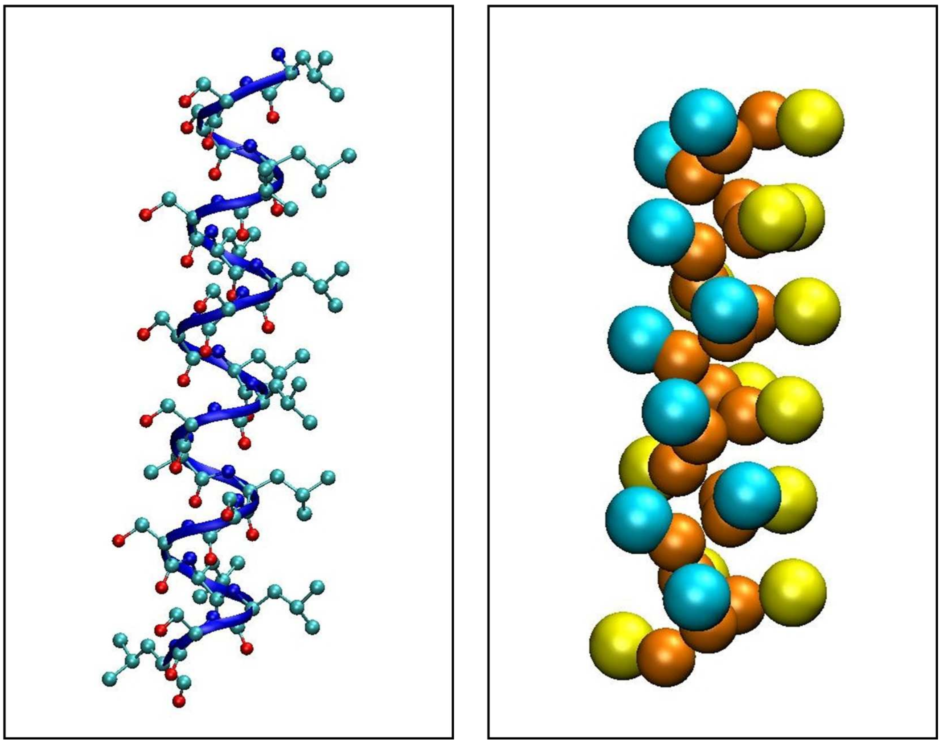

Figure 2.10: **Atomistic and coarse-grained representations for LS3 synthetic peptide**. Colours: a) for the atomistic representation: cyan=carbon, red=oxygen, blue=nitrogen, white=hydrogen, b) for the coarse-grained representation: blue=hydrophobic beads, light blue=hydrophilic beads and orange= backbone beads. The beads are not shown to scale.

2.7 Data analysis tools

In the current study I am interested in getting information about the dynamics and structural features and rearrangements of a peptide-membrane system. VMD software is used throughout this investigation for the direct visualization of the systems under study [146]. There are however features that cannot be identified simply by viewing the evolution of a system through time. For this reason, density profiles, peptide angle distributions, the radii of formatted pores as well as their self-diffusion coefficient are calculated in this study. For the later, GROMACS software was used to get the mean squared displacement and by using the Einstein relation and weighted least squares I estimated the self-diffusion coefficient [147]. More details about these calculations will be given in the relevant chapter. For the other features I developed a range of programs which will be described in the following sections.

2.7.1 Density profiles

A density profile is one of the results from MD simulations that can be, in some cases, directly compared with experimental data. In order to compare our results with the available data, I developed a program that calculates the density profiles of a selected residue. This program reads a molecular dynamics trajectory and returns the density distribution of the chosen residue along the bilayer normal. The basic steps for this calculation can be listed as follows:

1. **Calculation of the bilayer plane**: the program reads a file with the coordinates of the lipids and, by using least squares, calculates their centre of mass and the normal of the bilayer. The output is the plane that passes from the centre of the bilayer and is parallel to the lipid heads.
2. **Calculation of the distance of the chosen molecule from the bilayer plane.**
3. **Density profile calculation**: the distances calculated at the previous step are grouped into histograms. I then normalize these histograms and the resulting data correspond to the probability distribution of finding a chosen molecule at a certain distance from the centre of the bilayer.

2.7.2 Angle distribution

The calculation of the angle distribution is a very useful tool in the studies of peptide-membrane systems. In particular, it can be used as a way of differentiating fusion or oblique peptides and interfacial peptides by calculating the relative angle between the helical axis and the bilayer normal (Figure 2.11).

In order to calculate the angle distribution, I follow the following steps:

1. **Calculation of the bilayer plane**: in particular for this program we only need the normal of the bilayer (see previous paragraph).
2. **Define the helix axis:** At this step the program determines the tensor of inertia of the peptide with respect to its centre of mass. The principal axes of intertia passing through the centre of mass of the peptide, and their corresponding mo-

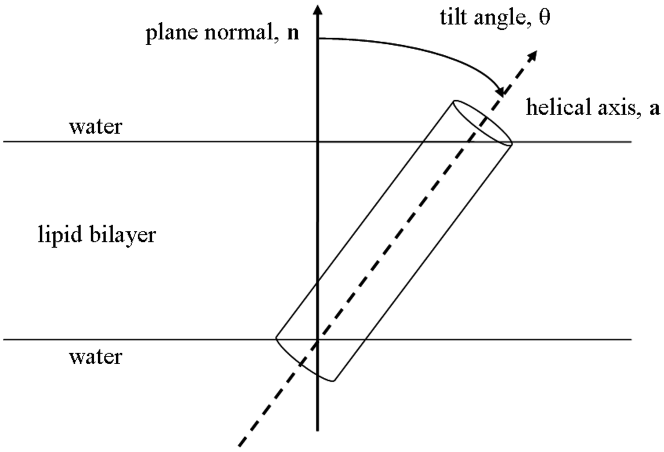

Figure 2.11: **Angle calculation**.

ments of inertia are the eigenvectors and eigenvalues of the inertia tensor. The helix axis is the one corresponding to the smallest eigenvalue [148].

3. **Calculation of the tilt of the peptide relative to the bilayer normal**: this is simply done by using the inner product of the bilayer normal and the helix axis vectors:

$$\mathbf{n} \cdot \mathbf{a} = |\mathbf{n}| \cdot |\mathbf{a}| \cdot cos(\theta) \tag{2.103}$$

   where **n** and **a** are the vectors of the bilayer normal and the helix axis respectively and θ is angle between them.

4. **Angle distribution**: in a similar manner as in the density distribution, the calculated angles are grouped in the histograms, the average values of each histogram are normalized, resulting in the probability of finding the peptide at a specific orientation.

The previous procedure can be used for the calculation of the tilt of a peptide bundle.

2.7.3 Geometrical features of supramolecular assemblies

In the case of pore-forming peptides, one of the features that can be calculated through MD simulations is the size of the pore. Apart from the exact number of helices taking part in the pore, that can be viewed by a simple visualization of the trajectory, the diameter of the pore can also be estimated.

For the calculation of the pore diameter, I developed a program that can be broken down into the following steps:

1. Create a lattice inside the pore.
2. Calculate all the distances of the lattice points and the centres of the coarse-grained beads representing the peptides.
3. Keep the smallest of these distances for each lattice point, L.
4. If any of these distances is smaller than the coarse-grained bead radius remove it.
5. Create an array with the $R = L - d/2$ values and pick the biggest. d is the diameter of the beads.

This program can be used for the calculation of an estimate of the inner or outer diameter of a bundle.

CHAPTER 3

Coarse-grained model validation: Application to different classes of amphipathic α-helical peptides

Until now, I have introduced the biological and modelling background on peptide-membrane interactions. In this chapter, I focus on several types of interactions between lipid membranes and α-helical peptides, based on the distribution of hydrophobic and hydrophilic residues along the helix. I employed the MARTINI force field and tested its ability to capture diverse types of behaviour. For example, the simulations provided us with useful insights on the formation of a barrel-stave pore. Amphipathic nonspanning peptides were also described with sufficient accuracy. However, the picture was not as clear for fusion and transmembrane peptides. For each class of peptides, I calculated the potential of mean force (PMF) for peptide translocation across the lipid bilayer and demonstrated that each class has a distinct shape of PMF. The reliability of these calculations, as well as wider implications of the results, are discussed.

3.1 Introduction

In the effort to test the validity and scope of the MARTINI coarse-grained model, I was guided by a general classification of possible modes of peptide-membrane interactions for α-helices employed in a series of publications by Brasseur and co-workers [6, 149, 150]. This classification is based on a view of α-helical peptides as amphiphilic entities with a well-defined geometry. The idea is that the distribution of hydrophobic and hydrophilic residues along the α-helix plays a central role in the partition of the peptide between the hydrophilic aqueous media and the hydrophobic core of the lipid membrane. Thus, depending on this distribution, several possible scenarios can be identified and are schematically depicted in Figure 3.1. In these schematics α-helices are represented as cylinders with their hydrophobic regions shaded yellow. The top part of each subfigure provides a side-view of the cylinders. From this side-view, one can observe the difference in the hydrophobicity distribution among various classes of peptides. At the bottom of each subfigure, I present the proposed interaction mechanism for each class. The helices are represented as cylinders coloured orange. Although this is a simplified description, and not all of the α-helical peptides feature a well-defined distribution of hydrophobic groups, there are many of them whose structure and behaviour does indeed fall in one of these general classes. Let us briefly review some of the examples here.

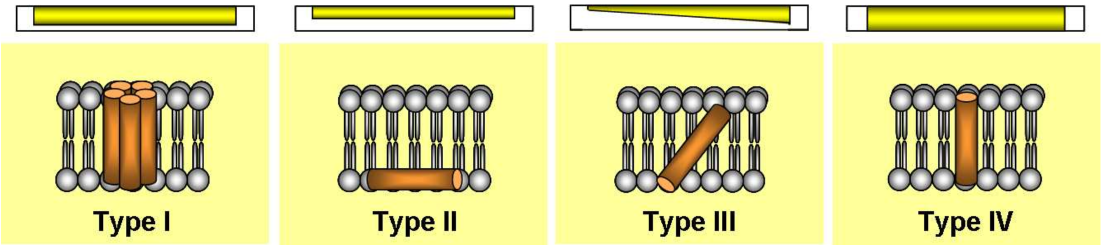

Figure 3.1: **Schematic view of the different classes of α-helical peptides according to their hydrophobicity distribution along the axis**. Top of subfigures: side-view of the α-helices. The helices are represented as cylinders with their hydrophobic regions yellow. Bottom of subfigures: proposed interaction mechanism for each class. The helices are represented as cylinders coloured orange. (Adapted from figures 3, 4 and 5 in reference [6].)

Typical representatives of Type I class are the α-helical peptides forming (and derived from) protein ion-conducting channels (Figure 3.1, Type I). These helices usually consist of two strands of hydrophobic and hydrophilic residues along their helical axis, with the hydrophobic region being dominant. In the membrane, several peptides form a bundle, with the hydrophobic groups facing the core of the membrane.

During the past two decades, a number of model channel systems, consisting of synthetic helices of this type, have been studied. The 'synporins', synthetic peptides developed by Montal and co-workers [151–153], as well as the 'template-assembled synthetic proteins' (TASPs) used by Mutter and co-workers [154, 155], are two examples of ion channels formed by synthetic peptides in lipid bilayers. Moreover, Lear *et al.* synthesized three model peptides containing only leucine and serine residues, in order to investigate the mechanism by which these helices associate into transmembrane bundles [16]. For example, one of these synthetic peptides, LS3, features all the characteristics of a membrane spanning helix as well as the necessary amphiphilicity to provide the desired aggregation of polar faces, thus leading to spontaneous formation of well-defined transmembrane ion channels. In the bundle formed by LS3 helices, the peptides are tightly aligned with the tails of the neighbouring lipids stretching along them. This kind of bundle is often classified as a barrel-stave pore (Figure 3.1, Type I).

The peptides whose hydrophobic region is either the same or smaller than the hydrophilic region do not have the ability to span the membrane. Examples of these peptides are provided by the synthetic lipid-associating peptide, LAP-20, and the lipid-associating peptides of the plasma apolipoproteins, apoA-I. It has been shown that these peptides interact with the membrane so that the contact area of the helices with the aqueous phase is either comparable in size with that with the lipid phase (LAP-20, Figure 3.1, Type II), or larger (apoA-I) [6]. This leads to either an interfacial orientation of the peptide or formation of discoidal particles (included in the original Brasseur classification, but not considered here).

In the case of fusion peptides (Figure 3.1, Type III), there is a non-uniform distribution of hydrophobic residues along the helical axis. This characteristic has been suggested as one of the main reasons behind the oblique orientation of fusion peptides relative to the bilayer [6, 149, 150]. Moreover, several experimental and theoretical studies linked this particular mode of peptide insertion to the fusogenic activity of these peptides [149, 156–158]. The fusion peptides of Simian Immunodeficiency Virus (SIV) [149, 159, 160], Newcastle Disease Virus (NDV) [161] and Human Immunodeficiency Virus (HIV) [159, 162] were some of the first representatives of this class to be identified.

Those helices that are long enough to span the hydrophobic medium of the membrane, with most or all of their residues being hydrophobic, tend to adopt a transmembrane position in a lipid bilayer (Figure 3.1, Type IV). These transmembrane helices have a uniform distribution of hydrophobic residues both around and along their helical axis. Among this kind of helices are the Glycophorin A (GpA) [100, 163], the pHLIP peptide [164–167] as well as the TMX-1 synthetic peptide [54].

Selected representative peptides from each class were chosen in order to probe the ability of a coarse-grained protocol to capture these diverse scenarios. The selected peptides satisfy one or more of the following criteria: there should be well-reported experimental data on their behaviour, they should be sufficiently simple (short), have a confirmed α-helical structure in the presence of the membranes and be of a certain technological importance. In Table 3.1, I summarize the peptides considered in this work and the class of behaviour they belong to.

Table 3.1: **Summary of the peptides under study and their primary sequences**.

Peptide	Sequence	Type	Ref.
LS3	$(\mathrm{LSSLLSL})_3$	I	[16]
LAP20	VSSLLSSLKEYWSSLKESFS	II	[168]
SIV	GVFVLGFLGFLA	III	[29]
TMX-1	WNALAAVAAALAAVAAALAAVAASKSKSKSK	IV	[54]
pHLIP	ACEQNPIYWARYANWLFTTPLLLLNLALLVDADEGTG	IV	[164]

In Figure 3.2, I present the side and top view of the peptides under study. For simplicity, I represent the backbone beads of the helices with orange, the side chain beads of all the hydrophilic residues with light blue and all the side chain beads of the hydrophobic residues with yellow. Alanine is represented by one bead coloured yellow as an indication of its hydrophobic nature. In the top view of the helices, the hydrophilic beads have been removed in order to show the distribution of the hydrophobic beads around the helical axis.

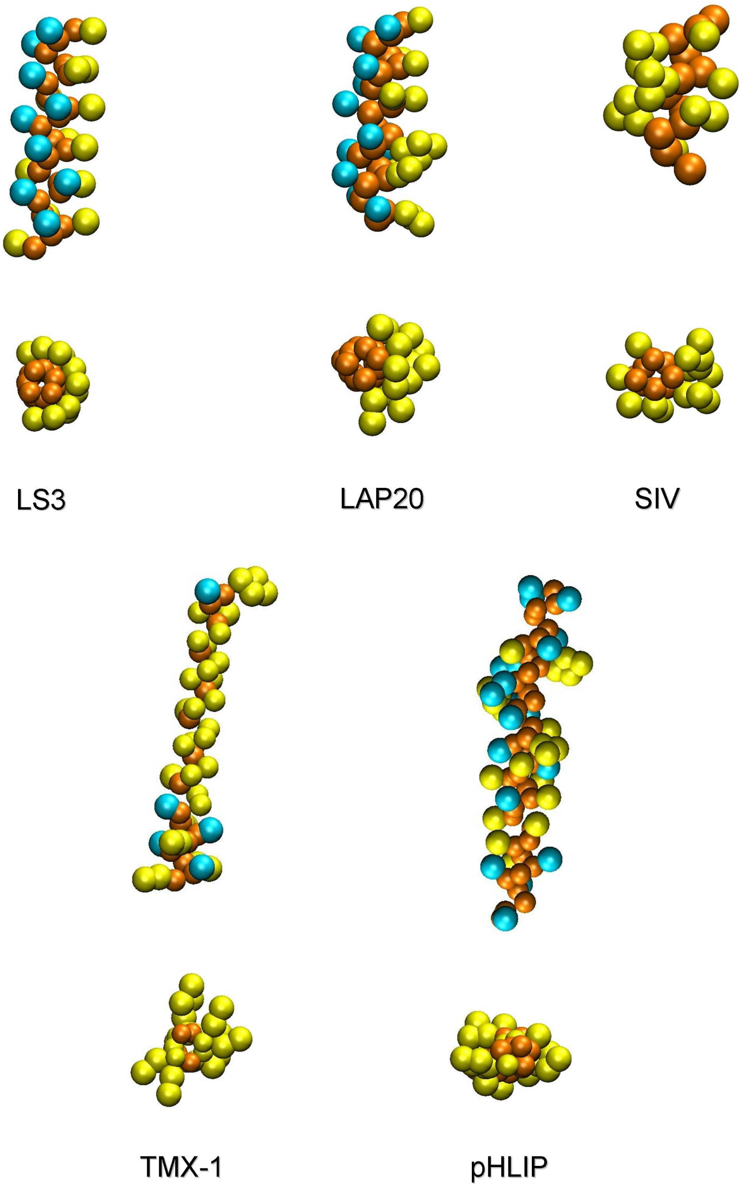

LS3 LAP20 SIV

TMX-1 pHLIP

Figure 3.2: **Side and top views of LS3, LAP20, SIV, TMX-1 and pHLIP peptides**. Their backbone beads are shown in orange, their hydrophobic residues in yellow and their hydrophilic residues in light blue. Alanine is represented by one yellow bead.

3.2 Simulation parameters

The simulations presented in this study were performed with GROMACS simulation package, version 3.3.2 [169]. Initially, I employed molecular dynamics simulations of lipid and water components, in order to obtain the initial bilayer structures that were used in our studies. These preliminary simulations were up to 200 ns long depending on the size of the bilayer. The protocol and the simulation parameters used for these assembly simulations have previously been employed by Marrink and co-workers [82]. Three different types of lipid bilayer systems were considered: 1,2-Dipalmitoyl-sn-Glycero-3-phosphocholine or DPPC, 1,2-Dioleoyl-sn-Glycero-3-phosphocholine or DOPC and 1-Palmitoyl,2-oleoyl-sn-Glycero-3-phosphocholine or POPC. I chose different lipid systems in order to have a direct comparison with the corresponding experimental studies for each peptide.

The atomistic structures of the peptides were generated using HyperChem 8.0 software [170]. To coarse-grain these structures, I applied the script provided on the MARTINI force field web page [171]. All peptides of interest were considered to be in the α-helical secondary structure[1]. In the coarse-grained description their α-helical structure was maintained via the constraints imposed by the MARTINI force field. All the peptides were capped at their termini apart from the LS3 peptide. After minimizing the energy of individual peptide molecules, I randomly inserted them in the system of interest. In the cases where the peptides under study were charged, ions were inserted in the system to maintain the overall system electroneutrality. For each system, I then performed energy minimization using the steepest descent method. Finally, molecular dynamics (MD) simulations with constant pressure, temperature and number of particles (NPT ensemble) were performed. The temperature was kept constant for each group, at 323 K for the DPPC/peptides systems and 300 K for the DOPC/peptide and POPC/peptide systems, using the Berendsen thermostat with a relaxation time of 1 ps [135]. The pressure of the system was semi-isotropically coupled and maintained at 1 bar using the Berendsen algorithm with a time constant of 5 ps and a compressibility of 4.5×10^{-5} bar^{-1} [135]. The non-bonded potential energy functions were cut-off and shifted at 12 Å, with forces smoothly decaying between 9 Å and 12 Å for van der Waals forces and throughout the whole interaction range for the treatment of elec-

---

[1] In the case of SIV fusion peptide the C-terminus is left flexible. See also section 3.2.1.

trostatic forces. The simulations were performed using a 25 fs integration time step. The simulation parameters applied in our membrane-peptide studies have previously been proposed and used by other groups [100, 105].

3.2.1 Atomistic simulations

For the specific case of the SIV fusion peptide, I also performed atomistic molecular dynamics simulations in a DOPC bilayer. I used the united atom lipid parameters initially developed by Berger *et al.* [172], and modified for DOPC lipids by Siu *et al.* [173, 174], combined with the GROMOS96 force field and Simple Point Charge (SPC) model for water proposed by Berendsen [175]. I assumed that the peptide is in an α-helical secondary structure, apart from its C-terminus which is left flexible, in agreement with previous observations [29]. To maintain the secondary structure, I put restraints between the i^{th}- ($i^{th}+4$) α-carbons, starting from the third residue of the peptide. I performed a number of self-assembly molecular dynamics simulations, up to 100 ns long, initially with the lipids and water randomly mixed and allowed to spontaneously form a lipid bilayer. From the formed lipid bilayers, I chose a system of 97 DOPC molecules and 4947 water molecules. I then randomly inserted the SIV fusion peptide in the water phase of the system, and performed NPT molecular dynamics simulations. All simulations were carried out using the GROMACS simulation package [169], following the approach proposed by de Vries *et al.* [176], at $T = 300$ K, $P = 1$ bar, with a time step of 2.5 fs, using the Berendsen thermostat and barostat [135].

3.2.2 Potential of mean force calculations

I am interested in the potential of mean force (PMF) as a function of the distance between the peptide and the lipid bilayer. In this study, the PMF was calculated using the umbrella sampling protocol [143]. This calculation was performed for coarse-grained models of peptides only. All PMF calculations were carried out for a single peptide interacting with a bilayer. The total separation distance between the peptide and the centre of the bilayer was 5 nm and was divided into 50 small windows of 0.1 nm each. For each peptide, three sets of umbrella sampling simulations with 50 windows were performed. In each set and in each window, I used different independent initial configurations, with the peptide placed at the corresponding distance from the centre of the bilayer. The system was then left to equilibrate for several nanoseconds. Afterwards, a 100 ns long simulation was performed, with the biasing potential applied to restrain the centre of mass of the peptide at a required distance from the centre of the bilayer. Thus, a single PMF profile required 50 simulations, covering the whole separation range of interest, with a total simulation time of 5 μs. A force constant of 1000 kJ mol^{-1} nm^{-2} was applied, following the approach by Monticelli *et al.* [105]. The system used in the case of the longer peptides featured a large enough water phase to avoid possible effects associated with the system size and peptide-peptide interactions over periodic boundaries. The peptides were left free to rotate around their restrained centre of mass. In order to obtain the unbiased PMFs, I used the weighted histogram analysis method (WHAM) [144], with 50 bins and a tolerance of 10^{-5} kT for the convergence of WHAM equations. The final PMF profile for each peptide and its errors were calculated as the average and standard deviation of the three independent sets of simulations and were symmetrized with respect to the center of the bilayer.

3.3 Results

3.3.1 Pore forming peptides

The conduction of ions across a membrane is an important biological process performed by ion channel proteins. It is therefore of great interest to understand how these structures form and function. The synthetic peptides suggested by Lear *et al.* are an excellent model system for this study, since they are simple, and there is experimental evidence that they form bundles with properties similar to that of the ion channel proteins [16]. One of these model peptides, LS3, is a 21-residue amphiphilic peptide with a repeating motif (LSSLLSL)$_3$ (Figure 3.2). Its hydrophobic residues (leucine, L) and its hydrophilic residues (serine, S) form two parallel bands on the surface of the helix, as shown in Figure 3.2. Due to its amphiphilic nature, LS3 shows a tendency to hide its hydrophobic residues either by adopting an interfacial orientation as a monomer, or by taking part in the formation of pores. The formation of ion conducting bundles by approximately six LS3 helices has been confirmed in a number of experimental [16–18, 177] and theoretical [178] studies. Thus, LS3 can be classified as a pore-forming peptide (Figure 3.1, Type I). It has also been reported that the application of transmembrane voltage significantly enhances the pore formation, due to the asymmetric charge distribution within the helix (the N-terminus is positive and the C-terminus is negative) [179].

I performed molecular dynamics simulations with different peptide/lipid ratios in a DPPC membrane. I randomly placed the peptides in a system with a preassembled DPPC lipid bilayer of 256 lipids and 3228 waters (some of them happened to be at the membrane-water interface and some in the bulk), and ran MD simulations for several microseconds. I observed the formation of different complexes, including the formation of a barrel-stave pore, as well as the interfacial orientation of some peptides. Figure 3.3 shows a number of system configurations from the simulation with the barrel-stave pore formation. During the formation, several peptide complexes were observed, including dimers and trimers with some of the peptides at the surface of the bilayer and others inside the bilayer at an oblique angle. The actual pore formation seemed to be initiated when two or more peptides adopted a proper transmembrane orientation. More specifically, in the first snapshot taken at the 5^{th} nanosecond of simulation, a peptide is at a transmembrane position whereas three more are close to it. After about 100 nanoseconds, two more peptides adopt a transmembrane position. The third snapshot shows a configuration where three peptides are inside the lipid bilayer and three more are close to the trimer at the interface, having adopted a tilt orientation. Finally, at the last snapshot a pore is formed by six peptides and is stable for the rest of the simulation time (about 14 μs). From the configurations of the lipid molecules in the vicinity of the bundle, this structure can be classified as a barrel-stave pore.

Simulations of several microseconds with a single LS3 peptide placed in the water phase of a lipid bilayer have also been performed. The peptide adopted an interfacial positioning in all three simulations. No transmembrane orientation has been observed.

It is of great importance that, by using a simple coarse-grained model like the MARTINI, I managed to capture the spontaneous formation of a barrel-stave pore by LS3 peptide as well as its interfacial positioning as a monomer. To add further significance to these results, the formed pore features similar characteristics to the one predicted from the experiments: it is formed by six helices and has an internal diameter of about

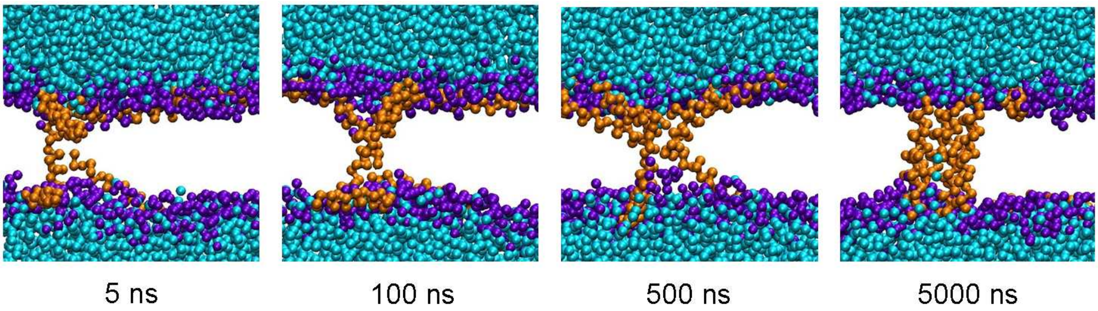

Figure 3.3: **Formation of a barrel-stave pore by six LS3 peptides**. Colours: water=light blue, peptide backbone beads=orange, phospholipid heads=purple. For reasons of clarity the lipid tails are not shown.

5.2 Å. In the next chapter, I will present in more detail the results from the simulations with LS3 peptide and I will further discuss some of the properties of the barrel-stave pore.

In Figure 3.4, I present the potential of mean force (PMF) for the transfer of LS3 peptide across a DPPC lipid bilayer, calculated with the umbrella sampling method, as described in Section 3.2.2. The PMF is represented by a solid line whereas the dashed lines correspond to the averaged location of the phospholipid heads. The peptide seems to have two favourable positions in the lipid bilayer; one close to the lipid heads and one in the hydrophobic core of the membrane. The minima are about -43 kTs compared to the water phase. However, a barrier of 8 kTs needs to be overcome so that the peptide can cross the membrane-water interface and adopt a transmembrane orientation.

3.3.2 Amphipathic non-spanning helices

The second class of peptides under study is the one of amphipathic nonspanning helices. In this work, I focused on LAP-20 as a typical representative of this class. LAP-20 (VSSLLSSLKEYWSSLKESFS) is a synthetic lipid-associating peptide with a behaviour similar to that of apolipoproteins [168]. This peptide adopts an α-helical secondary structure in the vicinity of a lipid bilayer. In Figure 3.2, we can see that LAP-20 has most of its hydrophobic residues grouped together on the same side along its helix. Because of this distribution of its hydrophobic and hydrophilic residues, LAP-20 adopts

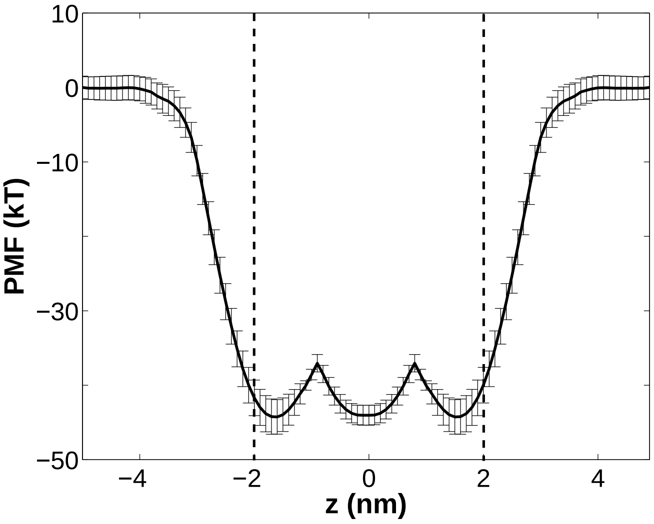

Figure 3.4: **Potential of mean force for the transfer of the LS3 synthetic peptide from the water phase across a DPPC lipid bilayer.** The PMF is represented by a solid line whereas the dashed lines correspond to the averaged location of the phospholipid heads. (Error bars: standard deviations of the three independent PMF calculations.)

an interfacial orientation relative to a lipid bilayer (Figure 3.1, Type II) [6].

I performed MD simulations with one LAP-20 peptide in a DOPC lipid bilayer, consisted of 128 lipids and 1500 waters, and tried to capture the interfacial orientation proposed by Brasseur [6]. During the 1 μs of the simulations, LAP-20 adopted an interfacial orientation with most of its hydrophobic residues hidden in the phospholipid heads (Figure 3.5). Furthermore, I calculated the angle distribution of the peptide relative to the bilayer normal (Figure 3.6). The peptide orientation was calculated as the angle between the helical axis and the bilayer normal (see Section 2.7.2). From the figure, it is evident that LAP20 has a preference for an interfacial orientation as expected from previous theoretical studies [6].

The PMF profile of the LAP20 synthetic peptide is consistent with the behaviour seen in the MD simulations (Figure 3.7). This PMF has a minimum, about -35 kTs, at the membrane/water interface in agreement with the observed location and orientation of the peptide. The centre of the bilayer is an energetically unfavourable location with a maximum of more than 30 kTs compared to the water phase.

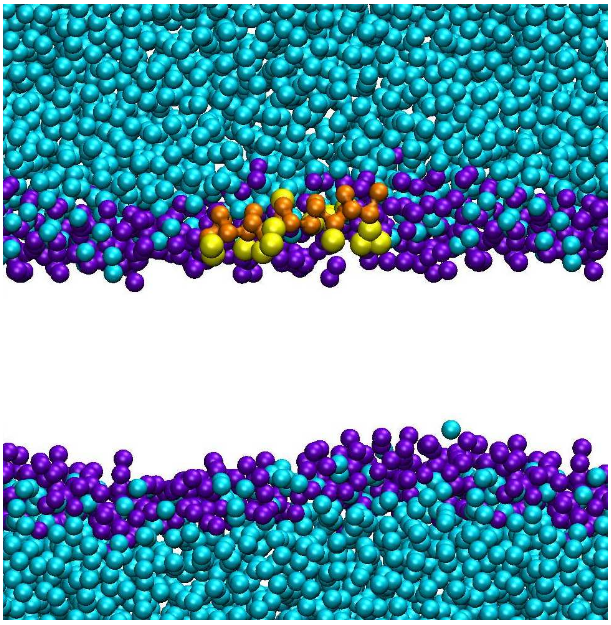

Figure 3.5: **Final snapshot from the simulation of the LAP20 synthetic peptide.** The backbone beads of the peptide are coloured orange, the hydrophobic side chains yellow, the water light blue and the phospholipid heads purple. For clarity the hydrophilic side chains and the lipid tails are not shown. The beads are not to scale.

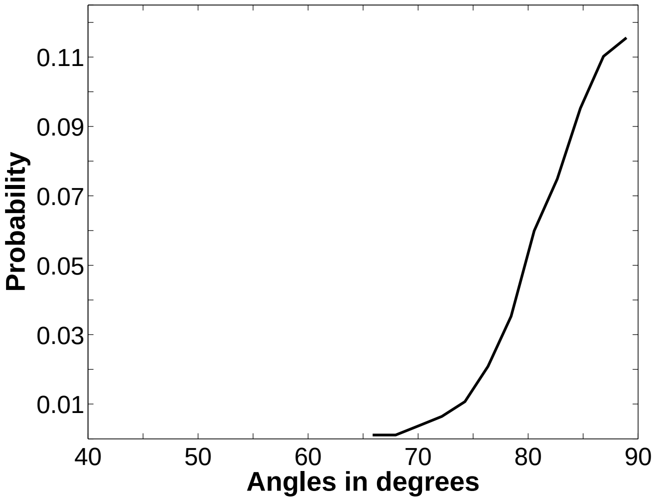

Figure 3.6: **Angle distribution for the LAP-20 peptide.** A distinct preference for horizontal orientation relative to the lipid bilayer is observed.

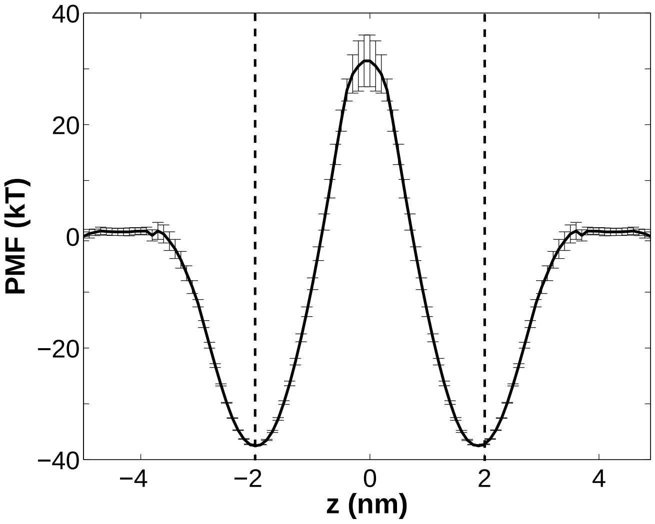

Figure 3.7: **Potential of mean force for the transfer of LAP20 synthetic peptide from the water phase across the DOPC lipid bilayer**. The PMF is represented by a solid line whereas the dashed lines correspond to the averaged location of the phospholipid heads. (Error bars: standard deviations of the three independent PMF calculations.)

3.3.3 Fusion peptides

In general, fusion peptides share some common features: they are short, about 10-20 residues long, $\alpha-$helical in the presence of a lipid membrane, with a gradient of hydrophobicity along their axis. In this study, I focused on one of the most studied fusion peptides, the fusion peptide of Simian Immunodeficiency Virus (SIV). SIV features twelve residues (GVFVLGFLGFLA) and is α-helical in the presence of lipid bilayers (Figure 3.2). All its residues are hydrophobic (except for the small, weakly hydrophilic glycine) and the imbalance in the hydrophobicity, characteristic of fusion peptides, arises from the aromatic rings of three phenylalanine residues aligned and grouped together on one side of the helix. Bradshaw and co-workers have performed a series of important experimental and theoretical studies on SIV fusion peptide [29, 55, 56]. In one of them, the authors carried out neutron diffraction measurements from stacked multilayers of DOPC and determined the location and orientation of specifically deuterated SIV fusion peptides within the bilayer [29]. The results from this study showed that there are two different populations of peptides: one major population close to the bilayer surface, and a smaller population hidden in the hydrophobic core. Two equally plausible orientations at 55^o and 78^o with respect to the bilayer normal, were found consistent with the experimental observations. However, based on the additional FTIR data from previous studies [26], the oblique orientation at 55^o was accepted as the most probable one.

I performed coarse-grained MD simulations with SIV fusion peptide in a DOPC lipid bilayer consisted of 128 lipids and 1500 waters. The total simulation time was 1.7 μs. To calculate the average orientation of the peptide relative to the bilayer normal, I performed an analysis of the angle distribution similar to that employed for LAP20, described in Section 2.7.2. In order to closely reflect the experimental observations which indicate that the C-terminus of SIV tends to be more disordered [29], I excluded the first two residues at the C-terminus from participation in the $\alpha-$helical secondary structure. (This is achieved simply by removing the secondary structure constraints imposed by the MARTINI for the beads of the first two residues). The principal axes of inertia were then calculated based on the residues in the $\alpha-$helical formation only. The results are presented in Figure 3.8. SIV prefers to be at an angle of 70^o relative to the bilayer normal, but a wide range of angles from about 45^o to almost completely horizontal orientation is explored by the peptide. This observation seems to be consistent with the ability of fusion peptides to access a wide range of configurations [180, 181]. However, the actual preferred orientation does not seem to be in agreement with the oblique angle of 55^o suggested by Bradshaw and co-workers [29]. To test the reliability of this result, I performed a fully atomistic simulation of the SIV peptide, interacting with a DOPC bilayer. The total simulation time was 90 ns. The orientation of the peptide was assessed using the same technique as in the coarse-grained simulations (again, the first two residues at the C-terminus do not participate in the α-helix and were not included in the angle distribution analysis). From the results presented in Figure 3.8, it is clear that a similar distribution of angles is observed in atomistic simulations, and thus the source of discrepancy of these results with the experiments must be elsewhere. Figure 3.9 shows a typical orientation of the SIV peptides in the atomistic and CG simulations.

To further extend the comparison of the SIV behaviour with the experimental results, I calculated the density profiles of different residues of the peptide in a lipid bilayer. In the original publication by Bradshaw and co-workers, density profiles for deuterated valine 2, leucine 8 and leucine 11 were presented and served as the main evidence of the two possible locations of the peptide within the bilayer (Figure 3.10) [29]. A double

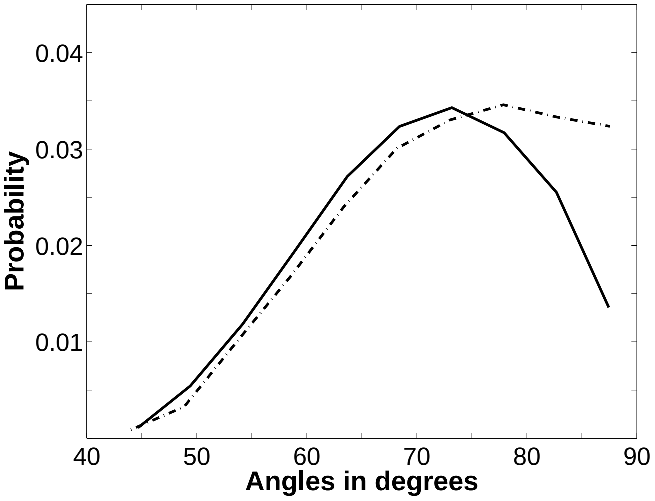

Figure 3.8: **Angle distribution for the SIV peptide**. Results from atomistic (solid line) and coarse-grained simulations (dashed line).

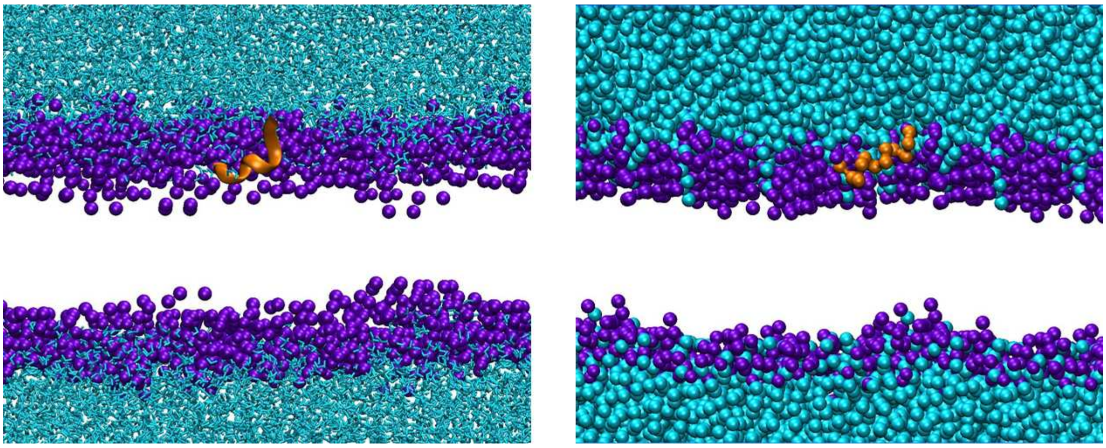

Figure 3.9: **Representative snapshots from simulations of SIV fusion peptide**. Snapshots from atomistic *(left)* and coarse-grained *(right)* simulations of SIV fusion peptide in a DOPC lipid bilayer corresponding to a tilt angle of 70^o. The backbone of the peptides is shown in orange, water is shown in blue and the phospholipid heads in purple. The side chains of the helices as well as the lipid tails are not shown for clarity. The beads are not shown to scale.

peak is evident for leucine 8 and therefore I focused on this residue.

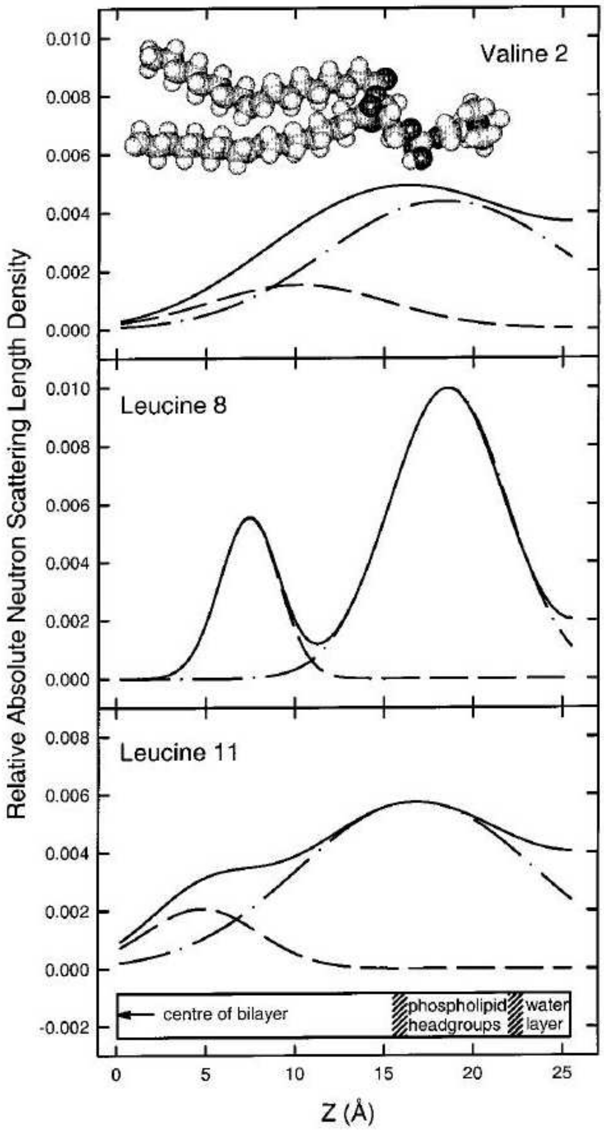

Figure 3.10: **Neutron scattering length density profiles for Val2, Leu8 and Leu11 of SIV peptide**. (- -) minor population , (-.-) major population, and (solid line) sum of major and minor populations. Figure adapted from [29].

In Figure 3.11, I present the density profile for leucine 8 of the SIV fusion peptide from both the atomistic and the coarse-grained simulations. Since the thickness of the bilayer is somewhat different in the atomistic and coarse-grained representations, the z-axis is given in dimensionless units with the lipid length in a particular representation being the scaling parameter. The atomistic simulations predict a deeper positioning of leucine 8 in the bilayer, whereas in the CG simulations the peptide lies closer to the phospholipid heads. Neither of the simulations generated a double peak in density as observed in the experiments.

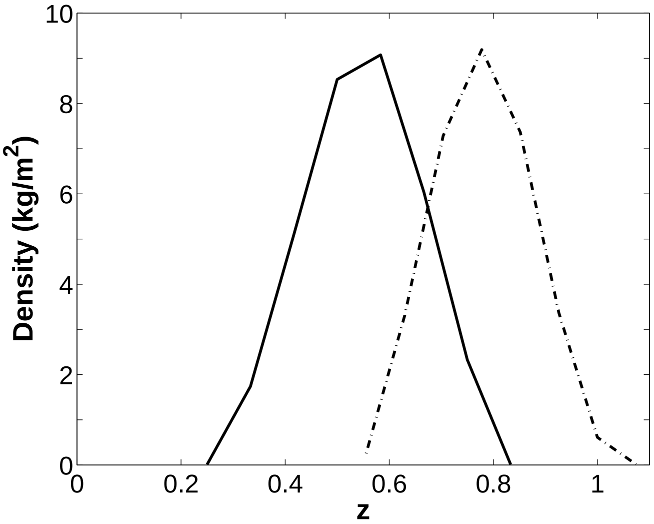

Figure 3.11: **Density profiles of leucine 8 as a function of the distance z from the centre of the bilayer**. z has been normalized with the appropriate lipid length corresponding to the atomistic and the coarse-grained models. The solid line corresponds to the atomistic simulation and the dashed line to the coarse-grained simulation, respectively.

I have also calculated the radial distribution function (RDF) for a DOPC lipid bilayer in the presence of SIV fusion peptide and compared it with the corresponding RDF for the pure bilayer. In Figure 3.12, I present the RDFs for the PO4 group and the first carbon of the lipid chain of DOPC. With blue solid line I have represented the results from the pure lipid bilayer and with black dashed line the results from the bilayer in the presence of SIV fusion peptide. No significant differences can be observed.

Finally, to complete the analysis, I present the PMF calculations for the SIV peptide in Figure 3.13. Note, that the shape of the PMF is quite different from those observed for the other classes of peptides. I believe the PMF presented in Figure 3.13 is consistent with the MD behaviour of the SIV peptide. Specifically, the two minima in the PMF correspond to the interfacial location, whereas the centre of the bilayer is a less preferred location, but not fully excluded (particularly, when compared with LAP20 peptide).

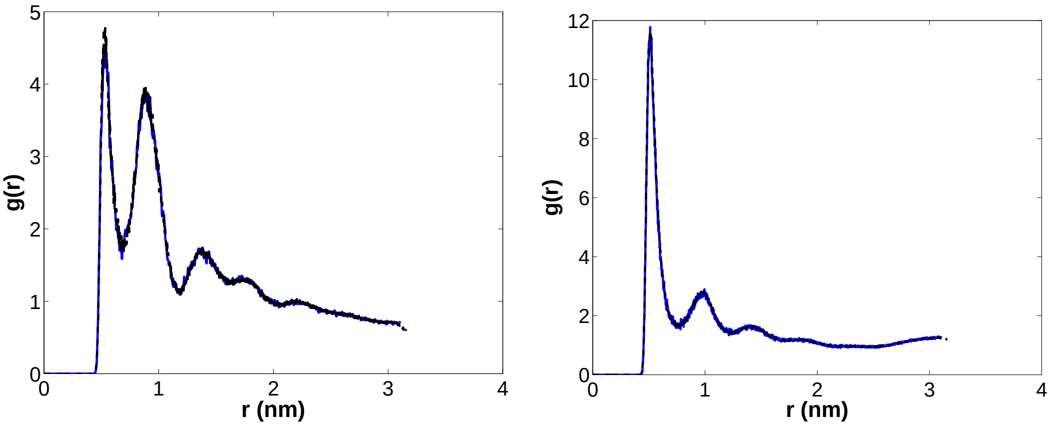

(a) (b)

Figure 3.12: **Radial distribution function for DOPC bilayer in the presence of SIV fusion peptide**. RDFs for the PO4 group (a) and the first carbon of the lipid chain of DOPC (b) are shown. With blue solid line I have represented the results from the pure lipid bilayer and with black dashed line the results from the bilayer in the presence of SIV fusion peptide.

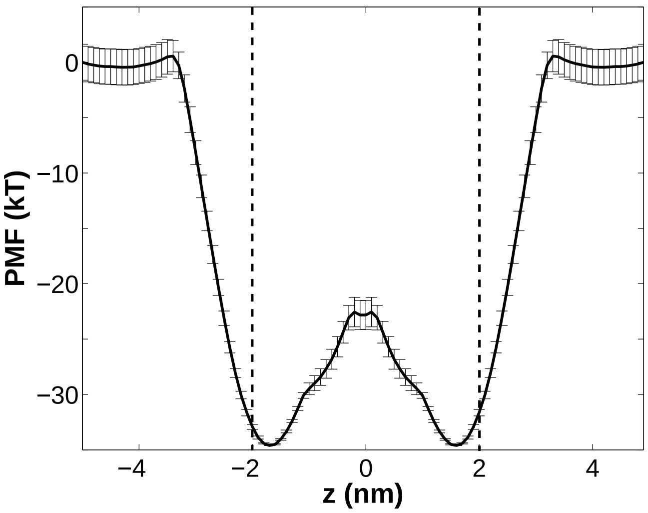

Figure 3.13: **Potential of mean force for the transfer of the SIV fusion peptide from the water phase across a DOPC lipid bilayer**. The PMF is represented by a continuous line whereas the dashed lines correspond to the averaged location of the phospholipid heads. (Error bars: standard deviations of the three independent PMF calculations.)

3.3.4 Transmembrane helices

In the original description of various classes of peptides provided in Figure 3.1, the transmembrane helices span the lipid bilayer due to the match between the hydrophobic region of the α-helix and the width of the hydrophobic core of the lipid bilayer. Alternatively, one could employ a functional definition of transmembrane peptides as structures capable of spontaneous insertion in the bilayer, leading to a characteristic transmembrane orientation. This ability of transmembrane peptides to cross lipid bilayers is of great interest in the development of novel drug vectors and other applications. However, the details of the translocation mechanisms are not yet understood. Studies of these peptides have been carried out both through experiments and simulations. For example, Bond and Sansom captured the spontaneous insertion of GpA helix by means of CG simulations [100]. Another peptide, that has been studied in a series of experiments by the group of Engelman, is pH (low) insertion peptide, known as pHLIP [164–167]. pHLIP (ACEQNPIYWARYADWLFTTPLLLLDLALLVDADEGTG) is a peptide derived from the integral membrane protein bacteriorhodopsin C. It exhibits high solubility at neutral pH in a non helical conformation, however, at lower pH (pK_a of 6.0), the peptide adopts a transmembrane position in an α-helical conformation. It has been proposed that this pH-dependent mechanism of translocation can be exploited in the early detection of pathological conditions in cells. In one of their studies, Engleman and co-workers, designed two variants of pHLIP in order to check the specificity of the function of the peptide in tumours and test its mechanism of insertion. In one of the variants, N-pHLIP (ACEQNPIYWARYA**N**WLFTTPLLLL**N**LALLVDADEGTG), the aspartic acid (Asp, D) residues are replaced by asparagine (Asn, N). This peptide remains an α-helical structure in the presence of liposomes over a wide pH range and adopts a transmembrane position in a lipid bilayer. I have chosen this pHLIP version for the studies of transmembrane helices.

I carried out a series of MD simulations with pHLIP in a DOPC (512 lipids and 6000 waters) and in a POPC (512 lipids 6000 waters) bilayer. I did not observe the pHLIP insertion in any of our simulations unless the peptide was initially half-inserted in the lipid bilayer (Figure 3.14). In Figure 3.14, water is represented by blue beads, lipid heads by purple beads and the backbone of the peptide is coloured orange. The hy-

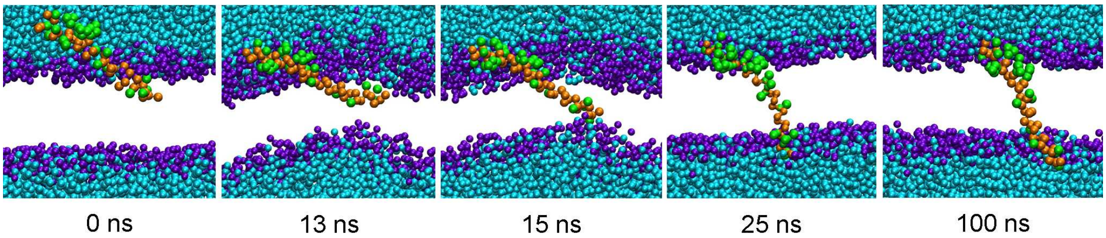

Figure 3.14: **Snapshots from the pHLIP simulation.** From the left to the right: The peptide is initially half-inserted in the lipid bilayer. As the simulation evolves the peptide perturbs the bilayer, adopts a transmembrane orientation and stays there until the end of the simulation. The backbone beads are coloured orange, water is coloured blue, the phospholipid heads are represented by purple beads and the hydrophilic side chains beads of pHLIP are represented by green beads. The hydrophobic residues of the peptide as well as the lipid tails are not shown for clarity. The beads are not to scale.

drophilic side chains of the peptide are shown in green. Initially half-inserted in the bilayer, the peptide created a perturbation to the bilayer after a few nanoseconds and finally adopted a transmembrane orientation in which it stayed until the end of the simulation (350 ns). More details about our studies on pHLIP peptide will be presented in Chapter 5.

TMX-1 is another interesting example of transmembrane helix. It has been synthesized to test to what extent it is possible to design helices that insert spontaneously in a lipid bilayer [54]. TMX-1 (WNALAAVAAALAAVAAALAAVAASKSKSKSK), has a 21-residue non-polar core, N- and C-caps, and a highly polar C-terminus. It has been shown to adopt an α-helical secondary structure in the lipid environment and to insert spontaneously across the lipid membranes with 50% probability [54]. Here, I carried out MD simulations with TMX-1 in a DOPC lipid bilayer (512 lipids, 12000 waters, 4 Cl-). The total simulation time is 2.3 μs, and the peptide maintained an interfacial orientation during the whole simulation. In Figure 3.15, I present a characteristic position of TMX-1 during our simulation: the polar C-terminus of the helix remained in contact with water and the non-polar central part was hidden in the lipid heads area. The N-terminus also appeared to prefer a position close to the membrane/water interface probably due to its tryptophan residue.

I also performed umbrella sampling simulations for both pHLIP and TMX-1 peptides. The lipid bilayers used for these simulations were a POPC lipid bilayer for pHLIP and

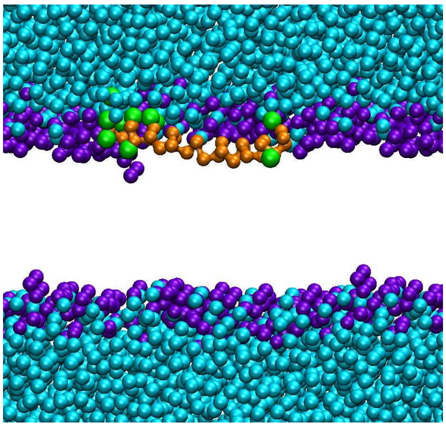

Figure 3.15: **Final snapshot from the TMX-1 simulation.** The peptide adopts an interfacial orientation with a characteristic orientation where its polar C-terminus remains in contact with water and its non-polar central part is hidden in the lipid heads area. The backbone beads are coloured orange, water is coloured blue, the phospholipid heads are represented by purple beads and the hydrophilic side chains beads are represented by green beads. The hydrophobic residues of TMX-1 as well as the lipid tails are not shown for clarity. The beads are not to scale.

a DOPC lipid bilayer for TMX-1. Both membranes consisted of 512 lipids and 12000 water molecules as well as chloride ions to maintain the system neutrality. During the umbrella sampling simulations, the helices were left free to rotate. Both TMX-1 and pHLIP were parallel to the interface in the head group region. Close to the centre of the bilayer, the peptides adopted different orientations, with the perpendicular one being the most favourable. A similar behaviour was observed by Bond *et al.* for WALP23 [182]. In Figure 3.16, I present the resulting PMFs. Again, the generated curves seem to exhibit a shape specific for this particular class of peptides. Both peptides showed very strong preference for the transmembrane position (with minima at the centre of the bilayer at -90kTs and -110kTs for pHLIP and TMX-1 respectively) and both PMFs are quite similar, indicating that indeed pHLIP and TMX-1 must belong to the same class of peptides. Moreover, these PMFs indicate that one would expect to observe a spontaneous, seamless insertion of those peptides in a lipid bilayer in an MD simulation. This however is not the case. Although the peptides that are initially placed at a transmembrane orientation remain in this, I never observed a spontaneous insertion of pHLIP or TMX-1. This discrepancy in our observations will be addressed in more detail in the Discussion section.

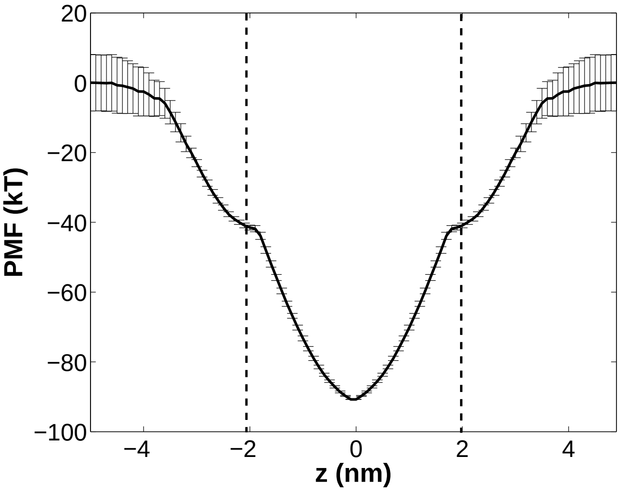

(a) pHLIP

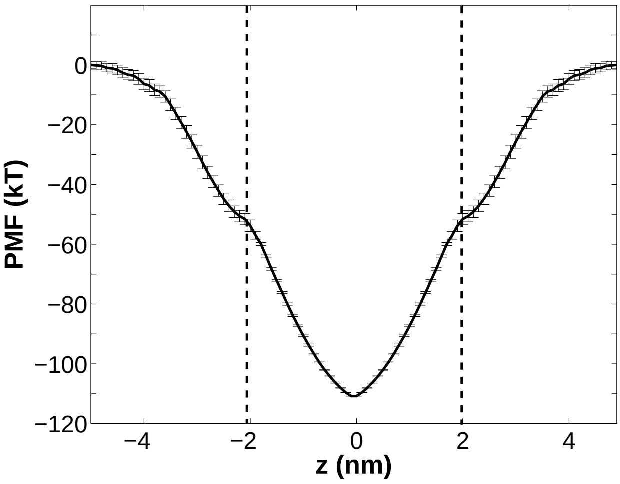

(b) TMX-1

Figure 3.16: **Potential of mean force for the transfer of pHLIP and TMX-1 transmembrane helices across POPC and DOPC lipid bilayers respectively.** The PMF is represented by a continuous line whereas the dashed lines correspond to the averaged location of the phospholipid heads. (Error bars: standard deviations of the three independent PMF calculations.)

3.4 Discussion

The results reported in this chapter suggest that the MARTINI coarse-grained model is able to describe several classes of interactions between α-helical peptides and lipid bilayers. The self-assembly of a barrel-stave pore and the behaviour of interfacial non-spanning peptides are within the scope of the MARTINI. Furthermore, the model is able to provide new important insights regarding the details of peptide self-assembly in the vicinity of a lipid bilayer. The number of helices constituting the pore as well as its effective diameter predicted from our simulations are in agreement with previous experimental studies [16, 17].

I performed potential of mean force (PMF) calculations for each peptide considered in this study. In Figure 3.17, I present a summary of the different PMFs. The PMF provides an estimate of the free energy profile as the peptide crosses the bilayer, and can be used directly to calculate the partition of the peptide between the water phase and the lipid phase. I showed that each class of peptide-bilayer interaction has a very distinct form of PMF (Figure 3.17). For example, the PMF for LS3 features three energy minima of comparable depth, one at the centre of the bilayer and two additional minima at the interfaces of the bilayer. A very distinct PMF is observed for the fusion SIV peptide, with the energy minimum corresponding to the lipid interface and the energetic penalty for SIV's location in the centre of the bilayer of about 15 kT. pHLIP and TMX-1 peptides exhibit barrier-less PMFs with -90 kT and -110 kT minima respectively at the centre of the bilayer, signifying a very strong preference for the transmembrane orientation. Although this result agrees with our expectations and experimental observations [54, 165], it contradicts our MD studies, where no spontaneous insertion of the peptides in the bilayer is observed. Let us briefly explore possible sources of the discrepancy.

First, I would like to ensure that the observed PMF is not an artefact resulting from the technical limitations of the applied methods. Specifically, the system features large enough water phase to eliminate possible periodic boundary condition effects. In the original setup, I used the Berendsen thermostat to control the temperature of the system and this method has been criticized for not being able to provide correct distribution of velocities. For one of the smaller peptides, I repeated the simulations with the Nosé-Hoover thermostat and, not surprisingly, observed marginal differences. Also,

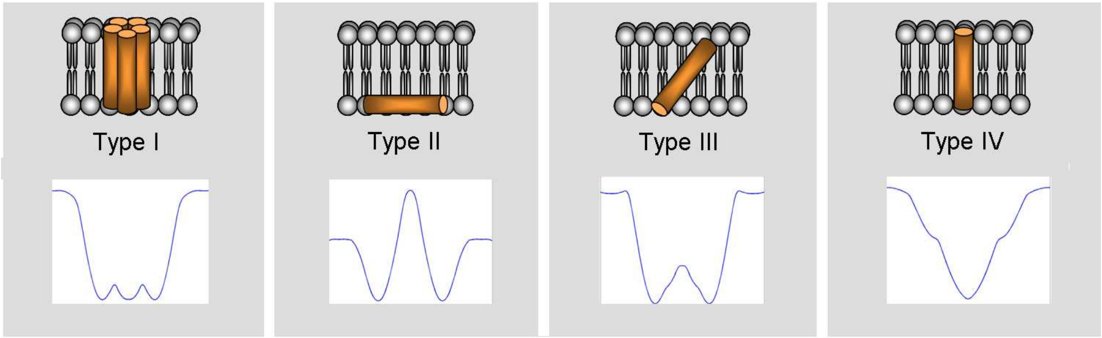

Figure 3.17: **Map of PMF types for the different classes of α-helical peptides.**

in our studies, I applied a simple cut-off and shift procedure to electrostatic interactions and this could possibly be viewed as inaccurate. Thus, I recalculated the PMF for one of the smaller peptides, using Particle Mesh Ewald method (PME) to treat electrostatic interactions and observed rather small effects on the final results (see Appendix C). Moreover, the length of sampling for each window in the umbrella protocol is important. Most likely the energy profiles reported for large pHLIP and TMX-1 peptides are reflections of a few preferential orientations of the peptides, rather than a result of properly sampled configurational space. From the error analysis presented in this study, it seems that generation of additional independent PMF trajectories may not be able to resolve this issue. Nevertheless, striking similarity between PMFs for pHLIP and TMX-1 suggests that at least the shape of these energy profiles is characteristic for this particular class.

With these reservations regarding the last two PMFs, I believe that the PMF analysis can be used to complement the original classification of peptide-membrane interactions shown in Figure 3.1 as well as to reveal new types of behaviour. Most importantly, it is evident that the PMF analysis is an indispensable tool to elucidate and explain intimate links between different classes of peptides and an exhaustive study of these links would be impossible in atomistic simulations. It would also be interesting to investigate how the presence of other peptide molecules would affect the energy profiles.

CHAPTER 4

Pore-formation by α-helical peptides

This chapter is a presentation of more in-depth studies on pore formation mechanisms. These mechanisms play an important role in many biological processes, from ion-conduction across cell membranes to antimicrobial defence mechanisms and many more. For this study, I chose LS3 synthetic peptide, because of its simplicity (it has only two types of amino acids) and its potential to form pores. I have already shown that the spontaneous formation of a LS3 barrel-stave pore can be successfully captured by means of coarse-grained molecular dynamics simulations. In this chapter, I present a series of simulations that provide further evidence of the propensity of LS3 to form pores as well as structural and dynamical information about them. I also investigate how pore formation mechanisms depend on the structural modifications of LS3.

4.1 Pore-forming peptides

Pore-formation is an important mechanism that takes place in different biological processes. There are several types of peptides inducing the formation of pores in membranes, with α-helical antimicrobial peptides being one of the most studied family. These antimicrobial peptides are about 20-40 amino acids long, cationic and have the ability to target specific cells and disrupt their membrane, leading eventually to cell-death. In Figure 4.1, I show one example where a cationic antimicrobial peptide is used for the treatment of Escherichia coli.

Since the early 1970's until recently, it was believed that the pores formed by antimicrobial peptides follow the barrel-stave model (Figure 4.2(a)) [183]. However, in addition to the barrel-stave mechanism, antimicrobial peptides may also form transient toroidal pores (Figure 4.2(b)). In a toroidal pore the peptides usually have a hydrophobic part shorter than the thickness of the bilayer, and they impose a positive curvature strain on the bilayer, that leads to a toroidal structure formed by lipid leaflets and covered by peptide molecules (Figure 4.2(b)).

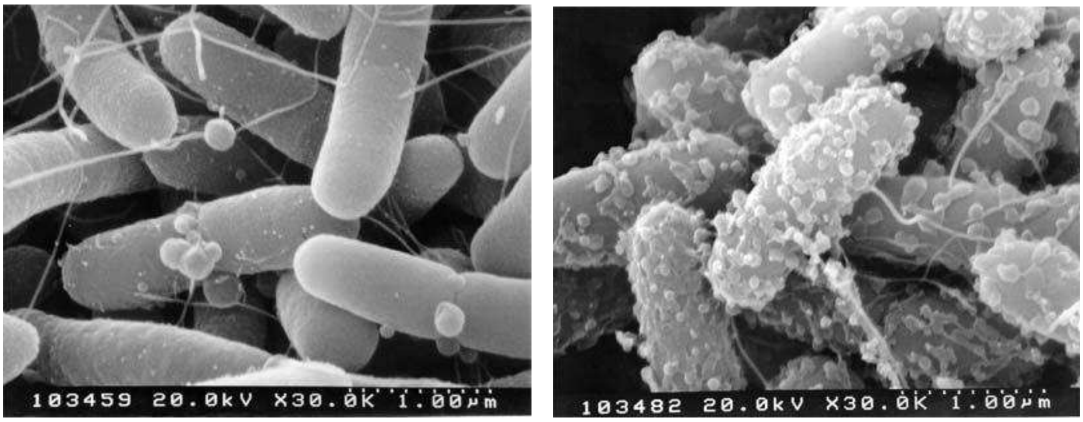

(a) (b)

Figure 4.1: **Escherichia coli treated with an antimicrobial cationic peptide**. (a) At low concentration and (b) at high concentration. In figure (b), we can notice the formation of blebs that are coming off the bacterium. Courtesy REW Hancock Laboratories [184].

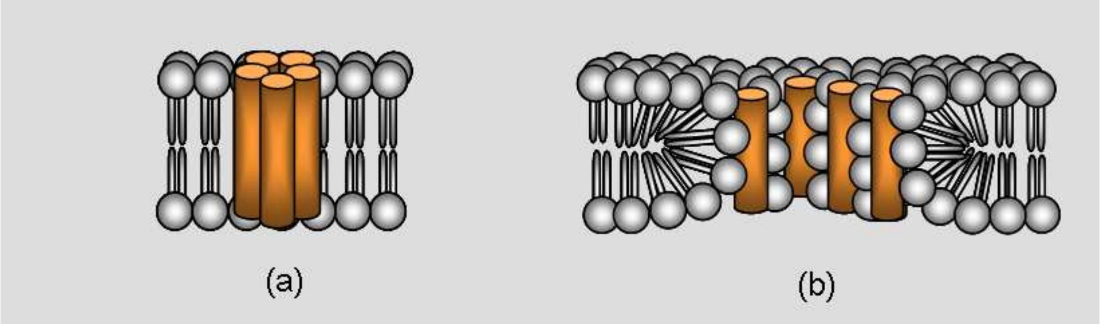

Figure 4.2: **Schematic of the barrel-stave (a) and toroidal (b) pore**. The structure of lipids in the vicinity of the pores is one of their main differences.

Another type of peptides of interest here is the family of pore-forming toxins (PFT). PFTs are soluble and act on cell membranes by forming transmembrane channels, for example β-barrels (in the case of α-toxin from Staphylococcus aureus) [185]. There are a few cases of PFTs with α-helical secondary structure that form unstable pores.

α-helical peptides forming (and derived from) protein ion-conducting channels are another family of pore-forming peptides. In the membrane, several helices form a bundle, that can be classified as a barrel-stave pore (Figure 4.2(a)). There is a number of model channel systems, consisting of synthetic helices of this type, with 'synporins' [151–153] and 'template-assembled synthetic proteins' (TASPs) [154, 155], being two representative examples.

There are several simulation studies on pore-forming peptides, and in particular the ones with α-helical structure. I will briefly mention a few representative works. Nielsen and co-workers have recently combined NMR and molecular dynamics simulation studies to study alamethicin antimicrobial peptide [186, 187]. One of the first simulation studies of antimicrobial peptides and toroidal pore formation mechanisms was presented by Leontiadou *et al.* in [188]. In this publication the authors showed that magainin-H2, above a certain concentration, induced the formation of a toroidal pore. A series of simulation studies performed by the same group showed among others that the shape of a toroidal pore may be very disordered, with peptides and lipids at oblique orientations lining the pore [77, 78]. Moreover, the MARTINI coarse-grained model has been shown to be able to capture both the barrel-stave pore formation (for LS3 synthetic peptide) [109] and toroidal mechanisms (for magainin-H2 and melittin antimicrobial peptides) [78, 105] of pore formation.

In the previous chapter, I presented the formation of a barrel-stave pore from LS3 peptide. Here, I will discuss in more detail the characteristics of the pore and present a series of simulations I performed with LS3 at different concentrations.

In an effort to examine the characteristics of LS3 that lead to the formation of a pore, I performed simulations with a 14-residue version of LS3, $(LSSLLSL)_2$, that as has been experimentally shown does not form discrete, stable channels [16]. To our surprise this peptide at relatively high concentrations formed complexes in the lipid bilayer, resembling toroidal pores. These pores were transient, disordered and with a very small radius. I carried out a series of simulations to examine the link between the formation of these pores and the concentration of the peptide. I also performed simulations with magainin-H2 peptide in order to be able to compare the structures of the pores formed by magainin and the short version of LS3. Finally, I performed PMF calculations that showed a different profile for $(LSSLLSL)_2$ compared to $(LSSLLSL)_3$.

4.2 Summary of simulations

I have performed a range of NPT molecular dynamics simulations for LS3 and $(LSSLLSL)_2$ in a DPPC membrane, at 323 K and 1 bar, and with peptide/lipid ratios varying from 6/256 to 12/256. The MARTINI force field was used. First, I randomly put the peptides in a system with a preassembled DPPC lipid bilayer (some of them happened to be at the membrane-water interface and some in the bulk), and, after energy minimization of the system, I carried out MD simulations for several microseconds. The rest of the simulation parameters are the same as described in Section 3.2. Summaries of the simulations for the two peptides are presented in Tables 4.1 and 4.2. There seems to be no connection between the orientation of the termini in the oligomers.

I also performed two simulations for magainin-H2 peptide. The MARTINI force field was used with simulation parameters as described in Section 3.2. The system had 128 DPPC lipids, 2000 waters and 7 peptides. The peptides were randomly placed in a system with a preassembled DPPC lipid bilayer. An energy minimization run was performed, followed by an equilibration run. MD simulations in the NPT ensemble at

323 K and 1 bar were employed for more than 4 microseconds for both simulations.

Finally, I performed umbrella sampling simulations for the calculation of the potential of mean force for $(LSSLLSL)_2$. The protocol I followed is described in Section 3.2.

Table 4.1: **Summary of the performed simulations and key observations for LS3 peptide**. The lipid bilayer consists of 256 lipids in all simulation systems. The duration refers to the total simulation time. In the cases where complexes or pores are formed, the remaining peptides are in interfacial orientation.

Concentration	**Duration** (μs)	**Behaviour**
6 peptides	5.0	interfacial
	5.4	trimer
	6.3	interfacial
7 peptides	5.5	dimer, trimer
8 peptides	6.0	interfacial
	6.2	trimer
	17.0	2 trimers
9 peptides	5.9	interfacial
	6.0	interfacial
	6.2	trimer
10 peptides	5.8	dimer
	5.8	interfacial
	11.2	pentamer
	17.2	hexamer
	18.7	trimers/hexamer
11 peptides	5.1	tetramer
	5.6	tetramer, dimer
	5.9	tetramer
12 peptides	5.2	interfacial
	6.2	trimer/tetramer

Table 4.2: **Summary of the simulations for (LSSLLSL)$_2$ peptide**. The lipid bilayer consists of 256 lipids in all simulation systems. For each toroidal pore, I report a pair of numbers that correspond to the fully inserted peptides in perpendicular orientation (first number) and the peptides that are inserted at oblique angle close to the bilayer-water interface (second number). The duration refers to the total simulation time.

Concentration	**Duration** (μs)	**Behaviour**
6 peptides	2.8	interfacial
	2.8	interfacial
	3.0	interfacial
7 peptides	2.9	interfacial
	3.2	interfacial
8 peptides	2.6	interfacial
	3.8	interfacial
9 peptides	8.1	4-2 toroidal
	8.2	4-4 toroidal
	8.2	4-4 toroidal
10 peptides	3.2	interfacial
	3.5	interfacial
	6.9	3-3 toroidal
11 peptides	3.0	interfacial
	3.3	interfacial
12 peptides	3.1	interfacial
	3.2	interfacial
	3.3	interfacial

4.3 Results

4.3.1 LS3 complexes

From the simulations of LS3 at different peptide/lipid ratios, I observed the formation of different complexes as well as the interfacial orientation of peptides. Regarding the orientation of the termini of the helices within the bilayer, there seemed to be no particular preference in the absence of the transmembrane potential. It is also worth mentioning that at higher concentrations of the peptide, the propensity to form large complexes and pores was higher, while at smaller concentrations dimers and trimers were more common. However, a high concentration of peptides did not necessarily lead to a pore formation (Table 4.1).

From the observed complexes, the dimers and trimers were formed at different concentrations and were stable for several microseconds. The tetramers were also very stable (for more than 10 microseconds in some cases) with some of them having the shape of a pore. Also, a complex of five helices has been observed once (Figure 4.3, *bottom left*). The hexameric bundle observed in one of our simulations can be classified as a barrel-stave pore, both by its shape and by the configuration of the lipids around it (Figure 4.3, *bottom right*) [109]. Complexes consisted of six helices, without the formation of an open pore have also been observed. For example, the formation of a hexameric complex was captured when two trimers approached each other and merged into one structure. In Figure 4.4, I present top view snapshots from the formation of the hexamer. In the figure, the backbone beads are coloured orange and water is coloured blue.

In Figure 4.3, I present the top view of complexes of different sizes. I have chosen representative complexes where their structure and the distribution of their hydrophilic residues are easy to observe. There are cases where these structures are more disordered. As shown in the figure, most of the hydrophilic residues of the peptides (coloured blue) are lying at the inner surface of the complexes. The hydrophobic residues are not shown in the figure.

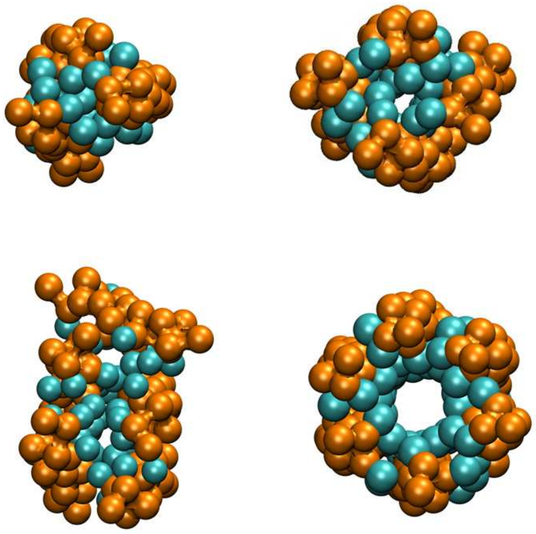

Figure 4.3: **Representative snapshots of different types of complexes observed in LS3 simulations**. Trimeric *(top left)*, tetrameric *(top right)*, pentameric *(bottom left)* and hexameric *(bottom right)* complexes. The backbone beads are presented in orange and the hydrophilic residues in light blue. Other groups are omitted for clarity.

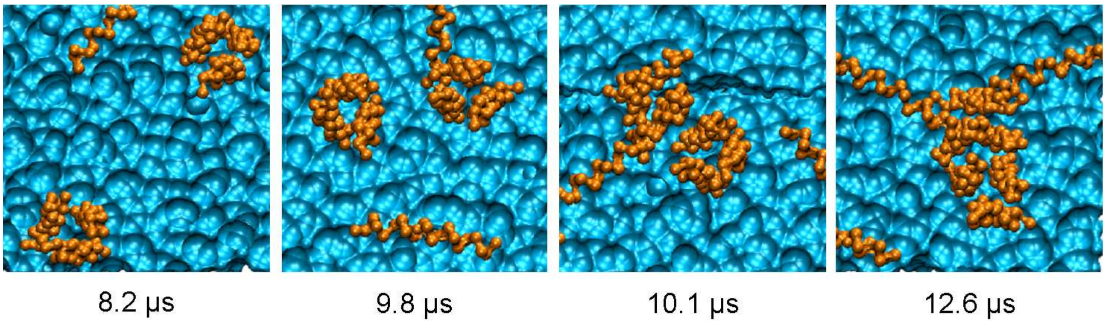

Figure 4.4: **Snapshots from the formation of a hexameric complex from two trimers**. The backbone beads are coloured orange and water is represented by a light blue surface. The lipids are not shown in the figure.

4.3.2 Hexameric barrel-stave pore

In the previous chapter, I showed that the formation of a barrel-stave pore can be captured by means of coarse-grained molecular dynamics simulations. In this section, I will describe in more detail the characteristics of this pore.

Figure 4.5 shows in detail characteristics of the pore formed by six peptides (view of the pore with only the backbone beads *(left)*, the backbone beads and the hydrophobic beads *(centre)* and all beads *(right)*). Note that most of the hydrophilic groups (serine, S) face the interior of the bundle.

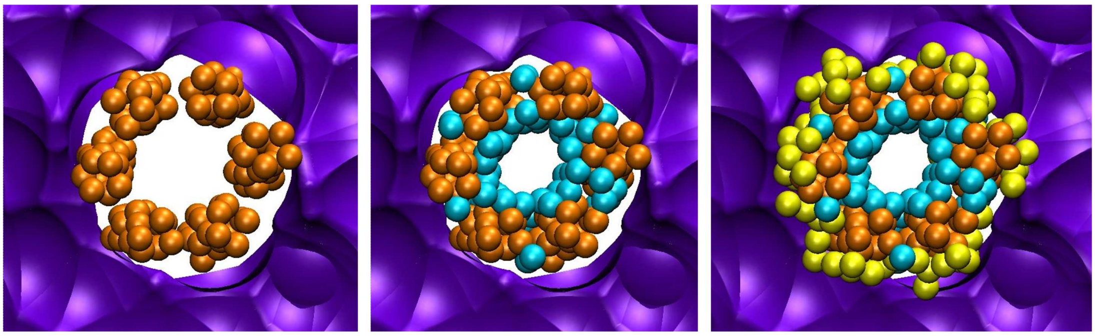

Figure 4.5: **Top view of the hexameric pore**. View of the pore with only the backbone beads *(left)*, the backbone beads and the hydrophobic beads *(centre)* and all beads *(right)*. Colours: hydrophobic beads=yellow, hydrophilic beads=light blue, peptide backbone beads=orange and lipid heads=purple surface. The beads are not shown to scale.

To check if the formed pore is similar to the one seen in experiments, I calculated its diameter. I used a program I developed for this purpose (see Section 2.7). The inner diameter of the pore was found to be about 5.2 Å, in good agreement with previous experimental studies [16, 17]. The outer diameter was calculated to be 20 Å. It is important to note that the pore is filled with water. In Figure 4.6, I show a characteristic configuration of the pore filled with water. The peptides are represented only by their backbone beads coloured in orange. Some of them are not included in the figure in order to be able to observe the water inside the pore. Water is coloured blue and the lipid heads purple. The lipid tails are not shown in the figure.

Apart from the visualization of the water crossing the bilayer through the pore, I have also calculated the density of water in the system along the bilayer normal. In Figure 4.7(a), I show the water density for the whole system along the normal of the bilayer in beads per nanometer. In Figure 4.7(b), I have zoomed in the area close to the bilayer centre. The figure clearly shows the presence of water in the pore. However, the mobility of water molecules in the pore is limited. For example, the residence time of a water molecule may exceed 500 ns. This is probably caused by the size of the coarse-grained beads used in the representation of the system that limits the diffusion of the water inside the pore.

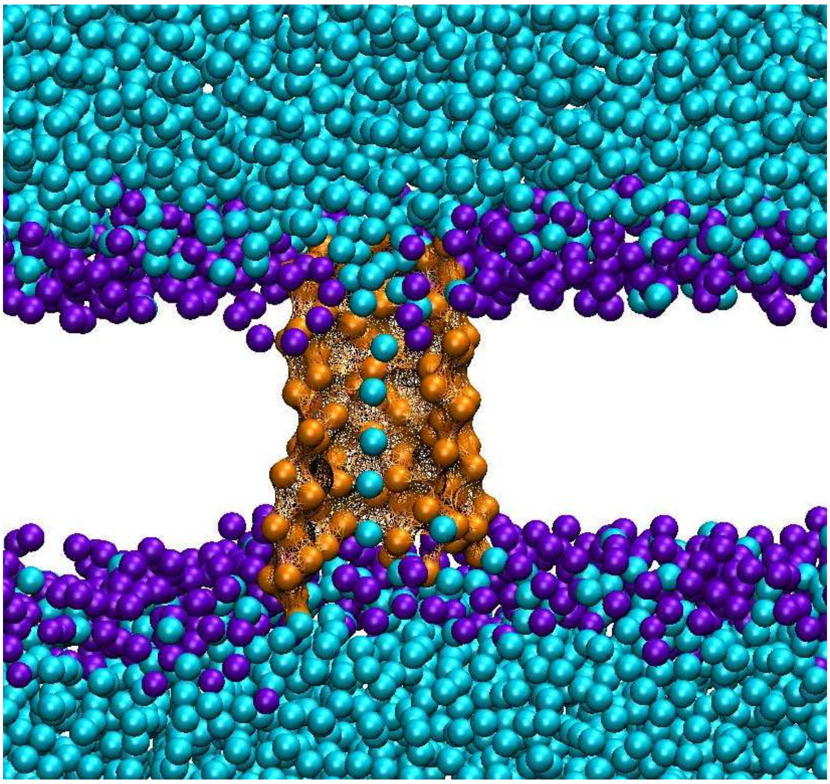

Figure 4.6: **Hexameric pore filled with water**. Colours: water=blue, peptide backbone beads=orange, lipid heads=purple. For reasons of clarity the lipid tails are not shown.

Self-diffusion coefficient of the barrel-stave pore

Computer visualization of the dynamics of the system showed that the mobility of the peptides within the bundle is quite limited. However, the bundle as a whole was able to freely move within the bilayer plane. To estimate the lateral self-diffusion coefficient of the bundle within the lipid bilayer, I performed seven 500-ns-long simulations starting from different initial configurations. The initial configurations were snapshots from the simulation of the barrel-stave pore. I then computed the average mean square

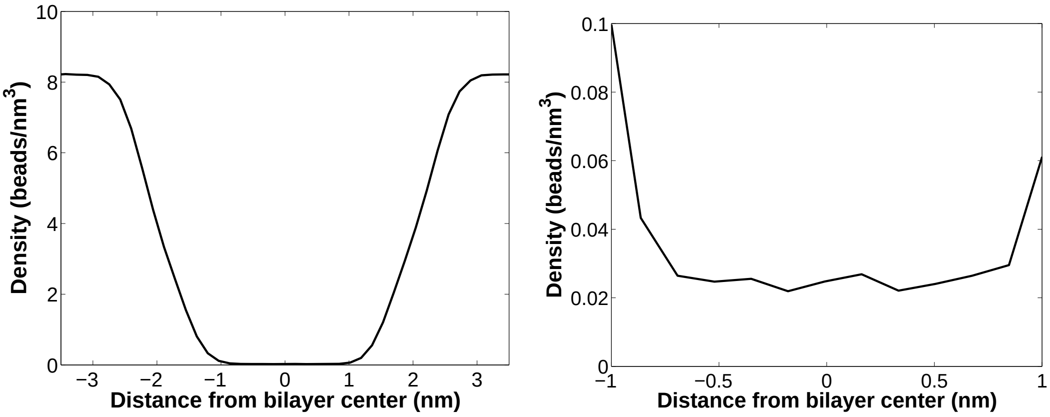

(a) (b)

Figure 4.7: **The density of water in a LS3 barrel-stave pore**. In Figure (b), I have zoomed in the center of the bilayer, where the presence of water in the pore is evident.

bundle displacement from the seven runs.

The lateral diffusion coefficient, D_{lat}, is related to the Mean Square Displacement (MSD) by

$$MSD = 4D_{lat}t, \tag{4.1}$$

where t is time. The lateral self-diffusion coefficient can be extracted by fitting a straight line to the mean square displacement (MSD) of the pore. In order to avoid large statistical errors due to poor sampling, I used the MSDs with time intervals smaller or equal to 250 ns. The mean square displacement as a function of time is shown in Figure 4.8, and it seems that two distinct regimes of behaviour can be identified. Specifically, below 100 ns the slope of the curve is clearly steeper than that for longer times. In molecular dynamics simulations, a mixture of ballistic and linear Einstein diffusion mechanisms is sometimes observed on short time scales. I calculated the self-diffusion coefficient for three different sets of time intervals, from 1 to 100 ns, from 1 to 250 ns and from 100 to 250 ns, in order to check the influence of different time intervals in the overall mobility of the barrel-stave pore. Moreover, due to the different number of observations for each time interval, I used the weighted least squares method for the calculation of the slope. The weight for each interval is the number of its measurements divided by the total number of measurements for all the time intervals. By using weighted least squares, I included the uncertainty of the measurements in the calculation of the self-diffusion coefficient at longer times, and, therefore, made sure that the approximation was the best possible with the available data.

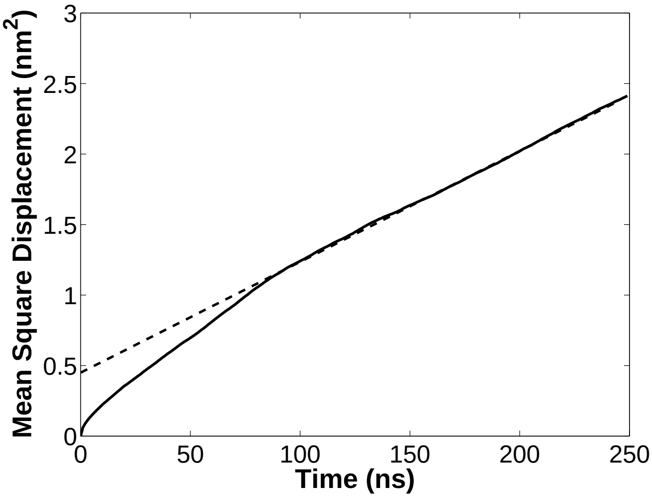

Figure 4.8: **Mean square displacement versus time for the LS3 bundle**. Mean square displacement versus time (solid line) and fitted line (dashed line). The fit is applied to the data beyond the first 100 ns and has the unscaled slope of 7.86 10^{-6} nm^2/ps.

It has been noted in previous studies that the effective dynamics appear to be faster in coarse-grained simulations because of the smoothed potentials [106]. To take this into account, I scaled the calculated self-diffusion coefficient by a factor of 4, as suggested in earlier simulation studies [106]. Finally, $D_{lat}^{1-100} = 0.8715 \pm 0.0129\ \mu m^2/s$, $D_{lat}^{1-250} = 0.688 \pm 0.0067\ \mu m^2/s$ and $D_{lat}^{100-250} = 0.4912 \pm 0.0005\ \mu m^2/s$, where the superscripts indicate the range of time intervals the coefficients correspond to.

To our knowledge there are no reported values for the self-diffusion coefficient of an LS3 pore. However, the values calculated from our CG MD simulations are remarkably close to reported values for membrane proteins. For example, for tetraspanin CD9, that consists of 229 amino acids (LS3 pore consists of 126 amino acids), the lateral diffusion coefficient was calculated to be 0.23 $\mu m^2/s$ [189], whereas for bacteriorhodopsin, which is formed by seven transmembrane α-helices, the diffusion is 0.31 $\mu m^2/s$ [190].

Tilt of the pore

It is also worth mentioning that, during the simulation, the relative angles between the helices were very small (a few degrees), as the peptides were strongly aligned, whereas each of the helices adopted an orientation of around 20^o relative to the bilayer normal, resulting in an similar orientation (of about 20^o) of the bundle as a whole. This is in good agreement with previous simulation studies [191]. The distribution of the tilt angle for the hexameric pore is shown in Figure 4.9.

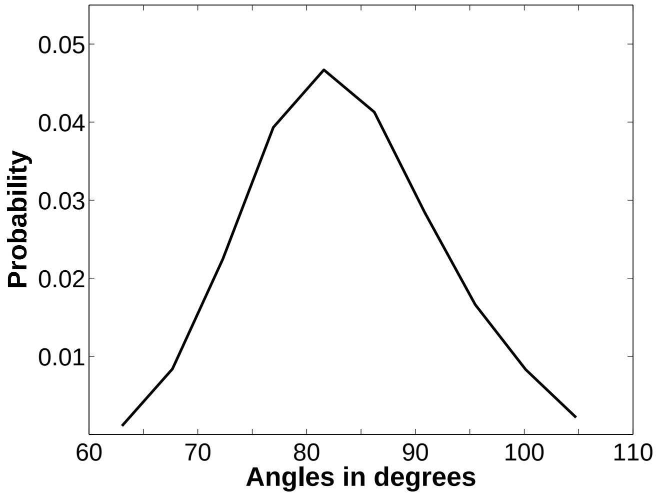

Figure 4.9: **Tilt angle of the hexameric peptide bundle**.

4.3.3 The toroidal pore

In our efforts to define the characteristics of a pore-forming peptide, I used a shortened version of LS3 that has been experimentally shown to fail to form discrete, stable pores [16]. $(LSSLLSL)_2$ has the same proportion of hydrophobic and hydrophilic residues and the same distribution as LS3. Thus, one would expect this peptide to show a similar behaviour to that of LS3. However, in our simulations, $(LSSLLSL)_2$ preferred either an interfacial positioning or the formation of complexes. This kind of interaction could be explained by the hydrophobic mismatch between the peptide and bilayer thickness. $(LSSLLSL)_2$, in order to position its hydrophilic residues away from the hydrophobic lipid tails, creates complexes involving several peptides, some of them inserted in the bilayer and the others located at the bilayer interface.

Several variations of the complex self-assembly were observed in (LSSLLSL)$_2$ simulations. For example, in Figure 4.10, I present characteristic snapshots from the formation mechanisms of a typical (LSSLLSL)$_2$ complex formation. Typically, the complexes consisted of three or four peptides in the hydrophobic area of the lipids with another three to four peptides close to the membrane/water interface, creating a toroidal-shaped structure. Because of the size of the complex (the complex internal diameter was less than 0.5 Å), no water was observed in these bundles. The complexes appeared to be less stable than the bundles formed with LS3. The number of peptides taking part in the complex varied with time. For example, in one of the simulations, a complex was formed and disassembled after about a microsecond. This contrasts with the case of LS3 where all complexes, once formed, were stable until the end of the simulations, for several microseconds. I should also mention that a common feature of these complexes seen in our simulations is the coexistence and cooperation of the peptides inside the bilayer and at the bilayer/water interface.

A similar structure has been observed for antimicrobial peptide magainin-H2 [105]. In an effort to compare these two observations, I repeated the simulations with magainin-H2 and reproduced the formation of a toroidal pore. In Figure 4.11, I show a snapshot from a simulation with (LSSLLSL)$_2$, with a complex consisting of three inserted and three tilted helices *(right)* and a snapshot from a simulation with magainin *(left)*. Although the two complexes have considerably different sizes, which is due to the difference in the length of the helices (magainin is a 23-residue peptide whereas (LSSLLSL)$_2$ is only 14 residues long), one can observe that they share some common features, for example in both cases there are peptides at the bilayer/water interface that seem to stabilize the pore. Based on these similarities between the two complexes, as well as the instability and the shape of the (LSSLLSL)$_2$ complex, it can be classified as a toroidal pore.

I also performed umbrella sampling simulations to obtain the PMF for (LSSLLSL)$_2$ translocation across the lipid bilayer. In Figure 4.12, I present a comparative graph with the potential of mean force for transfer of LS3 (solid black line) and (LSSLLSL)$_2$ (dashed blue line) from the water phase across a DPPC lipid bilayer. From the PMF shape, one can observe a remarkable difference between (LSSLLSL)$_2$ and (LSSLLSL)$_3$. The PMF for (LSSLLSL)$_2$ features strongly pronounced minima at the interfacial po-

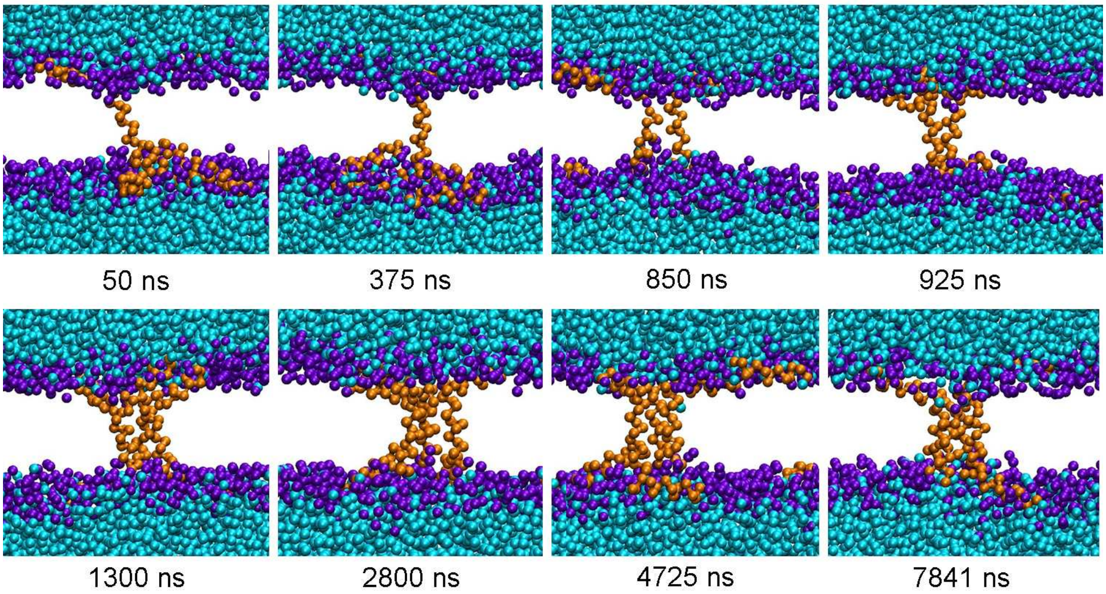

Figure 4.10: **Characteristic snapshots of a simulation with typical (LSSLLSL)$_2$ complex formation**. 50 ns: a peptide is in the bilayer and three more are grouped together and close to it. 375 ns: the peptide remains at a transmembrane position and another peptide has come closer to the complex. 850 ns: a second peptide is now at a transmembrane position, and three more are at the interface and close to the ones inside the membrane. 925 ns: the complex is taking a more stable form. 1300 ns: a third peptide adopts a transmembrane position and five in total peptides are at the interface stabilizing the trimeric complex. 2800 ns: the three peptides are still at a transmembrane position and one of the peptides at the interface has left the group. 4725 ns: the three peptides remain inside the bilayer and only three peptides are now close to the trimer. 7841 ns: another peptide joins the trimer with three interfacial peptides stabilising the complex. Colours: water=blue, lipid heads=purple and peptide backbone beads=orange. For reasons of clarity the lipid tails are not shown.

sitions (about -30 kTs, compared to the water phase), while the centre of the bilayer is not a preferred location (+2 kTs compared to the water phase). This is consistent with the observations from the molecular dynamics simulations, where (LSSLLSL)$_2$ strongly prefers the interfacial orientation, and can be positioned inside the bilayer only as part of a larger entity, with these entities being quite unstable. Thus, by changing the length of the peptide (in other words by changing the hydrophobic match), we can drastically affect the type of the observed behaviour.

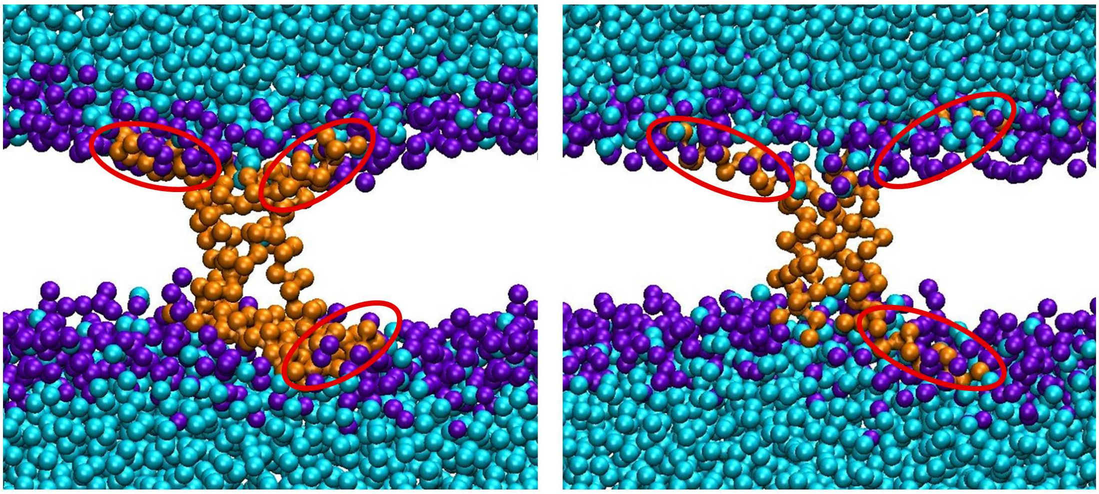

Figure 4.11: **Characteristic snapshots from the simulations with magainin (left) and (LSSLLSL)$_2$ peptide (right) forming toroidal pores**. Colours: water=blue, lipid heads=purple and peptide backbone beads=orange. The interfacial peptides have been circled. For reasons of clarity the lipid tails are not shown.

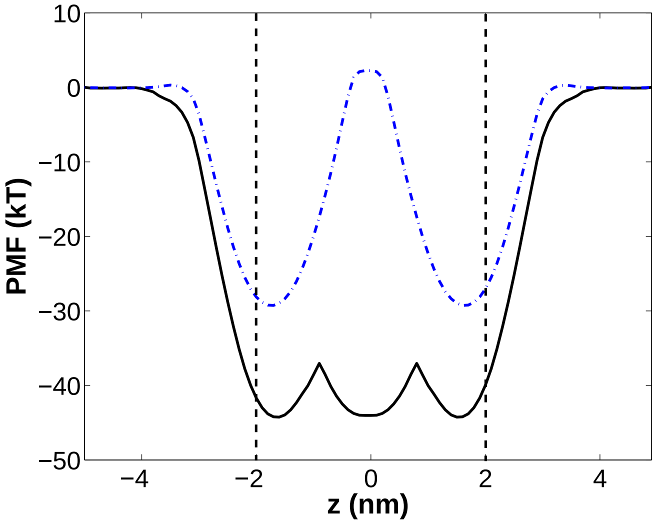

Figure 4.12: **Comparative plot of the PMF patterns of LS3 and (LSSLLSL)$_2$**. Both LS3 (solid black line) and (LSSLLSL)$_2$ (dashed blue line) peptides have a minimum close to the lipid heads. In the case of LS3 a second minimum is observed at the centre of the lipid bilayer.

4.4 Barrel-stave versus toroidal pore

In this section, I will present a more thorough study on the differences between the barrel-stave and the toroidal pore, formed by LS3 and $(LSSLLSL)_2$ respectively.

Initially, to compare the different pore structures and their effect on the lipid bilayer, I calculated the P_2 order parameters, as defined in Section 2.7 of Methodology. In these calculations, I have included all the lipids of the system, even the ones that do not interact with the pores directly. Thus, these order parameters correspond to a peptide/lipid ratio of 9/256 for $(LSSLLSL)_2$, 7/128 for magainin and 6/256 for LS3 systems. The results of these calculations are shown in Figure 4.13. From Figure 4.13(b), where I have zoomed in the area of the lipid tails, we can see that in the case of the barrel-stave pore, the lipids have the same orientation as in the pure membrane. In the systems where a toroidal pore is formed, the lipid order is decreased relative to the one of the peptide-free bilayer, indicating a more random orientation of the lipid tails in these systems.

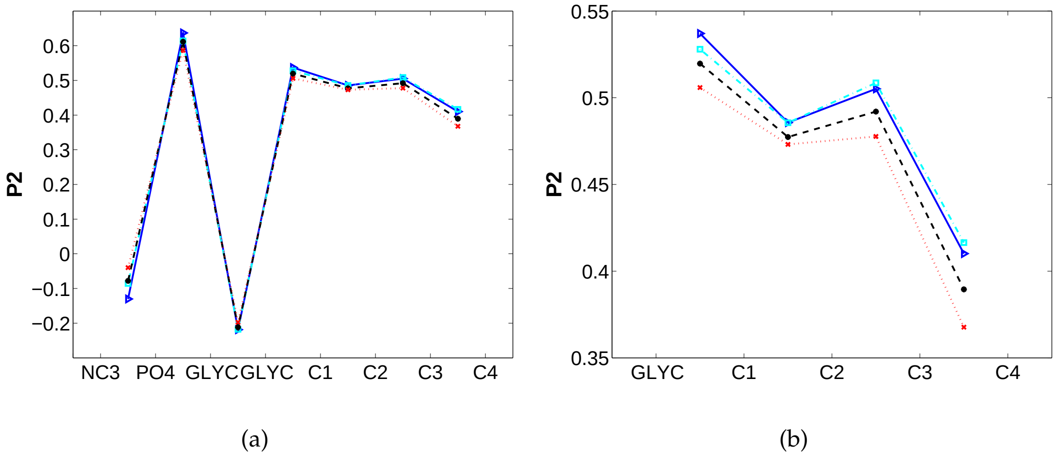

Figure 4.13: **P_2 order parameter of consecutive bonds with respect to the bilayer normal**. The results from the pure DPPC lipid bilayer (- ▷, blue), the bilayer in the presence of the barrel-stave pore (-.- □, cyan), the $(LSSLLSL)_2$ toroidal pore (– ◇, black) and the magainin toroidal pore (— •, red) are quite similar. In figure (b), where I have zoomed in the region of the hydrocarbon tails, we can see that the lipid order is decreased in the systems where a toroidal pore is formed.

I also calculated the lipid order parameters in the vicinity of the different pores, in order to see how their structure affects locally the orientation of the lipids. In this calculation, I included only the lipids at a distance smaller than 1.5 nm from the center of mass of the pores. Thus, these order parameters correspond to a much bigger peptide/lipid ratio, with a maximum value of 9/40 in the case of $(LSSLLSL)_2$ toroidal pore and 6/37 for the barrel-stave pore. In the case of the toroidal pores, both for $(LSSLLSL)_2$ and magainin, the lipids around the pores seem to adopt a more random orientation than in a pure lipid bilayer or even in the case of the barrel-stave pore (Figure 4.14). It is also important to note that $(LSSLLSL)_2$ toroidal pore seems to create more local perturbation in the lipid orientation than the one of magainin.

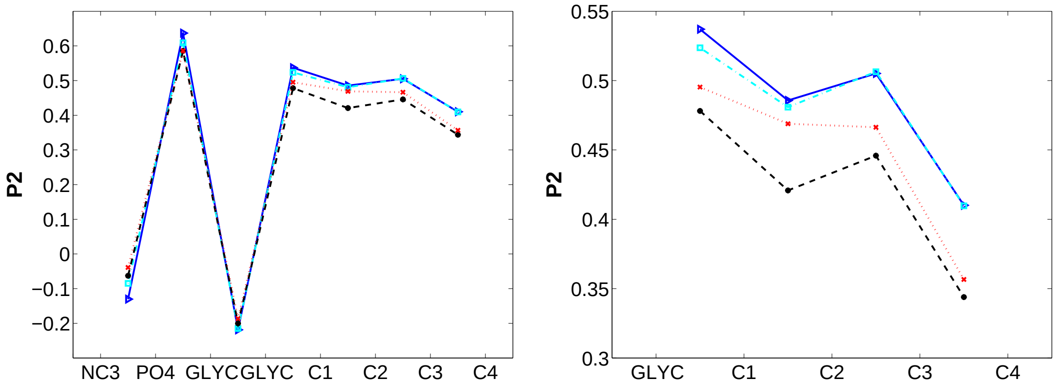

(a) (b)

Figure 4.14: **P_2 order parameter of consecutive bonds with respect to the bilayer normal in the vicinity of the pores**. Again, the results from the pure DPPC lipid bilayer (- ▷, blue), the bilayer in the presence of the barrel-stave pore (-.- □, cyan), the $(LSSLLSL)_2$ toroidal pore (− ♢, black) and the magainin toroidal pore (— •, red) are quite similar. However, as shown in figure (b), where I have zoomed in the region of the hydrocarbon tails, the lipid order is decreased in the systems where a toroidal pore is formed, especially in the case of $(LSSLLSL)_2$.

Another difference between the two types of pores is the presence of water in them. I calculated the water density in each of the two systems. In Figure 4.15, I show the central part of the pores with respect to the bilayer normal. The figure shows that in the system with the barrel-stave pore, water density at the central area of the lipid bilayer is non-zero whereas in the case where a $(LSSLLSL)_2$ pore is formed there is almost no water in the bilayer.

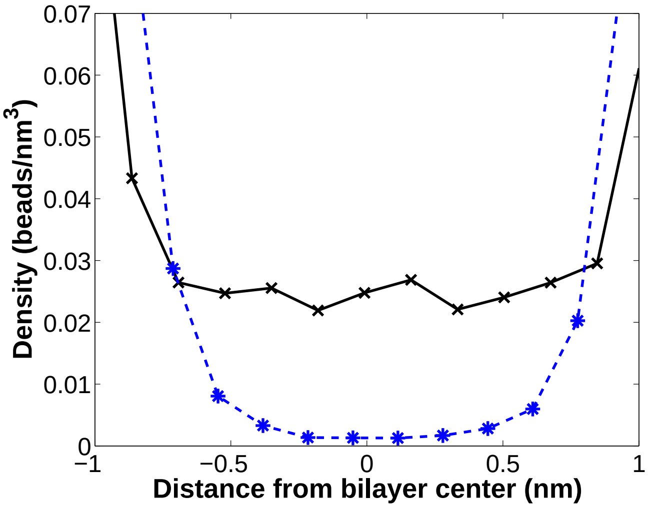

Figure 4.15: **Water density in the barrel-stave and the toroidal pore**. The plot corresponds to the central part of the pores and the distance is with respect to the bilayer normal. In the case of the barrel-stave pore (black solid line, x) we can see that there is water at the central part of the bilayer whereas in the case of (LSSLLSL)$_2$ pore (blue dashed line, $*$) the density of water is close to zero.

I have also calculated the apparent area per lipid and volume per lipid in the presence of the two different kinds of pores. The systems under study have 256 DPPC lipids and 3228 waters. The area per lipid was obtained by dividing the area of the plane of the lipid bilayer by the number of lipids present in each leaflet. For the calculation of the volume per lipid the following formula was used:

$$V_L = \frac{A_L L_z}{2} - N_w V_w, \tag{4.2}$$

where A_L is the area per lipid, L_z is the length of the simulation box in the direction of the bilayer normal, N_w is the number of waters per lipid molecule and V_w[1] is the volume per water. In Table 4.3, we summarize the results. The apparent area per lipid is increased in the presence of the pores, as expected. In the case of the toroidal pore this increment is slightly bigger. The value for the volume per lipid is very similar in all three systems.

---

[1] V_w was calculated by a simulation with bulk water at the same conditions.

Table 4.3: **Apparent area and volume per lipid in the presence of barrel-stave and toroidal pore**.

	peptide-less membrane	**Barrel-stave pore**	**Toroidal pore**
Apparent area per lipid (Å^2)	63.7 ± 0.8	68.0 ± 0.4	68.9 ± 0.5
Apparent volume per lipid (Å^3)	1300.0 ± 4.2	1371.0 ± 1.9	1371.0 ± 2.0

Finally, in Table 4.4, I present a summary of the differences between the two different types of pores.

Table 4.4: **Summary of the differences between the barrel-stave pore formed by LS3 peptides and the toroidal pore formed by (LSSLLSL)$_2$ peptides**.

Barrel-stave pore	**Toroidal pore**
ordered	disordered
number of peptides is fixed	number of peptides varies
lipids aligned along peptides	some peptides at the surface, others inside the bilayer
stable (more than 15 μs)	transient (not stable)
open (5.2 Å)	closed (0.5 Å)

4.5 Conclusions

In this chapter, I showed that the spontaneous formation of a barrel-stave as well as a toroidal pore can be captured by means of a CG model. I have performed extensive MD simulations, beyond 15-μs-long in some cases, and observed the formation of different complexes by LS3 synthetic peptide and its 14-residue version.

The formation of a hexameric barrel-stave pore is one of the most interesting results. The pore was stable for more than 14 μs and filled with water. I have also estimated the self-diffusion coefficient of the pore in the lipid bilayer. Although, depending on the calculation procedure, there is some variation in the estimate ($D_{lat} = 0.49 - 0.87\ \mu m^2/s$), the key observation is that these values are similar to the experimentally measured values for membrane proteins, such as bacteriorhodopsin [190]. Thus, from this point of view, the hexameric peptide pore behaves as a small membrane protein.

Interestingly, the barrel-stave pore forms in the absence of a transmembrane potential, and naturally, there is no preferred orientation of the peptides within the bilayer. However, the impact of the applied electrostatic field will be investigated in future work.

Remarkably, the simulations of a shorter version of this peptide, $(LSSLLSL)_2$, showed that this peptide has a much lower propensity for poration and, when a complex does form, it has a toroidal structure. These complexes were different to the barrel-stave pore or the other complexes formed by LS3. They had a small diameter that does not allow for water to pass through it. Also, they were unstable, with the number of peptides taking part in them varying during the simulation. Another difference between the two observed pores was the structure of lipids in their vicinity. I calculated the order parameters of the lipids around the pores, and I showed that in the case of the toroidal pore the lipids have a decreased order relative to those close to the barrel stave pore.

I also calculated the apparent area and volume per lipid in the systems with the two different pores. The values were higher for the toroidal pore although its size was smaller. This is another indication of the disordered structure of the toroidal pore. It is important to note here that the values calculated by our simulations can be directly compared to measurements by Langmuir balance or diffraction techniques and thus, give information about the possible formation of a pore.

Also, the PMF for $(LSSLLSL)_2$ is dramatically different from that of LS3, with the energy minima at the bilayer interfaces and the core of the bilayer being an unfavourable location of the peptide. In the light of this PMF, the strong propensity of $(LSSLLSL)_2$ for the interfacial orientation in MD simulations is not surprising. Furthermore, there are clear similarities between the PMF of LAP20 peptide, presented in Chapter 3 and the PMF calculated for $(LSSLLSL)_2$, with the features of the $(LSSLLSL)_2$ PMF magnified in the LAP20 case. Thus, it seems that from this point of view the two peptides belong to the same class of nonspanning peptides. Whether or not under certain circumstances LAP20 exhibits self-assembly behaviour similar to the toroidal structures of $(LSSLLSL)_2$ remains an open question.

To close this chapter, I would like to draw the attention of the reader to what I believe is a very important conclusion from this study. Our extensive simulation studies show a potential link between the length of a peptide and its ability to form either stable, ordered and open pores or transient, disordered and closed pores. The formation of a toroidal-like pore by an uncharged and short peptide seems contradictory to the typical toroidal-pore forming peptides, the antimicrobial peptides (AMPs). The AMPs are 20-40 amino acids long and usually cationic. Their positive charge is often used as an explanation for their interaction with bacterial membranes that are usually anionic. However, an explanation for the pore-forming abilities of $(LSSLLSL)_2$ lies in the hydrophobic mismatch between the length of the peptide and the thickness of the bilayer. Also, the formation of the toroidal pore in our simulations seems to be initiated when at least one peptide is initially half-inserted in the lipid head area. Moreover, in some AMPs the hydrophobic region along the helical axis is shorter than the bilayer thickness that could also be another reason for the shape of the pore. Thus, a possible conclusion could be that the formation of a toroidal pore may be initiated by the electrostatic interactions between the peptide and the membrane, however, the shape of the pore seems to be linked to the distribution of hydrophobic residues along the helical axis.

CHAPTER 5

Cell-penetrating peptides

In this chapter, we will extend our studies to the self-assembly and membrane internalization mechanisms of cell-penetrating peptides, which have the ability to transfer large macromolecules across cellular membranes. We have chosen two particularly interesting cases, pHLIP and Pep-1 peptides. It has been experimentally shown that pHLIP serves as an efficient drug carrier without poration or self-assembly process. On the other hand, the translocation mechanism of Pep-1 has been a subject of controversy over the last years and is not yet established.

We will start the chapter with a short introduction to the area of cell-penetrating peptides, emphasising in their importance and possible applications, and focusing on the two chosen peptides. We will follow with the methodology and the results. The chapter closes with a discussion on the main outcomes of our study.

5.1 Introduction

High molecular weight biomolecules have been playing an increasingly important role as new, more effective therapeutic drugs. The bioavailability of drugs depends significantly on their solubility properties; they must be polar enough to dissolve in biological fluids, but not so polar that the drug cannot enter the cell. As a consequence, many drug candidates, being out of this polarity range, fail to advance clinically. One of the most promising approaches to resolve this problem is the use of peptide-carriers, commonly known as cell-penetrating peptides (CPPs).

Cell-penetrating peptides (CPPs) are a family of short, highly basic and amphipathic peptides. They have been successfully used to transport large macromolecules, such as proteins, peptides, antisense oligonucleotide (ON), siRNAs, plasmids and other large particles, like liposomes, across cellular membranes both *in vitro* and *in vivo*. The initial discovery of CPPs originated from the observation that some intracellular proteins, when added to an extracellular medium, had the ability to translocate across the membrane. Tat transactivator of HIV virus type 1 [192] and pAntp, Drosophila antennapedia transcription protein [193], were the first peptides to be identified with this ability.

A number of studies have been made on the ability of cell-penetrating peptides to inhibit tumour growth *in vivo* [194–196]. They can be used as delivery vectors of tumour suppressors, such as human p53 or lac tumour suppressor, or other proapoptotic proteins. In another example, it has been shown that, using a cell-penetrating peptide, nitric oxide synthesis could be inhibited and inflammation could be reduced in an animal model [197]. Furthermore, the incorporation of CPPs into vaccines is currently being studied as there are indications that they could constitute a useful ingredient that would ensure an effective T-cell response. These are just a few from numerous examples of successful applications of cell-penetrating peptides as drug-delivery vectors.

Despite the extensive research on how CPPs traverse cell membranes and promote the intracellular uptake of various cargo molecules, the underlying mechanism remains unclear. Depending on their charge, size, and structure, different CPPs utilize different internalization mechanisms. It is also possible that after cargos are linked to the peptides, this internalization mechanism changes. Possible mechanisms include endocytosis-mediated entry, translocation by means of the sinking-raft model, the formation of pores or translocation through formation of an inverted micelle. Some of the possible mechanisms have already been introduced in Chapter 1 (Figure 1.4). The molecular details of the various translocation processes are not well understood. It is thus important to (i) *elucidate these details* and (ii) *link the properties of the peptides to the various mechanisms of peptide-membrane interaction they induce*. This would be an important step towards the rational design of peptides with tailored functionalities.

Molecular dynamics simulations can play an important role in the overall process of understanding and elucidating the mechanisms of interactions of CPPs with lipid bilayers. In this study, we chose two particularly interesting cell-penetrating peptides, pHLIP and Pep-1. We have already introduced pHLIP in Chapter 3, however for the purposes of this chapter, we will provide further information about its translocation mechanism.

pHLIP is an amphipathic peptide that has been shown to accumulate in the membranes of cells in acidic environments and to have the ability to transfer attached molecules across them. In other words, pHLIP can act as a nanosyringe [164, 167]. Some of its possible applications include diagnostic imaging, drug therapy or genetic control. These potential uses of pHLIP are based on the fact that in many diseases there are naturally occurring acidic environments, ranging from 5.5 to 6.5 pH (e.g. tumours, sites of inflammation or stroke-afficted tissues). There is a generally accepted mechanism of pHLIP translocation which is shown in Figure 5.1. At pH=7, pHLIP is soluble in water in a random conformation, and at lipid/peptide ratios larger than 100, it binds to the membrane/water interface where conformational changes happen. When pH<6, it adopts a transmembrane position in a α-helical structure [164, 167, 198]. We should also note that for low lipid/peptide ratios, no translocation across the membrane has been observed [166]. Moreover, in the same publication, the authors suggest that the hydrophobic C-terminus of pHLIP seems to be the one adsorbed first, when the peptide is bound to the membrane.

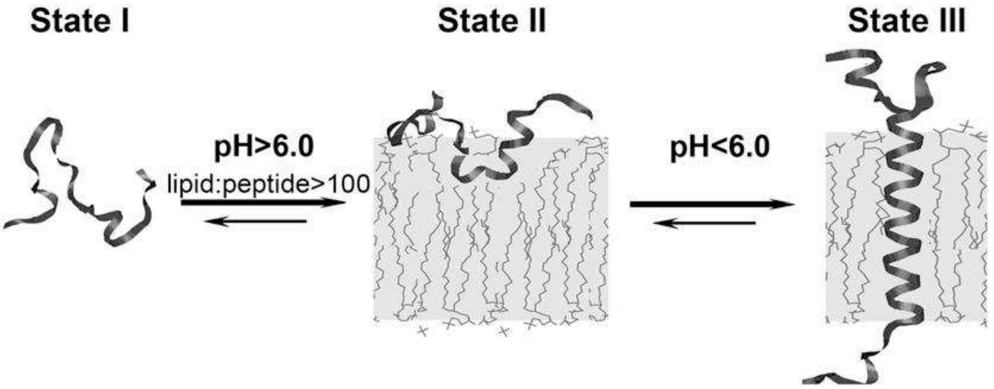

Figure 5.1: **Proposed pHLIP translocation mechanism across a lipid bilayer**. pHLIP is soluble in water at pH=7 (State I), bound to the membrane/water interface at lipid/peptide molar ratio 100 (State II), and at a transmembrane position at pH<6 (State III). The figure was taken from [198].

For Pep-1 peptide the story is not as evident and its translocation mechanism has been a subject of controversy over the last years. However, before we address the subject of Pep-1 internalization, we will introduce some basic information about it.

Pep-1, or transport system Chariot[1], is a 21-residue peptide (KETWWETWWTEWSQP-KKKRKV) with primary amphipathicity[2] [13, 199]. It can be described as a protein transfection agent that interacts with non-covalent interactions with the protein to be delivered. It is considered to be one of the most promising cell-penetrating peptides as it combines no toxicity up to a concentration of 100 μM and high efficacy in delivering drug vectors. Pep-1 can be separated into three domains; a hydrophobic tryptophan-rich domain that is necessary for the efficient targeting to the cell membrane, a hydrophilic lysine-rich domain that improves the intracellular delivery and solubility of the peptide and a spacer domain that consists of one proline residue that connects and improves the flexibility and the integrity of the other two domains. The important role of tryptophan in the interaction of peptides with lipid bilayers has been reviewed in [200]. Because of its special sequence, Pep-1 adopts different secondary structures, depending on its environment. In particular, in water and at low concentrations, it has a disordered structure whereas in a lipid environment the hydrophobic N-terminal region (residues 4-13) is α-helical, and the hydrophilic region unstructured [201].

---

[1] Active Motif, France, http://www.activemotif.com

[2] Amphipathicity resulting from the amino acid sequence itself, and not from the folding structure.

Different internalization mechanisms of Pep-1 have been suggested. In [201], the results indicate that Pep-1 follows an endocytic pathway for cellular uptake. Figure 5.2 shows the different steps of this pathway. First, Pep-1 interacts with the cargo via the tryptophan residues and the complex approaches the membrane (1). Tryptophan residues bind the peptide-cargo complex with the membrane (2). Then, a concave surface curvature is created (3) and finally an endosome is formed and released into the cytoplasm (4). Another proposed mechanism for the translocation of Pep-1 across membranes is the formation of membrane ion channels [13] (Figure 5.3). In [13], the authors suggest that this translocation mechanism has the following steps: (1) formation of a complex with the cargo, (2) membrane uptake, (3) translocation through the bilayer, and (4) release into the cytoplasm. In another study, Henriques *et al.* suggest that the translocation of Pep-1 is mainly driven by the charge imbalance between the outer and the inner leaflet of the membranes and is initiated by nonlytic perturbation of the lipids [202]. Moreover, in [203], it was proposed that Pep-1 peptides form amorphous peptide complexes in the absence of cargo, whereas when a cargo is attached to them, they have the ability to form nanoparticles (Figure 5.4).

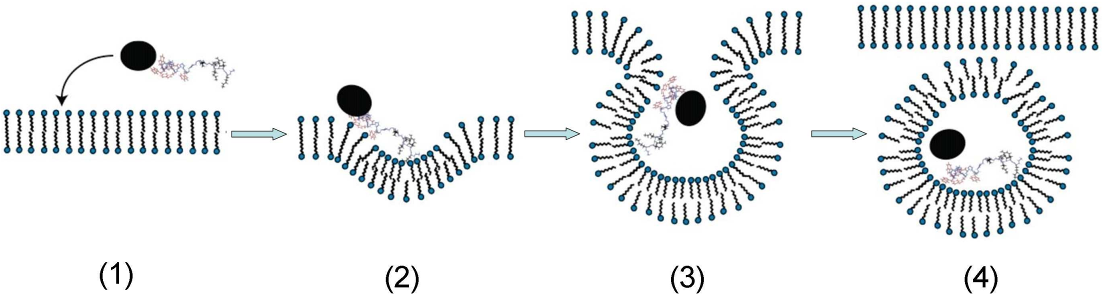

Figure 5.2: **Proposed Pep-1 translocation mechanism across a lipid bilayer I: Endocytosis**. First, Pep-1 interacts with the cargo with the tryptophan residues and the complex approaches the membrane (1). Tryptophan residues bind the peptide-cargo complex with the membrane (2). Then, a concave surface curvature is created (3) and finally an endosome is formed and released in the cytoplasm (4). The figure was adapted from [201].

pHLIP and Pep-1 peptides are particularly challenging cases as either the exact manner (pHLIP) or the whole translocation mechanism (Pep-1) are unknown. Here, we study possible interactions of Pep-1 and pHLIP with a lipid bilayer and how changes like protonation, capped or uncapped termini, lipid bilayer size or type of lipids affect these interactions. The effect of different peptide concentrations was also examined.

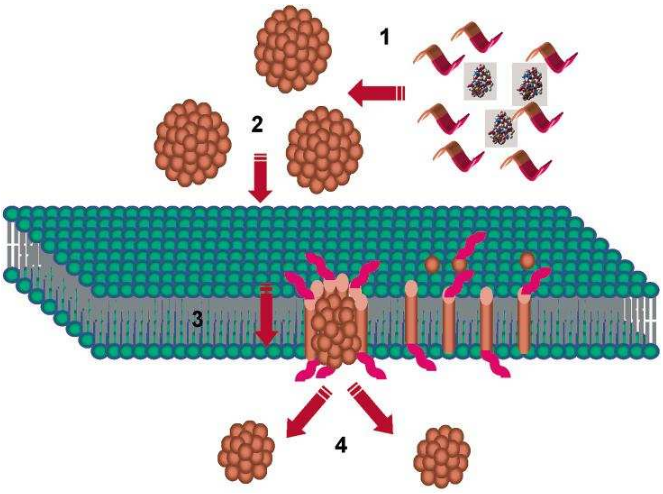

Figure 5.3: **Proposed Pep-1 translocation mechanism across a lipid bilayer II: Pore formation**. (1) Formation of the complex, (2) membrane uptake, (3) translocation through the bilayer, and (4) release into the cytoplasm. The figure was adapted from [13].

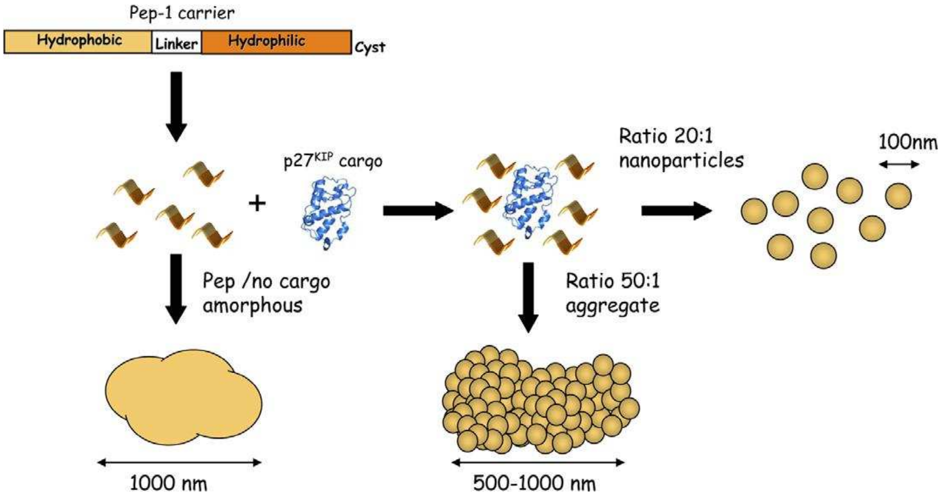

Figure 5.4: **Proposed features of Pep-1/cargo complexes**. Pep-1 forms peptide complexes in the absence of cargo. After being attached to a cargo, it has the ability to form nanoparticles. The figure was adapted from [203].

5.2 Methodology

Simulation setup

We performed MD simulations of pHLIP and Pep-1 peptides in different lipid bilayer systems and at different concentrations. All simulations were performed with GROMACS simulation package, version 3.3.2 [169] and the MARTINI force field was used for the description of the systems [106]. The simulation parameters and methodology were as defined in Chapter 3.

Lipid bilayers

The lipid bilayer systems that were used in this study are presented in Table 5.1. For the construction of the big DPPC membrane, we first started with a preassembled DPPC lipid bilayer with 512 lipids and replicated it in the X and then Y directions, so that a bilayer with 2048 lipids was formed. After equilibrating the system, we replicated it once more in X direction. The final lipid bilayer with the 4096 lipids was further equilibrated. The smaller bilayers were taken from previous MD simulations.

Table 5.1: **Systems of lipid bilayers used in pHLIP and Pep-1 simulations**.

	Type of lipids	Number of lipids	Number of waters
System 1	POPC	128	1500
System 2	POPC	128	2000
System 3	POPC	512	6000
System 4	POPC	512	8500
System 5	DOPC	512	12000
System 6	DOPC	128	1500
System 7	DPPC	4096	203337

Steered MD simulations

Steered MD simulations were performed for Pep-1 peptide, in an effort to capture a potential endocytic pathway, which is a large scale and slow process. We used a preassembled peptide complex, a pentamer formed in one of the MD simulations. We used a harmonic potential with a force constant of 5000 kJ/(mol·nm^2) applied to the centre of the complex with the direction of the normal of the bilayer towards its centre. The pulling rate was 0.0005 nm/ps. The complex' motion in the XY plane was not restrained.

5.3 pHLIP peptide

In Figure 5.5, we present the amino acid sequence of pHLIP and a summary of its observed or proposed behaviour. In our studies, pHLIP is treated as an α-helix in the whole system (even when it is in water). We believe that for the purposes of our study, this representation is adequate.

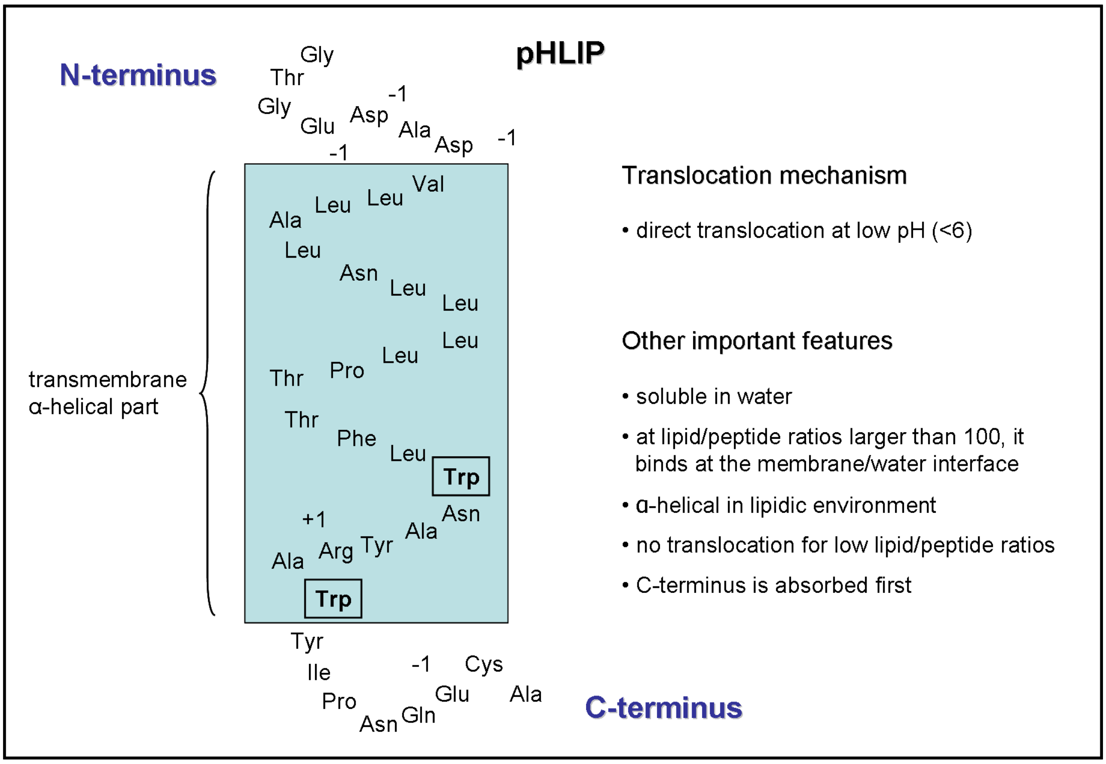

Figure 5.5: **pHLIP peptide: A short summary**.

We started our simulations with a single pHLIP peptide in different lipid bilayer systems. We performed a set of simulations (Set I), and a summary is presented in Table 5.2. In Set I, pHLIP was capped and protonated. Protonation of acidic amino acids was used in order to mimic the low pH environment. The results showed that generally pHLIP was adsorbed on the surface of the lipid bilayer, with its tryptophan side chains embedded in the lipid heads. In one of the simulations, where the N-terminus of the peptide was initially inserted in the bilayer, we observed the insertion of pHLIP (see Figure 3.14).

Table 5.2: **Summary of simulations for pHLIP peptide Set I**. In this set of simulations, pHLIP is capped and protonated. In the last simulation, we used N0 bead type for all backbone beads.

	Duration (μs)	**Behaviour**
System 2	1.2	interfacial positioning
System 3	0.4	the N-terminus of the peptide initially in the bilayer, finally transmembrane position
System 3	0.2	interfacial positioning
System 3	0.2	interfacial positioning
System 4	0.4	the peptide remained in the water phase until the end of the simulation
System 5	1.0	interfacial positioning
System 5	0.3	interfacial positioning

In the second set of simulations, we wanted to test the ability of pHLIP to form complexes. For this reason, we performed MD simulations of pHLIP at different concentrations in a small membrane (System 1, with only 128 POPC lipids and 1500 waters). By using a low lipid/peptide ratio, we were able to compare our observations with available experimental results [166]. In these simulations, pHLIP was uncapped and not protonated. At all concentrations, we observed the formation of complexes that were bound to the lipid heads region by the tryptophan residues. The C-termini of the peptides were adsorbed on the surface of the membrane whereas the N-termini preferred a positioning in the water phase. At very low lipid/peptide ratio, with five peptides in a system of 128 lipids, big undulations of the membrane were observed. In Figure 5.6, we show a snapshot from the simulation with five peptides forming a peptide complex and causing local perturbations to the lipid bilayer. Also, several lipid heads were 'squeezed out', and a defect in the membrane surface was observed. In all the simulations, strong interactions between the uncapped termini seemed to take place. A summary of Set II simulations is presented in Table 5.3.

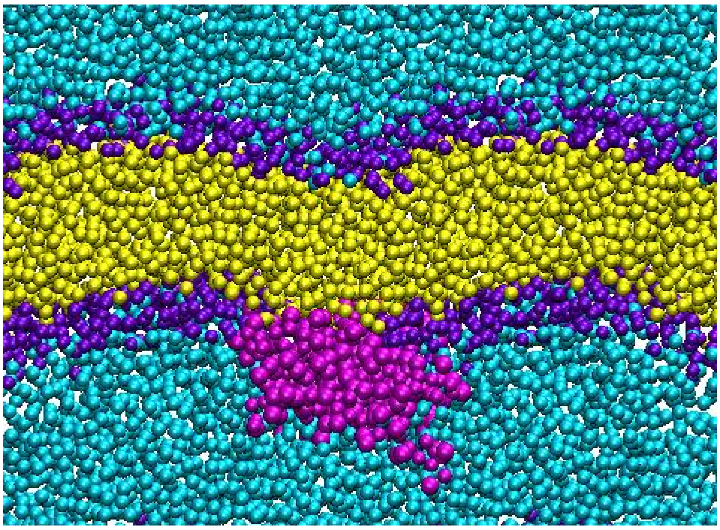

Figure 5.6: **Strong membrane undulations induced by a pentameric pHLIP complex**. Colours: water=blue, lipid heads=purple, lipid tails=yellow and peptide complex=magenta.

Table 5.3: **Summary of simulations for pHLIP peptide Set II**. In this set of simulations, pHLIP is uncapped and not protonated. System 1 was used.

Concentration	**Duration** (μs)	**Behaviour**
2 peptides	5.7	formation of a complex, adsorption on membrane surface
3 peptides	4.5	formation of a trimeric complex, adsorption on the surface of the membrane
4 peptides	4.4	tetrameric complex, interfacial positioning,
5 peptides	4.1	peptide complex on the membrane surface, strong undulations induced by low lipid/peptide ratio

Finally, we performed three simulations with six peptides placed in three different lipid bilayer systems. A summary of these simulations is presented in Table 5.4. Our goal was to test the ability of pHLIP to form pores. Keeping in mind the way the formation of a pore was induced in the case of LS3 (Chapter 4), we initially placed one or two peptides in the lipid bilayer. We also performed a simulation with no peptides inserted but with very low lipid/peptide concentration. No formation of a pore was observed in any of our simulations. However, we were able to capture other interesting phenomena. In the smallest system (System 1), the peptides formed a complex that lied on the surface of the membrane until the end of the simulation. Undulations were caused to the membrane and a defect in its surface was observed. In the biggest system (System 5), one peptide was initially inserted in the bilayer and remained there until the end of the simulation. A complex of five peptides was also formed.

In Figure 5.7, we present three snapshots from a simulation in System 5, two peptides initially inserted in the lipid bilayer and four more in the water phase (Set III). The two peptides remained at a transmembrane position until the end of the simulation. After about 2 μs from the beginning of the simulation, they came at a close distance, started interacting with each other, and finally they created a complex. In the meanwhile, interactions with the rest of the peptides, that had already formed a complex in the

Table 5.4: **Summary of simulations for pHLIP peptide Set III**. In this set of simulations, six pHLIP peptides were inserted in the system. In all cases, pHLIP is not protonated and uncapped.

	Duration (μs)	**Behaviour**
System 1	4.3	big complex formed, interfacial positioning, strong undulations
System 5	4.5	one peptide initially inserted in the bilayer and remained there, aggregation of the rest peptides
System 5	4.4	two peptides, initially inserted in the bilayer, stayed there aggregation of the other four peptides

water phase, were observed. However, this interaction between the complex and the inserted peptide did not lead to a pore formation.

To summarize, in most of the simulations we performed with pHLIP, the peptide was adsorbed at the surface of the membrane. The lipids in the vicinity of the peptide, or the complex, are 'squeezed' aside and a defect in the surface of the lipid bilayer was created. This was more evident in the case where complexes of more than four peptides were formed. As an example, we chose the simulation where a tetramer was formed and was interacting with two peptides at a transmembrane position (Set III, last in Table 5.4). In Figure 5.8, we present the top view of the lipid bilayer (dark purple surface) with and without the peptide complex (coloured in magenta). The snapshot is from the last nanosecond of this simulation. The creation of a hole at the surface of the bilayer is in agreement with the proposed behaviour of pHLIP reported in [166]. Figure 5.9 is a schematic of the defect caused at the surface of the lipid bilayer by a pHLIP complex.

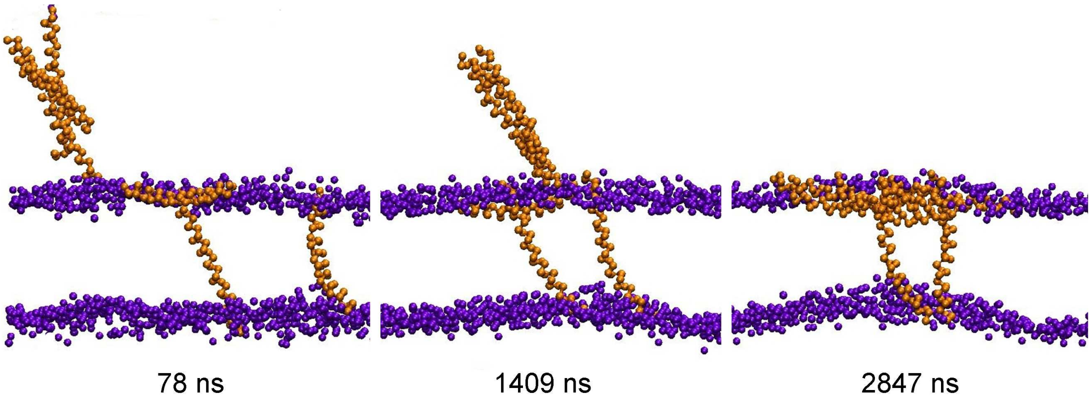

Figure 5.7: **Snapshots from pHLIP simulations**. Two peptides are initially placed at a transmembrane position and remain there until the end of the simulation. After about 2 μs from the beginning of the simulation, they come at a close distance and start interacting with each other, and finally they create a complex. In the meanwhile, interactions with the rest of the peptides, that have already formed a complex in the water phase, are observed. However, this interaction between the complex and the inserted peptide does not lead to a pore formation. Colours: lipid heads=purple and peptide backbone beads=orange. The water and lipid tails have been removed for reasons of clarity.

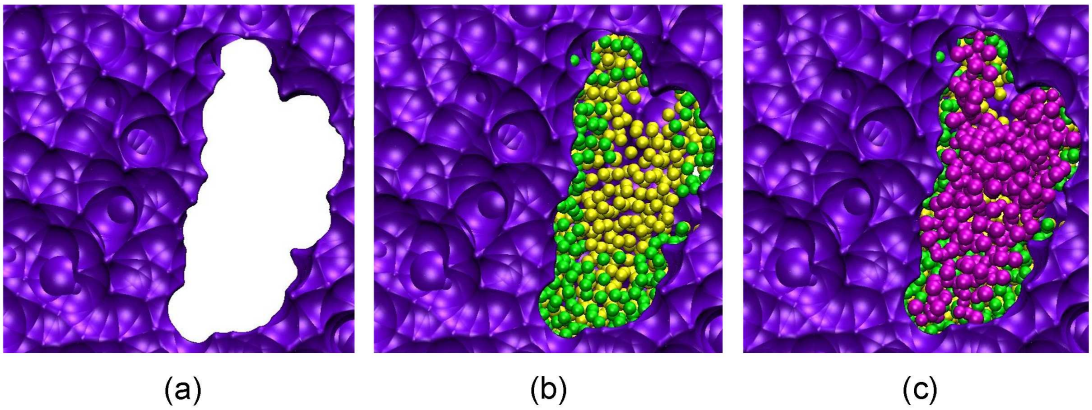

Figure 5.8: **Top view of the defect created by the pHLIP complex on the surface of the lipid bilayer**. (a) Snapshot of the defect with only the surface of the bilayer shown as a surface coloured purple. (b) Snapshot with the lipid tails shown as green and yellow beads corresponding to the top and bottom leaflet respectively. (c) Snapshot where the peptide complex is also included and coloured in magenta.

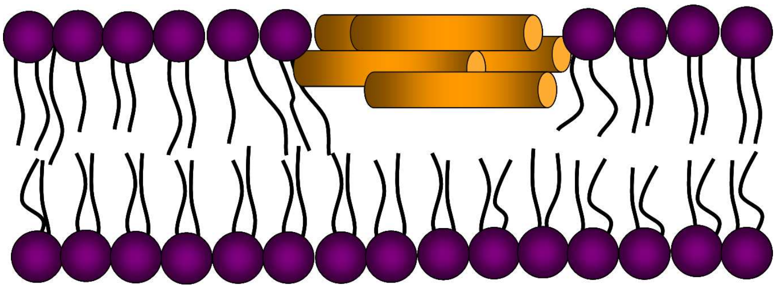

Figure 5.9: **Schematic of the defect caused at the surface of the lipid bilayer by a pHLIP complex**. Colours: lipid heads=purple and peptide=orange.

We also calculated the apparent area per lipid in the presence of the pHLIP complex on the surface of the lipid bilayer, and it was 0.7200 ± 0.0033 nm^2, slightly bigger than the area per lipid of the DOPC bilayer without the peptides (0.6920 ± 0.0034 nm^2). In order to see the effect of the presence of the pHLIP complex on the structure of lipids, we calculated their P_2 order parameters in the vicinity of the complex. In Figure 5.10, we can see the decrease in the lipid order due to the presence of pHLIP peptides in the system.

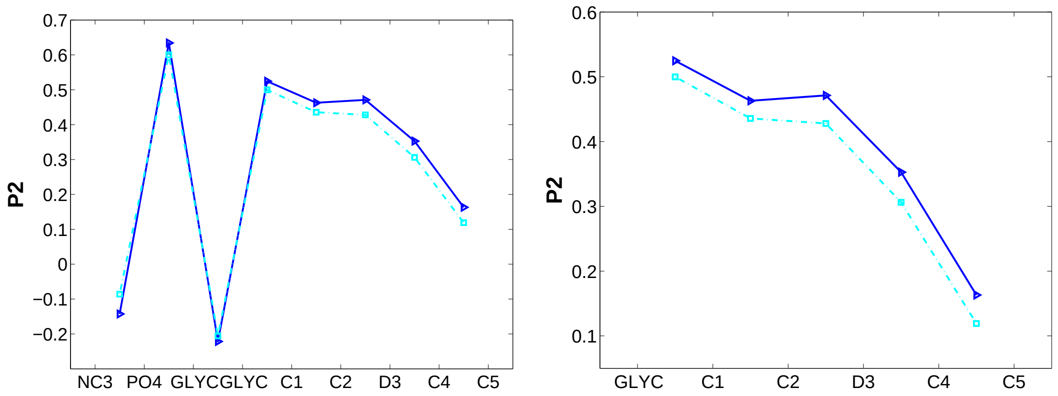

(a)

(b)

Figure 5.10: **P_2 order parameter of consecutive bonds with respect to the bilayer normal**. (a) Results from the pure DOPC lipid bilayer (- ▷, blue) and the bilayer in the vicinity of the tetrameric pHLIP complex (-.- □, cyan). (b) Same as (a), but zoomed in the region of the hydrocarbon tails. There is a decrease in the lipid order induced by the presence of the pHLIP complex.

5.4 Pep-1 peptide

The simulation strategy we followed for Pep-1 was different. We performed different simulation sets, based on the experimentally captured behaviour of Pep-1. However, as described in the introduction of this chapter, this behaviour is still a matter of intense research and discussion. In Figure 5.11, we present the amino acid sequence of Pep-1, with the distribution of charges along this sequence. We have also included a list with the proposed mechanisms of interaction of Pep-1 with a membrane, as well as some of its features that have been experimentally captured. This list has guided us in our simulation strategy. As shown in Figure 5.11, Pep-1 has a hydrophobic part that is α-helical, a hydrophilic part with random structure and a proline residue that works as the linker between these two parts. In our simulations with Pep-1, we have represented the hydrophobic part as an α-helix and the rest of the peptide as a random coil.

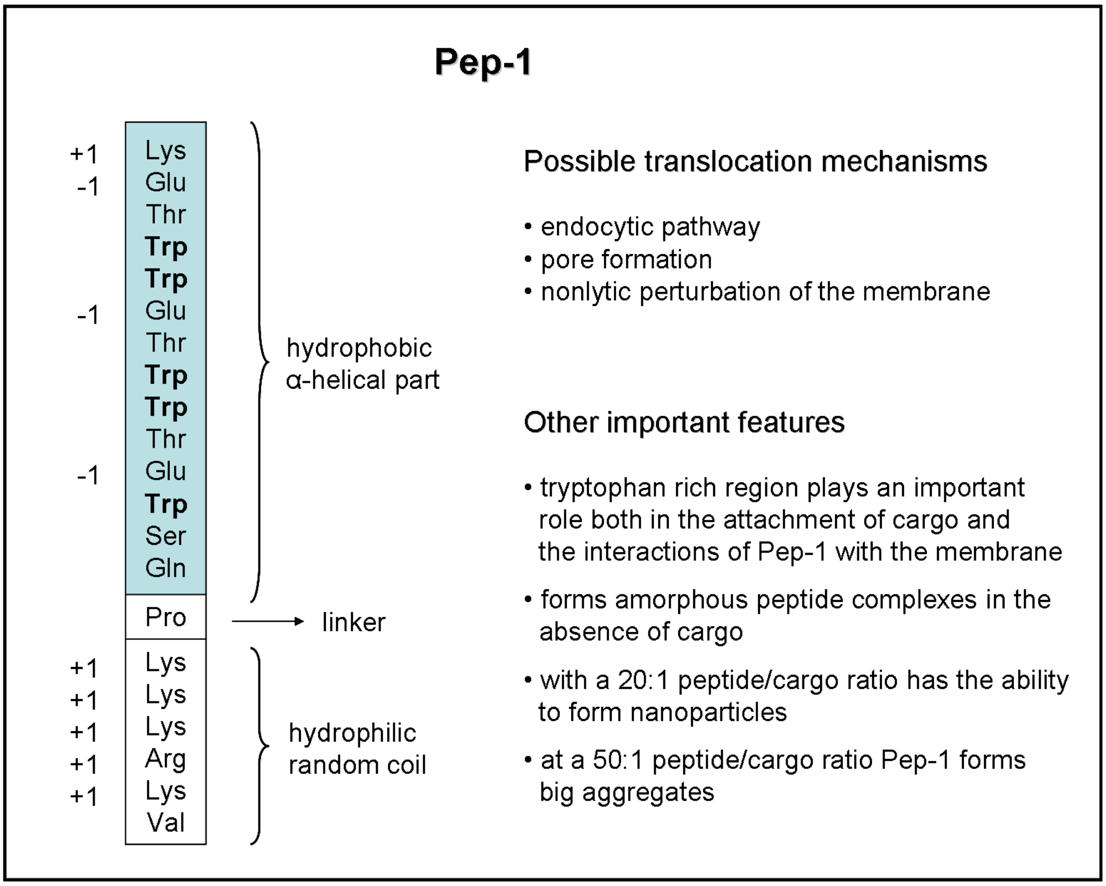

Possible translocation mechanisms

- endocytic pathway
- pore formation
- nonlytic perturbation of the membrane

Other important features

- tryptophan rich region plays an important role both in the attachment of cargo and the interactions of Pep-1 with the membrane
- forms amorphous peptide complexes in the absence of cargo
- with a 20:1 peptide/cargo ratio has the ability to form nanoparticles
- at a 50:1 peptide/cargo ratio Pep-1 forms big aggregates

Figure 5.11: **Pep-1 peptide: A short summary**.

We first performed a series of simulations with uncapped Pep-1 peptides at different concentrations in a small system of 128 DOPC lipids and 1500 waters (System 6). The summary of these simulations is presented in Table 5.5. We used a small membrane in order to promote a possible formation of a pore. A key observation from these simulations was the role of tryptophan in the binding of Pep-1 to the membrane as well as with other peptides. When one peptide was inserted in the system, it quickly adopted an interfacial positioning, with its tryptophan residues adsorbed on the lipid bilayer surface. Its positively charged C-terminus preferred a location in the water phase. When more than one peptides were placed in the system, a complex always formed. Complexes with two, three, four and five peptides were observed. In all cases, tryptophan residues were either embedded in the lipid heads or hidden in the peptide complex. In Figure 5.12, we show the density profiles of tryptophan and valine residues from the simulation with one peptide. From the profiles, we can see that tryptophan residues (dashed blue line) were adsorbed on the surface, under the phospholipid heads (solid black line). Valine seemed to be more flexible, with two populations, one close to the phospholipid heads and one further out of the membrane surface. We carried out the same set of simulations, but with Pep-1 capped. A similar behaviour was captured with complexes formed in all cases and tryptophan residues playing an important role in the overall process of peptide-membrane interaction (Table 5.6).

Table 5.5: **Summary of simulations for Pep-1 peptide Set I**. In this set of simulations, Pep-1 is uncapped. System 6 from Table 5.1 was used.

Concentration	**Duration** (μs)	**Behaviour**
1 peptide	2.2	interfacial positioning
2 peptides	7.2	interfacial positioning
3 peptides	5.4	interfacial, peptide complex is formed
4 peptides	5.5	interfacial, peptide complex is formed
5 peptides	4.1	a pentameric complex is formed, one of the peptides is hidden in the lipid heads

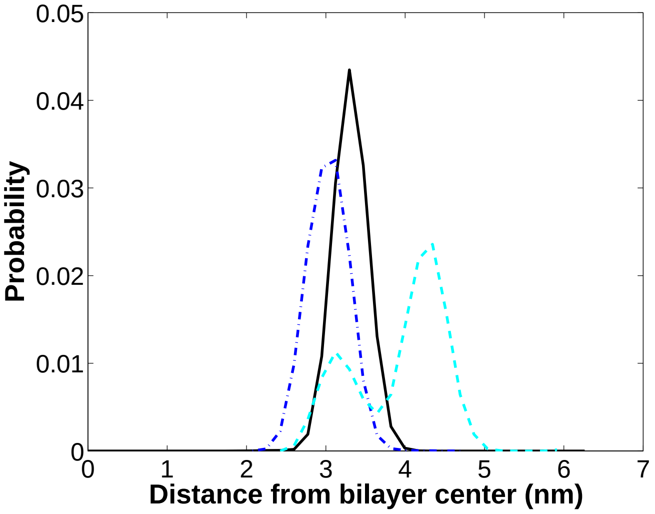

Figure 5.12: **Density profile of tryptophan and valine residues of Pep-1**. Tryptophan residues (dashed blue line) were adsorbed on the surface, under the phospholipid heads (solid black line). Valine (dashed light blue line) is more flexible, with two populations, one close to the phospholipid heads and one further out of the membrane surface.

The propensity of Pep-1 to form aggregates observed in the previous simulations, induced us to study large lipid bilayer systems with the incorporation of six or more peptides in them. Thus, we performed three simulations in a lipid bilayer system of 512 DOPC lipids and 12000 water coarse-grained beads (System 5). The summary of these simulations is shown in Table 5.7. We inserted six and twenty peptides in the system, and waited for several microseconds to observe the behaviour of Pep-1 in a large aqueous phase. Again, complexes with different number of peptides were formed with the biggest consisting of 12 peptides. The complexes were stable and were located either close to the lipid bilayer surface or in the water phase. They showed an inherent stability and only association and not dissociation of the peptides was observed. The shape of the complexes was close to spherical in the case of the hexameric aggregate and was varying in the case of the large aggregate.

In Figure 5.13, we present a series of snapshots from the simulation where twenty peptides were inserted in the lipid bilayer system. Five of these peptides were already in a form of a complex, taken from previous simulations, and the helical parts of two peptides were initially placed inside the lipid bilayer at a transmembrane position. After a few nanoseconds, they started interacting with each other, and created a complex inside the bilayer, resembling a dimer. They remained as a complex for more than 200 ns.

Table 5.6: **Summary of simulations for Pep-1 peptide Set II**. In this set of simulations, Pep-1 is capped. System 6 from Table 5.1 was used.

Concentration	Duration (μs)	Behaviour
1 peptide	2.2	helical part adsorbed on the membrane surface
2 peptides	5.0	interfacial positioning, complex formed
3 peptides	7.0	complex is formed, membrane perturbations
4 peptides	5.5	formation of two dimer-like complexes,
5 peptides	5.2	pentameric complex is formed, interfacial positioning
6 peptides	9.3	a hexameric complex is formed, interfacial positioning

They created local perturbations to the membrane, that were particularly pronounced when the complex was slowly moving out of the membrane. During this process, tryptophan residues played an important role in the perturbation of the lipid bilayer. In Figure 5.14, we have taken a snapshot of the simulation where tryptophan residues can be observed in the hydrophobic core of the bilayer (yellow beads). These residues seem to 'drag' some lipid head groups towards the inner part of the bilayer. During this simulation, we observed several lipid heads as well as water molecules inside the hydrophobic core of the lipid bilayer. The perturbations of the lipid bilayer lasted for about 200 ns. After that the peptides adopted a positioning at the surface of the bilayer and remained there until the end of the simulation. The pentameric complex, by the end of the simulation, became an aggregate of 12 peptides, with maximum dimension of about 7.3 nm.

Another simulation was performed with a pentameric complex initially half-inserted in the lipid bilayer. The configuration of the complex was taken from previous simulations. It was formed in the water phase and most of its hydrophilic sidechains lay at the outer surface of the complex. In Figure 5.15, we show a series of snapshots from this simulation. The complex from the half-inserted position (a), starts going out from the membrane (b), taking with it several lipid heads shown in violet. In the third

Table 5.7: **Summary of simulations for Pep-1 peptide Set III**. System 5 was used.

Concentration	**Pep-1**	**Duration** (μs)	**Behaviour**
6 peptides	uncapped	3.8	a complex of two, four and finally five peptides is formed and located close to the membrane surface, the complex is stable for 1 μs
6 peptides	capped	3.7	a pentameric complex is formed, it is located in the water
20 peptides	uncapped	2.4	an amorphous complex of 12 peptides is formed trimeric and pentameric complexes are observed

snapshot (c), the complex has induced the formation of a water pore. The pore has a toroidal shape and the complex is at its entrance, close to the surface of the lipid bilayer. In Figure 5.15(d), the pore is closed. Finally, the peptide complex is in the water phase but still in contact with the bilayer (e).

Finally, we carried out a 500 ns MD simulation with a peptide complex and ten more peptides randomly inserted in System 3. The complex remained united during the whole simulation. One of the peptides, that was initially at a transmembrane position, remained there. Because of Pep-1 secondary structure the dimers that were formed seemed to be stabilized by the helix-helix interactions. The coiled part of the peptides moved randomly. When the two dimers came to a relatively close distance, they created a tetramer that again appeared to be maintained by the interactions between the helices.

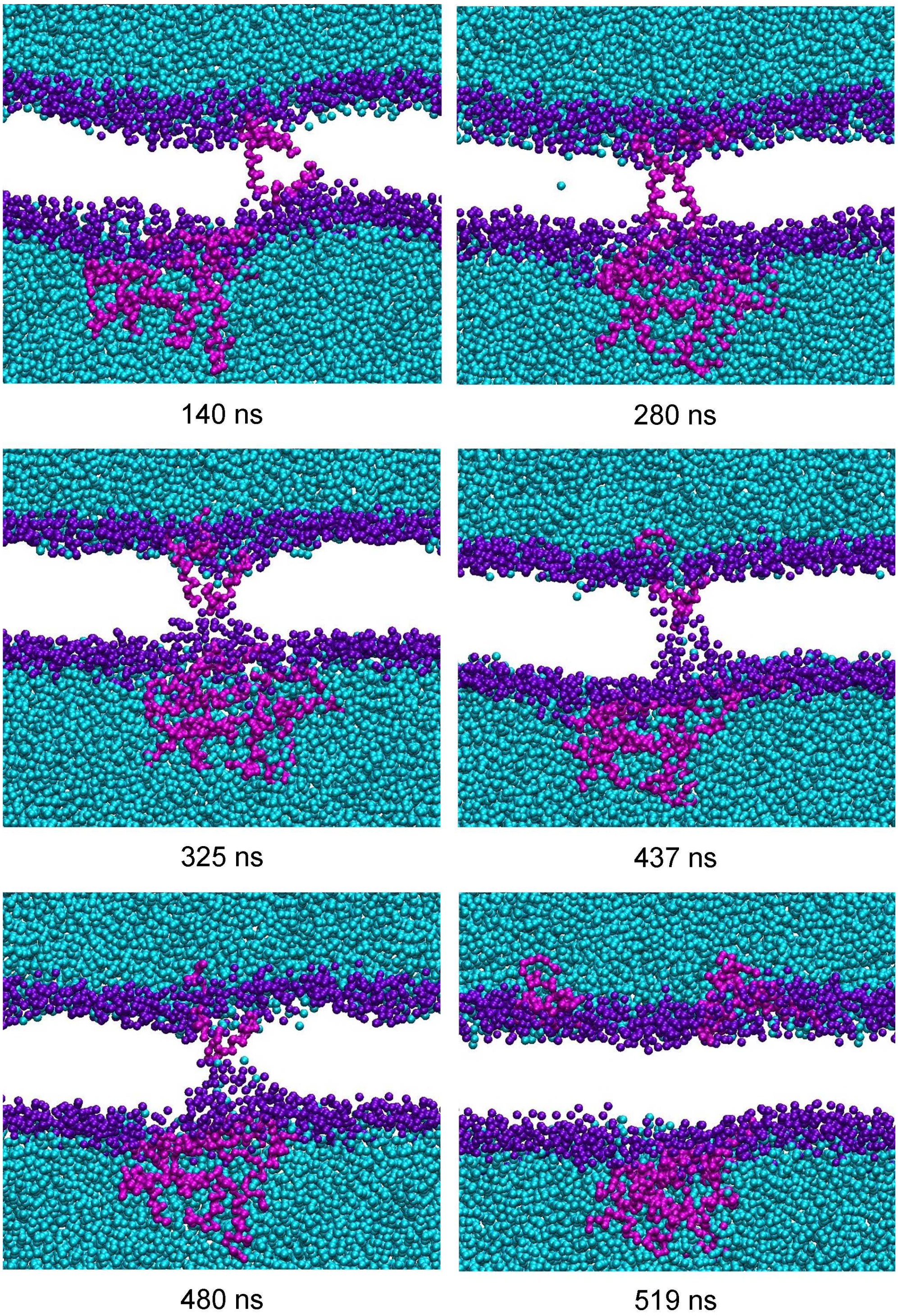

140 ns

280 ns

325 ns

437 ns

480 ns

519 ns

Figure 5.13: **Snapshots from Pep-1 simulations**. 20 peptides were inserted in a DOPC lipid bilayer. Two peptides that were initially put at a transmembrane position, remained there for more than 400 ns, causing strong local perturbations to the membrane. Finally, the two peptides adopted a positioning at the surface of the lipid bilayer. Colours: water=cyan, lipid heads=dark purple and peptide backbone beads=magenta. The lipid tails are not shown for clarity.

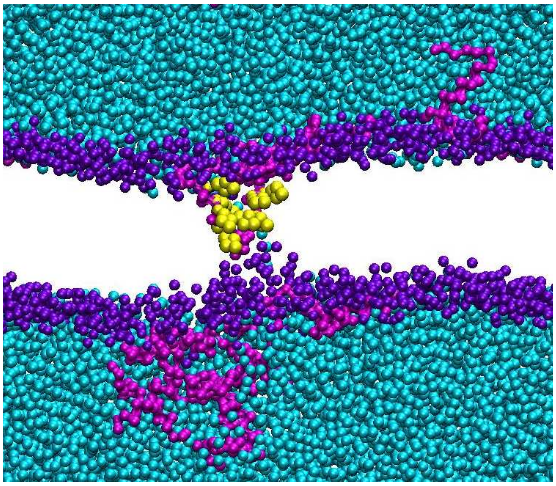

Figure 5.14: **The effect of tryptophan in Pep-1/membrane interaction**. Colours: water=blue, lipid heads=purple and peptide backbone beads=magenta. Tryptophan residues that are inside the lipid bilayer are coloured yellow.

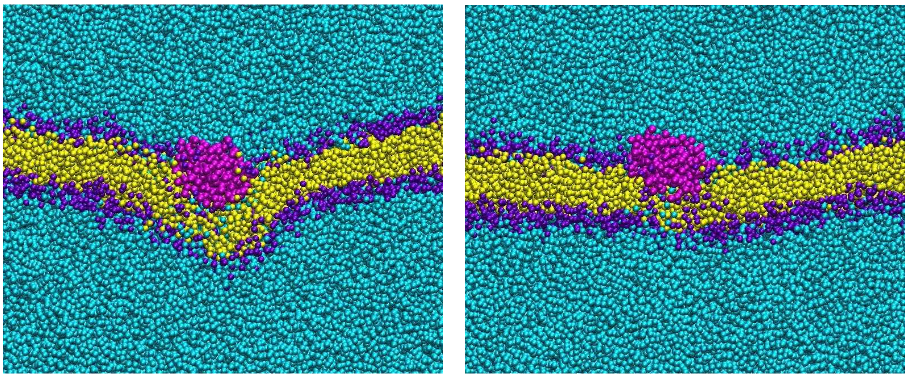

(a) 1 ns

(b) 2 ns

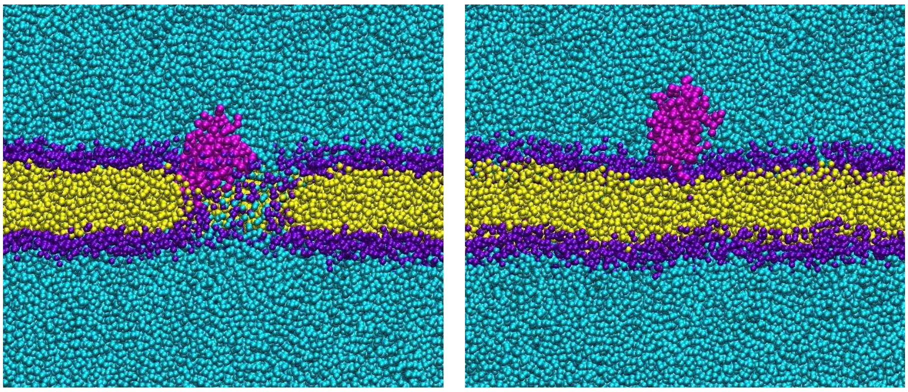

(c) 30 ns

(d) 40 ns

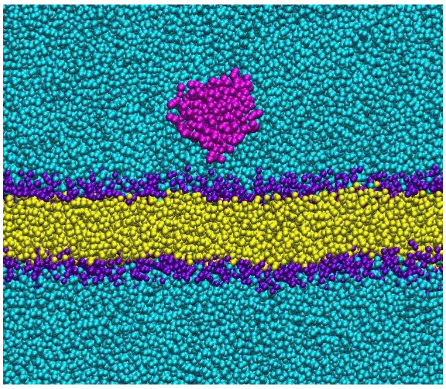

(e) 88 ns

Figure 5.15: **Snapshots from the MD simulations of Pep-1 complex**. Colours: water=blue, lipid heads=purple, lipid tails=yellow and peptide complex=magenta.

Steered MD

In Figure 5.17, we present snapshots from a Steered MD simulation we performed with a pentameric complex initially placed at a distance of 0.5 nm from the lipid bilayer surface. In Figure 5.17(a), we can see the evolution of the system as the peptide complex is pulled inside the lipid bilayer. When the complex is at the surface of the bilayer, small perturbations can be observed. While pulling, these perturbations become stronger, led to an interdigitated state, and finally to the disintegration of the lipid bilayer. In another Steered MD simulation, again with the pentameric complex very close to the lipid bilayer surface, we observed the formation of a transient water pore while the peptide complex is pulled inside the lipid bilayer. Figure 5.17(b) and Figure 5.16 show the side view of this pore. Again the pore has a toroidal shape like the one observed from the MD simulations (Figure 5.15(c)). After the formation of the pore, and as the complex is further pulled, the membrane loses stability and ruptures are observed on its surface (Figure 5.17(c)). In Figure 5.18, we have plotted the area per lipid for the second of the two Steered MD simulations, where we can see the point of the membrane rupture. At about 3.5 ns, and when the peptide has moved about 1.75 nm along the bilayer normal towards the center of the lipid bilayer, the membrane starts expanding in X and Y directions and after half nanosecond the system ruptured.

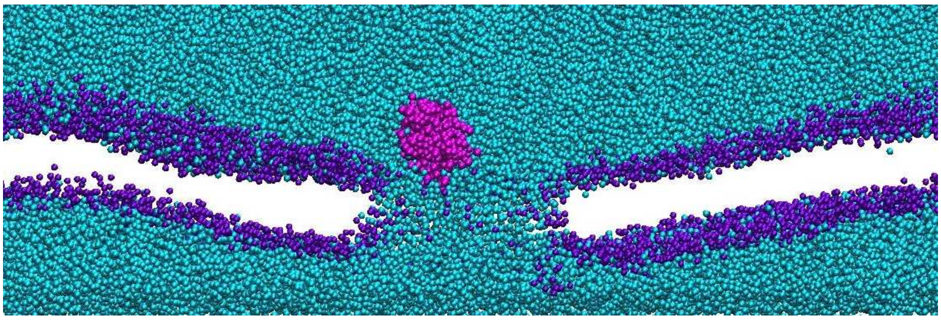

Figure 5.16: **Transient water pore formed by Pep-1 complex**.

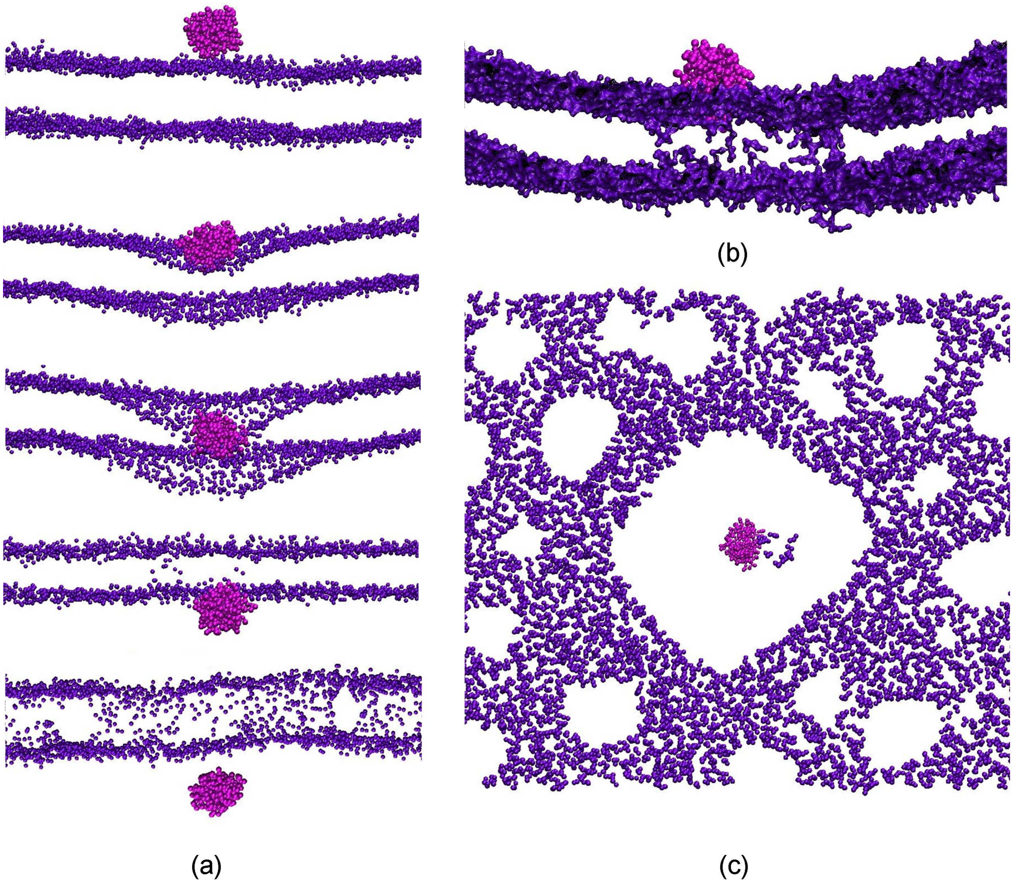

Figure 5.17: **Snapshots from the Steered MD simulations with Pep-1**. (a) The peptide is pulled from the water phase inside the lipid bilayer along the bilayer normal. Local perturbation of the lipid bilayer that eventually lead to an interdigitated state, the formation of a defect and finally to the rupture of the lipid bilayer. The snapshots from top to bottom correspond to the 1st, 3rd, 6th, 8th and 10th nanosecond respectively. (b) Side view of the transient pore that is formed when Pep-1 is pulled inside the lipid bilayer. (c) Deformation of the lipid bilayer due to the strong interaction with Pep-1. The lipid heads are coloured dark purple and the peptide complex magenta.

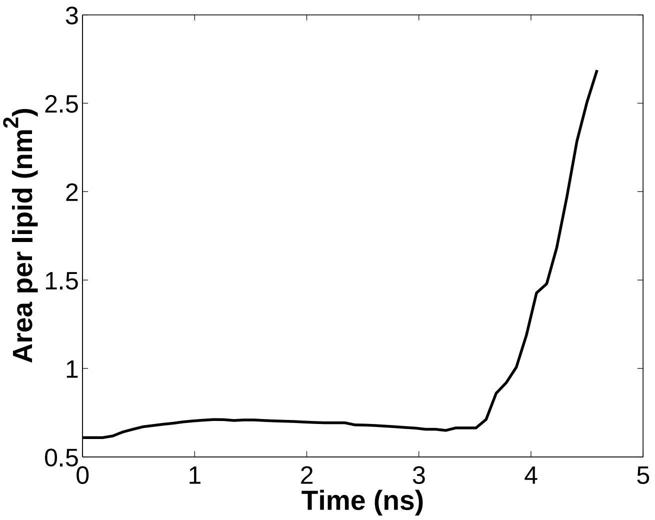

Figure 5.18: **Area per lipid from the Steered MD simulations of Pep-1 complex**. The membrane rupture can be observed starting at about 3.5 ns, with the peptide complex moved about 1.75 nm from the surface towards the center of the lipid bilayer.

5.5 Conclusions

The initial objective of this study was two-fold and could be summarized in the following questions:

- Can we capture pHLIP translocation?
- Is pore formation, direct translocation or endocytosis the uptake mechanism for Pep-1?

The simulation results, however, cannot be directly used to answer any of these questions. In the case of pHLIP peptide, no translocation was observed both at low and high lipid/peptide ratios. However, it is important to note that all of the available experimental data have been taken from *in vivo* studies of the peptide, and thus a direct comparison with simulation results is difficult to be made.

The formation of complexes of different sizes and the adsorption of pHLIP on the lipid bilayer surface were the two key observations of our simulations. Although the formation of complexes has not been captured experimentally, it has not been excluded as a possible scenario [166]. Moreover, the binding of pHLIP to the surface of the membrane has been proposed in several studies [164, 166, 167, 198]. pHLIP tends to 'squeeze out' the lipid heads, and lead to the formation of defects in the surface of the bilayer. Also, from the calculation of the order parameters of the lipids close to a tetrameric peptide complex, we observed a decrease in the ordering of lipid chains that is probably caused by the interactions of pHLIP with the lipid heads.

Another key observation from our simulations is the positioning of the C-terminus of pHLIP in the lipid heads region when a single peptide was considered. This observation is in agreement with previous experimental studies [166]. In the case where the N-terminus of the peptide was half-inserted in the lipid bilayer, we observed its insertion in the hydrophobic core. The initiation of the insertion only when one terminus was inside in the bilayer, may signify that there is probably something missing in the description of pHLIP-membrane interactions in our studies. A better treatment of the electrostatic interactions or even a more realistic representation of the membrane could be possible improvements of the description of the system.

In the case of Pep-1, we observed the formation of complexes of different sizes. In particular, an interesting result was the formation of a peptide complex consisting of 12 peptides. The complex, once formed, remained stable until the end of the simulation. This was the case for all the different complexes we observed. The complexes were stable, with a constant number of peptides unless another free peptide approached and joined the aggregate. The formation of complexes is in agreement with available experimental observations, where the peptide formed large aggregates in the absence of cargo [203].

Also, tryptophan seems to play and important part in the interaction of Pep-1 with the lipid bilayer as well as in peptide-peptide interactions. We showed by plotting the density profiles of tryptophan and valine residues that tryptophan was under the layer of phospholipid heads during the whole simulation, whereas valine seemed to be more flexible and covered a bigger area close to the surface of the lipid bilayer. This observation is also in agreement with experimental results [201].

Another notable result is the formation of transient pore-like structures, once the peptide or the peptide complex is slightly inside the lipid bilayer, close to the lipid head region. This was captured both by MD and Steered MD simulations. These structures had a toroidal shape and in two cases they were filled with water. As in the case of pHLIP with the insertion, this initial driving force that is needed in order for these pores to form seems to be missing from our description of the system. Probably the absence of cargo or a different treatment of electrostatic interactions are the missing parameters that should be included in order to have a more realistic representation of the system. However, many key features of Pep-1 interactions are captured in our results and show that further investigations and improvement in the description of the system could provide us with a better understanding of these interactions.

CHAPTER 6

Interactions between nanoparticles and lipid membranes

The wide use of nanoparticles in a variety of products, such as drug and gene delivery materials, and the results from our simulation studies on cell-penetrating peptides, with the formation of nanosized complexes, were two of the reasons that inspired this study. Nanoparticles of two sizes (1 nm and 3 nm diameter) with different surface chemistry were constructed, with different types and distribution of CG beads on their surface. MD and Steered MD simulations were then performed in order to obtain insights about the nanoparticle-membrane interactions. Some qualitative results will be presented mainly by means of visualization and some first observations will be discussed.

6.1 Methodology

Simulation setup

All simulations were performed with GROMACS simulation package, version 3.3.3 [169]. The MARTINI force field was used for the description of the lipid bilayer and the nanoparticles [106]. The simulations were carried out under periodic boundary conditions at constant temperature and pressure. The temperature was kept constant for each group, at 323 K for the DPPC systems and 300 K for the DOPC, using the Berendsen thermostat with a relaxation time of 1 ps [135]. The pressure of the system was semi-isotropically coupled and maintained at 1 bar using the Berendsen algorithm with a time constant of 5 ps and a compressibility of 4.5×10^{-5} bar^{-1} [135]. The non-bonded potential energy functions were cut off and shifted at 12 Å, with forces smoothly decaying between 9 Å and 12 Å for van der Waals forces and throughout the whole interaction range for the treatment of electrostatic forces. The simulations were performed using a 20 fs integration time step.

Nanoparticles

In our study, we considered two sizes (1 nm and 3 nm) and six different types of nanoparticles. The types were chosen so that we could either be able to compare with available experimental studies (for example, the striped nanoparticles from [119]) or with the peptide complexes formed in our simulation studies (Chapter 5). The nanoparticles were constructed by placing evenly spaced CG beads of different types at the surface of a 1 nm and a 3 nm sphere. Bonds with a force constant of 1250 kJ nm^{-2}mol^{-1} were used for neighbouring beads. Also, the beads at a distance equal to the radius of the sphere were restrained with a a force constant of 2250 kJ nm^{-2}mol^{-1} to maintain the shape of the nanoparticle. The different types of nanoparticles are presented in Table 6.1, where the nature, the name and the CG representation of each nanoparticle are shown. For the construction of the nanoparticles with more than one bead type, we used an approach similar to that introduced in [119], with striations of alternating groups (Figures 6.1 and 6.2).

Table 6.1: **Types of nanoparticles used in this study**.

Type	Name	CG Representation
Hydrophobic	C-type	C1
Polar	P-type	P5
Mixed	CP-type	C1 and P5
Charged-acceptor and polar	Qa+P-type	Qa and P5
Charged-donor and polar	Qd+P-type	Qd and P5
Charged-acceptor and hydrophobic	Qa+C-type	Qa and C1

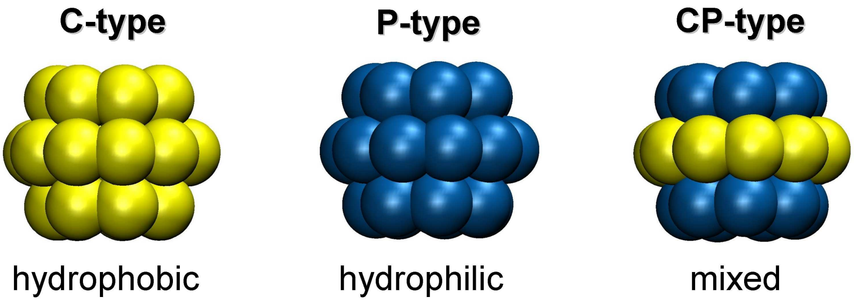

Figure 6.1: **Nomenclature for the 1 nm nanoparticles**. All nanoparticles have 24 coarse-grained beads. The mixed nanoparticle has 10 C1 type and 14 P5 type beads. The beads are not to scale. Colours: hydrophobic beads=yellow and hydrophilic beads=dark blue.

Pure lipid bilayers

The lipid bilayer systems used in this study are shown in Table 6.2. For the simulations with the 3 nm nanoparticles, we mainly used very big systems with enough water phase in order to avoid artefacts caused by the interactions over periodic boundaries (for example undulations). For the construction of the big membranes, we first started with a preassembled DPPC lipid bilayer with 512 lipids and replicated it in the X and then Y directions, so that a lipid bilayer with 2048 lipids was formed. After equilibrating the system, we replicated it once more in X direction. The final lipid bilayer with the 4096 lipids was further equilibrated. In the cases where bigger water phase was needed, we replicated the water slab from one side of the bilayer as many times as needed, with intermediate equilibration runs.

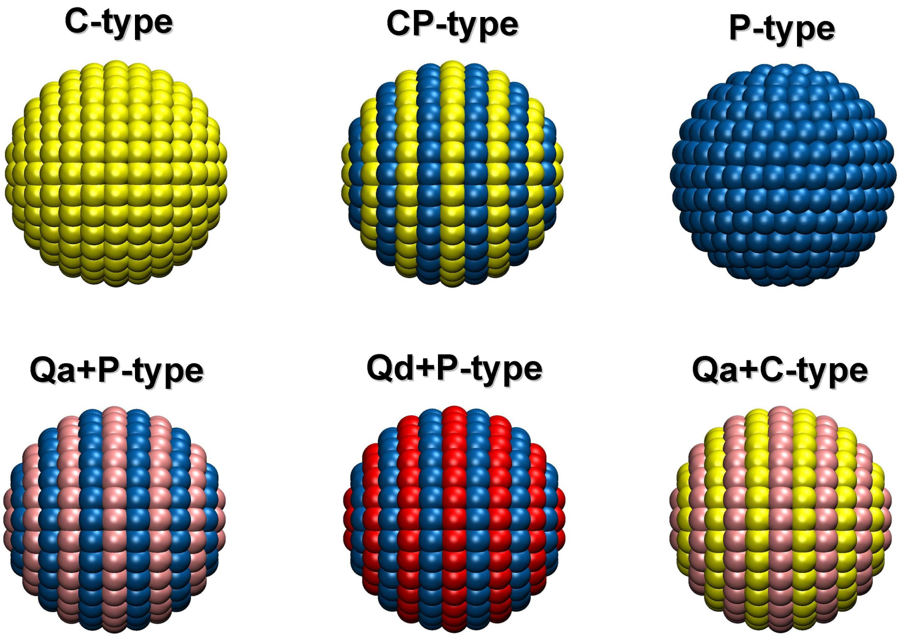

Figure 6.2: **Nomenclature for the 3 nm nanoparticles**. All nanoparticles have 271 coarse-grained beads, evenly shared between the different types. The beads are not to scale. Colours: hydrophobic beads=yellow, hydrophilic beads=dark blue, charged and donor beads=red and charged and acceptor beads=pink.

Table 6.2: **Systems used for the steered MD simulations.**

	Type of lipids	**Number of lipids**	**Number of waters**
System 1	DPPC	4096	95963
System 2	DPPC	4096	120533
System 3	DPPC	4096	203337
System 4	DPPC	512	11414
System 5	DOPC	512	11722

Nanoparticle-bilayer systems

After the preparation of the lipid bilayers, we performed a series of Steered MD simulations. The initial configurations for these simulations were prepared as follows: first, we created an empty sphere in the water phase of each lipid bilayer system, by removing the corresponding water beads. To avoid overlaps, the diameter of this sphere was 1 nm bigger than the diameter of the nanoparticle to be inserted. For the systems where charged particles were used, we added ions to maintain the overall neutrality of the system. An equilibration simulation of about 50-100 ns, depending on the system size, was then performed.

Steered MD

In order to speed up the process of interaction of a nanoparticle with a lipid bilayer, which in the case of the pore formation or the interdigitated state seen in experiments may be a very slow event, we applied an external force to the nanoparticle. We used a harmonic potential with a force constant of 5000 kJ/(mol·nm^2) applied to the centre of the nanoparticle with the direction of the normal of the bilayer. The pulling rate was 0.0005 nm/ps. Due to the size of the lipid bilayers we used in this study, it is possible that their response to the pulling of the nanoparticles through them will not be fast enough and could cause mechanical instability to the system. Thus, in some cases that will be specified in the results section, we used a pulling rate of 0.00005 nm/ps and a force constant equal to 1000 kJ/(mol·nm^2), in order to examine if indeed the response of the big lipid bilayers may lead to artefacts depending on the pulling rate and force constant. The nanoparticle motion in the XY plane was not restrained and the nanoparticle is free to rotate. The simulation parameters were as described before in this section, apart from the pressure coupling that for the Steered MD was anisotropic.

6.2 Results

6.2.1 1 nm nanoparticles

We performed steered molecular dynamics simulations for each of the nanoparticle types introduced in the Methodology. The summary of these simulations is presented in Table 6.3. System 1 from Table 6.2.

Table 6.3: **Summary of simulations for the 1 nm nanoparticles.**

Nanoparticle	Steered MD	Simple MD
C-type	insertion	
P-type	bilayer thinning, holes formation	positioning at the bilayer surface
CP-type	insertion	under the phospholipid heads

From the pulling simulations, the C- and CP-type nanoparticles inserted into the lipid bilayer. The hydrophobic nanoparticle passed very smoothly in the hydrophobic core of the bilayer, whereas the mixed nanoparticle induced a curvature to the membrane, by dragging several lipid heads with it. The polar nanoparticle, although of a small size, induced thinning and high curvature to the lipid bilayer. If we compare our observations with that reported in [122], we will see that they are not contradictory. Actually, in our simulations, both the polar and the mixed nanoparticle induced really high curvature to the membrane without disrupting it (Figure 6.3(a)). Thus, using the same terminology as in [122], 'the lipid bilayer followed the topographical features of the nanoparticle'.

Thinning of the bilayer was also observed for the C- and CP-type nanoparticles. The thinning of the bilayer happened while pulling the nanoparticles out of the hydrophobic core of the bilayer. In all the cases where this thinning was captured, after a few nanoseconds the membrane returned to its original state.

We have calculated the order parameters of the lipids in the vicinity of the nanoparticles (Figure 6.3(b)). We used only one snapshot for each type (shown next to the order parameters plot), and in the case of the polar and mixed nanoparticles this snapshot was at the critical point before the beginning of the membrane thinning. For the hydrophobic nanoparticle, we used a snapshot with the nanoparticle inside the hydrophobic core of the bilayer (Figure 6.3(a), *top*). The order parameters show a big decrease in the ordering of lipids in the system with the polar and mixed nanoparticles, compared with the pure lipid bilayer and the hydrophobic nanoparticle. We should also note that the actual defects on the membrane were a consequence of pulling the nanoparticles after the critical point before the lipid bilayer thinning.

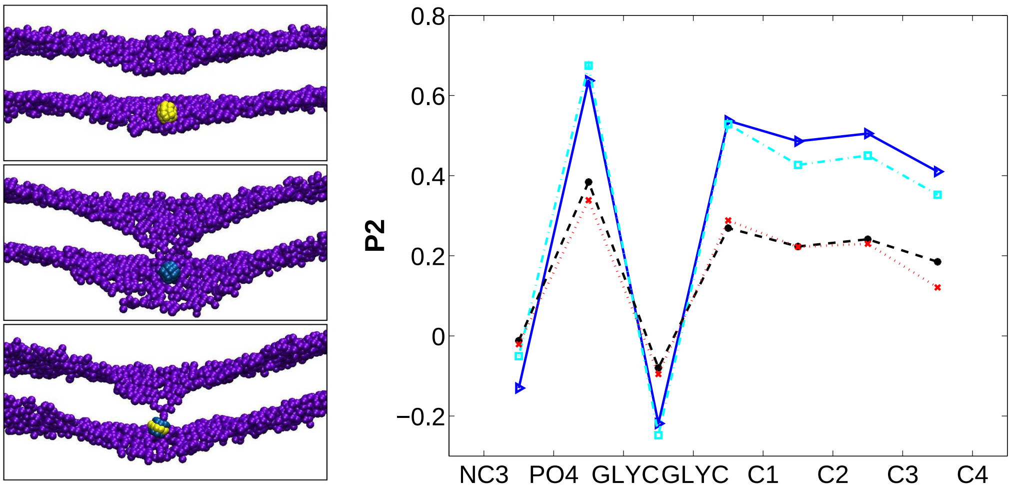

(a) (b)

Figure 6.3: **P_2 order parameter of consecutive bonds with respect to the bilayer normal in the vicinity of the nanoparticles**. Pure lipid bilayer(- ▷, blue), the bilayer in the presence of the Ctype nanoparticle (-.- □, cyan), CPtype nanoparticle (– ◇, black) and Ptype nanoparticle (— •, red) show significant differences.

In Figure 6.4, we have plotted the area per lipid for the system with the mixed nanoparticle. From the figure, we can notice the reaction of the membrane to the pressure imposed by the pulling, and the relaxation time until reaching the area per lipid of the liquid phase (≈ 63 Å). The increase of the area per lipid reaches a factor of 1.67 which is in agreement with reported values indicating a transition to an interdigitated state [204]. A similar behaviour was observed for the hydrophobic and polar nanoparticle at the exit and entrance from the bilayer respectively. An important note here is that the induction of an interdigitated state was experimentally captured for nanoparticles of a 5-nanometer diameter in [123] .

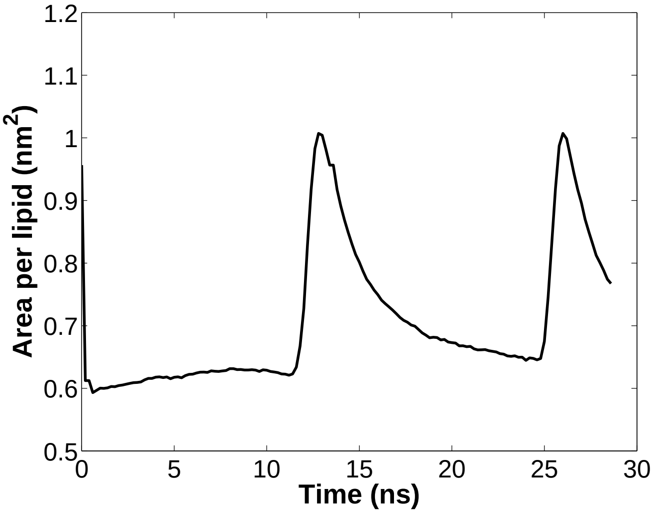

Figure 6.4: **Area per lipid for the CP-type 1-nm nanoparticle**. We can observe the point where the interdigitated state occurs and the reaction of the lipid bilayer to it.

We also performed MD simulations of the polar and mixed nanoparticles (Table 6.3). We used as initial configurations the last configurations before the interdigitated state. The polar nanoparticle adopted a positioning at the surface of the lipid bilayer, whereas the mixed nanoparticle remained close to the phospholipid heads.

6.2.2 3 nm nanoparticles

We first performed some steered molecular dynamics simulations with hydrophobic, polar or mixed nanoparticles. In Table 6.4, we present a summary of these simulations. We carried out three simulations for the hydrophobic, four for the polar and 2 for the mixed nanoparticle. The third simulation for the C and P types was performed with a pulling rate of 0.00005nm/ps, whereas in the fourth simulation with the polar nanoparticle a smaller force constant was used (1000 kJ/(mol·nm^2)).

The hydrophobic nanoparticle, in all three simulations, crossed the lipid bilayer. However, this was not the case for the polar nanoparticle, where no insertion was observed. In two of the simulations, the nanoparticle, after inducing a high curvature to the membrane, led to an interdigitated state and finally disruption of the lipid bilayer.

Table 6.4: **Summary of simulations for the nanoparticles of 3-nm diameter.**

Nanoparticle	**Simulations**	**Behaviour**
C-type	3	insertion, bilayer thinning while pulling out
P-type	4	no insertion, bilayer thinning, holes
CP-type	2	insertion, lipid heads in the hydrophobic core, bilayer thinning while pulling out

In Figure 6.5, we show a detail from the lipid bilayer in a liquid and in an interdigitated state from one of the simulations with the polar nanoparticle. In the figure, the lipid heads are coloured purple, the hydrophobic tails of the top leaflet orange and the hydrophobic tails of the bottom leaflet yellow. From Subfigure 6.5(b) we can see the characteristic lipid structure seen for an interdigitated state. The bilayer thickness was also calculated and was found to be $\sim$ 4.7 nm in the liquid phase and $\sim$ 2.8 nm in the interdigitated state.

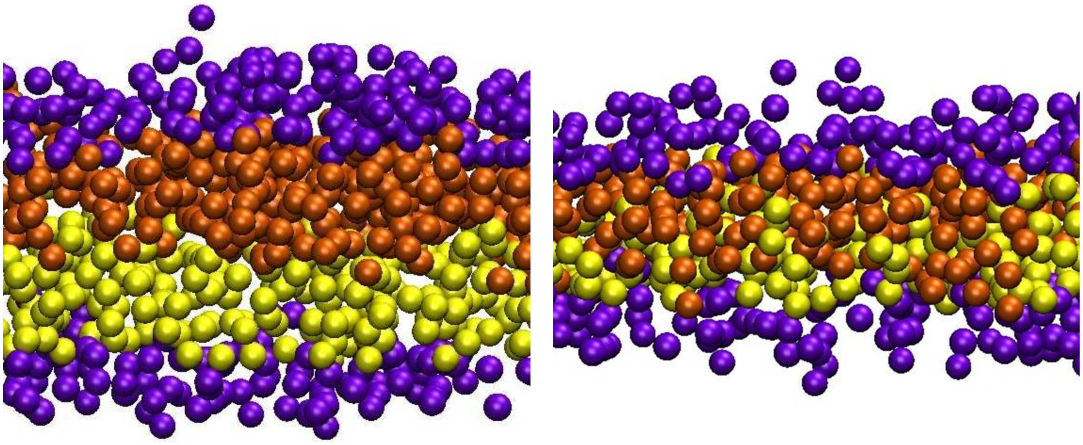

(a) (b)

Figure 6.5: **Detail of the interdigitated state of a lipid bilayer**. (a) Lipid bilayer in liquid phase. (b) Lipid bilayer in an interdigitated state from the pulling simulation of a P-type nanoparticle. Colours: lipid heads=purple, hydrophobic tails top leaflet=orange and hydrophobic tails bottom leaflet=yellow.

In Figure 6.6, we present some characteristic snapshots from the simulations with the polar nanoparticle. In Subfigure (a), a high curvature is induced by the nanoparticle, leading to an interdigitated state and finally membrane rupture. We have also observed the formation of a transient pore (Figures 6.6(b) and (c)). This pore was filled with water, with some of the lipid heads lining the pore at a toroidal shape. While pulling, the pore increased in diameter and finally more pores were created on the lipid bilayer (Figure 6.6(d)).

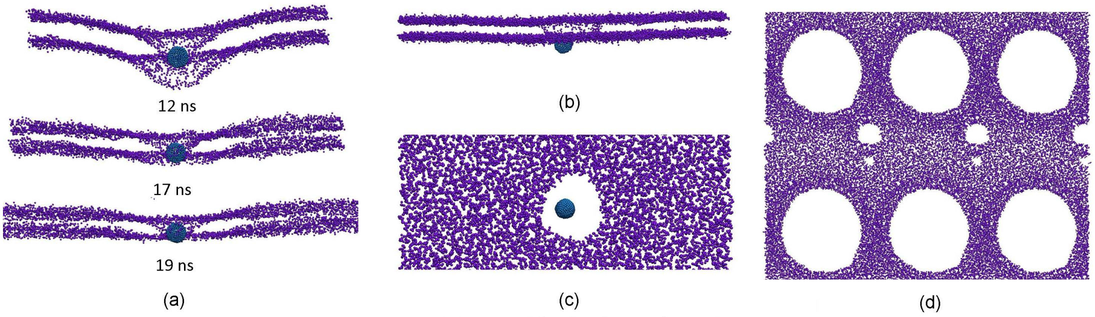

Figure 6.6: **Interdigitated state and transient pore formation from the polar nanoparticle**. (a) Snapshots from one of the pulling simulations with a P-type nanoparticle. High bilayer curvature, thinning and disruption can are observed. (b), (c) Side and top view of the transient pore induced by the pulling of a polar nanoparticle across the lipid bilayer. (d) Transient pore and periodic images. Smaller pores have been created at other points as well. The nanoparticle is not shown. Colours: lipid heads=purple, polar beads=dark blue.

The mixed nanoparticle crossed the lipid bilayer in both simulations. Its crossing was different from that of the C-type nanoparticle, as it 'dragged' several lipid heads in the hydrophobic core of the bilayer. In Figure 6.7, we show a series of snapshots from one of the simulations with the CP-type nanoparticle. A similar behaviour was observed in the other simulation. From the figure, we can observe the thinning of the bilayer and its expansion in X direction as the nanoparticle was pulled out of the bilayer. Also, some lipid heads can be noticed in the hydrophobic area of the bilayer.

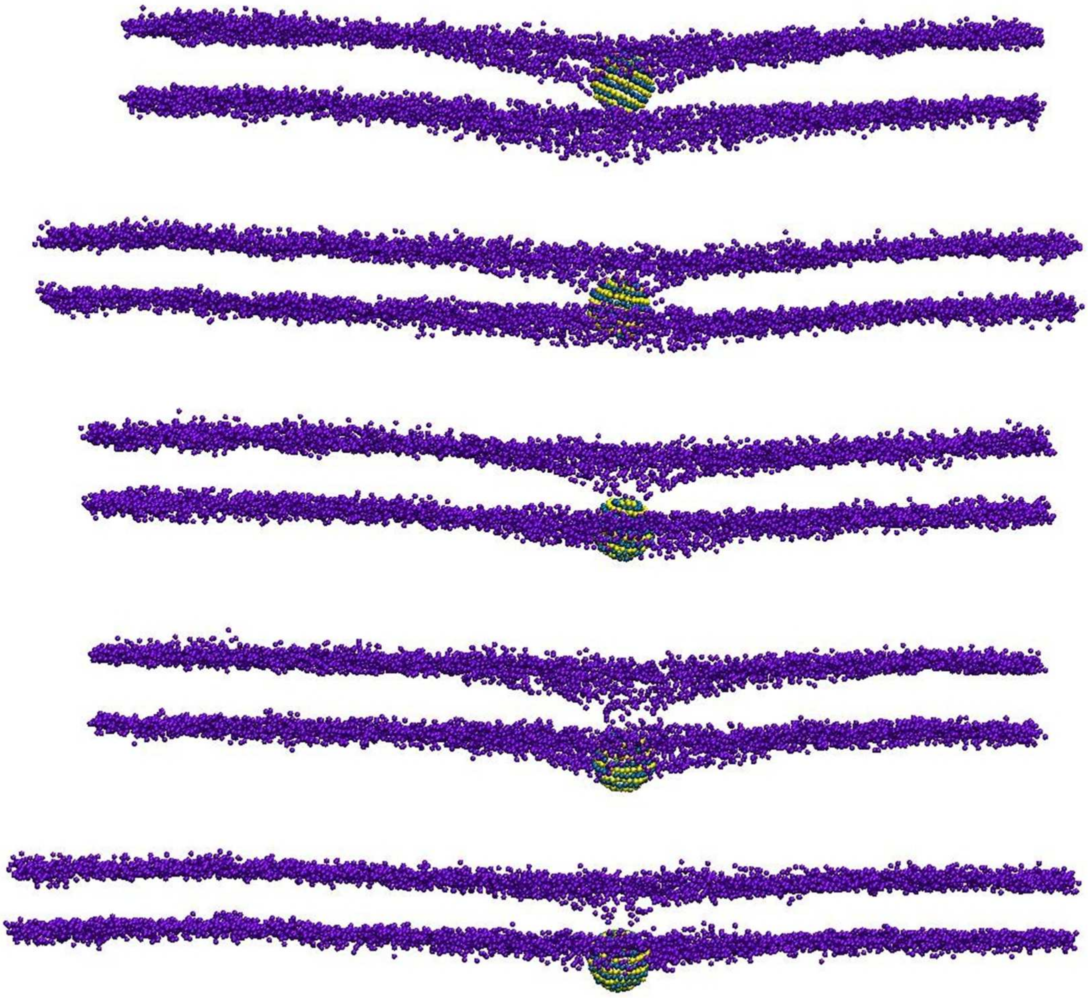

Figure 6.7: **Mixed nanoparticle insertion in the lipid bilayer**. Snapshots from the pulling simulation with CP-type nanoparticle. The nanoparticle enters the bilayer and drags several lipid heads into its hydrophobic core. A thinning of the bilayer is observed while pulling the nanoparticle out of the bilayer. Colours: lipid heads=purple, polar beads=dark blue.

It is important to note that we observed thinning of the bilayer in all of the performed simulations. In the cases of the hydrophobic and mixed nanoparticles, this happened while pulling the nanoparticles out of the lipid bilayer. For the hydrophilic nanoparticle this thinning and disruption of the membrane occurred while pulling it inside the bilayer. As in the case of the small nanoparticles, we calculated the area per lipid for the different types and the different simulations. We found an increase of the area per lipid by a factor of about 2.6. The value of this factor is similar for all types of nanoparticles and is probably indicative of their and lipid bilayer relative sizes. The configurations of the membranes resemble the ones observed in the simulations with the small nanoparticles. The main difference is that due to the expansion of the bilayer in X and Y directions, and consequently the 'shrinking' in Z direction, the bilayer interacted with its periodic images and eventually the system collapsed.

6.2.3 Charged nanoparticles

In this study, we considered three types of charged nanoparticles, positively charged and polar (Qd+P-type), negatively charged and hydrophobic (Qa+C-type) and negatively charged and polar (Qa+P-type). We have performed MD simulations with Qa+C- and Qa+P-type nanoparticles. Typical snapshots from these simulations are shown in Figure 6.8. Both nanoparticles adopted a positioning close to the surface of the lipid bilayer. In the case of the Qa+P-type nanoparticle, molecules of water lied between the nanoparticle and the phospholipid heads, whereas the Qa+C-type nanoparticle seemed to directly interact with the lipid bilayer. During the 30 nanoseconds of the simulations, we did not observe any distinct curvature of the membrane induced by the interaction with the nanoparticles.

We also performed Steered MD simulations for the three different charged nanoparticles. In all three simulations, we observed a high curvature and thinning of the bilayer until the systems collapsed due to the interactions with the periodic images of the bilayers and the nanoparticles.

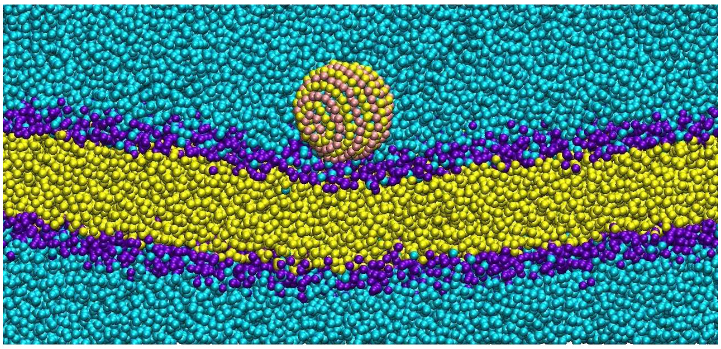

(a)

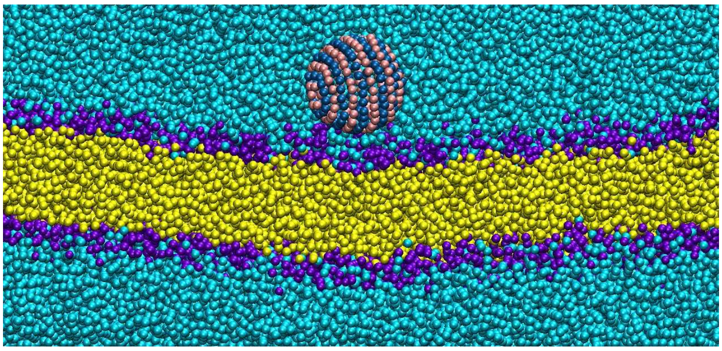

(b)

Figure 6.8: **Final snapshots from the MD simulations of the charged nanoparticles**. Colours: water=cyan, lipid heads=violet, Qa=pink, hydrophobic particles=yellow, polar particles=blue .

6.2.4 The effect of membrane size

We also tried to examine the effect that a smaller lipid bilayer may have to our results. We used a 3 nm polar nanoparticle with two different types of membranes DPPC and DOPC (Systems 4 and 5 respectively). The summary of these simulations is shown in Table 6.5. A similar behaviour to that for the big lipid bilayer was observed. However, in one of our simulations, we captured the formation of a transient water pore. Then, strong undulations of the lipid bilayer and partial engulfment of the nanoparticle were observed. Snapshots of this simulation are shown in Figure 6.9.

Table 6.5: **Summary of simulations for a big polar nanoparticle in a small lipid bilayer.**

	Behaviour
System 4	thinning of the lipid bilayer, hole around the nanoparticle
System 4	holes, membrane disruption
System 5	strong undulations
System 5	formation of transient water pore, strong undulations

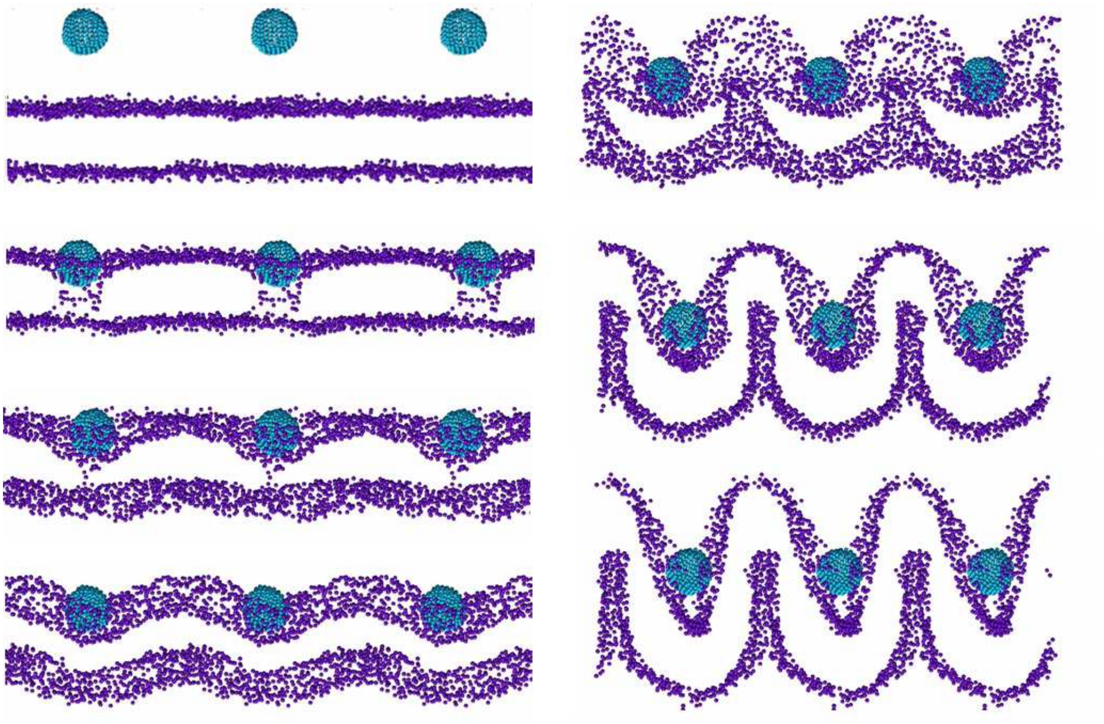

(a) (b)

Figure 6.9: **Pulling in a small membrane**. (a) A transient water pore opens and closes due to the nanoparticle pulling. (b) Big undulations and partial engulfment of the nanoparticle. The lipid heads are coloured purple and the hydrophilic nanoparticle blue.

6.3 Discussion

We performed simple and steered molecular dynamics simulations with nanoparticles of different sizes and nature. From the small nanoparticles, with a diameter of 1 nm, we observed the insertion of the hydrophobic and mixed nanoparticle in the bilayer. The mixed nanoparticle, however, seemed to 'drag' several phospholipid heads inside the lipid bilayer. The hydrophilic nanoparticle induces high curvature to the bilayer that eventually leads to the bilayer thinning and the creation of holes. From the calculation of the area per lipid and the configuration of the lipid bilayer, we could classify this thinning as an interdigitated state. The interdigitated state was also observed in the study by Ahmed and Wunder [123] with 5 nm diameter nanoparticles, and could be also linked to the thinning of the membrane reported in [122]. A thinning of the bilayer was also observed for our simulations with the C- and CP-type nanoparticles, only this time, it was induced by the pulling of the nanoparticles out of the bilayer.

Another important observation from our simulations with the small nanoparticles is that, in the case of the P- and CP-type, a disorder in the structure of the lipids can be captured by visualization and order parameter calculations. The order parameters in these two cases are significantly different to that of a pure lipid bilayer, indicating the level of interaction between the nanoparticles and the lipids.

A similar behaviour was captured in our simulations with the big nanoparticles. The C- and CP-type nanoparticles inserted into the bilayer, whereas the polar nanoparticle caused significant deformation to the lipid bilayer, including thinning and formation of holes. Thinning of the bilayer was also observed for the hydrophobic and mixed nanoparticles while pulling them out of the bilayer.

Sensitivity analysis has also been performed. We carried out two simulations, one for polar and one for hydrophobic nanoparticle, with a very small pulling rate in order to allow enough time for the membrane to react to the interaction with it. These simulations gave similar results to those from the simulations with the higher pulling rate. We also performed one simulation with a polar nanoparticle and a ten times smaller force constant. The results did not present differences to the previous ones.

From the MD simulations with the Qa+C and Qa+P nanoparticles, we observed an interfacial positioning. For the first case, a positioning very close to the lipid heads was captured. In the case of the Qa+P-type nanoparticle, we observed some water molecules between the nanoparticle and the lipid bilayer. We also performed Steered MD simulations with three types of charged nanoparticles. In all cases thinning of the bilayer was observed. I should mention here that better treatment of the electrostatic interactions, for example use of PME instead of the shift method, could give a more realistic description of the system and improve the accuracy of the results.

We need to keep in mind that the non-equilibrium simulations may provide some insight of otherwise difficult to capture events, however they should always be considered with caution. Future studies could be combined with more MD simulations. Also, nanoparticles with random distribution of hydrophobicity or charges could also constitute an interesting case study and could be compared with our 'striped' nanoparticles. An improvement in the description of our system would be to use a bigger water phase in order to avoid possible interaction between the bilayer and its periodic images due to the thinning effect.

We should mention again that this work is at a preliminary stage and it could only be used as a starting point for a more detailed study of the interaction of nanoparticles with lipid bilayers.

CHAPTER 7

Summary and conclusions

7.1 Summary of dissertation

Peptide-membrane interactions play an essential role in cells. A few of their functions include antimicrobial defence mechanisms, viral translocation, signal transduction and membrane fusion. Because of their importance in these processes, peptide-membrane interactions have been extensively investigated, both through theoretical, computational and experimental studies.

In this work, molecular dynamics simulations have been employed in the studies of peptide-membrane interactions. I am particularly interested in α-helical peptides, that constitute a potentially vast family of membrane-active peptides. The processes of interest, such as pore formation or self-assembly processes, run over long time and length scales. On the other hand, atomistic simulations are limited to several hundreds of nanoseconds and tens of nanometers. To overcome these limitations, in this study, a coarse-grained approach was adopted.

In the first chapter, I introduced the biological background of the system of interest (peptides and membranes). I elaborated on importance of peptide-membrane interactions, how computer simulations and molecular modelling can be instrumental in gaining information about them and reviewed the state of the art in this field.

A short description of the methodology used in this work followed in Chapter 2. Some basic ideas of statistical mechanics were presented, and the principles of molecular dynamics, free energy calculations and other methods employed in this work were reviewed. I then introduced the model used in this study. Specifically, a short description of the MARTINI coarse-grained model, the molecular mapping and the representation of lipids, lipid bilayers and peptides were presented.

In Chapter 3, I focused on several types of interactions between lipid membranes and α-helical peptides, based on the distribution of hydrophobicity along the helix. I employed the MARTINI coarse-grained force field and tested its ability to capture diverse types of behaviour. Four different classes of amphipathic α-helical peptides were considered: pore-forming, non-membrane-spanning, fusion and transmembrane peptides. The simulations provided us with useful insights on the formation of a barrel-stave pore. Also, amphipathic nonspanning peptides were described with sufficient accuracy. However, the picture was not as clear for fusion and transmembrane peptides. For SIV fusion peptides, our results both from atomistic and coarse-grained simulations seemed to underestimate the oblique insertion of the peptide that has been captured through experiments. In the case of transmembrane peptides, I did not manage to capture the spontaneous insertion. However, once a peptide was half-inserted in the lipid bilayer, it adopted a transmembrane position and remained there until the end of our simulations (a few microseconds). For each class of peptides, I also calculated the potential of mean force (PMF) for peptide translocation across the lipid bilayer and demonstrated that each class has a distinct shape of PMF.

Pore formation mechanisms play an important role in many biological processes, from ion-conduction across cell membranes to antimicrobial defence mechanisms and many more. I chose a synthetic peptide, LS3, which is simple (it has only two types of amino acids) and has the potential to form pores. I showed that the spontaneous formation of a barrel-stave pore formed by LS3 is within the limits of the employed coarse-grained protocol. In Chapter 4, I presented a series of simulations that provide further evidence of the propensity of LS3 to form pores as well as structural and dynamical information about them. For example, the barrel-stave pore captured in our studies was open for more than 14 μs and filled with water. Moreover, the calculated self-diffusion coefficient ($D_{lat} = 0.49 - 0.87\ \mu m^2/s$) is similar to the experimentally measured values for membrane proteins. I also investigated how pore formation mechanism depends on the structural modifications of LS3. Remarkably, the simulations of a shorter version of this peptide, (LSSLLSL)$_2$, showed that this peptide has a much lower propensity for poration and, when a complex does form, it has a toroidal structure. These complexes were different to the barrel-stave pore or the other complexes formed by LS3. They had a small diameter that does not allow for water to pass through it. Also, they were unstable, with the number of peptides taking part in them varying during the simulation. Another difference between the two observed pores was the structure of lipids in their vicinity, as shown by order parameters calculations. The PMF for (LSSLLSL)$_2$ was dramatically different to that of LS3, with the energy minima at the bilayer interfaces and the core of the bilayer being an unfavourable location of the peptide.

In Chapter 5, I extended our studies to the self-assembly and membrane internalization mechanisms of cell-penetrating peptides. In particular, I chose two peptides of significant technological importance, pHLIP and Pep-1. The formation of complexes of different sizes and the adsorption of pHLIP on the lipid bilayer surface were the two key observations of our simulations. These complexes were bound to the membrane surface and ‘squeezed out’ the lipid heads, resulting in the formation of defects on the surface of the bilayer. In the case of Pep-1, formation of complexes of different sizes was observed. The complexes were stable, with a constant number of peptides unless another free peptide approached and joined the aggregate. An interesting observation was that tryptophan seems to play and important role in the interaction of Pep-1 with the lipid bilayer as well as in peptide-peptide interactions. Another notable result was the formation of transient pore-like structures, once the peptide or the peptide ‘lump’ was slightly inside the lipid bilayer, close to the lipid head region. This was captured both by MD and Steered MD simulations. These structures had a toroidal shape and in two cases they were filled with water.

Finally, in Chapter 6, I presented some preliminary qualitative results from our simulation studies on interactions between nanoparticles and lipid membranes. Molecular dynamics simulations as well as Steered MD simulations were performed. Two different sizes, with 1 and 3 nm diameter, as well as different surface chemistry ranging from fully hydrophobic to charged nanoparticles were considered. An important observation from our simulations is the induction of an interdigitated state of the membrane when small hydrophilic or larger nanoparticles with some degree of polarity were pulled inside the lipid bilayer. From the molecular dynamics simulations of the charged nanoparticles an interfacial positioning was observed in all cases.

In summary, it has been shown that the formation and evolution of pores in membranes, the interfacial positioning of non-membrane-spanning peptides as well as other self-assembly processes are within the limits of coarse-grained molecular dynamics simulations. An important link between the barrel-stave and the toroidal mechanism and the length of the peptides was also established. Overall, this work has demonstrated that coarse-grained simulation models can be used to address biologically relevant processes.

7.2 Final thoughts and future directions

Some of the conclusions and future directions of this study could be summarized in five main subjects: *free energy calculations*, *implications of coarse-grained approaches and multiscale modelling*, *representation of the membrane*, *nanoparticles studies and other peptide systems* and *treatment of electrostatic interactions*. Here, I present some of our ideas and possible future directions in these five subjects.

Potential of mean force calculations

Potential of mean force (PMF) is a very useful tool in the studies of peptide-membrane interactions. I calculated the PMF for peptide translocation across the lipid bilayer and demonstrated that each class of the studied peptides has a distinct shape of PMF. A natural step forward in this study would be the calculation of PMF for more peptides belonging to each of the different classes in order to establish a general map of interactions. In addition to this, the effect of the presence of peptides, proteins or other biological entities in the lipid bilayer on the PMF profile could add further information in this map of behaviours. Also, calculation of the PMF with two reaction coordinates, the distance along the normal of the bilayer as well as the orientation of the peptide relative to it, could lead to a better understanding of the translocation mechanisms of α-helical peptides and in particular transmembrane helices.

The representation of the membrane

In our studies, the membrane is treated as a lipid bilayer with only one component. This could be one of the reasons for not being able to capture the direct translocation of a peptide unless an initial perturbation of the membrane was imposed. A more realistic approach would be the incorporation of membrane proteins, cholesterol or more than one lipid types in the description of the membrane. For example, incorporating membrane proteins in the membrane could apply a stress to the lipid bilayer important for several of its functions, such as peptide translocation across it. Also, the presence of cholesterol in the lipid bilayer would make it stiffer and more difficult to pass. PMF calculations under these two different conditions, the presence of membrane proteins or cholesterol, could give important insights in the peptide-membrane interactions and the factors that influence them.

Treatment of electrostatic interactions

The use of cut-off and shift techniques for the treatment of electrostatic interactions is a matter of extensive discussion and controversy in the area of molecular modelling. In the present study, I adopted the most widely used approach for MARTINI force field, the shift method. However, the use of PME method could be the next step to a more realistic representation of the system. For example, in the case of pHLIP or Pep-1 peptides the electrostatic interactions with the membrane may play an important role in the translocation mechanism. Moreover, in the studies of nanoparticles, where most of the available experimental data and applications are related to cationic particles, PME could possibly be a better treatment for the description of the system. Some simulations have already been performed with the charged nanoparticles and PME without however giving significantly different results. More investigation in the area is necessary.

Nanoparticles studies

The importance of nanoparticles in everyday life is indisputable. The studies presented in this dissertation are preliminary and limited to qualitative observations. Further more detailed information on the systems could offer a better understanding of the mechanisms of interactions of the nanoparticles with the lipid membranes. Also, simulations with the charges randomly placed at the surface of the nanoparticles could offer direct comparison with the available experimental data. Larger nanoparticles and systems could also be considered.

Coarse-grained approaches and multiscale modelling

Despite the overall success of the MARTINI force field to capture the behaviour of several types of α-helical peptides, there are still some reservations regarding its use in new systems. To start with, the MARTINI protocol implies that the secondary structure of the peptides is known and does not change in the process of interest. However, for several cases, like pHLIP peptide, this description is not adequate, as complex conformational evolution of a peptide is often an integral part of the peptide-membrane interaction mechanism. Furthermore, the CG treatment of water where several disjoint degrees of freedom are fused together in a single Lennard-Jones site also presents a well recognized issue. ‘Structureless’ and chargeless water is unable to describe water ordering in the vicinity of hydrophobic surfaces or orientation of water molecules in electric fields. This leaves a number of important peptide-membrane processes beyond the scope of the MARTINI. For example, the higher propensity of LS3 to form barrel-stave pores in the presence of a weak transmembrane potential most likely will not be adequately described by the MARTINI. Translocation of cationic peptides, such as many examples from the family of cell-penetrating peptides, also requires accurate description of water properties.

Even with these limitations, the MARTINI and other CG approaches provide a computationally powerful tool to identify and elucidate mechanisms of peptide-membrane interactions and self-assembly processes. The potential structures identified in the CG simulations can then serve as a starting point and be refined in more detailed atomistic studies. A further step in the peptide-membrane studies could be to adopt a multiscale approach and develop it as necessary in order to capture the different phenomena at the desired resolution. This approach may include sequential inverse mapping, hybrid simulations with different levels of resolution used simultaneously or an adaptive method which will allow for individual molecules to switch between different resolution levels.

Direct extension of the MARTINI (or any other CG approach) to new classes of peptides should be approached with caution. It seems that application of a CG approach to a new class of peptide-membrane interaction should involve careful validation (and if necessary re-calibration) of the approach against known experimental observations for several reference systems within the class. Once the applicability of the CG model is established, the CG approach can indeed provide a number of valuable insights on the behaviour of the system as a function of various system parameters.

APPENDIX A

Appendix A

Table A.1: History of classical molecular dynamics simulations of biomolecular systems.

year	molecular system	length of simulation (s)
1957	first MD simulation (hard discs, 2D)	
1964	atomic liquid (argon)	10^{-11}
1974	molecular liquid (water)	$5 \cdot 10^{-12}$
1977	protein (no solvent)	$2 \cdot 10^{-11}$
1983	protein in water	$2 \cdot 10^{-11}$
1989	protein-DNA complex in water	10^{-10}
1997	polypeptide folding in solvent	10^{-7}
2000	micelle formation	10^{-7}
200x	folding of a small protein	10^{-3}

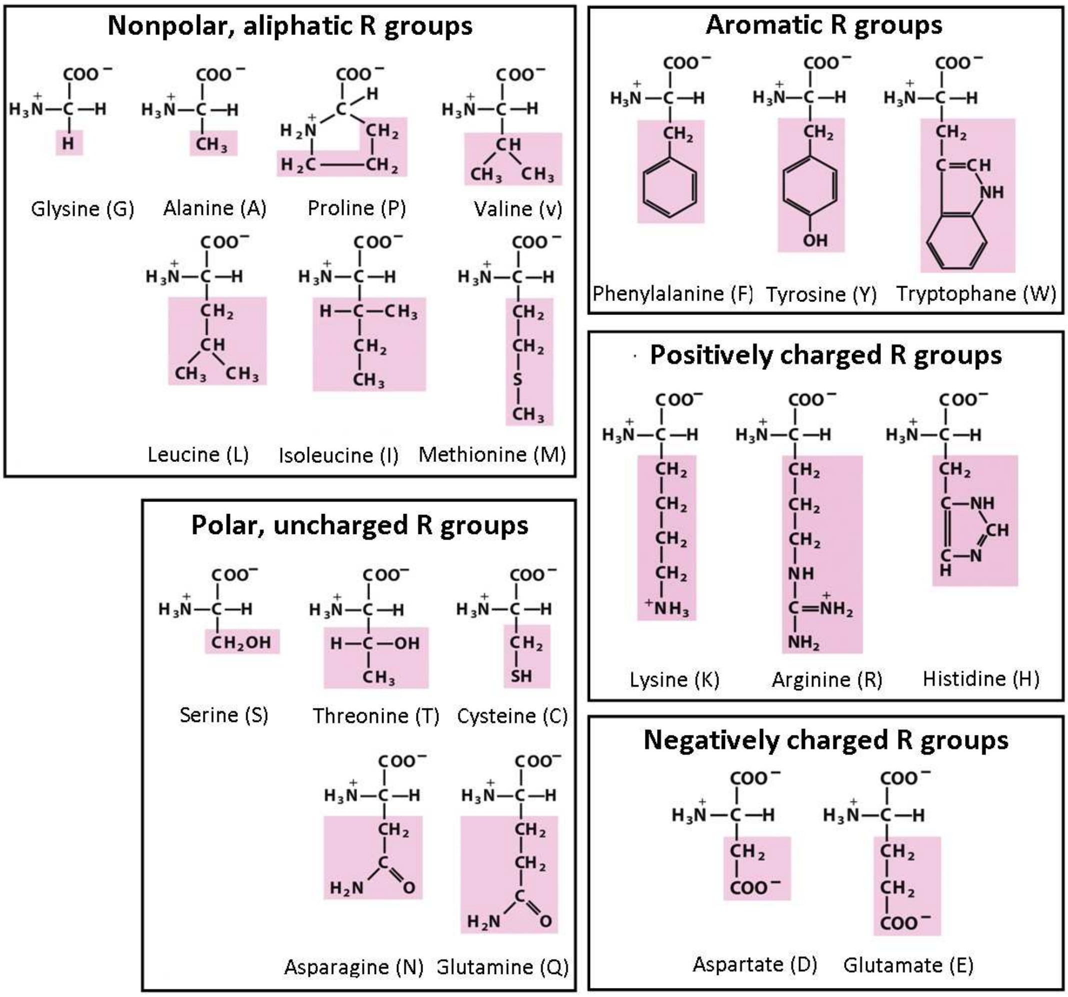

Figure A.1: **The 20 common amino acids**. The pink shaded parts represent the R group of each amino acid. In the case of histidine the R group is shown as uncharged, however at pH 7.0 a fraction of the group is positively charged. The figure has been adapted from [5].

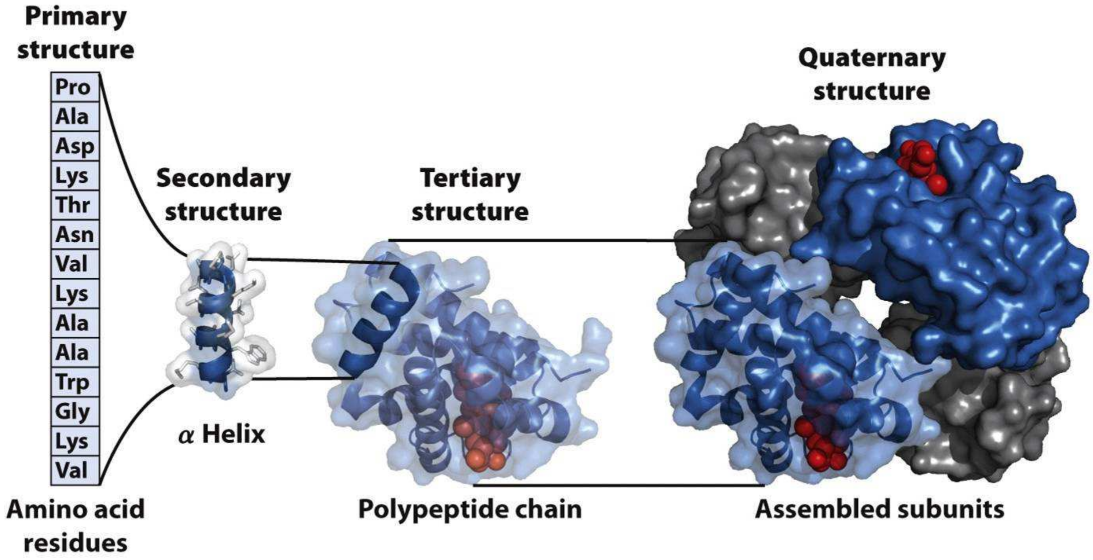

Figure A.2: **Different levels of structure in proteins - Hemoglobin.** Primary and secondary structures of a peptide chain that belongs to hemoglobin. In the tertiary structure we can see the position of the α-helical peptide in one of the polypeptide chains of the protein, whereas in the quaternary structure the whole protein is presented. The figure has been adapted from [5].

APPENDIX B

Appendix B

In this section, we will shortly describe the molecular dynamics program we have developed as part of this PhD.

1. The NVE ensemble:

(a) NVE with the leap-frog integrator scheme:

Firstly, we developed a code for the NVE ensemble using the leap-frog integrator scheme. In table B.1, we present the comparative results from the house code and a code that calculates the pressure and the potential energy based on the LJ equation of state. We can see that our results are in good agreement with those predicted by the equation of state[1].

---

[1] From now on all the quantities are in reduced units

Table B.1: **NVE with LF integrator vs EOS**. The results are for the same conditions, density $\rho = 0.7$, timestep $\Delta t = 0.005$, number of particles $nMol = 125$, and 30.000 timesteps.

$< T >$	$< P >$	$< P >_{eos}$	$< U >$	$< U >_{eos}$
1.1551	1.0391	0.7834	-4.4084	-4.4056
1.5028	2.1013	1.8659	-4.2091	-4.2111
1.8566	3.1605	2.9061	-3.9926	-4.0092

(b) NVE with the Gear predictor-corrector integrator scheme:

In order to achieve greater numerical accuracy, we implemented the NVE ensemble but this time using the Gear predictor-corrector algorithm. As we can see from the comparative table B.2, we have very good agreement between the two different approaches.

Table B.2: **Leap Frog vs Gear Predictor-Corrector**. These runs were performed for density $\rho = 0.7$, timestep $\Delta t = 0.005$, number of particles $nMol = 125$ and 30.000 timesteps.

T_{init}	$< T >_{LF}$	$< T >_{Gear}$	$< U >_{LF}$	$< U >_{Gear}$	$< P >_{LF}$	$< P >_{Gear}$
1.5	1.1551	1.1637	-4.4084	-4.4051	1.0391	1.0698
2.0	1.5028	1.5222	-4.2091	-4.1874	2.1013	2.1564
2.5	1.8566	1.9007	-3.9926	-3.9838	3.1605	3.2533

2. NVT ensemble:

However, in order to describe phenomena like the formation of a bilayer or the peptide insertion into a membrane, a more realistic approach should be followed. For this reason, the NVT ensemble where temperature is fixed is more appropriate. Consequently, the next step in the development of our MD code was from the NVE to the NVT ensemble.

For the application of the NVT ensemble, we chose to use the Nosé-Hoover thermostat which is considered one of the most accurate methods for keeping the temperature constant.

In order to validate the NVT program, we calculated the average temperature from the NVE code and imposed this temperature to the NVT ensemble. This way, we are able to compare the average quantities from both systems.

In tables B.3 and B, we present the comparative results from the NVE and NVT ensembles, respectively. We can see that the results from the NVT ensemble are in good agreement with those from the NVE ensemble.

Table B.3: **Average quantities - NVE ensemble with the Gear predictor-corrector integrator**. $\rho = 0.7$, $\Delta t = 0.005$, $nMol = 125$, 30.000 timesteps.

T_{init}	$< T >$	$< P >$	$< U >$	$< E_{kin} >$	$< E_{tot} >$
1.5	1.1637	1.0698	-4.4051	1.7316	-2.6768
2.0	1.5222	2.1564	-4.1874	2.2650	-1.9299
2.5	1.9007	3.2533	-3.9838	2.8283	-1.1521

Table B.4: **Average quantities - NVT ensemble**. $\rho = 0.7$, $\Delta t = 0.005$, $nMol = 125$, 30.000 timesteps, $Q = 10$.

T_{init}	$< T >$	$< P >$	$< U >$	$< E_{kin} >$	$< E_{tot} >$
1.1637	1.1636	1.0456	-4.4086	1.7315	-2.6784
1.5222	1.5218	2.1456	-4.1880	2.2646	-1.9281
1.9007	1.9005	3.2540	-3.9756	2.8281	-1.1558

In figure B.1, we see the basic characteristics of the thermostat parameter ξ. The oscillations around zero and the relative evolution of ξ and $d\xi/dt$ are two of the main features of the Nosé-Hoover thermostat.

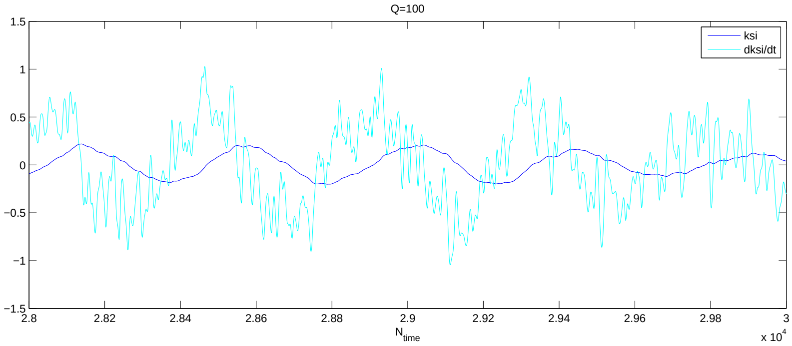

Figure B.1: ξ **and** $\dot{\xi}$ **versus time.**

3. NPT ensemble:

An even more realistic approach is the NPT ensemble where the pressure instead of the volume is conserved. This is more appropriate in our case since membranes tend to change their volume and keep the pressure almost constant. For the implementation of the NPT ensemble, we chose to use the Nosé-Hoover barostat.

In order to validate our NPT code, we ran the NVT Nosé-Hoover program for 125 particles, $V^* = 178,57$ and $T^* = 1,5$ and calculated $< U >$, $< K >$ and $< P >$. Then, we ran the NPT Nosé-Hoover program for 125 particles, $P_{ext} =< P >_{NVT}= 2,05$ and $T = T_{NVT} = 1,5$ and calculated again $< U >$, $< K >$ and $< P >$. The comparison is shown in the table below (table B.5).

Table B.5: **Comparative table.**

	NVT	NPT
$< U >$	-4.2083	-4.1793
$< K >$	2.2306	2.2466
$< V >$	178.57	179.8013

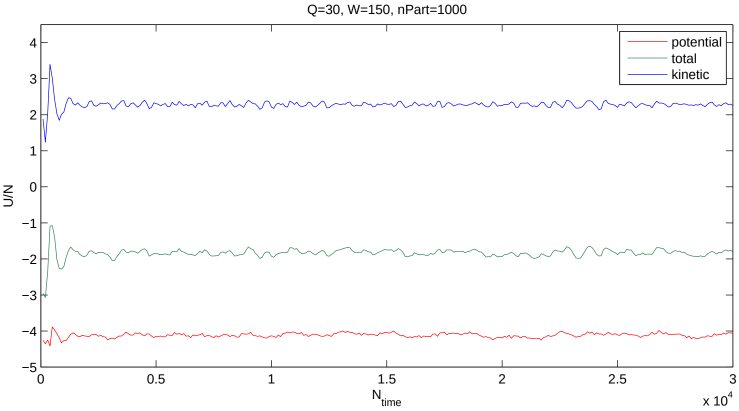

Figure B.2: **U/N versus time** ($\Delta t = 0.0005$, Q=30, W=150).

In the following figures, we observe the evolution of the average quantities for barostat $W = 50$.

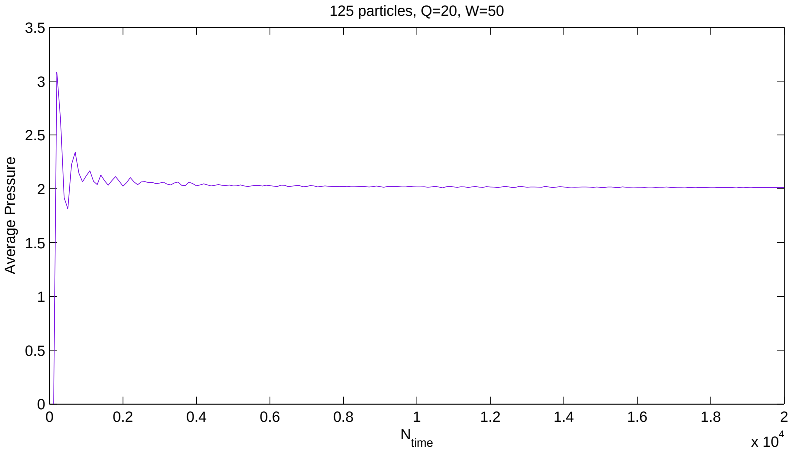

Figure B.3: **Average pressure vs N$_{time}$.**

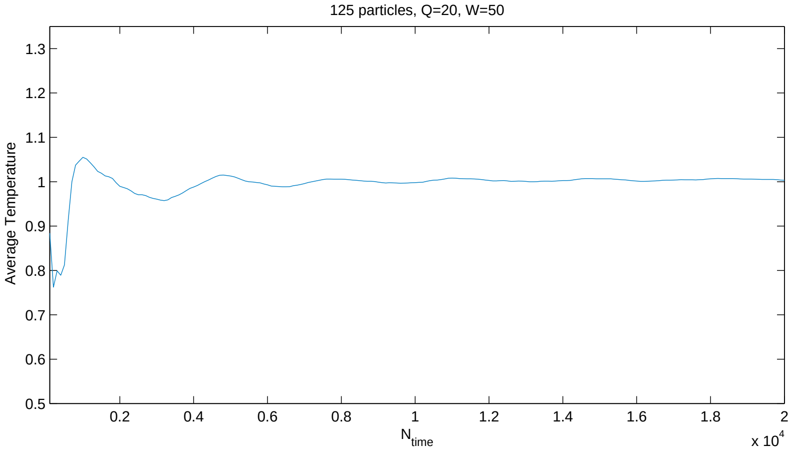

Figure B.4: **Average temperature vs N$_{time}$.**

APPENDIX C

Appendix C

In the figure below, we present the free energy profiles for the translocation of SIV fusion peptide across a DOPC bilayer, calculated by using different methods for the treatment of electrostatics and pressure coupling. In particular, we perform an umbrella sampling simulation with the Nosé-Hoover thermostat and one with the Particle-mesh Ewald (PME) for the treatment of electrostatic interactions. For the PME scheme, we use a grid spacing of 0.12 nm and quadratic interpolation. The rest of the parameters in the two simulations are as in the original.

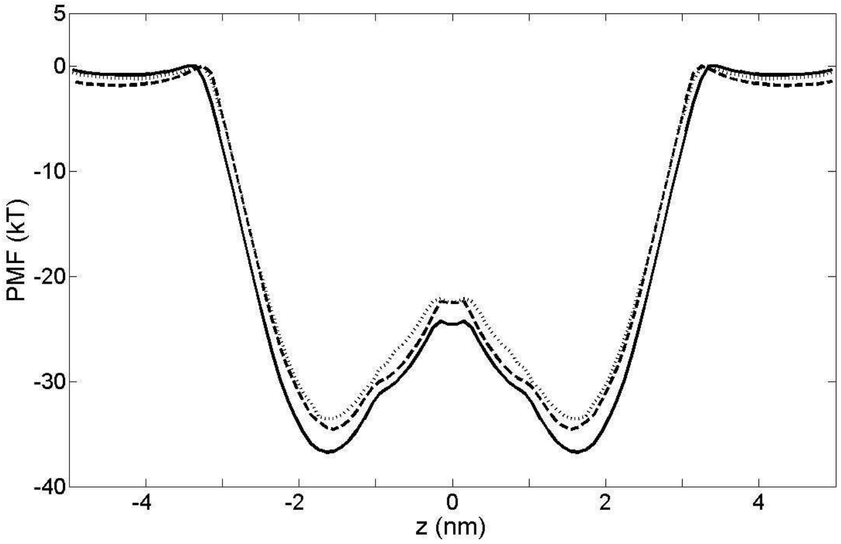

Figure C.1: **Potential of mean force for the transfer of SIV peptide from the water phase across a DOPC lipid bilayer**. The PMF calculated by and umbrella sampling simulation with cut-off treatment for electrostatics and Berendsen thermostat is represented by a continuous line, with Nosé-Hoover thermostat by a dashed line and the with PME by a thin dashed line.

References

[1] S. J. Singer and G. L. Nicolson, "Fluid mosaic model of structure of cell-membranes," *Science*, vol. 175, no. 4023, pp. 720–731, 1972.

[2] Encyclopedia Britannica, Inc. http://www.britannica.com (accessed Nov. 21, 2009).

[3] J. Seddon, "Structure of the inverted hexagonal (HII) phase, and non-lamellar phase-transitions of lipids," *Biochimica et Biophysica Acta*, vol. 1031, no. 1, pp. 1–69, 1990.

[4] K. Balali-Mood, T. Harroun, and J. Bradshaw, "Molecular dynamics simulations of a mixed DOPC/DOPG bilayer," *European Physical Journal E*, vol. 12, no. Suppl. 1, pp. S135–S140, 2003.

[5] D. L. Nelson and M. M. Cox, *Principles of Biochemistry*. W. H. Freeman and Company, fifth ed., 2008.

[6] R. Brasseur, "Differentiation of lipid-associating helices by use of three-dimensional molecular hydrophobicity potential calculations," *Journal of Biological Chemistry*, vol. 266, no. 24, pp. 16120–16127, 1991.

[7] M. Yeaman and N. Yount, "Mechanisms of antimicrobial peptide action and resistance," *Pharmacological Reviews*, vol. 55, no. 1, pp. 27–55, 2003.

[8] U. Langel, *Handbook of cell-penetrating peptides*. Taylor & Francis, 2nd ed., 2007.

[9] S. El-Andaloussi, T. Holm, and U. Langel, "Cell-penetrating peptides: Mechanisms and applications," *Current Pharmaceutical Design*, vol. 11, pp. 3597–3611, 2005.

[10] A. Pokorny, T. Birkbeck, and P. Almeida, "Mechanism and kinetics of delta-Lysin interaction with phospholipid vesicles," *Biochemistry*, vol. 41, no. 36, pp. 11044–11056, 2002.

[11] O. Toke, "Antimicrobial peptides: New candidates in the fight against bacterial infections," *Biopolymers*, vol. 80, no. 6, pp. 717–735, 2005.

[12] G. B. Melikyan, "Common principles and intermediates of viral protein-mediated fusion: the HIV-1 paradigm," *Retrovirology*, vol. 5, 2008.

[13] S. Deshayes, A. Heitz, M. C. Morris, P. Charnet, G. Divita, and F. Heitz, "Insight into the mechanism of internalization of the cell-penetrating carrier peptide Pep–1 through conformational analysis," *Biochemistry*, vol. 43, pp. 1449–1457, 2004.

[14] R. Fischer, M. Fotin-Mleczek, H. Hufnagel, and R. Brock, "Break on through to the other side - biophysics and cell biology shed light on cell-penetrating peptides," *ChemBioChem*, vol. 6, pp. 2126–2142, 2005.

[15] D. Allende, S. Simon, and T. J. McIntosh, "Melittin-induced bilayer leakage depends on lipid material properties: Evidence for toroidal pores," *Biophysical Journal*, vol. 88, no. 3, pp. 1828 – 1837, 2005.

[16] J. D. Lear, Z. R. Wasserman, and W. F. Degrado, "Synthetic amphiphilic peptide models for protein ion channels," *Science*, vol. 240, no. 4856, pp. 1177–1181, 1988.

[17] K. S. Åkerfeldt, J. D. Lear, Z. R. Wasserman, L. A. Chung, and W. F. Degrado, "Synthetic peptides as models for ion channel proteins," *Accounts of Chemical Research*, vol. 26, pp. 191–197, 1993.

[18] J. D. Lear, J. P. Schneider, P. K. Kienker, and W. F. DeGrado, "Electrostatic effects on ion selectivity and rectification in designed ion channel peptides," *Journal of American Chemical Society*, vol. 119, pp. 3212–3217, 1997.

[19] L. Chaloin, E. De, P. Charnet, G. Molle, and F. Heitz, "Ionic channels formed by a primary amphipathic peptide containing a signal peptide and a nuclear localization sequence," *Biochimica et Biophysica Acta-Biomembranes*, vol. 1375, no. 1-2, pp. 52–60, 1998.

[20] E. De, L. Chaloin, A. Heitz, J. Mery, G. Molle, and F. Heitz, "Conformation and ion channel properties of a five-helix bundle protein," *Journal of Peptide Science*, vol. 7, no. 1, pp. 41–49, 2001.

[21] P. Haris and D. Chapman, "The conformational-analysis of peptides using Fourier-Transform IR spectroscopy," *Biopolymers*, vol. 37, no. 4, pp. 251–263, 1995.

[22] L. Tamm and S. Tatulian, "Infrared spectroscopy of proteins and peptides in lipid bilayers," *Quarterly Reviews of Biophysics*, vol. 30, no. 4, pp. 365–429, 1997.

[23] E. Goormaghtigh, V. Raussens, and J. Ruysschaert, "Attenuated total reflection infrared spectroscopy of proteins and lipids in biological membranes," *Biochimica et Biophysica Acta-Reviews on Biomembranes*, vol. 1422, no. 2, pp. 105–185, 1999.

[24] V. Vie, N. Van Mau, L. Chaloin, E. Lesniewska, C. Le Grimellec, and F. Heitz, “Detection of peptide-lipid interactions in mixed monolayers, using isotherms, atomic force microscopy, and Fourier transform infrared analyses,” *Biophysical Journal*, vol. 78, no. 2, pp. 846–856, 2000.

[25] S. Frey and L. Tamm, “Orientation of melittin in phospholipid-bilayers - A polarized attenuated total reflection infrared study,” *Biophysical Journal*, vol. 60, no. 4, pp. 922–930, 1991.

[26] I. Martin, M. Dubois, F. Defrisequertain, T. Saernark, A. Burny, R. Brasseur, and J. Ruysschaert, “Correlation between fusogenicity of synthetic modified peptides corresponding to the NH2-terminal extremity of Simian Immunodeficiency Virus GP32 and their mode of insertion into the lipid bilayer - An infrared-spectroscopy study,” *Journal of Virology*, vol. 68, no. 2, pp. 1139–1148, 1994.

[27] Wang, J and Lee, S-H and Chen, Z, “Quantifying the ordering of adsorbed proteins in situ,” *Journal of Physical Chemistry B*, vol. 112, no. 7, pp. 2281–2290, 2008.

[28] I. de la Arada, J.-P. Julien, B. G. de la Torre, N. Huarte, D. Andreu, E. F. Pai, J. L. R. Arrondo, and J. L. Nieva, “Structural constraints imposed by the conserved fusion peptide on the HIV-1 gp41 epitope recognized by the broadly neutralizing antibody 2F5,” *Journal of Physical Chemistry B*, vol. 113, no. 41, pp. 13626–13637, 2009.

[29] J. P. Bradshaw, M. J. M. Darkes, T. A. Haroun, J. Katsaras, and R. M. Epand, “Oblique membrane insertion of viral fusion peptide probed by neutron diffraction,” *Biochemistry*, vol. 39, no. 22, pp. 6581–6585, 2000.

[30] L. Chaloin, P. Vidal, A. Heitz, N. VanMau, J. Mery, G. Divita, and F. Heitz, “Conformations of primary amphipathic carrier peptides in membrane mimicking environments,” *Biochemistry*, vol. 36, no. 37, pp. 11179–11187, 1997.

[31] M. Lindberg, J. Jarvet, U. Langel, and A. Graslund, “Secondary structure and position of the cell-penetrating peptide transportan in SDS micelles as determined by NMR,” *Biochemistry*, vol. 40, no. 10, pp. 3141–3149, 2001.

[32] M. Magzoub, K. Kilk, L. Eriksson, U. Langel, and A. Graslund, “Interaction and structure induction of cell-penetrating peptides in the presence of phospholipid vesicles,” *Biochimica et Biophysica Acta-Biomembranes*, vol. 1512, no. 1, pp. 77–89, 2001.

[33] R. Ketchem, W. Hu, and T. Cross, “High-resolution conformation of Gramicidin-A in a lipid bilayer by solid-state NMR,” *Science*, vol. 261, no. 5127, pp. 1457–1460, 1993.

[34] B. Bechinger, “The structure, dynamics and orientation of antimicrobial peptides in membranes by multidimensional solid-state NMR spectroscopy,” *Biochimica et Biophysica Acta-Biomembranes*, vol. 1462, no. 1-2, pp. 157–183, 1999.

[35] J. Yang, C. Gabrys, and D. Weliky, “Solid-state nuclear magnetic resonance evidence for an extended beta strand conformation of the membrane-bound HIV-1 fusion peptide,” *Biochemistry*, vol. 40, no. 27, pp. 8126–8137, 2001.

[36] S. Yamaguchi, T. Hong, A. Waring, R. Lehrer, and M. Hong, “Solid-state NMR investigations of peptide-lipid interaction and orientation of a β-sheet antimicrobial peptide, protegrin,” *Biochemistry*, vol. 41, no. 31, pp. 9852–9862, 2002.

[37] F. Porcelli, B. Buck, D. Lee, K. Hallock, A. Ramamoorthy, and G. Veglia, “Structure and orientation of pardaxin determined by NMR experiments in model membranes,” *Journal of Biological Chemistry*, vol. 279, no. 44, pp. 45815–45823, 2004.

[38] A. Ramamoorthy, S. Thennarasu, D. Lee, A. Tan, and L. Maloy, “Solid-state NMR investigation of the membrane-disrupting mechanism of antimicrobial peptides MSI-78 and MSI-594 derived from magainin 2 and melittin,” *Biophysical Journal*, vol. 91, no. 1, pp. 206–216, 2006.

[39] S. Bhattacharjya and A. Ramamoorthy, “Multifunctional host defense peptides: functional and mechanistic insights from NMR structures of potent antimicrobial peptides,” *FEBS Journal*, vol. 276, no. 22, pp. 6465–6473, 2009.

[40] B. Bechinger, M. Zasloff, and S. Opella, “Structure and orientation of the antibiotic peptide magainin in membranes by solid-state nuclear-magnetic-resonance spectroscopy,” *Protein Science*, vol. 2, pp. 2077–2084, DEC 1993.

[41] S. Opella, F. Marassi, J. Gesell, A. Valente, Y. Kim, M. Oblatt-Montal, and M. Montal, “Structures of the M2 channel-lining segments from nicotinic acetylcholine and NMDA receptors by NMR spectroscopy,” *Nature Structural Biology*, vol. 6, pp. 374–379, APR 1999.

[42] S. J. Opella, A. C. Zeri, and S. H. Park, “Structure, dynamics, and assembly of filamentous bacteriophages by nuclear magnetic resonance spectroscopy,” *Annual Review of Physical Chemistry*, vol. 59, pp. 635–657, 2008.

[43] Brasseur, R and Deleu, M and Mingeot-Leclercq, M-P and Francius, G and Dufrene, Y F., “Probing peptide-membrane interactions using AFM,” *Surface and Interface Analysis*, vol. 40, no. 3-4, pp. 151–156, 2008.

[44] H. You, X. Qi, G. Grabowski, and L. Yu, “Phospholipid membrane interactions of saposin C: In situ atomic force microscopic study,” *Biophysical Journal*, vol. 84, no. 3, pp. 2043–2057, 2003.

[45] S. Morandat and K. El Kirat, “Real-time atomic force microscopy reveals cytochrome C-induced alterations in neutral lipid bilayers,” *Langmuir*, vol. 23, no. 22, pp. 10929–10932, 2007.

[46] Wang, H and Obenauer-Kutner, L and Lin, M and Huang, Y and Grace, M. J. and Lindsay, S. M., “Imaging glycosylation,” *Journal of American Chemical Society*, vol. 130, no. 26, pp. 8154–8155, 2008.

[47] M. L. Kraft, P. K. Weber, M. L. Longo, I. D. Hutcheon, and S. G. Boxer, “Phase separation of lipid membranes analyzed with high-resolution secondary ion mass spectrometry,” *Science*, vol. 313, no. 5795, pp. 1948–1951, 2006.

[48] P. D. Veith, S. G. Dashper, N. M. O'Brien-Simpson, R. A. Paolini, R. Orth, K. A. Walsh, and E. C. Reynolds, "Major proteins and antigens of Treponema denticola," *Biochimica et Biophysica Acta-Proteins and Proteomics*, vol. 1794, no. 10, pp. 1421–1432, 2009.

[49] S. G. Boxer, M. L. Kraft, and P. K. Weber, "Advances in imaging secondary ion mass spectrometry for biological samples," *Annual Review of Biophysics*, vol. 38, pp. 53–74, 2009.

[50] H. Mozsolits, H. Wirth, J. Werkmeister, and M. Aguilar, "Analysis of antimicrobial peptide interactions with hybrid bilayer membrane systems using surface plasmon resonance," *Biochimica et Biophysica Acta-Biomembranes*, vol. 1512, no. 1, pp. 64–76, 2001.

[51] H. Mozsolits and M. Aguilar, "Surface plasmon resonance spectroscopy: An emerging tool for the study of peptide-membrane interactions," *Biopolymers*, vol. 66, no. 1, pp. 3–18, 2002.

[52] H. Mozsolits, W. Thomas, and M. Aguilar, "Surface plasmon resonance spectroscopy in the study of membrane-mediated cell signalling," *Journal of Peptide Science*, vol. 9, no. 2, pp. 77–89, 2003.

[53] M. M. Domingues, P. S. Santiago, M. A. R. B. Castanho, and N. C. Santos, "What can light scattering spectroscopy do for membrane-active peptide studies," *Journal of Peptide Science*, vol. 14, no. 4, pp. 394–400, 2008.

[54] W. Wimley and S. White, "Designing transmembrane alpha-helices that insert spontaneously," *Biochemistry*, vol. 39, no. 15, pp. 4432–4442, 2000.

[55] J. Bradshaw, M. Darkes, J. Katsaras, and R. Epand, "Neutron diffraction studies of viral fusion peptides," *Physica B*, vol. 276, pp. 495–498, 2000.

[56] T. Harroun, K. Balali-Mood, I. Gourlay, and J. Bradshaw, "The fusion peptide of simian immunodeficiency virus and the phase behaviour of N-methylated dioleoylphosphatidylethanolamine," *Biochimica et Biophysica Acta-Biomembranes*, vol. 1617, no. 1-2, pp. 62–68, 2003.

[57] F. Leemakers and J. Scheutjens, "Statistical thermodynamics of association colloids .1. Lipid bilayer-membranes," *Journal of Chemical Physics*, vol. 89, no. 5, pp. 3264–3274, 1988.

[58] L. Meijer, F. Leermakers, and J. Lyklema, "Self-consistent-field modeling of complex molecules with united atom detail in inhomogeneous systems. Cyclic and branched foreign molecules in dimyristoylphosphatidylcholine membranes," *Journal of Chemical Physics*, vol. 110, no. 13, pp. 6560–6579, 1999.

[59] R. Kik, F. Leermakers, and J. Kleijn, "Molecular modeling of lipid bilayers and the effect of protein-like inclusions," *Physical Chemistry Chemical Physics*, vol. 7, no. 9, pp. 1996–2005, 2005.

[60] Q. Liang and Y.-Q. Ma, "Inclusion-mediated lipid organization in supported membranes on a patterned substrate," *Journal of Physical Chemistry B*, vol. 112, no. 7, pp. 1963–1967, 2008.

[61] Q. Liang and Y. Q. Ma, "Organization of membrane-associated proteins in lipid bilayers," *European Physical Journal E*, vol. 25, no. 2, pp. 129–138, 2008.

[62] C.-l. Ren and Y.-q. Ma, "Structure and organization of nanosized-inclusion-containing bilayer membranes," *Physical Review E*, vol. 80, no. 1, Part 1, 2009.

[63] P. Lague, M. Zuckermann, and B. Roux, "Protein inclusion in lipid membranes: A theory based on the hypernetted chain integral equation," *Faraday Discussions*, vol. 111, pp. 165–172, 1998.

[64] P. Lague, M. Zuckermann, and B. Roux, "Lipid-mediated interactions between intrinsic membrane proteins: A theoretical study based on integral equations," *Biophysical Journal*, vol. 79, no. 6, pp. 2867–2879, 2000.

[65] P. Lague, M. Zuckermann, and B. Roux, "Lipid-mediated interactions between intrinsic membrane proteins: Dependence on protein size and lipid composition," *Biophysical Journal*, vol. 81, no. 1, pp. 276–284, 2001.

[66] P. La Rocca, Y. Shai, and M. Sansom, "Peptide-bilayer interactions: simulations of dermaseptin B, an antimicrobial peptide," *Biophysical Chemistry*, vol. 76, no. 2, pp. 145–159, 1999.

[67] P. La Rocca, P. Biggin, D. Tieleman, and M. Sansom, "Simulation studies of the interaction of antimicrobial peptides and lipid bilayers," *Biochimica et Biophysica Acta-Biomembranes*, vol. 1462, no. 1-2, pp. 185–200, 1999.

[68] W. Still, A. Tempczyk, R. Hawley, and T. Hendrickson, "Semianalytical treatment of solvation for molecular mechanics and dynamics," *Journal of American Chemical Society*, vol. 112, no. 16, pp. 6127–6129, 1990.

[69] W. Im, M. Feig, and C. Brooks, "An implicit membrane generalized born theory for the study of structure, stability, and interactions of membrane proteins," *Biophysical Journal*, vol. 85, pp. 2900–2918, NOV 1 2003.

[70] W. Im, M. Lee, and C. Brooks, "Generalized born model with a simple smoothing function," *Journal of Computational Chemistry*, vol. 24, pp. 1691–1702, NOV 15 2003.

[71] M. Ulmschneider, M. Sansom, and A. Di Nola, "Properties of integral membrane protein structures: Derivation of an implicit membrane potential," *Proteins-Structure function and bioinformatics*, vol. 59, no. 2, pp. 252–265, 2005.

[72] M. B. Ulmschneider, J. P. Ulmschneider, M. S. P. Sansom, and A. Di Nola, "A generalized Born implicit-membrane representation compared to experimental insertion free energies," *Biophysical Journal*, vol. 92, pp. 2338–2349, APR 1 2007.

[73] J. McCammon, B. Gelin, and M. Karplus, "Dynamics of folded proteins," *Nature*, vol. 267, no. 5612, pp. 585–590, 1977.

[74] K. Damodaran, K. Merz, and B. Gaber, "Interaction od small peptides with lipid bilayers," *Biophysical Journal*, vol. 69, no. 4, pp. 1299–1308, 1995.

[75] K. Belohorcova, J. Davis, T. Woolf, and B. Roux, "Structure and dynamics of an amphiphilic peptide in a lipid bilayer: A molecular dynamics study," *Biophysical Journal*, vol. 73, no. 6, pp. 3039–3055, 1997.

[76] S. Berneche, M. Nina, and B. Roux, "Molecular dynamics simulation of melittin in a dimyristoylphosphatidylcholine bilayer membrane," *Biophysical Journal*, vol. 75, no. 4, pp. 1603–1618, 1998.

[77] H. Leontiadou, A. E. Mark, and S. J. Marrink, "Antimicrobial peptides in action," *Journal of American Chemical Society*, vol. 128, pp. 12156–12161, 2006.

[78] D. Sengupta, H. Leontiadou, A. E. Mark, and S. J. Marrink, "Toroidal pores formed by antimicrobial peptides show significant disorder," *Biochimica et Biophysica Acta-Biomembranes*, vol. 1778, no. 10, pp. 2308–2317, 2008.

[79] H. D. Herce and A. E. Garcia, "Molecular dynamics simulations suggest a mechanism for translocation of the HIV-1 TAT peptide across lipid membranes," *Proceedings of the National Academy of Sciences of the United States of America*, vol. 104, no. 52, pp. 20805–20810, 2007.

[80] S. Yesylevskyy, S. J. Marrink, and A. E. Mark, "Alternative mechanisms for the interaction of the cell-penetrating peptides Penetratin and the TAT peptide with lipid bilayers," *Biophysical Journal*, vol. 97, no. 1, pp. 40–49, 2009.

[81] S. Izvekov and G. Voth, "Multiscale coarse-graining of mixed phospholipid/cholesterol bilayers," *Journal of Chemical Theory and Computation*, vol. 2, no. 3, pp. 637–648, 2006.

[82] S. J. Marrink, A. H. de Vries, and A. E. Mark, "Coarse grained model for semiquantitative lipid simulations," *Journal of Physical Chemistry B*, vol. 108, pp. 750–760, 2004.

[83] M. Venturoli, M. M. Sperotto, M. Kranenburg, and B. Smit, "Mesoscopic models of biological membranes," *Physics Reports*, vol. 437, pp. 1–54, 2006.

[84] S. J. Marrink, A. H. de Vries, and D. P. Tieleman, "Lipids on the move: Simulations of membrane pores, domains, stalks and curves," *Biochimica et Biophysica Acta-Biomembranes*, vol. 1788, no. 1, Sp. Iss. SI, pp. 149–168, 2009.

[85] T. Murtola, A. Bunker, I. Vattulainen, M. Deserno, and M. Karttunen, "Multiscale modeling of emergent materials: biological and soft matter," *Physical Chemistry Chemical Physics*, vol. 11, no. 12, pp. 1869–1892, 2009.

[86] D. J. Michel and D. J. Cleaver, "Coarse-grained simulation of amphiphilic self-assembly," *Journal of Chemical Physics*, vol. 126, no. 3, p. 34506, 2007.

[87] Smit, Berend and Hilbers, P. A. J. and Esselink, K. and Rupert, N. M. and van Os, N. M. and Schlijper, A. G., "Computer simulations of a water/oil interface in the presence of micelles," *Nature*, vol. 348, pp. 624–625, 1990.

[88] Smit, Berend and Hilbers, P. A. J. and Esselink, K. and Rupert, N. M. and van Os, N. M. and Schlijper, A. G., "Structure of a water/oil interface in the presence of micelles: a computer simulation study," *Journal of Physical Chemistry*, vol. 95, pp. 6361–6368, 1991.

[89] R. D. Groot and P. B. Warren, "Dissipative particle dynamics: Bridging the gap between atomistic and mesoscopic simulation," *Journal of Chemical Physics*, vol. 107, pp. 4423–4435, 1997.

[90] M. Kranenburg, M. Venturoli, and B. Smit, "Phase behaviour and induced interdigitation in bilayers studied with dissipative particle dynamics," *Journal Physical Chemistry B*, vol. 107, pp. 11491–11501, 2003.

[91] M. Venturoli, B. Smit, and M. Sperotto, "Simulation studies of protein-induced bilayer deformations, and lipid-induced protein tilting, on a mesoscopic model for lipid bilayers with embedded proteins," *Biophysical Journal*, vol. 88, no. 3, pp. 1778–1798, 2005.

[92] U. Schmidt, G. Guigas, and M. Weiss, "Cluster formation of transmembrane proteins due to hydrophobic mismatching," *Physical Review Letters*, vol. 101, no. 12, 2008.

[93] F. J.-M. de Meyer, M. Venturoli, and B. Smit, "Molecular simulations of lipid-mediated protein-protein interactions," *Biophysical Journal*, vol. 95, no. 4, pp. 1851–1865, 2008.

[94] R. Goetz and R. Lipowsky, "Computer simulations of bilayer membranes: Self-assembly and interfacial tension," *Journal of Chemical Physics*, vol. 108, no. 17, pp. 7397–7409, 1998.

[95] J. C. Shelley, M. Y. Shelley, R. C. Reeder, S. Bandyopadhyay, and M. L. Klein, "A coarse grained model for phospholipid simulations," *Journal of Physical Chemistry B*, vol. 105, pp. 4464–4470, 2001.

[96] J. C. Shelley, M. Y. Shelley, R. C. Reeder, S. Bandyopadhyay, P. B. Moore, and M. L. Klein, "Simulations of phospholipids using a coarse grain model," *Journal of Physical Chemistry B*, vol. 105, pp. 9785–9792, 2001.

[97] S. J. Marrink and A. E. Mark, "Molecular view of hexagonal phase formation in phospholipid membranes," *Biophysical Journal*, vol. 84, pp. 3894–3900, 2004.

[98] S. J. Marrink, J. Risselada, and A. E. Mark, "Simulation of gel phase formation and melting in lipid bilayers using a coarse grained model," *Chemistry and Physics of Lipids*, vol. 135, pp. 223–244, 2005.

[99] V. Knecht and S. J. Marrink, "Molecular dynamics simulations of lipid vesicle fusion in atomic detail," *Biophysical Journal*, vol. 92, pp. 4254–4261, 2007.

[100] P. J. Bond and M. S. P. Sansom, "Insertion and assembly of membrane proteins via simulation," *Journal of Americal Chemical Society*, vol. 128, pp. 2697–2704, 2006.

[101] P. J. Bond, J. Holyoake, A. Ivetac, S. Khalid, and M. S. P. Sansom, "Coarse-grained molecular dynamics simulations of membrane proteins and peptides," *Journal of Structural Biology*, vol. 157, pp. 593–605, 2007.

[102] S. Khalid, P. J. Bond, J. Holyoake, R. W. Hawtin, and M. S. P. Sansom, "DNA and lipid bilayers: self-assembly and insertion," *Journal of the Royal Society Interface*, vol. 5, no. Suppl. 3, pp. S241–S250, 2008.

[103] K. Balali-Mood, P. J. Bond, and M. S. P. Sansom, "Interaction of monotopic membrane enzymes with a lipid bilayer: A coarse-grained MD simulation study," *Biochemistry*, vol. 48, no. 10, pp. 2135–2145, 2009.

[104] K. Cox and M. S. P. Sansom, "One membrane protein, two structures and six environments: a comparative molecular dynamics simulation study of the bacterial outer membrane protein PagP," *Molecular Membrane Biology*, vol. 26, no. 4, pp. 205–214, 2009.

[105] L. Monticelli, S. K. Kandasamy, X. Periole, D. P. Tieleman, and S. J. Marrink, "The MARTINI Coarse-Grained Force Field: Extension to Proteins," *Journal of Chemical Theory and Computation*, vol. 4, pp. 819–834, 2008.

[106] S. J. Marrink, H. J. Risselada, S. Yefimov, D. P. Tieleman, and A. H. de Vries, "The MARTINI force field: coarse grained model for biomolecular simulations," *Journal of Physical Chemistry B*, vol. 111, pp. 7812–7824, 2007.

[107] H. J. Risselada and S. J. Marrink, "Curvature effects on lipid packing and dynamics in liposomes revealed by coarse grained molecular dynamics simulations," *Physical Chemistry Chemical Physics*, vol. 11, no. 12, pp. 2056–2067, 2009.

[108] A. Khalfa, W. Treptow, B. Maigret, and M. Tarek, "Self-assembly of peptides near or within membranes using coarse grained MD simulations," *Chemical Physics*, vol. 358, no. 1-2, pp. 161–170, 2009.

[109] P. Gkeka and L. Sarkisov, "Spontaneous formation of a barrel-stave pore in a coarse-grained model of the synthetic LS3 peptide and a DPPC lipid bilayer," *Journal of Physical Chemistry B*, vol. 113, no. 1, pp. 6–8, 2009.

[110] S. Izvekov and A. G. Voth, "A multiscale coarse-graining method for biolmolecular systems," *Journal of Physical Chemistry B*, vol. 109, pp. 2469–2473, 2005.

[111] J. Zhou, F. I. Thorpe, S. Izvekov, and A. G. Voth, "Coarse-grained peptide modeling using a systematic multiscale approach," *Biophysical journal*, vol. 92, pp. 4289–4303, 2007.

[112] J. Michel, M. Orsi, and J. W. Essex, "Prediction of partition coefficients by multiscale hybrid atomic-level/coarse-grain simulations," *Journal of Physical Chemistry B*, vol. 112, no. 3, pp. 657–660, 2008.

[113] M. Orsi, D. Y. Haubertin, W. E. Sanderson, and J. W. Essex, "A quantitative coarse-grain model for lipid bilayers," *Journal of Physical Chemistry B*, vol. 112, no. 3, pp. 802–815, 2008.

[114] M. Orsi, W. E. Sanderson, and J. W. Essex, "Permeability of Small Molecules through a Lipid Bilayer: A Multiscale Simulation Study," *Journal of Physical Chemistry B*, vol. 113, no. 35, pp. 12019–12029, 2009.

[115] S. Popielarski, S. Pun, and M. Davis, "A nanoparticle-based model delivery system to guide the rational design of gene delivery to the liver. 1. Synthesis and characterization," *Bioconjugate Chemistry*, vol. 16, no. 5, pp. 1063–1070, 2005.

[116] Y. B. Patil, S. K. Swaminathan, T. Sadhukha, L. Ma, and J. Panyam, "The use of nanoparticle-mediated targeted gene silencing and drug delivery to overcome tumor drug resistance," *Biomaterials*, vol. 31, no. 2, pp. 358–365, 2010.

[117] S. K. Dhoke and A. S. Khanna, "Electrochemical behavior of nano-iron oxide modified alkyd based waterborne coatings," *Materials Chemistry and Physics*, vol. 117, no. 2-3, pp. 550–556, 2009.

[118] A. E. Nel, L. Maedler, D. Velegol, T. Xia, E. M. V. Hoek, P. Somasundaran, F. Klaessig, V. Castranova, and M. Thompson, "Understanding biophysicochemical interactions at the nano-bio interface," *Nature Materials*, vol. 8, no. 7, pp. 543–557, 2009.

[119] A. Verma, O. Uzun, Y. Hu, Y. Hu, H.-S. Han, N. Watson, S. Chen, D. J. Irvine, and F. Stellacci, "Surface-structure-regulated cell-membrane penetration by monolayer-protected nanoparticles," *Nature Materials*, vol. 7, no. 7, pp. 588–595, 2008.

[120] T. Xia, L. Rome, and A. Nel, "Nanobiology - Particles slip cell security," *Nature Materials*, vol. 7, no. 7, pp. 519–520, 2008.

[121] P. R. Leroueil, S. A. Berry, K. Duthie, G. Han, V. M. Rotello, D. Q. McNerny, J. R. Baker, Jr., B. G. Orr, and M. M. B. Holl, "Wide varieties of cationic nanoparticles induce defects in supported lipid bilayers," *Nano Letters*, vol. 8, no. 2, pp. 420–424, 2008.

[122] Y. Roiter, M. Ornatska, A. R. Rammohan, J. Balakrishnan, D. R. Heine, and S. Minko, "Interaction of lipid membrane with nanostructured surfaces," *Langmuir*, vol. 25, no. 11, pp. 6287–6299, 2009.

[123] S. Ahmed and S. L. Wunder, "Effect of high surface curvature on the main phase transition of supported phospholipid bilayers on SiO2 nanoparticles," *Langmuir*, vol. 25, no. 6, pp. 3682–3691, 2009.

[124] H. Lee and R. G. Larson, "Coarse-grained molecular dynamics studies of the concentration and size dependence of fifth- and seventh-generation PAMAM dendrimers on pore formation in DMPC bilayer," *Journal of Physical Chemistry B*, vol. 112, no. 26, pp. 7778–7784, 2008.

[125] L.-T. Yan and X. Yu, "Enhanced permeability of charged dendrimers across tense lipid bilayer membranes," *ACS NANO*, vol. 3, no. 8, pp. 2171–2176, 2009.

[126] R. S. G. D'Rozario, C. L. Wee, E. J. Wallace, and M. S. P. Sansom, "The interaction of C-60 and its derivatives with a lipid bilayer via molecular dynamics simulations," *Nanotechnology*, vol. 20, no. 11, 2009.

[127] Y. Li and N. Gu, "Thermodynamics of charged nanoparticle adsorption on charge-neutral membranes: A simulation study," *Journal of Physical Chemistry B*, 2010.

[128] E. Egberts, S. Marrink, and H. Berendsen, "Molecular-dynamics simulation of a phospholipid membrane," *European Biophysics Journal with Biophysics Letters*, vol. 22, no. 6, pp. 423–436, 1994.

[129] H. C. Andersen, "Molecular dynamics simulations at constant pressure and/or temperature," *Journal of Chemical Physics*, vol. 72, no. 4, p. 2384, 1980.

[130] S. Nosé, "Constant temperature molecular dynamics methods," *Progress of Theoretical Physics Supplement*, vol. 103, 1991.

[131] W. G. Hoover, "Canonical dynamics: Equilibrium phase-space distributions," *Physical Review A*, vol. 31, no. 3, 1985.

[132] W. G. Hoover, "Constant-pressure equations of motion," *Physical Review A*, vol. 34, no. 3, p. 2499, 1986.

[133] S. Nosé, "A molecular-dynamics method for simulations in the canonical ensemble," *Molecular Physics*, vol. 52, no. 2, pp. 255–268, 1984.

[134] S. Nosé, "A unified formulation of the constant temperature molecular-dynamics methods," *Journal of Chemical Physics*, vol. 81, no. 1, pp. 511–519, 1984.

[135] H. J. C. Berendsen, J. P. M. Postma, W. F. Vangunsteren, A. Dinola, and J. R. Haak, "Molecular dynamics with coupling to an external bath," *Journal of Chemical Physics*, vol. 81, no. 8, pp. 3684–3690, 1984.

[136] P. Hunenberger H., "Thermostat algorithms for molecular dynamics simulations," *Advances in Polymer Science*, vol. 173, 2005.

[137] Leach, A. R., *Molecular Modelling, Principles and Applications*. Pearson Education Limited, 2nd ed., 2001.

[138] D. Frenkel and B. Smit, *Understanding Molecular Simulation*. Academic Press, 2006.

[139] M. P. Allen and D. J. Tildesley, *Computer Simulation of Liquids*. Oxford University Press, 1991.

[140] L. Verlet, "Computer experiments on classical fluids: I. Thermodynamical properties of Lennard-Jones molecules," *Physical Review*, vol. 159, no. 1, pp. 98–&, 1967.

[141] R. Hochney, S. Goel, and J. Eastwood, "Quiet high-resolution computer models of a plasma," *Journal of Computational Physics*, vol. 14, no. 2, pp. 148–158, 1974.

[142] C. Kandt, W. Ash L., and P. Tieleman D., "Setting up and running molecular dynamics simulations of membrane proteins," *Methods*, vol. 41, 2007.

[143] G. Torrie and J. Valleau, "Non-physical sampling distributions in Monte-Carlo free-energy estimation - umbrella sampling," *Journal of Computational Physics*, vol. 23, no. 2, pp. 187–199, 1977.

[144] S. Kumar, D. Bouzida, R. Swendsen, P. Kollman, and J. Rosenberg, "The weighted histogram analysis method for free-energy calculations on biomolecules .1. The method," *Journal of Computational Chemistry*, vol. 13, no. 8, pp. 1011–1021, 1992.

[145] A. Kukol, *Molecular Modeling of Proteins*. Humana Press, 2008.

[146] Humphrey, W. and Dalke, A. and Schulten, K., "VMD: Visual molecular dynamics," *Journal of Molecular Graphics*, vol. 14, pp. 33–38, 1996.

[147] D. van der Spoel, E. Lindahl, B. Hess, G. Groenhof, A. E. Mark, and H. Berendsen, "Gromacs: Fast, flexible, and free," *Journal of Computational Chemistry*, vol. 26, 2005.

[148] A. J. Kaats, H. L. Galiana, and J. L. Nadeau, "Standardizing the atomic description, axis and centre of biological ion channels," *Journal of Neuroscience Methods*, vol. 165, pp. 135–143, 2007.

[149] M. Horth, B. Lambrecht, M. Chuah Lay Kim, F. Bex, C. Thiriart, J.-M. Ruysschaert, A. Burny, and R. Brasseur, "Theoretical and functional analysis of the SIV fusion peptide," *The EMBO Journal*, vol. 10, no. 10, pp. 2747–2755, 1991.

[150] A. Schanck, J. Peuvot, and R. Brasseur, "Influence of the mode of insertion of SIV peptides into membranes on the structure of model membrane as studied by ^{31}P NMR," *Biochemical and Biophysical Research Communications*, vol. 250, no. RC989001, pp. 12–14, 1998.

[151] M. Oblatt-Montal, L. Buhler, T. Iwamoto, J. Tomich, and M. Montal, "Synthetic peptides and 4-helix bundle proteins as model systems for the pore-forming structure of channel proteins .1. Transmembrane segment M2 of the nicotinic cholinergic receptor-channel is a key pore-lining structure," *The Journal of Biological Chemistry*, vol. 268, no. 20, pp. 14601–14607, 1993.

[152] G. Reddy, T. Iwamoto, J. Tomich, and M. Montal, "Synthetic peptides and 4-helix bundle proteins as model systems for the pore-forming structure of channel proteins 2. Transmembrane segment M2 of the brain glycine receptor is a plausible candidate for the pore-lining structure," *The Journal of Biological Chemistry*, vol. 268, no. 20, pp. 14608–14615, 1993.

[153] C. Becker, M. Oblatt-Montal, G. Kochendoerfer, and M. Montal, "Chemical synthesis and single channel properties of tetrameric and pentameric TASPs (template-assembled synthetic proteins) derived from the transmembrane domain of HIV virus protein u (Vpu)," *The Journal of Biological Chemistry*, vol. 279, no. 17, pp. 17483–17489, 2004.

[154] M. Mutter, G. Tuchscerer, C. Miller, K. Altmann, R. Carey, D. Wyss, A. Labhartdt, and J. Rivier, "Template-assembled synthetic proteins with 4-helix-bundle topology - Total chemical synthesis and conformational studies," *Journal of American Chemical Society*, vol. 114, no. 4, pp. 1463–1470, 1992.

[155] A. Grove, M. Mutter, J. Rivier, and M. Montal, "Template-assembled synthetic proteins designed to adopt a globular, 4-helix bundle conformation form ionic channels in lipid bilayers," *Journal of American Chemical Society*, vol. 115, no. 14, pp. 5919–5924, 1993.

[156] R. F. Epand, I. Martin, J.-M. Ruysschaert, and R. Epand, "Membrane orientation of the SIV fusion peptide determines its effect on bilayer stability and ability to promote membrane fusion," *Biochemical and Biophysical Research Communications*, vol. 205, no. 3, pp. 1938–1943, 1994.

[157] A. Colotto, J. Martin, J.-M. Ruysschaert, A. Sen, and R. M. Epand, "Structural study of the interaction between the siv fusion peptide and model membranes," *Biochemistry*, vol. 35, no. 3, pp. 980–989, 1996.

[158] S. Kamath and T. C. Wong, "Membrane structure of the human immunodeficiency virus gp41 fusion domain by molecular dynamics simulation," *Biophysical Journal*, vol. 83, no. 1, pp. 135–143, 2002.

[159] M. Bosch, K. Fargnoli, S. Picciafuoco, F. Giombini, F. Wong-Staal, and G. Franchini, "Identification of the fusion peptide of primate immunodeficiency viruses," *Science*, vol. 244, no. 4905, pp. 694–697, 1989.

[160] I. Martin, F. Defrise-Quertain, V. Mandieau, and N. M. Nielsen, "Fusogenic activity of SIV Simian Immunodeficiency Virus peptides located in the gp32 amino terminal domain," *Biochemistry*, vol. 39, no. 22, pp. 6581–6585, 1991.

[161] Brasseur, R. and Lorge, P. and Goormaghtigh, E. and Ruysschaert, J.-M. and Espion, D. and Burny, A., "The mode of insertion of the paramyxovirus F1 N-terminus into lipid matrix, an initial step in host cell/virus fusion.," *Virus Genes*, vol. 1, no. 4, pp. 325–332, 1988.

[162] W. R. Gallaher, "Detection of a fusion peptide sequence in the transmembrane protein of human immunodeficiency virus," *Cell*, vol. 50, no. 3, pp. 327–328, 1987.

[163] S. Smith, D. Song, S. Shekar, M. Groesbeek, M. Ziliox, and S. Aimoto, "Structure of the transmembrane dimer interface of glycophorin A in membrane bilayers," *Biochemistry*, vol. 40, no. 22, pp. 6553–6558, 2001.

[164] Y. Reshetnyak, O. Andreev, U. Lehnert, and D. Engelman, "Translocation of molecules into cells by pH-dependent insertion of a transmembrane helix," *Proceedings of the National Academy of Sciences of the United States of America*, vol. 103, no. 17, pp. 6460–6465, 2006.

[165] O. A. Andreev, A. D. Dupuy, M. Segala, S. Sandugu, D. A. Serra, C. O. Chichester, D. M. Engelman, and Y. K. Reshetnyak, "Mechanism and uses of a membrane peptide that targets tumors and other acidic tissues *in vivo*," *Proceedings of the National Academy of Sciences of the United States of America*, vol. 104, no. 19, pp. 7893–7898, 2007.

[166] Y. K. Reshetnyak, O. A. Andreev, M. Segala, V. S. Markin, and D. M. Engelman, "Energetics of peptide (pHLIP) binding to and folding across a lipid bilayer membrane," *Proceedings of the National Academy of Sciences of the United States of America*, vol. 105, no. 40, pp. 15340–15345, 2008.

[167] M. Zoonens, Y. K. Reshetnyak, and D. M. Engelman, "Bilayer interactions of pHLIP, a peptide that can deliver drugs and target tumors," *Biophysical Journal*, vol. 95, no. 1, pp. 225–235, 2008.

[168] H. J. Pownall, A. M. J. Hu A. amd Gotto, J. J. Albers, and J. T. Sparrow, "Activation of lecithin: cholesterol acyltransferase by a synthetic model lipid-associating peptide," *Proceedings of the National Academy of Sciences of the United States of America*, vol. 77, no. 6, pp. 3154–3158, 1980.

[169] Berendsen, H. J. C. and van der Spoel, D. and van Drunen, R. , "Gromacs: A message-passing parallel molecular dynamics implementation," *Computer Physics Communications*, vol. 91, pp. 43–56, 1995.

[170] Hypercube, Inc. Home Page. http://www.hyper.com (accessed Nov. 21, 2009).

[171] MARTINI. http://md.chem.rug.nl/˜marrink/MARTINI/Parameters.html (accessed Nov. 21, 2009).

[172] O. Berger, O. Edholm, and F. Jahnig, "Molecular dynamics simulations of a fluid bilayer of dipalmitoylphosphatidylcholine at full hydration, constant pressure, and constant temperature," *Biophysical Journal*, vol. 72, no. 5, pp. 2002–2013, 1997.

[173] S. W. I. Siu, R. Vacha, P. Jungwirth, and R. A. Bockmann, "Biomolecular simulations of membranes: Physical properties from different force fields," *Journal of Chemical Physics*, vol. 128, no. 12, 2008.

[174] Theoretical & Computational Membrane Biology Home Page, Saarland University. http://www.bioinf.uni-sb.de/RB (accessed Nov. 21, 2009).

[175] Berendsen, H. J. C. and Postma, J. P. M. and van Gunsteren, W. F. and Hermans, J., *Intermolecular forces*, pp. 331–342. D. Reidel; Dordrecht, Holland, 1981.

[176] A. H. de Vries, A. E. Mark, and S. J. Marrink, "The binary mixing behavior of phospholipids in a bilayer: A molecular dynamics study," *Journal of Physical Chemistry B*, vol. 108, no. 7, pp. 2454–2463, 2004.

[177] P. K. Kienker, W. F. DeGrado, and J. D. Lear, "A helical-dipole model describes the single-channel current rectification of an uncharged peptide ion channel," *Proceedings of the National Academy of Sciences of the United States of America*, vol. 91, pp. 4859–4863, 1994.

[178] G. R. Dieckmann, J. D. Lear, Q. F. Zhong, M. L. Klein, W. F. DeGrado, and K. A. Sharp, "Exploration of the structural features defining ion channel conduction," *Biophysical Journal*, vol. 76, no. 2, pp. 618–630, 1999.

[179] L. Chung, J. Lear, and W. Degrado, "Fluorescence studies of the secondary structure and orientation of a model ion channel peptide in phospholipid-vesicles," *Biochemistry*, vol. 31, no. 28, pp. 6608–6616, 1992.

[180] L. Lins, B. Charloteaux, A. Thomas, and R. Brasseur, "Computational study of lipid-destabilizing protein fragments: Towards a comprehensive view of tilted peptides," *Proteins*, vol. 44, no. 4, pp. 435–447, 2001.

[181] R. Efremov, D. Nolde, A. Konshina, N. Syrtcev, and A. Arseniev, "Peptides and proteins in membranes: What can we learn via computer simulations?," *Current Medicinal Chemistry*, vol. 11, no. 18, pp. 2421–2442, 2004.

[182] P. J. Bond, C. L. Wee, and M. S. P. Sansom, "Coarse-grained molecular dynamics simulations of the energetics of helix insertion into a lipid bilayer," *Biochemistry*, vol. 47, no. 43, pp. 11321–11331, 2008.

[183] G. Baumann and P. Mueller, "A molecular model of membrane excitability," *Journal of Supramolecular Structure*, vol. 2, no. 5/6, pp. 538–557, 1974.

[184] The R.E.W. Hancock Laboratory. http://cmdr.ubc.ca/bobh/ (accessed April 12, 2010).

[185] P. Malovrh, G. Viero, M. D. Serra, Z. Podlesek, J. H. Lakey, P. Maek, G. Menestrina, and G. Anderluh, "A novel mechanism of pore formation," *Journal of Biological Chemistry*, vol. 278, no. 25, pp. 22678–22685, 2003.

[186] L. Thogersen, B. Schiott, T. Vosegaard, N. C. Nielsen, and E. Tajkhorshid, "Peptide Aggregation and Pore Formation in a Lipid Bilayer: A Combined Coarse-Grained and All Atom Molecular Dynamics Study," *Biophysical Journal*, vol. 95, no. 9, pp. 4337–4347, 2008.

[187] J. Dittmer, L. Thogersen, J. Underhaug, K. Bertelsen, T. Vosegaard, J. M. Pedersen, B. Schiott, E. Tajkhorshid, T. Skrydstrup, and N. C. Nielsen, "Incorporation of Antimicrobial Peptides into Membranes: A Combined Liquid-State NMR and Molecular Dynamics Study of Alamethicin in DMPC/DHPC Bicelles," *Journal of Physical Chemistry B*, vol. 113, no. 19, pp. 6928–6937, 2009.

[188] H. Leontiadou, A. E. Mark, and S. J. Marrink, "Molecular dynamics simulations of hydrophilic pores in lipid bilayers," *Biophysical journal*, vol. 86, 2004.

[189] C. Espenel, E. Margeat, P. Dosset, C. Arduise, C. Le Grimellec, C. A. Royer, C. Boucheix, E. Rubinstein, and P.-E. Milhiet, "Single-molecule analysis of CD9 dynamics and partitioning reveals multiple modes of interaction in the tetraspanin web," *The Journal of Cell Biology*, vol. 182, no. 4, pp. 765–776, 2008.

[190] Y. Gambin, R. Lopez-Esparza, M. Reffay, E. Sierecki, N. Gov, M. Genest, R. Hodges, and W. Urbach, "Lateral mobility of proteins in liquid membranes

revisited," *Proceedings of the National Academy of Sciences of the United States of America*, vol. 103, no. 7, pp. 2098–2102, 2006.

[191] H. Randa, L. Forrest, G. Voth, and M. Sansom, "Molecular dynamics of synthetic leucine-serine ion channels in a phospholipid membrane," *Biophysical Journal*, vol. 77, no. 5, pp. 2400–2410, 1999.

[192] A. D. Frankel and C. O. Pado, "Cellular Uptake of the Tat Protein from Human Immunodeficiency Virus," *Cell*, vol. 55, pp. 1189–1193, 1988.

[193] A. H. Joliot, C. Pernelle, H. Deangostini-Bazin, and A. Prochiantz, "Antennapedia homeobox peptide regulates neural morphogenesis," *Proceedings of the National Academy of Sciences of the United States of America*, vol. 88, pp. 1864–1868, 1991.

[194] Y. Li, Y. Mao, R. V. Rosal, R. D. Dinnen, A. C. Williams, P. W. Brandt-Rauf, and R. L. Fine, "Selective induction of apoptosis through the FADD/Caspase-8 pathway by a p53 C-terminal peptide in human pre-malignant and malignant cells," *International Journal of Cancer*, vol. 115, pp. 55–64, 2005.

[195] M. Jain, S. C. Chauhan, A. P. Singh, G. Venkatraman, D. Colcher, and S. K. Batra, "Penetratin improves tumor retention of single-chain antibodies: A novel step toward optimization of radioimmunotherapy of solid tumors," *Cancer Research*, vol. 65, no. 17, pp. 7840–7846, 2005.

[196] S. E. Perea, O. Reyes, Y. Puchades, O. Mendoza, N. S. Vispo, I. Torrens, A. Santos, R. Silva, B. Acevedo, E. Lopez, V. Falcon, and D. F. Alonso, "Antitumor effect of a novel proapoptotic peptide that impairs the phosphorylation by the protein kinase 2," *Cancer Research*, vol. 64, pp. 7127–7129, 2004.

[197] M. Bucci, J.-P. Gratton, R. D. Rudic, L. Acevedo, F. Roviezzo, G. Cirino, and W. C. Sessa, "*In vivo* delivery of the caveolin-1 scaffolding domain inhibits nitric oxide synthesis and reduces inflammation," *Nature Medicine*, vol. 6, no. 12, pp. 1362–1367, 2000.

[198] Y. Reshetnyak, M. Segala, O. Andreev, and D. Engelman, "A monomeric membrane peptide that lives in three worlds: In solution, attached to, and inserted across lipid bilayers," *Biophysical Journal*, vol. 93, no. 7, pp. 2363–2372, 2007.

[199] M. Morris, J. Depollier, J. Mery, F. Heitz, and G. Divita, "A peptide carrier for the delivery of biologically active proteins into mammalian cells," *Nature Biotechnology*, vol. 19, no. 12, pp. 1173–1176, 2001.

[200] J. Killian and G. von Heijne, "How proteins adapt to a membrane-water interface," *Trends in Biochemical Sciences*, vol. 25, no. 9, pp. 429–434, 2000.

[201] K. Weller, S. Lauber, M. Lerch, A. Renaud, H. Merkle, and O. Zerbe, "Biophysical and biological studies of end-group-modified derivatives of Pep-1," *Biochemistry*, vol. 44, no. 48, pp. 15799–15811, 2005.

[202] S. Henriques and M. Castanho, “Consequences of nonlytic membrane perturbation to the translocation of the cell penetrating peptide Pep-1 in lipidic vesicles,” *Biochemistry*, vol. 43, no. 30, pp. 9716–9724, 2004.

[203] M. A. Munoz-Morris, F. Heitz, G. Divita, and M. C. Morris, “The peptide carrier Pep-1 forms biologically efficient nanoparticle complexes,” *Biochemical and Biophysical Research Communications*, vol. 355, no. 4, pp. 877–882, 2007.

[204] R. McClain and J. Breen, “The image-based observation of the L beta I-to-L-beta phase transition in solid-supported lipid bilayers,” *Langmuir*, vol. 17, no. 16, pp. 5121–5124, 2001.

Epilogos

This is the point where I realize that I have reached the end of this PhD. It has been a great experience that made me stronger and more complete. It would not be like this if I did not have good friends with me to support me and give me a smile when difficulties arose.

Πὰνο, σ′ ϵυχαριστὼ που ὴσουν πὰντα δὶπλα μου.

Ζωὴ, αν και γνωριζὸμαστϵ λὶγο καιρὸ, σϵ αισθὰνομαι δικὸ μου ὰνθρωπο. Σ′ ϵυχαριστὼ.

Μϵροπὰκι, Μὶλλυ ϵυχαριστὼ.

Thanks to all my friends from the university.

Eduardo, espero que saibas que tu és uma das pessoas que eu mais gosto e que a tua amizade durante estes últimos anos foi realmente importante para mim. Não te esqueças de mim.

José, obrigada por me fazeres sorrir. Tú dás significado aquilo que eu faço...